

STATIC AND DYNAMIC CHARACTERISTICS OF INGAN-BASED LASER DIODES

THÈSE N° 6083 (2014)

PRÉSENTÉE LE 24 JANVIER 2014

À LA FACULTÉ DES SCIENCES DE BASE

LABORATOIRE EN SEMICONDUCTEURS AVANCÉS POUR LA PHOTONIQUE ET L'ÉLECTRONIQUE
PROGRAMME DOCTORAL EN PHOTONIQUE

ÉCOLE POLYTECHNIQUE FÉDÉRALE DE LAUSANNE

POUR L'OBTENTION DU GRADE DE DOCTEUR ÈS SCIENCES

PAR

Luca Alex Milo SULMONI

acceptée sur proposition du jury:

Prof. C. Moser, président du jury
Prof. N. Grandjean, Dr J.-F. Carlin, directeurs de thèse
Prof. B. Deveaud-Plédran, rapporteur
Dr J. Heffernan, rapporteur
Prof. M. Kneissl, rapporteur



ÉCOLE POLYTECHNIQUE
FÉDÉRALE DE LAUSANNE

Suisse
2014

If you can meet with Triumph and Disaster
And treat those two impostors just the same
— Rudyard Kipling, *If*

Ai miei genitori, per tutto...
A mio nonno, per assomigliarti...

Remerciements

En premier lieu, je veux remercier un professeur de thèse extraordinaire, Nicolas Grandjean. Nicolas, grâce à ta curiosité contagieuse et ta disponibilité sans faille, ces quatre années de thèse ont été un véritable plaisir. Tu n'as jamais manqué de m'apporter ton soutien et je t'en suis reconnaissant. Dans l'avenir, j'espère mettre à profit ton incroyable capacité à toujours trouver de nouvelles voies à poursuivre dans le cadre de la recherche scientifique (ou non), une attitude que tu m'as transmise sans cesse au cours de ma thèse. Je m'excuse d'avance pour ma soutenance publique.

Je voudrais ensuite remercier le Prof. Christophe Moser pour avoir présidé mon jury de thèse ainsi que tous les membres qui ont accepté de lire et de juger le présent travail: mon co-directeur de thèse, le Dr. Jean-François Carlin, les Profs. Benoît Deveaud, Michael Kneissl et Jon Heffernan.

Merci à tous les membres du LASPE qui ont rendu cette expérience très agréable et enrichissante (du nord au sud du couloir): Jacques, Georg, Nils, Gatien, Marcel, Lorenzo, Marlene, Christian, Marco M., Guillaume, Raphaël, Amélie, Alexei, Noelia, Jean-Michel, Lise, Etienne, Munise, Eric, Julien, Nino, Marco R., Jean-François, Denis et Aline. Avant tout un grand merci à Gatien, Nino, Julien et Jean-Michel pour l'incalculable formation à l'utilisation des salles blanches et aux techniques et procédés de microfabrication ainsi que pour les profondes discussions concernant l'interprétation de nombreuses données. Merci à Raphaël W. Butté (le W c'est pour wikipedia) pour son incroyable disponibilité à répondre à la moindre question avec laquelle invariablement je l'importunais et pour m'avoir appris la rigueur de la rédaction scientifique à coups de rouge. Je lui suis énormément reconnaissant pour toutes ses nombreuses corrections de l'anglais ainsi que du français qui ont caractérisées mes écrits, y compris ces lignes que vous lisez, merci Raph! Merci à Jean-François pour son aide concernant la croissance épitaxiale de tous les échantillons étudiés. Merci à Mehran et Gwénolé pour toutes les mesures résolues en temps que nous avons effectuées sur mes dispositifs ainsi qu'à Benoît Deveaud pour toutes les précieuses discussions scientifiques sur les sujets délicats de la superradiance et de la superfluorescence. Merci à Marlene et Christian pour toute l'assistance fournie au cours des mesures d'électroréflectance. Un grand merci aussi à tous les membres du projet européen Femtoblue avec lesquels j'ai eu le plaisir de collaborer pendant ces années de thèse. Merci en particulier à Thomas et Ulrich pour l'opportunité qu'ils m'ont offerte d'effectuer des mesures dynamiques en régime de self-pulsation et de mode-locking sur les MS-LDs.

Remerciements

Un grazie speciale agli amici che mi hanno accompagnato (indirettamente) in questi anni di dottorato all'EPFL. Sebastiano, per un'amicizia che prosegue da tempo immemorabile e per tutti i film in seconda serata (dobbiamo smetterla di vederci così!), grazie dal profondo del cuore! Mirco, per il tuo sostegno incondizionato nei momenti peggiori e per il Morra declinato. Mitica grande Sluts! Stefano, per tutti i pranzi, partite, birre e serate in cui hai cercato disperatamente di avere ragione. Diego, una delle persone più entusiaste che abbia mai conosciuto, grazie per tutti i preziosi consigli. Vai Doggy! Mariano, per esserci sempre stato in ogni momento e per essere il miglior complice che si possa desiderare. Michele, ci perseguitiamo fin dall'asilo ma grazie per tutte le partite a squash e le infinite afterdiscussions. Ferro, la tua pazzia mi ha tenuto vivo in questi anni, pregevole Bolla! Et, last but not least, un grand merci à tous les collègues du babyfoot: Gabriel, Dimitri, Adrien, Daniel, Ben, Michael, Hienhien, Diego, Nicola, Marc, Cyril, Yann,... Merci les gars! Ça n'aurait jamais été pareil sans vous...

Infine, vorrei ringraziare la mia famiglia per il loro sostegno durante tutti questi lunghi anni di studio. Ai miei genitori in particolare per non avermi mai fatto mancare niente. A mia sorella, la migliore che un fratellino pestifero possa mai desiderare. Grande Iaia! A mia zia un grazie particolare, senza tutti i tuoi libri tutto sarebbe stato un po' più difficile da capire. E un pensiero speciale a mio nonno che avrebbe sempre voluto vedermi laureare finalmente in chimica.

Un grazie dal profondo del cuore a Nina che con cipiglio severo ha supervisionato questi miei anni di dottorato. Quando ti accorgi che vuoi passare il resto della vita con qualcuno, vuoi che il resto della vita cominci il più presto possibile. Beh la tesi l'ho finita, gufa, ora tocca a noi... sei pronta a partire?

⊙

Lausanne, janvier 2014

L. S.

Abstract

III-nitride-based laser diodes (LDs) are compact and efficient source of highly coherent continuous wave light for optoelectronic applications in the short-wavelength range ($\lambda \sim 400$ nm). High peak-power and short-pulse generation in this spectral range has not yet been attempted and is of particular interest for applications such as, e.g., the next-generation of high-density optical data storage systems, ultraprecise nanoprocessing and fluorescence bio-imaging. More sophisticated devices like electrically-driven multi-section LDs (MS-LDs) with a monolithically integrated saturable absorber section (AS) would lay the foundation for miniature portable femtosecond lasers combining the well known advantages of semiconductor LDs such as their easy manufacturing, the absence of mechanical alignments, their low cost, compactness and high potential for integrability. MS-LDs are fabricated by simply defining an electrically separated p -contact section that acts as a saturable absorber along the waveguide of a standard laser resonator. This way, the multiple-contacted sections on the laser cavity share the same active region and are therefore optically coupled. Additionally, the particular design of a MS-LD allows to modulate *a posteriori* the internal absorption of the device, affecting both its static and dynamic regimes, as it will be shown in this thesis. Under appropriate modulation conditions for the AS, the induced variations in the absorption coefficient can develop non-linearities in the system. Accordingly, the MS-LD can then be operated in stable and, more importantly, controllable dynamic regimes of self-pulsation (SP), Q-switching and active/passive mode-locking.

The goal of the present study is to provide a detailed analysis of the system properties accounting for nitride specificities, to describe the static and dynamic mechanisms governing a GaN-based MS-LD and to present exhaustive interpretations of the experimental results and of the physical processes affecting the device performance. First, we design and grow high quality heterostructures with low defect density on free-standing GaN substrates. Achieving a high structural quality during the growth of InGaN multiple-quantum-well (MQW) is critical for the device performance. Using standard photolithography and dry etching techniques, we fabricate the MS-LDs with careful metallic deposition to define the cavity sections. Then, the LD structures are cleaved and tested on a probe station to define the optical emission characteristics. In particular, the trends of the main different observables (e.g., optical gain and loss distributions, lasing threshold current, absorption coefficient, pulsating frequency,...) and their respective issues are identified and commented. These measurements provide an important feedback for optimizing

the heterostructures and will be used as inputs for modeling the cavity and improving the design. For this purpose, several simulation approaches are carefully developed to support the qualitative understanding of the physical processes. The methods firstly developed in the case of a standard single-section LD are then generalized to the case of MS-LDs and the impact on the different dynamic operating regimes is discussed in regards to the driving conditions for a stable pulsating emission.

In this thesis we report detailed investigations on multi-contacted InGaN MQW LDs grown on *c*-plane freestanding GaN substrate consisting of an AS and an amplifier gain section. As a result of the interplay between external bias applied to the AS and the internal piezoelectric and spontaneous polarization fields inherent to *c*-plane InGaN MQWs, the devices exhibit non-linear non-monotonic variations in the threshold current due to the quantum-confined Stark effect that takes place in the AS MQWs. We report on how this effect governs the lasing characteristics and lasing dynamics, from steady-state cw lasing regime for unbiased AS to self-pulsation and Q-switching regimes at high negative absorber bias. In particular, we show how the charge carrier and photon density in the cavity start to mutually interact and eventually emit in one of the several dynamic regimes depending on the driving parameters.

In the last part of this thesis, we focus our attention on cooperative light-matter interaction named superradiance (SR). In 1954, Dicke was the first to point out a special emission mechanism involving the cooperative spontaneous emission from an ensemble of excited atoms interacting with each other via the radiation field. The interest on SR relies on the possibility to generate ultrashort pulses (a few hundreds of femtoseconds) with record peak optical powers (a few hundreds of watts) without even the need for defining a standard laser cavity resonator. In agreement with the semiclassical formalism adapted for slowly-varying observables, we have extended the common Maxwell-Bloch equations to consider the specific case of a multiple-contacted LD cavity. Such a theoretical model is then used to qualitatively interpret the experimental tests that we have carried out on our optically- and electrically-pumped III-nitride-based structures.

Keywords: Gallium nitride, III-nitrides, quantum well, light-emitting device, laser diode, multi-section laser diode, modal gain, saturable absorber, carrier lifetime, bistability, rate equations, self-pulsation, Q-switching, mode-locking, superradiance, superfluorescence.

Résumé

Les diodes lasers à base de nitrures d'éléments III sont une source compacte et efficace de lumière cohérente pour les applications optoélectroniques à courte longueur d'onde ($\lambda \sim 400$ nm). Dans cette gamme spectrale, la génération de courtes impulsions avec une puissance de crête élevée n'a pas encore été démontrée et elle serait d'un intérêt particulier pour des applications telles que, par exemple, la future génération de mémoires optiques à haute densité et l'obtention d'images de fluorescence pour les applications biomédicales. Des dispositifs plus sophistiqués comme les diodes lasers à sections multiples dans lesquelles une section d'absorbant saturable est intégrée de façon monolithique pourraient jeter les bases pour la réalisation de lasers femtosecondes miniaturisés combinant les avantages bien connus des diodes à semiconducteurs tels que leur facilité de fabrication, l'absence d'alignement mécanique, leur faible coût, leur compacité et leur fort potentiel d'intégration. Les diodes lasers à sections multiples sont fabriquées en séparant électriquement le contact p en différentes sections de façon qu'une partie agisse comme un absorbeur saturable le long du guide d'onde d'un résonateur laser standard. Ainsi, les différentes sections le long de la cavité laser partagent la même région active et sont donc couplées optiquement. En outre, la conception particulière d'une diode laser à sections multiples permet de moduler *a posteriori* l'absorption interne du dispositif, affectant à la fois les régimes statiques et dynamiques, comme il sera montré au cours de cette thèse. Dans des conditions appropriées de modulation électrique de la section absorbante, les variations induites dans le coefficient d'absorption peuvent développer des non-linéarités spécifiques dans le système. En conséquence, la diode laser à sections multiples peut ensuite être utilisée dans des régimes dynamiques stables et contrôlables d'auto-pulsation, de Q-switching et de mode-locking passif/actif.

L'objectif de la présente étude est de fournir une analyse détaillée des propriétés du système en tenant compte des spécificités des nitrures, de décrire les mécanismes statiques et dynamiques qui régissent une diode laser à sections multiples à base de GaN et de présenter des interprétations exhaustives des résultats expérimentaux et des processus physiques qui affectent les performances du dispositif. Tout d'abord, nous avons conçu et développé des hétérostructures de haute qualité avec une faible densité de défauts sur des substrats "free-standing" de GaN. L'obtention d'une grande qualité structurale lors de la croissance de puits quantiques à base d'InGaN est d'une importance cruciale pour la performance du dispositif. Par la suite, au moyen de techniques de photolithographie et de gravure sèche, nous avons fabriqué des lasers à sections multiples avec un dépôt

soigneuse de métal afin de mieux définir les différentes parties présentes dans la cavité. Enfin, ces structures laser ont été clivées et testées afin d'étudier leurs propriétés optiques d'émission. En particulier, l'évolution des principales grandeurs physiques (telles que, par exemple, les distributions spectrales du gain et des pertes optiques, le courant de seuil du laser, le coefficient d'absorption, la fréquence de pulsation,...) et les problèmes respectifs qui en découlent ont été identifiés et discutés. Ces expériences fournissent en retour des informations essentielles pour optimiser davantage les hétérostructures et seront utilisées par la suite comme données pour modéliser la cavité. Pour ce faire, différentes approches de simulation ont été soigneusement mises au point pour favoriser la compréhension qualitative des processus physiques. Les méthodes d'abord développées dans le cas d'un laser à simple section ont ensuite été généralisées au cas spécifique des diodes lasers à sections multiples et l'impact sur les différents régimes dynamiques a été discuté en terme de conditions de travail stable pour des régimes d'émission pulsée.

Dans cette thèse, nous présentons une étude détaillée des diodes lasers à sections multiples contenant des puits quantiques à base d'InGaN crûs sur des substrats "free-standing" de GaN le long de l'axe cristallographique c . Du fait de l'interaction entre la tension externe appliquée à la section absorbante et le champ électrique dû aux polarisations spontanée et piézoélectrique inhérent aux puits quantiques à base d'InGaN crûs le long de l'axe c , les dispositifs présentent des variations non-monotones et non-linéaires du seuil laser en raison de l'effet Stark confiné quantique. Ensuite, nous expliquons comment cet effet régit les caractéristiques d'émission laser, tout d'abord, à partir du régime laser statique puis nous le transposons au régime dynamique d'auto-pulsation et Q-switching en fonction de la tension appliquée. En particulier, nous montrons comment les populations de porteurs et de photons dans la cavité interagissent mutuellement et émettent dans différents régimes dynamiques en fonction des paramètres de fonctionnement.

Dans la dernière partie de cette thèse, nous concentrons notre attention sur l'interaction coopérative lumière-matière nommée superradiance. En 1954, Dicke a été le premier à rapporter un mécanisme particulier d'émission qui prévoit l'émission spontanée coopérative d'un ensemble d'atomes initialement excités et interagissant les uns avec les autres à travers le champ de rayonnement. L'intérêt pour la superradiance est principalement dû à la possibilité de générer des impulsions ultracourtes (quelques centaines de femtosecondes) avec de hautes puissances optiques de crête (quelques centaines de watts), sans même la nécessité de définir une cavité laser résonante. En accord avec le formalisme semiclassique adapté aux grandeurs physiques qui varient lentement, nous avons étendu les équations de Maxwell-Bloch jusqu'à considérer aussi le cas particulier d'une cavité laser à sections multiples. Ce modèle théorique est ensuite utilisé pour interpréter les résultats expérimentaux obtenus sur nos structures à base de nitrures sous pompage optique et électrique.

Mots-clés : nitrure de gallium, puits quantique, dispositif émetteur de lumière, diode laser, diode laser à sections multiples, gain modal, absorbeur saturable, temps de vie des porteurs, bistabilité, équations bilan, auto-pulsation, Q-switching, mode-locking, superradiance, superfluorescence.

Riassunto

I diodi laser a base di nitruri sono una fonte compatta ed efficiente di luce altamente coerente per applicazioni optoelettroniche a corta lunghezza d'onda ($\lambda \sim 400$ nm). In questo intervallo spettrale, la generazione di impulsi ad alta potenza di picco e di breve durata non è stata ancora ottenuta e sarebbe di particolare interesse per applicazioni quali, ad esempio, la futura generazione di sistemi di memoria ottica ad alta densità, processi tecnologici a scala nanometrica e immagini di fluorescenza per applicazioni bio-medicali. Dispositivi più sofisticati come diodi laser a sezione multipla in cui un assorbitore saturabile è integrato monoliticamente potrebbero porre le basi per la creazione di laser miniaturizzati a femtosecondi combinando così i vantaggi ben noti dei laser a semiconduttore come, per esempio, la loro facile fabbricazione, l'assenza di allineamenti meccanici, il basso costo, la compattezza e l'elevata integrabilità. I laser a sezione multipla sono fabbricati separando elettricamente il contatto p in diverse sezioni di modo che una parte agisca come assorbitore saturabile lungo la guida d'onda di un normale risonatore laser. In questo modo, le diverse sezioni lungo la cavità laser condividono la stessa guida attiva e sono quindi accoppiate otticamente. Inoltre, il particolare design di un tale diodo permetterebbe di modulare *a posteriori* l'assorbimento interno del dispositivo e conseguentemente sia sui regimi statici che su quelli dinamici, come verrà illustrato in questa tesi. In condizioni adeguate di modulazione elettrica della sezione assorbente, le variazioni indotte nel coefficiente di assorbimento possono indurre specifiche non-linearità nel sistema. Di conseguenza, il laser a sezione multipla può essere utilizzato in regimi dinamici stabili e controllabili di auto-pulsazione, Q-switching e mode-locking attivo/-passivo.

L'obiettivo del presente studio è quello di fornire un'analisi dettagliata delle proprietà del sistema tenendo conto delle peculiarità dei nitruri, di descrivere i meccanismi statici e dinamici che regolano un laser a sezione multipla a base di nitruri e di presentare interpretazioni esaustive dei risultati sperimentali e dei processi fisici che influenzano le prestazioni del dispositivo. In primo luogo, abbiamo progettato e sviluppato delle eterostrutture di alta qualità e con bassa densità di difetti su substrati "free-standing" a base di GaN. Una elevata qualità strutturale nel corso della crescita di pozzi quantici a base di InGaN è di cruciale importanza per le prestazioni del dispositivo. In seguito, per mezzo di tecniche di fotolitografia e di attacco secco, abbiamo fabbricato i laser a sezione multipla con un'attenta deposizione metallica per definire al meglio le diverse sezioni presenti nella cavità. Infine, queste strutture laser sono state clivate e testate in

modo da studiare le loro proprietà di emissione ottica. In particolare, l'evoluzione delle principali grandezze fisiche (come, per esempio, le distribuzioni spettrali del guadagno e delle perdite ottiche, la soglia di corrente laser, il coefficiente di assorbimento, la frequenza di pulsazione,...) e i rispettivi problemi sono stati identificati e commentati. Questi esperimenti forniscono un importante feedback per ottimizzare ulteriormente le eterostrutture e saranno utilizzati in seguito come input per la modellazione del design della cavità. A questo scopo, diversi approcci di simulazione sono stati accuratamente sviluppati per supportare la comprensione qualitativa dei processi fisici. I metodi dapprima elaborati nel caso di un normale laser a sezione singola sono stati in seguito generalizzati allo specifico caso dei laser a sezione multipla e l'impatto sui diversi regimi dinamici è stato discusso in termini di condizioni di lavoro stabili per regimi di emissione impulsata.

In questa tesi riportiamo lo studio dettagliato su laser a sezione multipla contenenti pozzi quantici a base di InGaN cresciuti su substrati GaN "free-standing" lungo l'asse cristallografico di crescita c . Questi laser sono costituiti da una sezione assorbente e una sezione di guadagno amplificato. Come risultato dell'interazione tra tensione esterna applicata alla sezione assorbente e il campo di polarizzazione spontanea e piezoelettrica inerente la crescita lungo il piano c presente nei pozzi quantici InGaN, i dispositivi mostrano variazioni non-monotone e non-lineari nella soglia laser dovute all'effetto Stark in caso di confinamento quantico. Riportiamo su come questo effetto governi le caratteristiche laser, a partire dal regime laser statico a quello dinamico di auto-pulsazione e Q-switching a seconda del voltaggio applicato. In particolare, mostriamo come le popolazioni di portatori e di fotoni nella cavità inizino a interagire mutuamente ed emettano in uno dei diversi regimi dinamici a seconda dei parametri di operazione.

Nell'ultima parte di questa tesi, concentriamo infine la nostra attenzione sull'interazione cooperativa da parte di luce-materia denominata superradianza. Nel 1954, Dicke fu il primo a segnalare uno speciale meccanismo di emissione che preveda l'emissione spontanea cooperativa di un insieme di atomi inizialmente eccitati e interagenti tra loro tramite il campo di radiazione. L'interesse della superradianza è principalmente dovuto alla possibilità di generare impulsi ultracorti (centinaia di femtosecondi) con potenze di picco record (centinaia di watt) senza nemmeno la necessità di definire una cavità laser risonante. In accordo con il formalismo semiclassico adattato per grandezze fisiche che variano lentamente, abbiamo esteso le comuni equazioni di Maxwell-Bloch fino a prendere in considerazione il caso specifico di una cavità laser a sezione multipla. Tale modello teorico verrà poi utilizzato per interpretare qualitativamente i risultati sperimentali ottenuti sulle nostre strutture a base di nitruri in pompaggio ottico ed elettrico.

Parole chiave: nitruro di gallio, pozzo quantico, dispositivo emettitore di luce, diodi laser a semiconduttori, laser a sezioni multiple, guadagno modale, assorbitore saturabile, tempo di vita dei portatori, bistabilità, equazioni di bilancio, auto-pulsazione, Q-switching, mode-locking, superradianza, superfluorescenza.

Contents

Remerciements	v
Abstract	vii
Résumé	ix
Riassunto	xi
Table of contents	xiii
Nomenclature	xvii
Introduction	1
Overview of III-nitride based optoelectronic devices	1
FemtoBlue Project: objectives and consortium	2
Outline of this PhD dissertation	3
1 III-nitride compound properties	5
1.1 Structural properties	5
1.1.1 Crystalline structure	5
1.1.2 Polarization properties	7
1.2 Growth	8
1.3 Optical properties	10
1.3.1 Energy bandgap and refractive index	10
1.3.2 Quantum confined Stark effect (QCSE)	13
1.4 Electrical properties	15
1.4.1 <i>n</i> -type doping	16
1.4.2 <i>p</i> -type doping	16
1.4.3 <i>p-n</i> junction	17
2 GaN-based laser diodes	21
2.1 Structure design	23
2.1.1 Inside the active region	23
2.1.2 Outside the active region	25
2.1.3 Sample fabrication	28

Contents

2.2	Single-section laser diodes	29
2.2.1	L - I - V characteristics	40
2.2.2	Single-section LD dynamics	42
2.3	Multi-section laser diodes	52
2.3.1	Motivation	52
2.3.2	State of the art	54
2.3.3	L - I - V characteristics	55
2.3.4	Multi-section LD dynamics	57
2.4	Microfabrication process	67
2.4.1	Design mask layers	67
2.4.2	Clean room process	69
	Summary of the results	72
3	Multi-section laser diodes: static characteristics	73
3.1	Epi-wafer mapping	73
3.2	Internal polarization field	76
3.2.1	Electro-reflectance on standard LED structures	78
3.3	Internal absorption coefficient	80
3.4	L - I - V curves and threshold current	83
3.5	Spontaneous and lasing emission	87
3.6	Optical bistability	92
	Summary of the results	96
4	Multi-section laser diodes: dynamic characteristics	97
4.1	Carrier lifetime	97
4.2	Self-pulsation	107
4.3	Mode-locking	111
	Summary of the results	114
5	Superradiance and superfluorescence: application to III-nitride semi-conductors	115
5.1	Motivation	116
5.2	State of the art	117
5.3	Theory	119
5.3.1	Large sample superradiance	124
5.3.2	Superradiance and superfluorescence in multi-section laser diodes .	130
5.4	Optically-pumped superfluorescence	139
5.4.1	Samples, design and microfabrication process	139
5.4.2	Experimental results	141
5.5	Electrically-pumped MS-LDs for SF purpose	144
	Summary of the results	146

Conclusion and perspectives	147
Summary of the experimental results	147
Outlook and perspectives	149
A Electro-reflectance measurements	151
B Electrical beatings in reverse-biased MS-LDs	157
Bibliography	159
Curriculum Vitae	179

Nomenclature

Acronyms

ac	Alternating current
AMI	Acetone, methanol, isopropanol solvents
AS	Absorber section
CSEM	Swiss Center for Electronics and Microtechnology
cw	Continuous wave operation
DBR	Distributed Bragg reflector
dc	Direct-current
DOS	Density of states
EBL	Electron blocking layer
EPFL	École Polytechnique Fédérale de Lausanne
ER	Electro-reflectance spectroscopy
FS	Free-standing (substrate)
FWHM	Full-width at half-maximum
GS	Gain section
HVPE	Hydride vapor phase epitaxy
IAF	Fraunhofer-Institut für Angewandte Festkörperphysik
ICP-RIE	Inductive coupled plasma-reactive ion etching
ICT	Information and communications technology
IR	Infrared
ITO	Indium tin oxide

Contents

Laser	Light amplification by stimulated emission of radiation
LD	Laser diode
LED	Light emitting diode
LEEBI	Low-energy electron-beam irradiation
L - I - V	Light-Current-Voltage
LO	Longitudinal optical
LPI	P.N. Lebedev Physical Institute
MBE	Molecular beam epitaxy
ML	Monolayer
MOVPE	Metal-organic vapor phase epitaxy
MQW	Multiple quantum well
MS-LD	Multi-section laser diode
nid	Non-intentionally doped
PECVD	Plasma-enhanced chemical vapor deposition
PL	Photoluminescence
PR	Photo-reflectance
QCFK	Quantum confined Franz-Keldysh effect
QCSE	Quantum confined Stark effect
QD	Quantum dot
QW	Quantum well
RIE	Reactive ion etching
RO	Relaxation oscillation
RT	Room temperature (300 K)
SCH	Separate-confinement heterostructure
SEM	Scanning electron microscope
SESAM	Semiconductor saturable absorber mirror
SF	Superfluorescence

SLED	Superluminescent light emitting diode
SP	Self-pulsation
SR	Superradiance
SRH	Shockley-Read-Hall
TDD	Threading dislocation density
TUB	Technische Universität Berlin
UCAM	University of Cambridge
UV	Ultraviolet
WKB	Wentzel-Kramers-Brillouin

Constants

a_B	Exciton Bohr radius		[nm]
α_i	Internal losses		[cm ⁻¹]
α_m	Mirror losses	eq. 2.30	[cm ⁻¹]
α_{TOT}	Total cavity losses	eq. 2.29	[cm ⁻¹]
β	Fraction of spontaneous emission emitted into laser modes	eq. 2.42	[-]
c	Speed of light in vacuum	299792458	[m/s]
ε_{sat}	Gain compression factor	eq. 2.46	[-]
Γ	Optical mode confinement factor	eq. 2.1	[-]
κ	Damping factor of the superfluorescent emission	eq. 5.16	[s ⁻¹]
k_B	Boltzmann constant	$1.380648813 \cdot 10^{-23}$	[J/K]
m_0	Electron rest mass	$9.1093821545 \cdot 10^{-31}$	[kg]
m_e/m_0	Electron effective mass	Table 1.1	[-]
$m_{e,b}$	Electron effective mass in the well barrier		[kg]
$m_{e,QW}$	Electron effective mass in the MQW		[kg]
m_{hh}/m_0	Heavy hole effective mass	Table 1.1	[-]
μ	Dipole moment of interband transitions		[C m]
n_g	Group refractive index		[-]

Contents

N_{QW}	Number of quantum wells in the active region		[-]
q	Elementary electric charge	$1.60217656535 \cdot 10^{-19}$	[C]
Q	Quality factor	eq.2.37	[-]
R	Reflectivity	eq.2.28	[-]
R_m	Ratio of the effective masses in the valence and conduction band		[-]
T_1	Population inversion relaxation time or spontaneous recombination time of electron-hole pairs		[ns]
T_2	Polarization relaxation time		[fs]
τ_c	Correlation time of the emission process		[fs]
T_E	Cavity field decay time		[fs]
ε_0	Vacuum permittivity	$8.854187817 \cdot 10^{-12}$	[C/V·m]
v_g	Speed of light in the waveguide of group refractive index n_g		[m/s]

Variables

α_0	Carrier-free absorption coefficient	eq. 2.21, 2.26	[cm ⁻¹]
E	Electromagnetic field in the cavity (3D notation)	eq. 5.24	[V/m]
E_b	Carrier barrier energy to escape the QW		[eV]
F_b	Electric field in the well barrier		[MV/cm]
F_{ext}	External electric field applied to the p - n junction	eq. 1.21	[MV/cm]
F_{int}	Internal electric field induced by polarization	eq. 1.4, 1.13	[MV/cm]
f_{SP}	Self-pulsation oscillation frequency		[GHz]
g_{AS}	Material gain in the absorber section (referred to also as α_{AS})		[cm ⁻¹]
g_{GS}	Material gain in the gain section		[cm ⁻¹]
I_{GS}	Injected current in the gain section		[mA]
I_{th}	Threshold current for lasing	eq. 2.29	[mA]
λ_{GS}	Wavelength at the peak of the GS curve emission (expressed in energy as E_{GS})		[nm]
λ_{lasing}	Emission wavelength above the lasing threshold		[nm]
L_{AS}	Length of the absorber section		[μm]

L_{TOT}	Length of the full cavity		[mm]
N	Charge carrier population (number notation)		[-]
N_{AS}	Charge carrier population in the absorber section (number notation)		[-]
N_{GS}	Charge carrier population in the gain section (number notation)		[-]
N_{th}	Threshold charge carrier number	eq. 2.29	[-]
N_{tr}	Transparency charge carrier number	eq. 2.6	[-]
P_{AS}	Polarization in the absorber section (3D notation)	eq. 5.26	[C/m ²]
P_{GS}	Polarization in the gain section (3D notation)	eq. 5.25	[C/m ²]
S	Photon population in the cavity (number notation)		[-]
τ_{AS}	Charge carrier lifetime in the absorber section		[ns]
τ_D	Delay time of the superradiant emission		[fs]
τ_{GS}	Charge carrier lifetime in the gain section		[ns]
τ_{nrad}	Non-radiative recombination carrier lifetime	eq. 1.16	[ns]
τ_{rad}	Radiative recombination carrier lifetime	eq. 1.16	[ns]
τ_r	Radiative carrier lifetime (in the absorber section)	eq. 4.2	[ns]
τ_{SP}	Pulse width of the self-pulsating oscillation		[ns]
τ_{SR}	Characteristic superradiant time-scale		[fs]
τ_{therm}	Thermionic carrier lifetime (in the absorber section)	eq. 4.3	[ns]
τ_{TOD}	Turn-on delay time	eq. 2.51	[ns]
τ_{tun}	Tunneling carrier lifetime (in the absorber section)	eq. 4.4	[ns]
V_{AS}	Bias applied to the absorber section		[V]
V_{MAX}	Absorber applied bias at which the absorption has a local maximum		[V]
V_{MIN}	Absorber applied bias at which the absorption has a local minimum (flat-band conditions)		[V]
w	Ridge width		[μm]
W_D	Width of the space charge region (or also depletion region)	eq. 1.19, 1.20	[nm]

Introduction

Overview of III-nitride based optoelectronic devices

To make an efficient light emitting device, a semiconductor material should possess three important characteristics: (i) an efficient radiative pathway, (ii) an appropriate energy bandgap and (iii) efficient p - and n -type doping with resistivities as low as possible [1]. III-V semiconductors and their alloys fulfill all these criteria with success. Thanks to the pioneering studies of Shuji Nakamura from Nichia Corporation in the early 1990s, group-III nitride optoelectronic devices have experienced a widely growing impact in the last two decades. The field of applications ranges from everyday-life technologies to specific industrial required equipments such as, e.g., domestic solid-state lighting devices or optical players and optical data storage devices (Blu-rayTM standard). By means of alloying, their tunable direct bandgap can span over a broad range of wavelengths from the ultraviolet (UV) down to the infrared (IR). Thanks to their record luminous efficiencies they are expected to become the main technological materials for a wide range of optoelectronic applications.

Over the past decades, the role of laser devices has grown considerably. In 1953, Gordon, Zeiger and Townes produced the first amplifier of microwave radiations and for this reason their device was called a “maser” [2]. Shortly after, in 1957, Townes and Schawlow extended the maser concept to shorter wavelength, the laser was born [3]. The first semiconductor laser diode (LD) was reported in 1962 by Hall *et al.* with a bulk GaAs-based device emitting at 850 nm [4]. Concerning III-nitrides, in 1994 Nakamura *et al.* realized a breakthrough with the first candela-class blue InGaN-based light emitting device (LED) [5]. One of the main drawbacks against the development of GaN-based optoelectronic devices was the achievement of efficient p -type doped layer. Amano *et al.* successfully reported in 1989 first p -doping using magnesium as a dopant [6]. More than 30 years after the first semiconductor laser was reported, in December 1995 Nakamura demonstrated a blue GaN-based LD producing 215 mW at 417 nm under pulsed current injection [7].

Beside cw-lasers, pulsed monolithic semiconductor lasers made from conventional III-V alloys have been demonstrated and studied for the past 20 years. These devices feature a strong absorption region which can saturate to allow for high frequency self-modulation [8]. In 2004, gain-switching operation with an encouraging high peak power up to 0.4

W was reported for the first time with an InGaN multiple-quantum-well (MQW) LD [9]. More recently, gain-switched InGaN LDs with repetition frequencies of 3 GHz and pulse width of 31 ps have been realized by Chuah and co-workers [10]. To break the threshold of 10 ps it is convenient to realize a novel monolithic LD, which is able to operate in the mode-locked regime. Such a device would be very promising for applications which require ultrashort picosecond or subpicosecond pulses. Lately, Miyajima *et al.* reported the first self-pulsating emission in a monolithic bi-section GaN-based LD with a repetition frequency of 0.9 GHz and a pulse width of 30 ps [11]. This particular multi-section design is defined by electrically separating the cavity in multiple *p*-contact pads. Then, each section can act as a gain section (GS) if forward-biased or as a saturable absorber section (AS) (or as a modulator section) if reverse-biased. The response of the device is significantly enhanced with the presence of a saturable absorber positioned inside the cavity. Indeed, in standard single-section LDs the charge carrier dynamics in the MQWs limits the device reaction to an external stimulation whereas the use of a saturable absorber allows the fast modulation of the output power above threshold both in a direct and a passive way [12]. By operating the defined sections under different driving conditions, we are then able to tailor the lasing characteristics and lasing dynamics. Interests, applications, and state of the art regarding multi-section LDs (MS-LDs) will be extensively described in Secs. 2.3.1 and 2.3.2. Eventually, superradiance (SR) and superfluorescence (SF) as potential physical effect to achieve ultrashort pulses will be discussed in Secs. 5.1 and 5.2.

Femtoblue Project: objectives and consortium

This thesis was part of the European Project “Femtoblue” (<http://femtoblue.epfl.ch>). The goal of the project was to investigate group-III nitride semiconductor materials for ultrafast LDs aimed at producing femtosecond coherent optical pulses in the blue and violet spectral range. Monolithic InGaN/GaN LD structures based on multi-section ridge waveguide cavities were thus planned. These devices were expected to produce extremely short pulses with high peak optical intensity in the mode-locking regime thus providing a substantial contribution in terms of efficiency and compactness to many fields. Dicke SR was also considered as a potential mechanism able to produce ultrashort pulses. The main objective of the project was to exploit the emerging technology based on InGaN/GaN heterostructures to fabricate a short-wavelength ultrafast source combining the proven approaches develop in the conventional GaAlAs and InGaAsP alloy systems. These III-nitride-based devices were almost not explored and the project had to face multiple challenges to get such ultrafast dynamic regimes to work in InGaN/GaN lasers.

In order to achieve this target, the project consortium had to master epitaxial growth technologies for nitride heterostructures, optimise the optical cavity design and tailor the dynamic regimes of LDs based on group-III-nitride materials. The Project Coordinator was Dr. Dmitri L. Boiko at the Swiss Center for Electronics and Microtechnology (CSEM)

in Neuchâtel. The growth, process and physics of such GaN-based diodes was undertaken by the École Polytechnique Fédérale de Lausanne (EPFL) in the violet wavelength range and by the Technische Universität Berlin (TUB) in the blue range. The experimental measurements of the different dynamic regimes was performed at the Fraunhofer-Institut für Angewandte Festkörperphysik (IAF), at the University of Cambridge (UCAM), and at the P.N. Lebedev Physical Institute (LPI). UCAM had a strong expertise in passive mode-locking, active mode-locking and hybrid mode-locking whereas LPI was engaged in ultrashort optical pulse generation and ultrafast semiconductor lasers, especially in the regimes of passive mode-locking and SR. IAF was also responsible for the assessment of the wafer quality and for the optical gain measurements via Hakki-Paoli spectroscopy.

Outline of this PhD dissertation

The aim of this PhD dissertation is the description of the realization and the characterization of a blue nitride-based multiple-contacted LD operating under different static and dynamic regimes.

In the first chapter, a brief overview of the main structural, optical and electrical properties of III-nitrides is presented. Particular attention is devoted to the band structure and band profile of III-nitride heterostructures, especially with respect to the polarization mismatch of the different binary compounds. Then, the impact of the quantum confined Stark effect on the optical features is discussed. Finally, the modes of operation of a typical p - n junction implemented in a MS-LD are introduced.

The second chapter introduces the theoretical models that will be extended and applied in detail in the subsequent chapters. First, the basic layout of quantum-well-based III-V devices is described. Then, the rate equation model for a standard and a MS-LD is introduced to facilitate the description of the dynamics of LDs. The optical modal gain and the recombination mechanisms, which provide light amplification in the resonator cavity are also discussed. A detailed analysis of the ABC model in the specific case of III-nitrides is carried out. The interpretation of the different mechanisms is scrupulously supported by simulations and the interplay of the gain section and the absorber one is emphasized. Finally, an overview of the microfabrication design and process is presented. In the third and fourth chapter the main static and dynamic characteristics of a III-nitride-based MS-LD are investigated. A careful study of the impact of the applied bias on the total polarization field in the MQWs is carried out and the consequences on the static features (such as, e.g., the threshold current, the emission wavelength and the optical bistability) are highlighted. Subsequently, a model is developed to describe the carrier lifetime dynamics in the AS under the influence of an external applied bias. The different pulsating regimes that have been observed during the experiments are then listed and analyzed.

The fifth chapter extends the discussion on the possible dynamic regimes to include the case of collective phenomena, namely SR and SF. First, a theoretical treatment

Introduction

of the cooperative emission is presented where a particular attention is paid on the sample shape. The evolution of an ensemble of N atoms is then compared to the case of a damped pendulum represented by a varying Bloch vector $\theta(z, t)$ and the different pulsating regimes are detailed. In the last sections, we report on the experimental results obtained when investigating collective emission in III-nitride-based heterostructures. Finally, the main experimental results are briefly reviewed and future research directions are discussed.

The present work was supported by the NCCR Quantum Photonics program of the Swiss National Science Foundation and by the European Community's Seventh Framework Programme FP7/2007-2013 under the Grant Agreement number 238556 (FEMTOBLUE).

1 III-nitride compound properties

Optoelectronic devices based on the group-III-nitride materials system exhibit unique features that have to be taken into account during their design and fabrication.

In this chapter, the main characteristics concerning structural, optical and electrical properties of III-nitrides are presented. First, the structural parameters and the subsequent polarization features of the different binary compounds are discussed. A brief overview of the growth techniques is presented. The main optical parameters involved in the development of a semiconductor emitting structure such as the bandgap energy and the quantum confined Stark effect (QCSE) are introduced in the specific case of nitride-based devices. At last, the design and the mode of operation of a typical GaN-based p - n junction is detailed.

1.1 Structural properties

1.1.1 Crystalline structure

III-nitride binary compounds, i.e., GaN, InN, AlN, and their alloys, can present two distinct structures: the zincblende (cubic) phase and the wurtzite (hexagonal) phase. The first structure is metastable and can be obtained only under particular growth conditions [13]. It consists in two intercalated face-centered cubic lattices with tetrahedral coordination. On the contrary, the second structure is thermodynamically stable and it is composed by two intercalated hexagonal close-packed lattices, one for the anions (the nitrogen atoms) and one for the cations (the metal atoms, namely Ga, In or Al). By close-packed, it is meant that the two planes of adjacent layers are displaced horizontally such that the distance between these two planes is minimized. This stacking sequence forms an anisotropic crystal structure. Many other important semiconductors with a large bandgap crystallize in the wurtzite structure such as ZnO, SiC, ZnS and CdS.

In Fig. 1.1, a schematic picture of wurtzite III-nitride crystal structure is shown. The c -plane corresponds to the $[0001]$ orientation, the m -plane to the $[10\bar{1}0]$ one and the

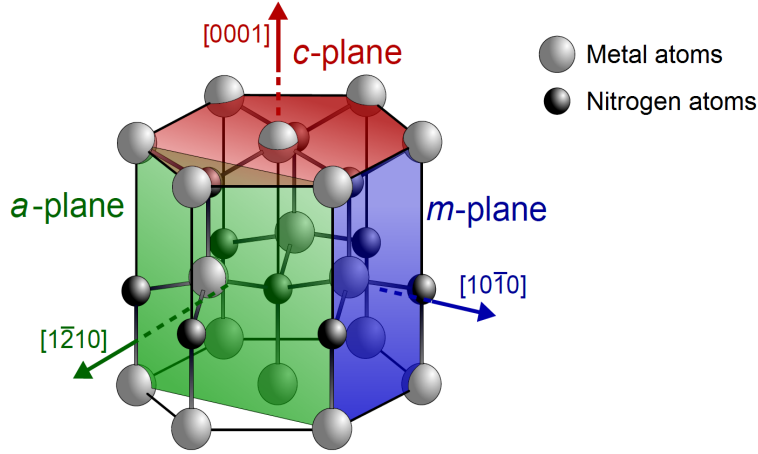


Figure 1.1: Wurtzite structure of III-nitride compounds for a polar (c -plane) and a non-polar (m - and a -plane) crystal orientations [14].

a -plane to the $[1\bar{2}10]$ one. In the present work, we will only focus on wurtzite structures grown along the c -axis, which satisfy the pseudomorphic condition.

In Table 1.1, the main structural parameters such as the lattice constants and the thermal expansion coefficients are given for III-nitride binary compounds. In the case of ternary alloys, the Vegard's law can be used to obtain the values of the lattice parameters for a given molar fraction x , i.e., from a simple linear interpolation of the crystal lattice parameter between the binary compounds [23]:

$$l_{M_{1,x}M_{2,1-x}N} = x \cdot l_{M_1N} + (1 - x) \cdot l_{M_2N}, \quad (1.1)$$

where l is the lattice parameter (c or a) for binary and ternary compounds and M_i one of the different metal atom species amongst Al, Ga and In. This linear approximation is no longer valid when taking into account some structural imperfections of the crystal such as a different electronegativity between species, a volume deformation in the band structure or even a structural relaxation of the alloys [23]. Therefore, a non-linear bowing term $bx(1 - x)$ should be subtracted to eq. 1.1, where b is known as the bowing parameter. Especially in the III-nitride-based structures, the laser performance is strongly affected by the composition of the individual layers due to issues induced by their unique materials properties. Indeed, the large lattice-mismatch between the different binary compounds ($>10\%$ between a_{GaN} and a_{InN}) and the lack of GaN native substrates produce a large strain through the heterostructure. This intrinsic strain will impact the optical characteristics of the heterostructure but can also lead to the formation of a large number of cracks and/or dislocations, especially in the active region, which is detrimental for the performance of optoelectronic devices [24].

1.1. Structural properties

	AlN	GaN	InN
Lattice constant a ($T = 300$ K) (nm)	0.3112	0.3189	0.3533
Thermal expansion coefficient $d \ln a / dT$ ($10^{-6}/\text{K}$)	4.2	5.6	3.8
Lattice constant c ($T = 300$ K) (nm)	0.4982	0.5185	0.5693
Thermal expansion coefficient $d \ln c / dT$ ($10^{-6}/\text{K}$)	5.3	3.2	2.9
Compound density (g/cm^3) [15]	3.23	6.15	6.81
Static dielectric constant, ϵ_r/ϵ_0 [16]	10.31	10.28	14.61
Band-to-band bandgap energy E_g ($T = 0$ K) (eV)	6.25	3.51	0.69
Band-to-band bandgap energy E_g ($T = 300$ K) (eV)	6.14	3.43	0.64
Electron effective mass, m_e/m_0 [17]	0.32	0.20	0.07
Heavy-hole effective mass, m_{hh}/m_0	0.26	1.4 [18]	1.56
Exciton binding energy (meV)	60	25 [19]	9
Exciton Bohr radius (nm)	1.4	3.48 [19]	8
Mg acceptor binding energy (eV)	0.51	0.17	0.06
Momentum matrix element energy E_p^{\parallel} (eV) [20]	16.97	17.29	8.74
Momentum matrix element energy E_p^{\perp} (eV) [20]	18.16	16.26	8.81
Spontaneous polarization P_{sp} (C/m^2) [21]	-0.090	-0.034	-0.042
Piezoelectric constant e_{33} (C/m^2) [21]	1.50	0.67	0.81
Piezoelectric constant e_{31} (C/m^2) [21]	-0.53	-0.34	-0.41

Table 1.1: Values of basic physical parameters of wurtzite InN, AlN, and GaN taken from [22] unless specified.

1.1.2 Polarization properties

In the III-nitride system, one of the consequences of the crystal anisotropy discussed in Sec. 1.1.1 results in a static, relative shift of positive and negative charges in the unit cell. Along the c -plane, this asymmetry leads to the appearance of the spontaneous polarization \mathbf{P}_{sp} through the crystal lattice, which exists even at equilibrium, i.e., without any external applied field. It is known as the *pyroelectric effect*. Thus, between the different crystal planes depicted in Fig. 1.1, the c -plane is referred to as the polar one and is generally the growth direction for GaN-based optoelectronic devices as it is the more stable thermodynamically. Values of the spontaneous polarization \mathbf{P}_{sp} for nitride binary compounds are given in Table 1.1. In the specific case of ternary alloys, \mathbf{P}_{sp} can be obtained by applying again equation 1.1 with a specific bowing parameter b [23]. In addition to this polarization effect, an external stress may cause atoms in the unit cell to shift with respect to each other. For example, applying a biaxial strain in the c -plane to any wurtzite III-nitride materials leads to a displacement of the atoms along $[0001]$. Such a shift can lead to further internal polarization known as the *piezoelectric effect*. In general, the piezoelectric polarization \mathbf{P}_{pz} is coupled to the strain via the tensor e_{ijk} of the piezoelectric coefficients:

$$P_{pz,i} = \sum_{jk} e_{ijk} \cdot \sigma_{jk}, \quad (1.2)$$

where σ_{jk} is the stress-field resulting from a deformation. The piezoelectric coefficients e_{ij} for the nitride binary compounds are listed in Table 1.1.

The total internal polarization \mathbf{P}_{int} can be obtained with a simple summation of these two contributions: $\mathbf{P}_{int} = \mathbf{P}_{sp} + \mathbf{P}_{pz}$. In the absence of free charges and considering an infinite interface between the media, the polarization charge satisfies $\nabla \cdot (\epsilon\epsilon_0\mathbf{E} + \mathbf{P}_{int}) = 0$ and is given by:

$$\sigma_P = -(\mathbf{P}_j - \mathbf{P}_i) \cdot \mathbf{n}_{ij}, \quad (1.3)$$

where \mathbf{n}_{ij} is the surface normal vector pointing from medium i to medium j . The total electric field \mathbf{F} in medium i can then be expressed by:

$$\mathbf{F}_i = -\frac{\sigma_P}{\epsilon_r\epsilon_0}\mathbf{n}_{ij}, \quad (1.4)$$

where ϵ_0 is the vacuum permittivity and ϵ_r is the relative permittivity of medium i . Obviously, the electric field in medium j has the opposite direction.

Typically, in a heterostructure the total polarization is not constant between the different constituents. Thus, at the heterointerfaces a charge density develops because of the polarization discontinuity. Free carriers can screen this built-in field in bulk materials but in heterostructures such as QWs this field can have a huge impact on the band structure, as shown in Sec. 1.3.2. The consequences might be an increase in the radiative recombination carrier lifetime, corollary a decrease of the oscillator strength, and a redshift of the transition energies [25]. More details about polarization effects can be found for instance in Ref. [26].

1.2 Growth

Group-III nitride semiconductors have emerged as the leading material for fabricating high efficiency and high reliability short wavelength emitters ($\lambda < 530$ nm). Heterostructures consist of (at least two) different semiconducting materials. To obtain electrical and optical characteristics compatible with optoelectronic devices, growth of high quality III-nitride heterostructures is necessary. Therefore, the thickness of layers in the active region has to be controlled down to the monolayer (ML) scale and hence sophisticated epitaxial growth methods are used. Current technology primarily employs three kinds of reactors to grow group-III-nitride thin films: hydride vapor phase epitaxy (HVPE), molecular beam epitaxy (MBE) and metal-organic vapor phase epitaxy (MOVPE).

Large growth rates can be achieved with HVPE. This technique is usually exploited for the growth of thick GaN epilayers as it allows for growth rates exceeding $500 \mu\text{m/h}$ [27]. Those thick GaN layers are often used for preparing free-standing (FS) GaN substrates with low threading dislocation density (TDD) [28]. On the contrary, MBE is performed in an ultrahigh vacuum chamber and presents a relatively low growth rate (often less than $1 \mu\text{m/h}$). The source materials are evaporated from effusion cells and directed toward the heated substrate [29]. This technique allows monitoring the growth rate with

a precision down to the ML thanks to *in situ* RHEED (reflection high energy electron diffraction) oscillations [29]. Moreover, a primary advantage of plasma-assisted MBE for III-nitrides is the low temperature of growth that can be realized thanks to the use of an atomic nitrogen plasma source, which results in lower thermal stress upon cooling, less diffusion, and reduced alloy segregation [1]. This low growth temperature is of high interest for the growth of indium rich InGaN alloys and for alloys with large thermal expansion coefficient mismatch. Another advantage of MBE is the absence of hydrogen passivation of as-grown *p*-GaN films [30].

LDs in the III-nitride materials system are commonly grown homoepitaxially by MOVPE on *c*-plane oriented FS GaN substrate. This technique allows an easy control of the growth parameters, a good reproducibility and is also well-suited for large scale production. MOVPE is a non-equilibrium growth technique (closer to thermodynamical equilibrium than MBE but less than HVPE), which consists in vapor transport of the precursors and subsequent reactions of group-III alkyls and group-V hydrides above a heated substrate. Precursor materials are metal-organic compounds, such as, e.g., liquid trimethylgallium (TMGa) or solid trimethylindium (TMIn). The crystal growth occurs after pyrolysis and catalysis of the compounds close to or on the substrate surface. The growth rate is typically higher than for MBE (1-10 $\mu\text{m/h}$). In 1994, Nakamura *et al.* realized a breakthrough with the fabrication of the first candela-class blue InGaN/AlGaIn-based LED device in a modified MOVPE system [5].

Several growth issues had to be faced to obtain high quality GaN thin films and consequently high-performance optoelectronic devices. For instance, the lack of single crystalline GaN substrates or other high quality single crystalline substrates with the same lattice parameters as GaN have hindered the growth of high quality nitrides for a while. So far, most of the nitride epitaxial growth for LEDs has been realized on sapphire or SiC. However, both sapphire and SiC have critical limitations for the manufacturing of LDs, i.e., large lattice parameter and thermal expansion coefficient mismatch to GaN, leading to TDD and/or cracks. The implementation of a nucleation layer, i.e., the deposition of a low temperature buffer layer, was a key discovery for improving the surface morphology and crystalline quality of GaN. Amano *et al.* reported that an AlN buffer layer relaxes the compressive strain between GaN and sapphire, and promotes lateral growth of GaN: as a result the subsequent layers have a much lower dislocation density [31]. In 1991 Nakamura *et al.* obtained high-quality GaN for the first time using a low temperature GaN buffer layer on a sapphire substrate [32]. Nowadays, these low-temperature buffer layers are standard and mandatory for the growth of GaN by MOVPE. More recently, better laser performance has been accomplished by performing growth on defect-reduced GaN templates, i.e., FS GaN substrates fabricated by HVPE. The main characteristics of those substrates are a TDD $< 10^6 \text{ cm}^{-2}$, a good thermal conductivity (see Table 1.1) enabling efficient device thermal management, and a good electrical conductivity for device back contacting.

1.3 Optical properties

Kroemer in 1963 proposed to combine “wide bandgap” semiconductors with “narrow bandgap” ones to form a *heterojunction* with extremely desirable properties unattainable in homostructures [33]. For this reason, one of the main interests of group-III-nitride materials is the possibility of bandgap engineering via alloying and to cover the spectral range spanning from the mid infrared (IR) with InN to the deep ultraviolet (UV) with AlN [Fig. 1.2 (a)]. In this section, the main optical properties of nitrides are presented such as their energy bandgap and their refractive index. A particular attention will be paid to the QCSE and its impact on the radiative efficiency and transition energy.

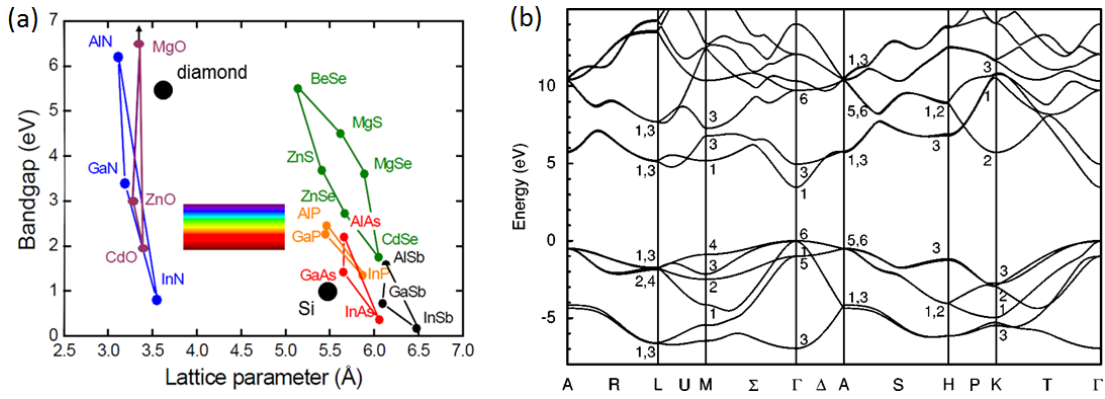


Figure 1.2: (a) Bandgap of the main semiconductors as a function of the in-plane lattice parameter. (b) Band structure of wurtzite GaN along high-symmetry lines in the Brillouin zone taken from Ref. [34].

1.3.1 Energy bandgap and refractive index

The design of a heterostructure (a key element of any optoelectronic devices) consists in assembling crystalline materials with different bandgaps and refractive indices but with similar lattice constants in order to obtain a pseudomorphic growth.

The energy bandgap E_g of III-nitride binary compounds and their alloys hold the interesting property to have a direct bandgap over a broad spectrum of frequency that covers the entire visible spectrum, the near IR, and the deep UV [see Fig. 1.2 (a)]. The bandgap is defined as “direct” if the crystal momentum of electrons and holes in the Brillouin zone is the same in both the conduction band and the valence band [e.g., at Γ point in Fig. 1.2 (b)]. In direct bandgap semiconductors, band-to-band radiative transitions are highly favorable since momentum will be conserved upon radiative recombination. This means a higher quantum efficiency of the structure. Values of E_g at low temperature (0 K) and at room temperature (RT, 300 K) of nitride binary compounds are listed in Table 1.1. The bandgap of any ternary alloys $M_{1,x}M_{2,1-x}N$ can

be estimated as follows:

$$E_g(M_{1,x}M_{2,1-x}N) = x \cdot E_g(M_1N) + (1-x) \cdot E_g(M_2N) - b \cdot x \cdot (1-x), \quad (1.5)$$

where b is the bowing parameter accounting for the deviation from an ideal linear interpolation between binary compounds (in nitride alloys, $b > 0$). Concerning biaxial strain in GaN epilayers, a tensile strain decreases the bandgap energy while a compressive strain increases it [35].

The direct bandgap of a semiconductor decreases with increasing the temperature and can be accounted for by the Varshni's semi-empirical law [36]:

$$E_g(T) = E_g(T=0) - \frac{\alpha T^2}{T + \beta}, \quad (1.6)$$

where α and β are empirical independent parameters proper to each compound. This behavior is related to the inter-atomic distance. Indeed, the presence of an anharmonic potential induces an increase of the lattice constant when increasing the temperature. The refractive index of wurtzite GaN is commonly measured via spectroscopic ellipsometry [37]. The refractive index of AlGaIn alloys can be experimentally determined directly from the material optical properties [38]. Nevertheless, the refractive index of ternary alloys such as AlGaIn and InGaIn can also be roughly estimated by shifting the energy scale of the refractive index of GaN, i.e., $n_{GaIn}(E)$. The shift thus reads [38]:

$$n_y(E) = n_{GaIn}(E - [E_g(y) - E_g(\text{GaN})]), \quad (1.7)$$

where $y = \text{In}_x\text{Ga}_{1-x}\text{N}$ or $\text{Al}_x\text{Ga}_{1-x}\text{N}$. The variation in bandgap energy with mole fraction for $\text{In}_x\text{Ga}_{1-x}\text{N}$ and $\text{Al}_x\text{Ga}_{1-x}\text{N}$ can be extrapolated from eq. 1.5 for the specific case of $M_i = \text{In}$ and/or Al [38, 39]:

$$E_g(\text{In}_x\text{Ga}_{1-x}\text{N}) = 3.42(1-x) + 2.65x - 3.94x(1-x) \quad [\text{eV}], \quad (1.8)$$

$$E_g(\text{Al}_x\text{Ga}_{1-x}\text{N}) = 3.45(1-x) + 6.13x - 1.3x(1-x) \quad [\text{eV}]. \quad (1.9)$$

The refractive index value in nitrides as in other materials is very important to achieve a proper confinement of light in the active region of a semiconductor. Accurate refractive index values for InGaIn and AlGaIn materials are required to optimize the LD design by exploiting the approach shown in eq. 1.7. The simplest approach is to consider a model based on harmonic oscillators with eigenfrequencies ν_{eo} that can properly describe the absorption and the optical index of the ensemble of transitions between the valence and conduction bands. The first-order Sellmeier equation accounts for the dependency of the real part of the refractive index on the wavelength λ below the bandgap via [40]:

$$n^2(\lambda) = 1 + \frac{E_{eo}E_d}{E_{eo}^2 - (h\nu)^2}, \quad (1.10)$$

where E_d is the dispersion energy and E_{eo} is the energy of a single effective oscillator transition with a resonant frequency ν_{eo} . Both of them are fitting parameters.

Normally, in free space, waves propagate in all directions as spherical waves. To avoid power losses proportional to the square of the distance R , specifically designed optical waveguides can be modeled to confine the wave and to force it propagating in one dimension thus, ideally, without losses. Typically, these waveguides are composed of a high refractive index material sandwiched between two low refractive index layers called cladding layers. Waves are therefore confined within the waveguide due to total internal reflection occurring at the guide-cladding interfaces (Fig. 1.3) and according to the Snell-Descartes and Fresnel law ($n_1 - n_2$) [41]:

$$n_1 \sin \theta_1 = n_2 \sin \theta_2. \quad (1.11)$$

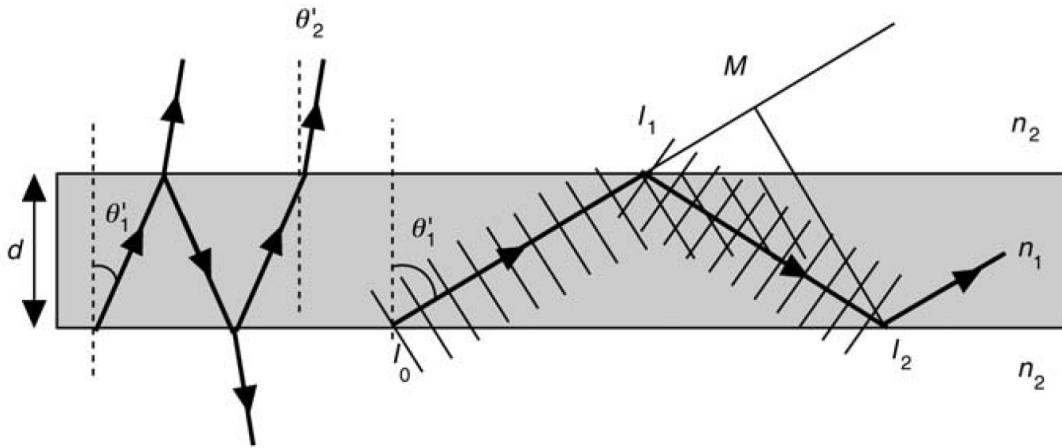


Figure 1.3: Optical confinement of light rays in a waveguide composed of media 1 and 2 taken from Ref. [40].

If $n_1 > n_2$, the lightwave in medium 1 is totally reflected for any incident angle lower than a critical angle θ_c . This condition is called *total internal reflection* and is given by $\theta_c = \arcsin \frac{n_2}{n_1}$. Unfortunately, not all electromagnetic waves satisfying the latter condition will be guided. Indeed, only the reflected waves that remain in phase with the waves produced by previous reflections (each reflection induces a ϕ_r phase shift) can interfere constructively with themselves. This will occur provided that the phase shifts resulting from multiple reflections are integer multiples of 2π and whereby we obtain the self-consistent condition for a confined wave [40]:

$$\frac{2\pi n_1}{\lambda_0} 2d \sin \theta_1 - 2\phi_r = 2\pi m, \quad (1.12)$$

where λ_0 is the vacuum wavelength of the electromagnetic wave, d is the thickness of the high refractive index material placed in the center of the waveguide and m is the number of multiple reflections. The main advantage of waveguides is to confine light where the

materials experience gain (see Sec. 2.1.2).

1.3.2 Quantum confined Stark effect (QCSE)

The presence of an electric field in III-V nitride MQWs when grown along the c -axis causes a redshift of the transition energy, which is the so-called *quantum confined Stark effect* (QCSE). Surface charges σ_{ij} and σ_{ji} with opposite sign appear at the interface between a well of material i and a thick barrier of material j [42]. The resulting total internal field F_{int} in such a single QW reads:

$$\mathbf{F}_{int} = \frac{\sigma_{ij} - \sigma_{ji}}{2\varepsilon_r\varepsilon_0} \mathbf{n}_{ij} = \frac{\sigma_{ij}}{\varepsilon_r\varepsilon_0} \mathbf{n}_{ij} = \frac{\mathbf{P}_i - \mathbf{P}_j}{\varepsilon_r\varepsilon_0}, \quad (1.13)$$

where ε_r is the relative permittivity in the well. This electric field \mathbf{F}_{int} (in the order of MV/cm) tilts the QW band structure leading to a triangular potential shape. For the sake of illustration, in Fig. 1.4 taken from Ref. [25], the band profile of a single InGa_N/Ga_N QW is shown for growth along the polar [Fig. 1.4 (a)] and non-polar [Fig. 1.4 (c) and (e)] axes. Growth along semi-polar axes offers interesting features as it combines the advantages of both polar and non-polar structures. For instance, depending on the alloy composition and the strain state, semi-polar orientations allow to reduce the internal polarization field F_{int} and so to get rid of the QCSE (similarly to non-polar ones) [43]. In addition, it allows for higher indium incorporation in the active region mandatory for applications in the green spectral range.

Miller *et al.* in 1984 first reported on the large shift in optical absorption in GaAs/AlGaAs QWs while experiencing an electric field perpendicular to the layers [44]. According to those authors, exciton resonances remain even for field values much higher than the classical ionization field because of the quantum confinement of carriers in thin semiconductor layers [44, 45]. In III-nitride heterostructures grown along the c -axis, part of the electric field is intrinsic but it can also come from a p - n or p - i - n junction.

It is worth mentioning that Miller *et al.* in a subsequent paper (Ref. [46]) succeeded in correlating the effects observed in the interband optical absorption to an extreme quantization of the so-called Franz-Keldysh effect. This phenomenon was thus described as the *quantum confined Franz-Keldysh effect* (QCFK). In the present work, quantum effects in the QWs will be mostly ascribed to the QCSE.

In nitrides, the first effect of quantum confinement provided by QWs on the optical emission within a triangular-shaped potential concerns the Stark shift. Indeed, the electric field within the QW lowers the QW fundamental transition energy $E_{e_1-hh_1}$ of the electron-hole pairs by a value equal to $-qd_{QW}\|\mathbf{F}_{int}\|$ [47]:

$$E_{e_1-hh_1}(\hbar\omega) = E_g + e_1 + hh_1 - E_X^b - qd_{QW}\|\mathbf{F}_{int}\|, \quad (1.14)$$

where E_g is the bandgap energy, e_1 and hh_1 are the confinement energies of the electron and the hole, respectively, E_X^b is the exciton binding energy in a QW and d_{QW} is the QW

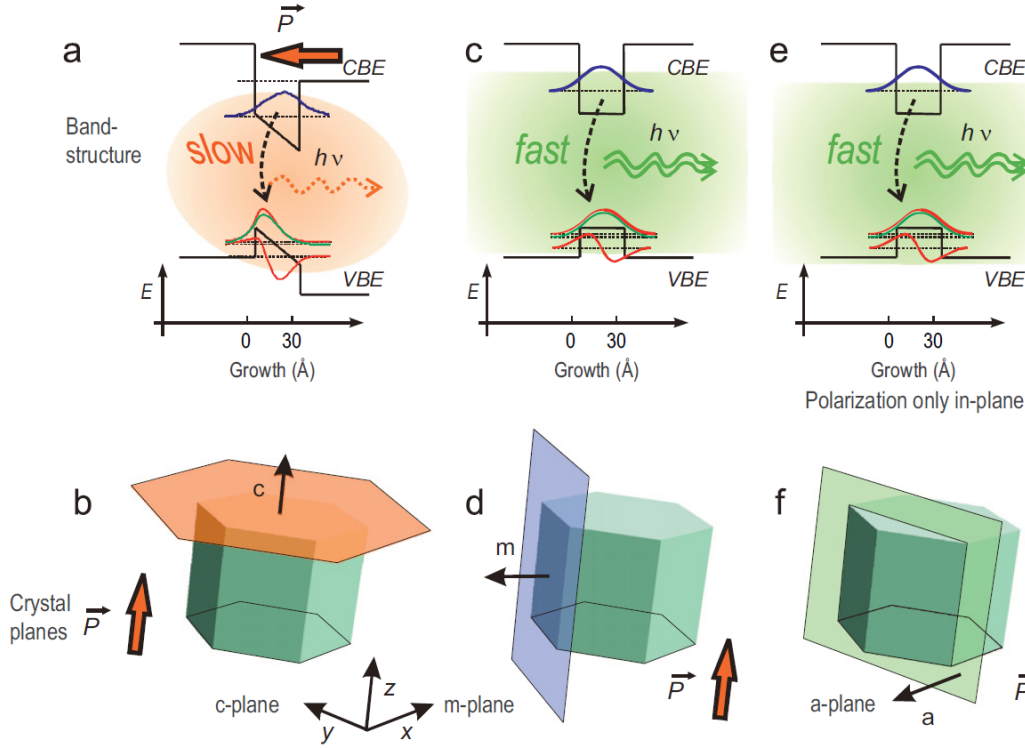


Figure 1.4: Schematic band structure diagram of a single InGaN/GaN QW oriented along different crystal axes (a, c, e). Sketch of QW plane in the hexagonal crystal structure (b, d, f). Situation of polar c -axis (a, b), non-polar m -axis (c, d), and non-polar a -axis growth (e, f). The acronyms CBE and VBE stand for conduction band energy and valence band energy, respectively. This picture is taken from Ref. [25].

width. Interestingly, these nitride native triangular-shaped QWs allow to potentially emit below the bulk material bandgap. As d_{QW} increases, the factor $-qd_{QW}\|\mathbf{F}_{int}\|$ further decreases the transition energy leading to $E_{e_1-hh_1} < E_g$. For instance, Grandjean *et al.* reported an emission below the GaN excitonic bandgap emission (3.478 eV at 10 K) already for $d_{QW} = 3$ nm with $F_{int} = 0.71$ MV/cm for a GaN/AlGaIn QW [48]. Chichibu *et al.* have stressed how the ratio between the products $d_{QW}\|\mathbf{F}_{int}\|$ and the confinement energy hh_1 (and e_1) for d_{QW} comparable to the Bohr radius a_B could determine the magnitude of the QCSE on the emission mechanism in InGaIn QWs [49]. Furthermore, the triangular-shaped potential induces carrier separation on opposite sides of the well (Fig. 1.4). This translates into a reduction of the overlap between electron and hole wavefunctions in the QWs, which induces a reduction in oscillator strength f_{osc} [40]:

$$f_{osc} = \frac{2m_e\hbar\omega_{if}}{\hbar^2} |\langle i|\mathbf{r} \cdot \boldsymbol{\varepsilon}|f\rangle|^2, \quad (1.15)$$

where m_e is the free electron mass (see Table 1.1), $\hbar\omega_{if}$ is the interband transition energy $i \rightarrow f$ and $|\langle i|\mathbf{r} \cdot \boldsymbol{\varepsilon}|f\rangle| = d_{if}$ is the dipolar matrix element of the optical transition from the initial state $|i\rangle$ to the final state $|f\rangle$, \mathbf{r} is the electron momentum operator and \mathbf{e} is the

unitary polarization vector. In the case of a QW, d_{if} is known to be proportional to the square modulus of the overlap integral between electron and hole wavefunctions f_e and f_h along the growth axis via $|d_{if}|^2 \propto |\int f_e(z)f_h(z)dz|^2$. Thus increasing the thickness of a QW causes a drastic decrease in the wavefunction overlap and therefore an increased radiative lifetime τ_{rad} [50]:

$$\tau_{rad} = \frac{2\pi\epsilon_0 m_e c^3}{n_g q^2 \omega_{if}^2 f_{osc}}, \quad (1.16)$$

where n_g is the group refractive index. This process is depicted in Fig. 1.4 with the notation “slow” (“fast”). Note that the QW internal quantum efficiency η_i can be written as $\eta_i = \frac{\tau_{nrad}}{\tau_{nrad} + \tau_{rad}}$, i.e., the amount of injected carriers that recombine radiatively divided by the total carrier recombinations, where τ_{nrad} is the non-radiative carrier lifetime [51]. The radiative carrier lifetime will be treated in more details in Sec. 4.1.

In conclusion, the influence of the QCSE on a GaN-based QW depends on both the well width and the strength of the polarization field. On one side, quantum confinement in narrow QWs provides an efficient confinement for the carriers even in the presence of a high electric field across the heterostructure. On the other side, the existence of a built-in field F_{int} in polar structures implies triangular-shaped QWs. It will break the symmetry of the wavefunctions by pushing electrons and holes toward opposite sides of the well and as a consequence the radiative recombination efficiency will drop compared with non-polar structures (see Fig. 1.4). The thicker the QWs and the higher the internal field, the stronger the QCSE. It is therefore crucial to minimize the impact of the QCSE to achieve high performance optoelectronic devices.

1.4 Electrical properties

High electrical conductivity is essential for optoelectronic devices. Thus, one of the most important technological challenges in semiconductor technology is *doping*, i.e., the controlled incorporation of impurities in a pure intrinsic semiconductor to enhance its electrical conductivity. These impurities can have electronic energy levels within the forbidden gap of the bulk host material, preferably close to the band edges. Before recombining in the active region, carriers (electrons and holes) are injected on opposite sides of the device and pass through several layers. Transport of holes requires the layer to be *p*-type doped (i.e., doped with acceptors) whereas transport of electrons requires *n*-type doping (doping achieved with donors). Typical impurity concentrations used for doping range from 10^{15} to 10^{20} cm⁻³.

In this section, the main features of doping and *p-n* junction in III-nitrides are presented. In particular, the impact of an electric field (internal and/or external) on a is detailed.

1.4.1 *n*-type doping

If no special care is taken III-nitride epilayers exhibit a tendency to be *n*-type: the electron background concentration is about $\sim 10^{17} \text{ cm}^{-3}$ [52]. Nowadays, the origin of non-intentionally doped (*nid*) GaN layers is likely due to impurities such as oxygen or silicon rather than nitrogen vacancies or any other types of native defects [53, 54].

The most commonly used donor impurity for achieving intentional *n*-type doping of III-nitrides is *silicon* (noted GaN:Si) [55, 56, 57]. In MOVPE, silicon doping is achieved by flowing gaseous silane (SiH_4) during growth. The activation energy of Si in GaN is about 17 meV for a donor concentration $N_D = 3 \cdot 10^{17} \text{ cm}^{-3}$ [58]. This means that all donor impurities are ionized at RT. When increasing the doping concentration beyond $N_D = 1 \cdot 10^{20} \text{ cm}^{-3}$, a dramatic degradation in the crystal quality occurs [59] and besides an impurity band may develop. Moreover, such high doping concentrations result in a degenerate system: electrons populate states within the conduction band which shift the Fermi level higher than the CBE. This is the so-called Burstein-Moss effect. In terms of electron mobility, the maximum value amounts to $1425 \text{ cm}^2\text{V}^{-1}\text{s}^{-1}$ for $N_D = 1.76 \cdot 10^{16} \text{ cm}^{-3}$ at RT [60].

Other possible donor sources for nitrides less often used are for example oxygen and germanium that exhibit an activation energy of 29 meV for $N_D = 1 \cdot 10^{18} \text{ cm}^{-3}$ and 19 meV for $N_D = 3 \cdot 10^{17} \text{ cm}^{-3}$, respectively [58]. In both cases, the ionization energy is sensitive to the concentration of the dopant [61].

1.4.2 *p*-type doping

The most common and efficient *p*-type dopant is currently *magnesium*. In MOVPE, magnesium doping is achieved by flowing a bis-cyclopentadienyl magnesium precursor (Cp_2Mg) during growth. However, in III-nitrides *p*-type doping has always been difficult to achieve. An efficient acceptor should indeed possess three main characteristics: (i) stability against compensation by other configurations of the acceptor dopant (e.g., hydrogen passivation), (ii) high solubility and (iii) low ionization energy [1]. Possible candidates are: Ca, Zn, Be and Mg. Magnesium is up to date the only acceptor which approaches all these criteria [62, 63].

Actually, in MOVPE-growth Mg-doped layers are highly resistive because of the formation of Mg-H complexes that are electrically inactive. A post-growth process that allows breaking Mg-H bonds and thus overcoming this hydrogen passivation is therefore required. Amano *et al.* in 1989 reported the first successful *p*-doping by using magnesium as dopant and applying an activation process based on low-energy electron-beam irradiation (LEEBI) [6]. Afterwards, Nakamura *et al.* demonstrated that a thermal annealing in N_2 ambient could also activate Mg impurities [64].

The conductivity is the product of dopant concentration by their mobility but unfortunately obtaining both a high hole mobility and a high hole concentration is challenging. Indeed, a high hole concentration can be obtained but at the expense of a strong degra-

dation of the mobility due to material defects and scattering (i.e., a high resistivity is observed) [1]. Indeed, the solubility limit of Mg in GaN is quite low (in the range of $\sim 10^{19} \text{ cm}^{-3}$) [58].

The acceptor should also be as shallow as possible, i.e., with the lowest activation energy. Mg is a deep acceptor as its ionization energy is around 170 meV (see Table 1.1). This means that at RT only a few percents of the acceptors are actually activated (typically $N_A = 10^{19} \text{ cm}^{-3}$ is required to obtain a few 10^{17} cm^{-3} free holes) [63]. Typical p -type doping features a hole mobility of $9 \text{ cm}^2\text{V}^{-1}$ for a hole concentration of 10^{18} cm^{-3} and a resistivity of $0.75 \text{ }\Omega\text{cm}$ [30].

In conclusion, the limit of Mg acceptor concentration and the deep acceptor energy level of Mg dopants limit the conductivity of p -type GaN layers, which can hinder the performance of optoelectronic devices.

1.4.3 p - n junction

Most of optoelectronic devices are based on semiconductor materials in which a p - n junction is included. Therefore, they are considered bipolar devices in contrast to unipolar ones like, e.g, the quantum cascade lasers. Thus, the junctions are commonly used as diodes: circuit elements that allow a flow of current in one direction but not in the opposite direction. The characteristics of an abrupt p - n junction at thermodynamic equilibrium are depicted in Fig. 1.5. A p - n junction is composed of a doped p -type semiconductor and a doped n -type semiconductor in contact. In the junction a depletion region (or also called space charge region) forms. The transport properties are determined by the recombination of the minority carriers while the depletion region collapses. These minority charge carriers can be trapped in one or multiple thin layers with a lower bandgap than the surrounding material in order to enhance their recombination and increase their local density. In this subsection, the creation and the subsequent control of these charge carriers will be analyzed.

An abrupt junction consists in a junction over which the doping changes from n to p over a very short distance, i.e., from acceptor impurity concentration N_A to donor impurity concentration N_D , as shown in Fig. 1.5 (a). So, when contacting the doped layers, a diffusion current appears due to the difference in charge carrier concentration: $J_{diff} = J_{diff,n} + J_{diff,p}$. The electrons diffuse from the n -region to the p -one and conversely for the holes. The regions nearby the p - n interface lose their neutrality and become charged forming a *depletion region* W_D (also called space charge region) where the charge carrier concentration is orders of magnitude lower than the fixed charge concentration given by ionized acceptors and donors. At thermal equilibrium, the electric field is zero at the boundaries of the depletion region (and obviously far from the junction on either side) while the space charge region must satisfy the neutrality condition: $N_A W_{D_p} = N_D W_{D_n}$, where W_{D_p} and W_{D_n} are the space charge extent in the p -type and n -type materials, respectively [Fig. 1.5 (b)]. Therefore, the electrostatic potential Ψ_{bi} created by this space charge region is opposed to the diffusion process for both electrons and holes [Fig. 1.5

(c)] and produces a drift electric field: $J_{drift} = J_{drift,n} + J_{drift,p}$. The total drift and diffusion current is given by the equation [51]:

$$J_i = \underbrace{q \mu_i i \mathbf{E}}_{drift} + \underbrace{q D_i \nabla i}_{diffusion} = \mu_i i \frac{dE_F}{dx}, \quad (1.17)$$

where μ_i are the mobility coefficient, \mathbf{E} is the drift electric field, D_i are the diffusion coefficients, i and ∇i are the concentration and the gradient of concentration for the i -type of carrier (n or p), respectively, and $\frac{dE_F}{dx}$ is the gradient of the intrinsic Fermi level E_F across the junction. The Einstein relation connects the diffusion coefficient D_i and the mobility μ_i via the relation $D_i/\mu_i = k_B T/q$ where T is the temperature and k_B the Boltzmann constant and allows the formulation of the second part of equation 1.17. At thermodynamical equilibrium (i.e., without external bias), the Fermi level E_F is constant across the junction [see Fig. 1.5 (d)]. No net current flows in this case: $J_i = 0$ and $J_{drift,i} = J_{diff,i}$. These two counterbalancing phenomena establish equilibrium: the drift current exactly compensates the diffusion current. This equilibrium leads to a well defined space charge region $W_D = W_{D_p} + W_{D_n}$ across the junction, which extends mostly on the lowest doped region [Fig. 1.5 (a)]. Consequently, the charge separation implies the presence of a built-in potential Ψ_{bi} , which writes [40]:

$$q\Psi_{bi} = E_g - k_B T \ln \frac{N_v N_c}{N_A N_D}, \quad (1.18)$$

where N_v and N_c are the effective density of states in the valence and conduction band, respectively. Ψ_{bi} is the direct consequence of charged (positively and negatively) regions induced by carrier diffusion and it is responsible for the established equilibrium between current flows in the junction. Typically, Ψ_{bi} amounts to 0.8 V for Si, 1.3 V for GaAs and 3 V for GaN.

The application of an external bias V to the p - n junction unbalances the drift/diffusion equilibrium via the relation $\Psi_{bi} - V$, which subsequently induces a difference between the quasi-Fermi levels on either side of the depletion region and therefore $J_i \neq 0$. A forward bias lowers Ψ_{bi} , which favors the diffusion of minority carriers and at the same time it reduces the width of the depletion region. Conversely, a reverse bias increases Ψ_{bi} opposing a higher resistance to the flow of charge carriers (until breakdown of the diode occurs) so that the depletion effect will then increase too. The width of the depletion layer W_D is given by [29]:

$$W_D = \sqrt{\frac{2\epsilon_r \epsilon_0}{q} \frac{N_A + N_D}{N_A N_D} (\Psi_{bi} - V - d_{QW} F_{int})}, \quad (1.19)$$

where F_{int} is the total internal polarization field given by equation 1.13.

In the specific case of a p - i - n junction (where a lightly doped region is placed within the

junction) the depletion region width reads [65, 66]:

$$W_D = -d_u + \sqrt{d_u^2 + \frac{2\varepsilon_r\varepsilon_0}{q} \frac{N_A + N_D}{N_A N_D} (\Psi_{bi} - V - d_{QW} F_{int})}, \quad (1.20)$$

where d_u is the width of their intrinsic region. This equation will be especially useful for simulating the behavior of standard GaN-based diodes where some active regions are left intentionally undoped (typically the QWs and the first p -side QW barrier) with the aim of preserving the crystal quality during growth. The application of an external bias V to this structure simply acts as a simple metal plate capacitor with a constant electric field in the intrinsic region [40, 65, 66]:

$$F_{ext} = \frac{\Psi_{bi} - V - d_{QW} F_{int}}{d_u + W_D/2}, \quad (1.21)$$

where the factor $1/2$ is used to maintain consistency with Poisson's equation. To get the total net-field applied across the heterojunction, the internal polarization contribution (eq. 1.4) must be added:

$$F_{QW} = F_{ext} + F_{int}. \quad (1.22)$$

When applying an external bias V , equation 1.17 is no longer balanced (i.e., $J_i \neq 0$) and a current establishes. It is given by the Shockley equation for an ideal diode, which for $\Psi_{bi} \neq 0$ reads:

$$J = J_0 \cdot (e^{q \frac{V - \Psi_{bi}}{\eta k_B T}} - 1), \quad (1.23)$$

where $J_0 = \frac{q D_n n_{p0}}{L_n} + \frac{q D_p p_{n0}}{L_p}$ is the diffusion current limit, i_{j0} is the minority carrier density i in the region j , L_i is the diffusion length with $L_n = \sqrt{D_n \tau_n}$ and $L_p = \sqrt{D_p \tau_p}$ and η is the ideality factor. This equation is only valid under the assumption of: an abrupt junction, Boltzmann approximation, low injection (i.e., the injected minority-carrier density is small compared to the majority-one density) and no generation-recombination current occurs in the depletion layer (i.e., electron and hole currents are constant throughout the depletion layer) [29]. In the case of GaN-based p - n junction, the ideality factor is usually much larger than 2 due to the still poor materials quality and the not fully optimized process technologies [67].

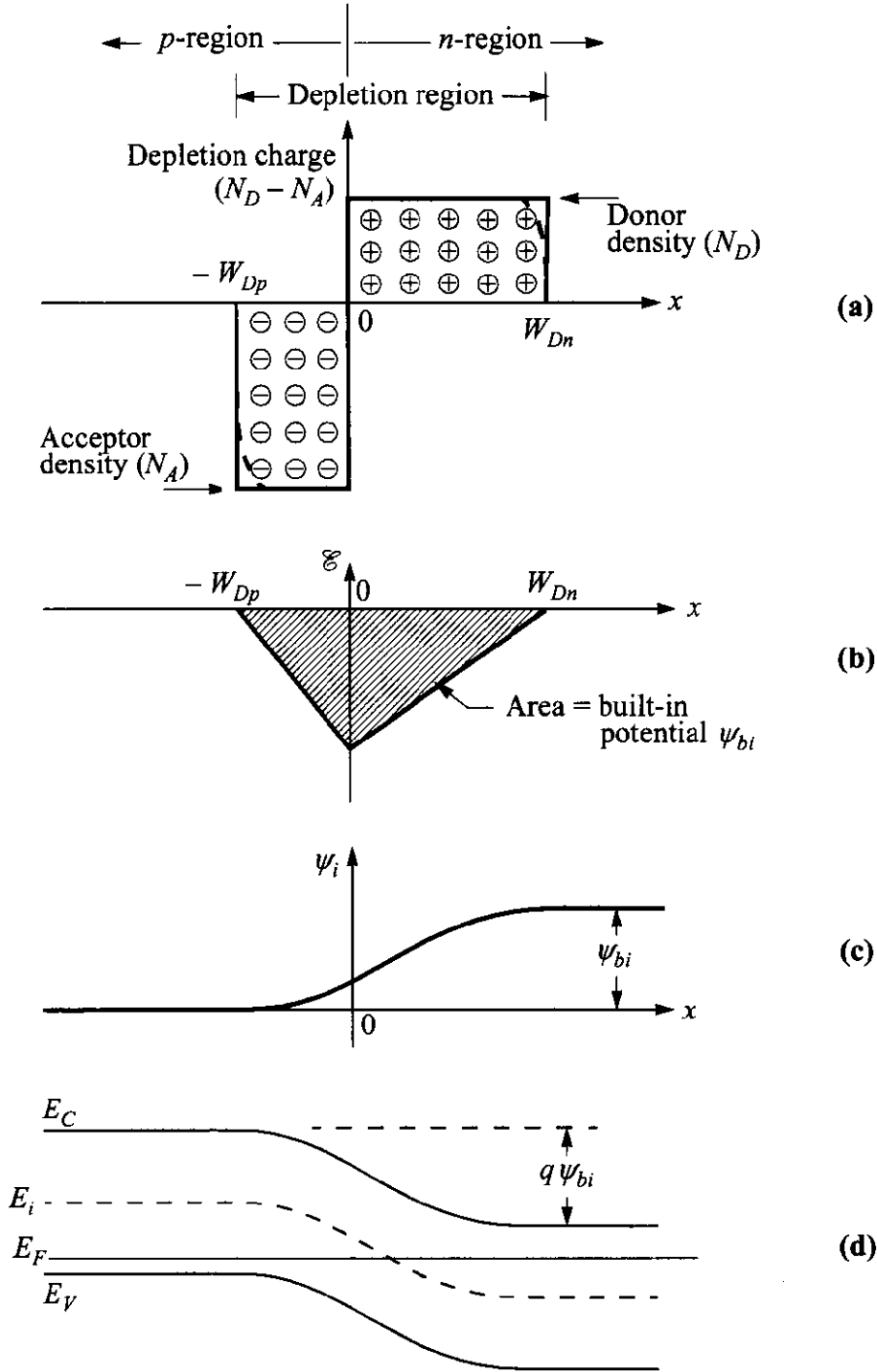


Figure 1.5: Abrupt p - n junction in thermal equilibrium adapted from Ref. [51]. (a) Space charge distribution. The dashed lines indicate corrections to the depletion approximation. (b) Electric field distribution. (c) Potential distribution where Ψ_{bi} is the built-in potential. (d) Energy band diagram. At equilibrium the Fermi level E_F is the same on both sides. However, by applying an external electric field, the Fermi level splits in two distinct quasi-Fermi levels.

2 GaN-based laser diodes

An active medium for light amplification via stimulated emission, a resonator for optical feedback and a pump source are the necessary elements for any laser system. In this chapter, the functional layers and the basic layout of III-nitride devices are outlined. Specificities about standard edge-emitting LDs and the so-called multi-section LDs (MS-LDs) are highlighted. In particular, the static and dynamic regimes involved in the active media are detailed in regards to the different device parameters. Finally, an overview of the microfabrication design and process is presented.

Note that as the III-nitride market is driven by leading commercial companies (such as Nichia, Osram, Samsung, . . .), it is often difficult to find reliable information concerning the device parameters. Thus, often the main reference for comparison relies on the know-how developed in the past decades on similar materials families such as GaAs. The main physical parameters for the III-nitride structures studied in this thesis are listed in Table 2.1.

	number notation	2D notation	3D notation
Coefficient A	$4.2 \cdot 10^7 \text{ s}^{-1}$ [68]	$4.2 \cdot 10^7 \text{ s}^{-1}$	$4.2 \cdot 10^7 \text{ s}^{-1}$
Coefficient B , linear model	0.202 s^{-1} [68]	$3.232 \cdot 10^{-6} \text{ cm}^2 \text{ s}^{-1}$	$1.454 \cdot 10^{-12} \text{ cm}^3 \text{ s}^{-1}$
Coefficient C , linear model	$1.71 \cdot 10^{-9} \text{ s}^{-1}$ [68]	$4.378 \cdot 10^{-19} \text{ cm}^4 \text{ s}^{-1}$	$8.865 \cdot 10^{-32} \text{ cm}^6 \text{ s}^{-1}$
Coefficient B , wavelength-dep. model	2.778 s^{-1}	$4.445 \cdot 10^{-5} \text{ cm}^2 \text{ s}^{-1}$	$2 \cdot 10^{-11} \text{ cm}^3 \text{ s}^{-1}$
Coefficient C , wavelength-dep. model	$3.16 \cdot 10^{-8} \text{ s}^{-1}$	$8.089 \cdot 10^{-18} \text{ cm}^4 \text{ s}^{-1}$	$1.638 \cdot 10^{-30} \text{ cm}^6 \text{ s}^{-1}$
Differential gain dg/dN	$4.3 \cdot 10^{-7} \text{ cm}^{-1}$ [68]	$7.5 \cdot 10^{-12} \text{ cm}$	$3.5 \cdot 10^{-18} \text{ cm}^2$
Transparency carrier N_{tr} , linear model	$3.3 \cdot 10^8$ [69]	$2.063 \cdot 10^{13} \text{ cm}^{-2}$	$4.583 \cdot 10^{19} \text{ cm}^{-3}$
Threshold carrier N_{th} , linear model	$4.69 \cdot 10^8$	$2.932 \cdot 10^{13} \text{ cm}^{-2}$	$6.512 \cdot 10^{19} \text{ cm}^{-3}$
Critical carrier N_c	$3.23 \cdot 10^7$	$2.02 \cdot 10^{12} \text{ cm}^{-2}$	$4.49 \cdot 10^{18} \text{ cm}^{-3}$
Transparency carrier N_{tr} , wavelength-dep. model	$2.22 \cdot 10^7$	$1.39 \cdot 10^{12} \text{ cm}^{-2}$	$3.09 \cdot 10^{18} \text{ cm}^{-3}$
Threshold carrier N_{th} , wavelength-dep. model	$8.58 \cdot 10^7$	$5.36 \cdot 10^{12} \text{ cm}^{-2}$	$1.19 \cdot 10^{19} \text{ cm}^{-3}$
Gain compression factor ε_{sat}	$1 \cdot 10^{-8}$ [69, 70]	$1.6 \cdot 10^{-13} \text{ cm}^2$	$3.6 \cdot 10^{-18} \text{ cm}^3$
Optical confinement factor Γ	0.015 for $\text{In}_{0.1}\text{Ga}_{0.9}\text{N}/\text{In}_{0.01}\text{Ga}_{0.99}\text{N}$ and 0.024 for $\text{In}_{0.1}\text{Ga}_{0.9}\text{N}/\text{In}_{0.05}\text{Ga}_{0.95}\text{N}$		
Kane energy E_p (eV)	17.292 [20]		
Bandgap energy E_g (eV)	2.941 for $\text{In}_{0.1}\text{Ga}_{0.9}\text{N}$		
Total cavity losses α_{TOT} ($\alpha_i + \alpha_m$) (cm^{-1})	60 (30 + 30)		
Injection efficiency η_{inj}	0.68 [68]		
Group refractive index n_g	3.84 for $\text{In}_{0.1}\text{Ga}_{0.9}\text{N}$ [69]		
Spontaneous emission factor β	$1 \cdot 10^{-5}$ [40]		
Electron effective mass, m_e/m_0	0.187		
Heavy-hole effective mass, m_{hh}/m_0	1.423		

Table 2.1: Experimental and theoretical values *per well* of the physical parameters used in the simulations. 2D and 3D densities have been calculated for an $\text{In}_{0.1}\text{Ga}_{0.9}\text{N}$ QW with $d_{QW} = 4.5 \text{ nm}$, $w = 2 \text{ }\mu\text{m}$ and $L_{TOT} = 800 \text{ }\mu\text{m}$. The A , B and C coefficients refer to the ABC model.

2.1 Structure design

Due to critical limitations that arise from the unique materials properties of III-nitrides, careful attention must be paid when conceiving the layer design of such optoelectronic device. The growth of pseudomorphically strained InGaN layers is very demanding due to the very large lattice constant difference between GaN and InN crystals. Furthermore, composition and thickness fluctuations will result in significant inhomogeneous broadening of the spontaneous emission and gain spectrum.

Many modern semiconductor devices rely on *heterostructures*, which consist in a complex stacking of materials of different bandgaps during the epitaxial growth, a technique called *bandgap engineering*. The simplest case is a planar interface, i.e., a layered system. The so-called active region consists then in creating a heterostructure thus forming a valence and conduction band discontinuity. Typically in III-nitrides, the ternary alloys AlGaIn and InGaIn are the most commonly used materials for these purposes. The samples studied in this thesis are composed of multiple InGaIn/GaN and GaIn/AlGaIn QWs (see Table 2.2). To investigate the relevant optical properties of a heterostructure such as the transition energy or the optical gain, the band structure of the QWs is calculated with the $6 \times 6 - \mathbf{k} \cdot \mathbf{p}$ method. These band structure calculations based on Kane theory of strained wurtzite semiconductors have been developed by G. Rossbach and J. Levrat at LASPE [14]. In this section, the design of a semiconductor laser device is presented in two parts: inside and outside the active region.

2.1.1 Inside the active region

To improve the injection efficiency (and so the recombination efficiency), a heterojunction composed of wide bandgap semiconductor and a narrower bandgap semiconductor (if possible with similar lattice constant) is designed [33]. Type-I heterostructure is preferred as both electrons and holes are confined in the same layers. A QW is a special type of heterostructure in which the thickness of the active region is of the order of the de Broglie wavelength of the electron in the semiconductor materials. An equivalent definition states that to have a QW, d_{QW} should be in the order of the 3D Bohr radius extension of the exciton. Basically, electrons and holes are trapped and confined so tightly in one spatial direction that discrete energy levels arise due to their wave-particle nature.

The devices studied during this thesis possess mostly an InGaIn/GaN and InGaIn/InGaIn active region (see Table 2.2). Those heterostructures allow for both strong carrier confinement into the active layer over a large part of the visible spectrum. However, the growth of high quality InGaIn alloy is extremely difficult and it needs to be performed at much lower temperatures than that of GaIn. Indeed, the dissociation temperature of InN is very low [71].

The QW active region is designed to restrain charge carriers in a small volume in which recombinations via spontaneous or stimulated emission are favored compared to all other non-radiative recombination channels. The Coulomb interaction between electron-hole

pairs (i.e., electrically neutral quasi-particles called excitons) is strongly enhanced by spatial confinement when a_B is comparable to d_{QW} : in a perfect two-dimensional system, the exciton binding energy E_X^b is four times larger than its bulk value [72]. The higher the bandgap energy difference between the heterojunction components, the higher the carrier confinement in the well. The potential barriers that trap the carriers in the well are the conduction band offset E_{CBO} (for the electrons) and the valence band offset E_{VBO} (for the holes) [Fig. 2.1 (a)].

In Sec. 1.3.2, we have seen how the existence of a built-in field \mathbf{F}_{int} in III-nitrides induces a tilt of the QW potential. As a consequence, the electron and hole wavefunctions drop into their respective triangular potential wells causing a c -axis directional separation and a reduction in the transition energy, which is the manifestation of the QCSE [49]. In Fig. 2.1, the impact of the QCSE on the electronic properties of a single $\text{In}_{0.1}\text{Ga}_{0.9}\text{N}/\text{GaN}$ QW is depicted. However, note that under electrical injection, the carriers can partially screen \mathbf{F}_{int} and blueshift the electroluminescence peak [1]. As shown in Fig. 2.1 (b),

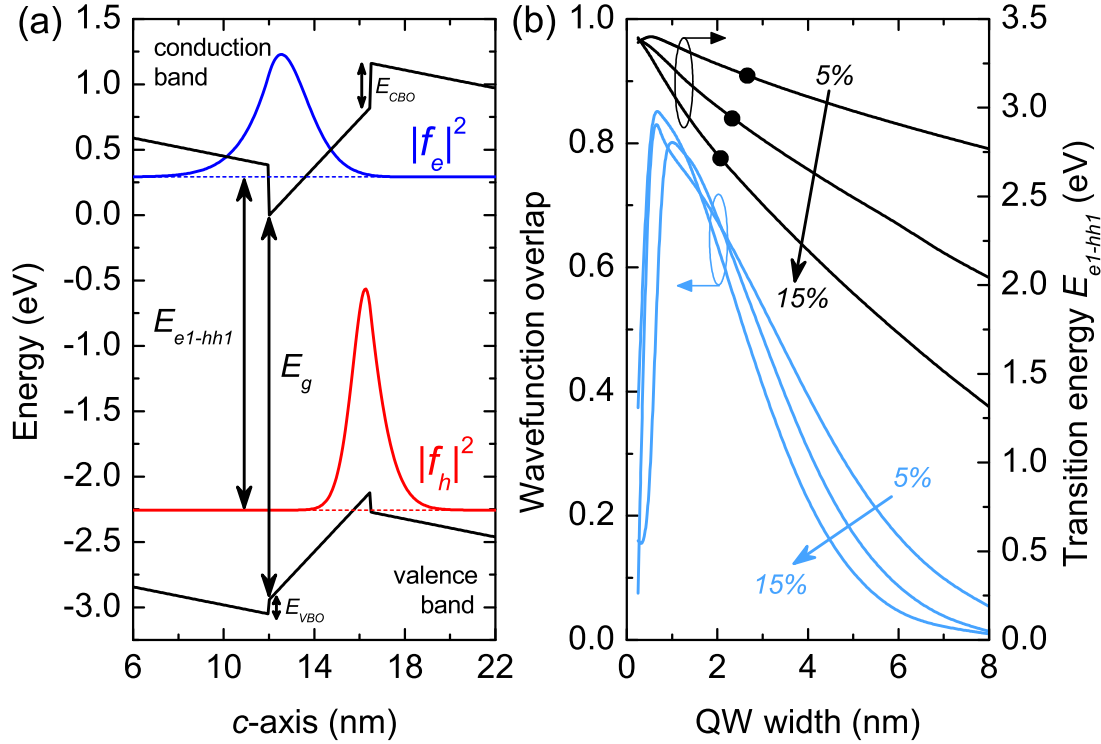


Figure 2.1: (a) Band profile of a 4.5 nm thick $\text{In}_{0.1}\text{Ga}_{0.9}\text{N}$ QW sandwiched between two 12 nm thick GaN barriers with electron and hole probability densities. The estimated \mathbf{F}_{int} is -1.84 MV/cm. Electron (blue) and hole (red) probability densities $\|f_e\|^2$ and $\|f_h\|^2$ are calculated in the envelope wavefunction approximation. (b) Squared electron-hole wavefunction overlap and transition energy for different indium contents in the QW ($\text{In}_{0.05}\text{Ga}_{0.95}\text{N}$, $\text{In}_{0.1}\text{Ga}_{0.9}\text{N}$ and $\text{In}_{0.15}\text{Ga}_{0.85}\text{N}$) as a function of the QW width. The black circles indicate the bandgap energy E_g for each indium content.

when increasing the thickness and/or the indium content in the QW, the transition energy and the wavefunction overlap decrease dramatically. More indium-rich QWs result in higher strain and stronger internal fields. Then, the effect of \mathbf{F}_{int} becomes huge for large well width. In fact, in wide QWs, electrons and holes are located on the opposite sides of the well and the recombination probability decreases. Therefore, QW widths are typically limited to a few nanometers in conventional devices grown on *c*-plane GaN. Note that the wavefunction overlap reaches a maximum for a well thickness of about 0.75 nm. The decrease for narrower wells is ascribed to lower confinement, which occurs earlier in triangular QWs [47].

2.1.2 Outside the active region

The design of a semiconductor device strongly depends on the active region itself, which is responsible for the recombination mechanisms necessary for the emission of light. On the contrary, the growth structure outside the active region is conceived to enhance the efficiency of the latter. More explicitly it should ensure an optimal flow of carriers up to the active region and a good overlap of the electromagnetic field with the QW layers. An undoped active region is usually placed at the interface between the *p*- and *n*-doped layers (technically, this consists in a *p-i-n* diode). Under a sufficient forward bias (greater than Ψ_{bi}), a current flows across the device, which corresponds to carrier recombination in the active region. In optoelectronic devices the main current is the recombination current, i.e., the electron-hole pairs trapped in the QWs that radiatively recombine and generate light. One can now understand the crucial importance of such wells to capture the carriers and hence to increase the recombination rate and the carrier density in the active region [33].

As mentioned in the first chapter of this thesis, electrons and holes have different mobility values in nitride alloys. The hole mobility is a few orders of magnitude smaller than the electron one [30, 60]. Therefore, holes are more efficiently trapped in the first QW (located on the *p*-side) while electrons tend to spread all over the QWs and even to escape the active region. To frustrate the overflow of electrons into the *p*-side, a thin AlGaN layer (typically with 20% aluminum) acting as an electron blocking layer (EBL) is introduced after the last QW barrier on the *p*-side (see Fig. 2.2) [73]. The blocking effect is indeed much stronger for electrons than for holes. This effect is stemming from the common anion rule that governs the band offsets of most semiconductors. Typically the ratio E_{CBO}/E_{VBO} is fixed to be 70:30 for the GaN/AlN system, 70:30 for InN/GaN and 40:60 for InN/AlN [74].

When designing an optical device (especially for LDs), another crucial factor is the efficient confinement of light in a specific region in order to promote the stimulated recombination rate. In other words, the region surrounding the heterostructure should act as an *optical waveguide* (see Sec. 1.3.1). The problem with QWs is that their thickness is simply too small to effectively confine the light. To optimize the overlap between the

electromagnetic light mode and electric carriers, thick cladding layers (usually hundreds of nm thick) are grown at the bottom and on top of the QW active region. These layers for an InGaN laser waveguide are typically composed of AlGaN due to its lower refractive index than GaN (Fig. 2.2) [75]. Such a design is called a separate confinement heterostructure (SCH) and its purpose is to confine the optical mode vertically and to maximize the overlap between the mode and the active region (see the inset of Fig. 2.2). The interaction between the optical mode and the gain region is then accounted for by the optical confinement factor Γ , i.e., the part of the wave that has a geometrical overlap with the gain medium. It is therefore the only region experiencing light amplification [40]:

$$\Gamma = \frac{\int_{-d/2}^{d/2} |E(z)|^2 dz}{\int_{-\infty}^{+\infty} |E(z)|^2 dz}, \quad (2.1)$$

where d is the active region thickness. The total electric field along the cavity can be written as $E(x, y, z) = E(x, y) \cdot E(z)$ with $E(z)$ the perpendicular component of the field. Interestingly, Rosencher and Vinter state that Γ is indeed the fraction of the wave which “sees” the absorbing medium or which experiences amplification in case of population inversion [40]. Unfortunately, the optical mode can interact not only with the gain region but also with lossy regions. For nitride-based heterojunctions, the dominant loss mechanism is the hole phonon-assisted absorption from non-ionized acceptors in the p -type layers [76]. The overall free-carrier absorption loss can be as high as a few tens of cm^{-1} . Therefore, careful attention should be paid to reduce the overlap of the optical mode with the p -type layers and to reduce as much as possible the internal absorption losses.

In order to optimize the efficiency of the waveguide in terms of overlap between the optical mode and the active region, the scalar wave equation obtained from Maxwell’s equations can be solved by numerical simulations. The electric field $\mathbf{E}(\mathbf{r}, t) = \mathbf{E}(x, y)e^{-i\beta z}e^{i\omega t}$ of an electromagnetic wave traveling along the Oz direction in a neutral medium (i.e., for a current $\mathbf{j} = 0$ and a charge density $\rho = 0$) possessing an index of refraction $n(\mathbf{r})$ is solution of [40]:

$$\left(\frac{\partial^2}{\partial x^2} + \frac{\partial^2}{\partial y^2} \right) \mathbf{E}(x, y) + [k^2 n^2(\mathbf{r}) - \beta^2] \mathbf{E}(x, y) = 0, \quad (2.2)$$

where $k = \omega/c$ is the norm of the wavevector \mathbf{k} , ω is the wave radial frequency and β is the propagation constant. In the case of the waveguide previously discussed, namely characterized by layers of respective refractive index $n_2/n_1/n_2$ that fulfill $n_1 > n_2$, the only stable solutions of eq. 2.2 have to satisfy the condition $kn_1 > \beta > kn_2$: the amplitude $E(x)$ is sinusoidal within the guide and decreases exponentially outside. These wavevectors are called *guided modes*.

Figure 2.2 shows one-dimensional optical mode simulations according to eq. 2.2 for the layer structure depicted on the left-hand side. The black curves correspond to the refractive indices of active regions with different indium compositions in the QW barriers:

$\text{In}_{0.1}\text{Ga}_{0.9}\text{N}/\text{In}_{0.01}\text{Ga}_{0.99}\text{N}$ (solid) and $\text{In}_{0.1}\text{Ga}_{0.9}\text{N}/\text{In}_{0.05}\text{Ga}_{0.95}\text{N}$ (dashed). The optical mode intensity is high at the QW position and shrinks toward the substrate. This is even more evident in the inset of Fig. 2.2 where a magnification of the active region is displayed. Per QW, simulations gives $\Gamma = 1.48\%$ for the $\text{In}_{0.1}\text{Ga}_{0.9}\text{N}/\text{In}_{0.01}\text{Ga}_{0.99}\text{N}$ and 2.36% for $\text{In}_{0.1}\text{Ga}_{0.9}\text{N}/\text{In}_{0.05}\text{Ga}_{0.95}\text{N}$ structures. Note that the optical mode is less confined and broader for the sample with lower indium composition in the well barriers due to the higher index contrast between the InGaN layers and the AlGaN cladding layer. For $\text{In}_{0.1}\text{Ga}_{0.9}\text{N}/\text{In}_{0.01}\text{Ga}_{0.99}\text{N}$ heterostructures the optical mode also couples to a guided mode in the substrate (the oscillations visible on the left-hand side of the graph in Fig. 2.2). Contrary to guided modes, these solutions of eq. 2.2 satisfy the condition $\beta < kn_2$: the amplitude $E(x)$ is sinusoidal everywhere and the wave escape from the waveguide. These kinds of wavevector are referred to as *leaky modes*. Mode leakage into the substrate can be seen on the laser far-field emission pattern and cause an increase in the threshold current required for lasing [69].

Lateral waveguiding of the optical mode is instead achieved using gain guiding and/or index guiding geometries. For gain-guided structures, the gain region (i.e., that where amplification of the guided light occurs) is defined by the stripe contact and the current flowing through it. Unfortunately, a very high pumping rate can reduce the refractive index and a competing antiguiding effect may appear [29]. On the contrary, index-guided

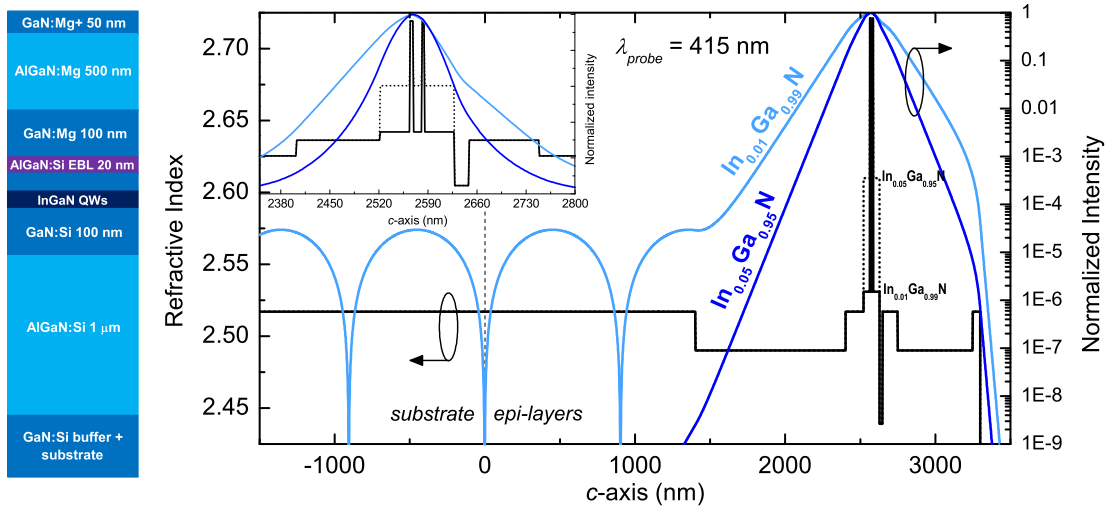


Figure 2.2: Intensity distribution of optical eigenmodes at 415 nm for a typical laser structure with two QWs and corresponding refractive index profile (black). The active regions are composed of $\text{In}_{0.1}\text{Ga}_{0.9}\text{N}/\text{In}_{0.01}\text{Ga}_{0.99}\text{N}$ (dark blue) and $\text{In}_{0.1}\text{Ga}_{0.9}\text{N}/\text{In}_{0.05}\text{Ga}_{0.95}\text{N}$ (light blue), respectively. The cladding layers contain 6% of aluminum. Refractive indices are calculated from eq. 1.7, 1.8 and 1.9 following the model described in Refs. [38], [39] and [77]. The inset shows a magnification of the active region emphasizing the configuration for a QW laser with separate confinement layers for both carriers and photons (referred to as a SCH laser). On the left-hand side the layer compositions of the structures along a vertical c -axis are shown.

structures provide efficient lateral light confinement by fabricating a mesa-like contact ridge (Fig. 2.16). The advantages of index-guided structures compared with gain-guided ones are their lower current spreading and the strong lateral optical confinement resulting from the refractive index contrast between the ridge (semiconductor material) and air. For all these reasons, it is really essential to have a proper design of the device heterostructure.

2.1.3 Sample fabrication

The samples studied during this thesis are grown by MOVPE in a low pressure reactor from Aixtron on 2-inch wide wafers. They are listed in Table 2.2. The notation $A-$ stands for the MOVPE horizontal reactor and $C-$ for the vertical one. According to their purpose we can divide them in two categories: samples for dynamic LDs and samples for SR studies.

The samples belonging to the first class are InGaN-based heterostructures. Laser structures with $\text{In}_{x_{QW}}\text{Ga}_{1-x_{QW}}\text{N}/\text{In}_{x_b}\text{Ga}_{1-x_b}\text{N}$ SCHs are grown on c -plane freestanding GaN substrates. The laser structure is composed of an n -type AlGaIn bottom cladding, a GaN n -type waveguide, a QW active region, a GaN p -type waveguide, and a p -type AlGaIn top cladding with a p -type GaN contact layer. The structure design is depicted in the inset of Fig. 2.2. Samples for dynamic LDs are numbered A1902, A2109, C128, C133 and C134.

The samples from the second class are InGaIn- and AlGaIn-based undoped heterostructures. Superradiant structures with $\text{In}_{x_{QW}}\text{Ga}_{1-x_{QW}}\text{N}/\text{In}_{x_b}\text{Ga}_{1-x_b}\text{N}$ and $\text{GaN}/\text{Al}_{x_b}\text{Ga}_{1-x_b}\text{N}$ SCHs are also grown on c -plane freestanding GaN substrates. The layer structure is kept

	N_{QW}	x_{QW}	x_b	d_{QW} [nm]	d_b [nm]	d_u [nm]	GaN substrate
A1902	2	In: 0.12	In: 0.01	3	12	25	FS Lumilog
A2109	2	In: 0.1	In: 0.01	4.5	12	12	FS Lumilog
C128	2	In: 0.1	In: 0.05	4.5	12	12	FS Lumilog
C133	3	In: 0.1	In: 0.05	3	8.5	8.5	FS Lumilog
C134	5	In: 0.1	In: 0.05	2	5.5	5.5	FS Lumilog
C182	3	In: 0.13	0	2.3	11	11	sapphire
C1094	7	In: 0.08	0	2.2	5	-	FS Sumitomo
C1095	7	0	Al: 0.1	2.2	5	-	FS Sumitomo
C1217	1	0	Al: 0.1	2.5	-	-	FS Sumitomo
C1233	5	0	Al: 0.1	2.5	5	-	FS Sumitomo

Table 2.2: List of samples analyzed in this thesis. N_{QW} is the number of QWs, x_{QW} and x_b are the concentrations of the element M_i in the $M_{i,x}\text{Ga}_{1-x}\text{N}$ alloy of the QW and of the barrier, respectively, d_b is the QW barrier width and d_u is the intrinsic layers width. All these values are estimated from parameter calibrations during the MOVPE growth, XRD fits and PL analyses.

as simple as possible and consists of a QW active region sandwiched between a top cap layer and a bottom buffer layer. Samples for SR studies are C1094, C1095, C1217 and C1233. In C1217 and C1233, a bottom AlGaIn cladding has been introduced to increase the confinement factor.

2.2 Single-section laser diodes

The term *laser* is the acronym standing for “light amplification by stimulated emission of radiation”. A laser device is able to emit light through an optical amplification process based on the stimulated emission of electromagnetic radiations. This emission is characterized with a high degree of coherence, both temporally (very narrow emission spectrum) and spatially (diffraction-limited narrow beam). Typically, a laser consists of a gain medium, i.e., a material that amplifies light by stimulated emission, and a cavity providing optical feedback. The process through which the supplied energy allows the gain medium to amplify light is called pumping.

Semiconductor lasers are usually electrically pumped diodes. Normally, standard single-section LDs (as opposed to multi-section described in Sec. 2.3) are essentially based on a forward-biased p - n junction providing excess charges in thermal non-equilibrium. Then, a current flows through the active region where most of the carriers recombine, i.e., relax into more favorable lower energy states. Unlike LEDs, under a sufficiently large pumping rate, it is possible to achieve the population inversion condition. Strictly speaking, population inversion, i.e., a situation where the carrier population density in the excited state is greater than that in the fundamental level, can only be developed in a perfect two-level system. As a semiconductor laser possess a continuous density of states (DOS), the statement “population inversion in a QW” is technically an abuse of terminology. Anyhow, the population inversion in such a system consists in the quenching of the semiconductor absorption. In fact, absorption becomes negative and gain is obtained for an electromagnetic wave having a frequency close to the resonant frequency of the system. This gain then allows the amplification of light via stimulated emission. For a perfect two-level system, the emission probability per unit time according to the Fermi golden rule is given by [40]:

$$P_{2 \rightarrow 1} = \frac{\hbar \omega_l}{\epsilon_0 L^3} (S + 1) |\langle 2 | q \mathbf{e}_l \cdot \mathbf{r} | 1 \rangle|^2 \delta(\hbar \omega = E_2 - E_1), \quad (2.3)$$

i.e., the emission probability for an electron in level 2 of eigenstate $|2\rangle$ and energy E_2 toward level 1 of eigenstate $|1\rangle$ and energy E_1 with emission of a photon of energy $\hbar \omega$ in mode l , where ω_l and S are the photon frequency and number of photons in mode l , respectively, L^3 is a fictitious volume box in which the waves will be confined and \mathbf{e}_l is the polarization vector of the mode l . In the case of the simple two-level system, eq. 2.3 easily distinguish between two distinct physical effects involved in the emission mechanism: spontaneous emission (due to vacuum fluctuations, which is the emission

regime of LEDs) and stimulated emission (proportional to the number of photons S already present in the cavity). The Bernard-Duraffourg condition will then allow to generalize this picture for the continuous DOS of a semiconductor laser (see eq. 2.6).

By finally placing the active medium in a cavity providing optical feedback, the emitted light can bounce back and forth and the system can oscillate naturally, resulting in laser oscillations. A typical optical cavity is the Fabry-Perot resonator composed of two mirrors facing each other and that surround the gain medium. Whenever crossing the cavity, stimulated photons interact with carriers in the excited states by generating photons with the same energy and the same phase. This is the stimulated emission phenomenon. Once the gain reaches the total cavity losses, the light is strongly amplified, the threshold condition is achieved and the onset of lasing is observed.

Hereafter, the different steps leading to lasing emission will be described in more detail. First, it is worth to specify the different notations regarding the carrier population that we will use throughout the thesis. The dimensionless *number notation* accounts for the total amount of carriers via their charge carrier number N . In order to obtain the respective values in terms of material parameters as the area density n_{2D} or volume density n_{3D} , one should scale the parameter N with the active region area or volume (generally expressed in centimeter units):

$$n_{2D} = \frac{N}{N_{QW}wL_{TOT}} \left[\frac{\#}{cm^2} \right], \quad (2.4)$$

$$n_{3D} = \frac{N}{N_{QW}d_{QW}wL_{TOT}} \left[\frac{\#}{cm^3} \right], \quad (2.5)$$

where N_{QW} is the number of QWs in the active region, w is the ridge width, L_{TOT} is the total cavity length and d_{QW} is the well width. For the sake of simplicity, to calculate the carrier and photon densities we have assumed the same active volume. Actually, the photon active volume is bigger than the carrier one by a factor of $1/\Gamma$. This is the reason why in eqs. 2.41 and 2.42 the confinement factor Γ is present only in the photon rate equation.

After pumping the system and the first subsequent thermalization processes, the carrier distribution in the bands can be considered as being ruled by the position of quasi-Fermi levels E_F^c and E_F^v in the conduction and valence band, respectively. Basically, quasi-Fermi levels describe the band filling of semiconductors out of equilibrium. The situation $E_g = E_F^c - E_F^v$ is called the *transparency condition*, i.e., the semiconductor material is transparent to photons of energy equal to and/or smaller than the bandgap E_g . Photons of energy $\hbar\omega$ experience stimulated emission if they fulfill the *Bernard-Duraffourg condition* that reads [40, 78]:

$$E_g \leq \hbar\omega \leq E_F^c - E_F^v. \quad (2.6)$$

The gain $g(\hbar\omega)$ is then generally defined as the parameter accounting for the amplification of the light intensity along a path l according to [29]:

$$I(l) = I(0)e^{gl}, \quad (2.7)$$

where $I(0)$ is the initial light intensity.

Hereafter, the subband structures in the QWs are treated as the direct product between the rapidly varying Bloch wavefunction and the slowly varying envelope function, which is calculated within the effective mass approximation. The electron and hole wavefunctions in the first subband are given by [40]:

$$|e_1(\mathbf{k}_{\parallel})\rangle = u_c(\mathbf{r})e^{i\mathbf{k}_{\parallel}\mathbf{r}_{\parallel}}e_1(z), \quad (2.8)$$

$$|hh_1(\mathbf{k}_{\parallel})\rangle = u_v(\mathbf{r})e^{i\mathbf{k}_{\parallel}\mathbf{r}_{\parallel}}hh_1(z). \quad (2.9)$$

The term $u_i(\mathbf{r})$ is the periodic portion of the Bloch wavefunctions accounting for the periodicity of the specific semiconductor crystal lattice. As for a plane wave, the term $e^{i\mathbf{k}_{\parallel}\mathbf{r}_{\parallel}}$ describes instead the free motion of carriers parallel to the well interfaces, where \mathbf{r}_{\parallel} is the position of the wave in the plane of the QW and \mathbf{k}_{\parallel} is the respective wavevector. Finally, the envelope functions $e_1(z)$ and $hh_1(z)$ deal with the quantization of motion perpendicular to the QW and are solutions to the one-dimensional Schrödinger equations:

$$H_{c(v)}|e(hh)_1\rangle = \left[\frac{p_z^2}{2m_{e(hh)}} + V_{e(hh)}(z) \right] |e(hh)_1\rangle = e(hh)_1|e(hh)_1\rangle, \quad (2.10)$$

where H_c and H_v are the conduction and valence band hamiltonians, $V_e(z)$ and $V_{hh}(z)$ are the electron and heavy hole potentials, p_z is the momentum observable along the z direction, m_e and m_{hh} are the electron and heavy hole effective masses, $|e_1\rangle$ and $|hh_1\rangle$ are the electron and heavy hole eigenstates, e_1 and hh_1 correspond to the electron and heavy hole energy dispersion curves of band 1.

Equation 2.10 allows then to calculate the electron and heavy hole subband energy dispersion near $k = 0$:

$$e(hh)_1(\mathbf{k}_{\parallel}) = e(hh)_1 + \frac{\hbar^2 k_{\parallel}^2}{2m_{e(hh)}}, \quad (2.11)$$

Note that the hole is interpreted as a virtual particle corresponding to a missing electron in the Fermi sea and therefore behaves as a particle of negative mass ($m_{hh} < 0$). e_1 (and hh_1) can be expressed as $\frac{\hbar^2 k_z^2}{2m_{e(hh)}}$, where $k_z = \sqrt{\frac{\pi^2 n^2}{d_{QW}^2}}$ is the z component along the growth axis with $n = 1, 2, 3, \dots$ the quantized level number.

Thus, the DOS for electrons and that for heavy holes in a two-dimensional QW are given by [47]:

$$\rho_{2D,e(hh)}(E) = \frac{m_{e(hh)}}{\pi\hbar^2} \theta(E - e(hh)_1), \quad (2.12)$$

where θ is the Heaviside function.

Thanks to this formalism, the gain $g(\hbar\omega)$ for the first $e_1 - hh_1$ transition of a QW system can be obtained by integrating over all the wavevectors k and reads [29, 40, 47, 79]:

$$g(\hbar\omega) = \alpha_0(\hbar\omega) \left[f_c^1(\hbar\omega) - f_v^1(\hbar\omega) \right] \theta(\hbar\omega - E_g - e_1 - hh_1), \quad (2.13)$$

where f_c^1 and f_v^1 are the Fermi-Dirac distributions in the first subband [40]:

$$f_c^1(\hbar\omega) = \frac{1}{1 + \exp\left(\frac{E_c^1 - E_F^c}{k_B T}\right)}, \quad (2.14)$$

$$E_c^1(\hbar\omega) = E_g + e_1 + \frac{m_r}{m_e} (\hbar\omega - E_g - e_1 - hh_1), \quad (2.15)$$

$$f_v^1(\hbar\omega) = \frac{1}{1 + \exp\left(\frac{E_v^1 - E_F^v}{k_B T}\right)}, \quad (2.16)$$

$$E_v^1(\hbar\omega) = -hh_1 - \frac{m_r}{m_{hh}} (\hbar\omega - E_g - e_1 - hh_1), \quad (2.17)$$

where m_r is the reduced mass given by $\frac{1}{m_r} = \frac{1}{m_e} + \frac{1}{m_{hh}}$.

The quasi-Fermi levels as a function of the charge carrier numbers N are then given by the conditions [40]:

$$E_F^c = E_g + e_1 + k_B T \ln \left(\exp \left(\frac{N}{N_c^e} \right) - 1 \right), \quad (2.18)$$

$$E_F^v = -hh_1 - k_B T \ln \left(\exp \left(\frac{N}{N_c^{hh}} \right) - 1 \right), \quad (2.19)$$

where N_c^e and N_c^{hh} are the critical carrier numbers. Basically, eqs. 2.18 and 2.19 are relying on the fact that the total carrier number N in the bands is obtained by integrating the DOS ρ_{2D} with the Fermi-Dirac distribution f_{FD} over all the energy states via $\int \rho \cdot f_{FD} dE$. When dividing N_c^e and N_c^{hh} by the extent of the active region perpendicular to the growth axis [namely, w and L_{TOT} , see Fig. 2.5 (a)], 2D critical carrier densities are obtained:

$$n_c^{e(hh)} = \rho_{2D,e(hh)} k_B T = \frac{m_{e(hh)} k_B T}{\pi \hbar^2}, \quad (2.20)$$

The prefactor $\alpha_0(\hbar\omega)$ appearing in eq. 2.13 is the empty conduction band absorption coefficient also called carrier-free absorption coefficient (i.e., that measured for a QW

with zero population) and is given by [40, 80]:

$$\alpha_0(\hbar\omega) = \sum_{i,f} \frac{q^2}{cn_g d_{QW} \varepsilon_0 \hbar} \frac{m_r}{m_0} \hbar\omega \frac{E_p}{E_g^2} \cdot |\langle i|f \rangle|^2, \quad (2.21)$$

where the sum runs over all bound electron $|i\rangle$ and hole $|f\rangle$ states in the QWs and E_p is the momentum matrix element energy also called Kane energy. In eq. 2.21, the dipolar matrix element μ_{cv}^2 is noted as $\frac{\hbar^2 E_p}{m_0 E_g^2}$ [40]. Sometimes the dipolar matrix element is occasionally written instead as the transition matrix element $|M_T|^2$. The two previous quantities are then related by $|M_T|^2 = m_0^2 \omega^2 \mu_{cv}^2$ [81]. Note that $\alpha_0(\hbar\omega)$ refers to the absorption coefficient in the case of thermodynamic equilibrium and it is the maximum possible value of the gain coefficient $g(\hbar\omega)$.

The Heaviside function appearing in eq. 2.13 can be approximated by an error function erf . Indeed, the error function can be viewed as the convolution of a Gaussian with the Heaviside step function via [82]:

$$\theta(\hbar\omega - E_{if}) \approx \frac{1}{2} \text{erf} \left(\frac{\hbar\omega - E_{if}}{\sqrt{2} E_{inh}} \right) + \frac{1}{2}. \quad (2.22)$$

In the limit of an infinitely narrow Gaussian, the error function coincides with the Heaviside function. This approximation is quite useful since it allows to introduce the concept of inhomogeneous broadening E_{inh} , originating essentially from well and barrier imperfections such as width fluctuations and alloy composition fluctuations [40, 79]. Therefore, the deviation from an ideal 2D step-like DOS is accounted for by the full-width at half-maximum (FWHM) E_{inh} of the convoluted Gaussian in eq. 2.22.

The homogeneous broadening due to charge carrier dephasing and scattering can be included in eq. 2.13 by the convolution of a sech-function integrated from the lowest possible energy difference between confined states (e.g., $E_{e_1-hh_1}$ for a QW and E_g for a bulk layer) to infinity [81, 82]:

$$G_{hom}(\hbar\omega) = \frac{1}{\pi E_{hom}} \int_{E_{e_1-hh_1}}^{+\infty} g_{mod}(\hbar\omega) \text{sech} \left(\frac{\hbar\omega' - \hbar\omega}{E_{hom}} \right) d\hbar\omega', \quad (2.23)$$

where E_{hom} is the homogeneous broadening energy. Typically, E_{hom} is set to 25 meV, i.e., the thermal energy of carriers at RT. However, the poor quality of InGaN-films does not allow to easily deconvolute the homogenous contribution from the inhomogeneous one, as the latter is normally greater than 50 meV in our structure. In general, taking also into account other mutual interactions between carriers (i.e., within a many-body effect approach) would allow to express a more sophisticated and rigorous description of the broadening parameter E_{hom} [82]. Concerning the specific form to be used in eq. 2.23 for the lineshape function, the sech-function presents the advantage to have less energy in the tails (thus less spurious absorption) compared to, e.g., a Lorentzian function [81]. A simple Gaussian function could be used as well [83].

Note that in a QW only a fraction of the wave has a geometrical overlap with the gain medium given by 2.13 and, as a first approximation, it is accounted for by the optical confinement factor Γ (eq. 2.1). The modal gain g_{mod} that is actually responsible for light amplification in the cavity can then be simply represented as the product of the total material gain g_{mat} (subject to population inversion) times the optical confinement factor via [81]:

$$g_{mod} = \Gamma g_{mat}. \quad (2.24)$$

Thus, only a fraction Γ of the total electromagnetic energy experiences amplification (or absorption if $g_{mat} < 0$).

Summarizing eq. 2.13, α_0 is the *gain amplitude* and mostly depends on the optical transition matrix element such as, e.g., the overlap between the electron and hole wavefunctions. $[f_c^1(\hbar\omega) - f_v^1(\hbar\omega)]$ is the *gain distribution* and it represents the carrier population filling the bands via the Bernard-Duraffourg condition. At last, $\theta(\hbar\omega - E_g - e_1 - hh_1)$ is the *gain quantization* resulting from the DOS imposed by the 2D dimensionality and the quantum effects of the QW.

To exemplify the properties of a 2D DOS, we will now discuss the 3D case. The 3D critical carrier densities $n_{c,3D}$ and the 3D carrier-free absorption coefficient $\alpha_{0,3D}$ are now expressed as follows in the Boltzmann approximation [40, 47]:

$$n_{c,3D}^{e(hh)} = \frac{1}{4} \left(\frac{2m_{e(hh)} k_B T}{\pi \hbar^2} \right)^{3/2}, \quad (2.25)$$

$$\alpha_{0,3D}(\hbar\omega) = \frac{q^2}{2\pi c n_g \varepsilon_0 \hbar^2} \frac{(2m_r)^{3/2}}{m_0} \hbar\omega \frac{E_p}{E_g^2}. \quad (2.26)$$

Equation 2.13 can then be modified to:

$$g(\hbar\omega) = \alpha_{0,3D}(\hbar\omega) [f_c(\hbar\omega) - f_v(\hbar\omega)] \sqrt{\frac{\hbar\omega - E_g}{\hbar}}. \quad (2.27)$$

In Fig. 2.3, the modal gain spectrum for an InGaN QW is calculated from eq. 2.13 in the free-carrier model (i.e., discarding Coulomb interaction) and with the assumption of maximal overlap (i.e., for the flat-band condition, $\mathbf{F}_{QW} = 0$) at a charge carrier density of $1.4 \cdot 10^{13} \text{ cm}^{-2}$. G_{hom} (that accounts for the homogeneous contribution) has been also calculated using eq. 2.23 for $E_{hom} = 25 \text{ meV}$ (blue curve). Homogeneous and inhomogeneous broadenings and the filling of the energy states in the band structure via $f_c^1(\hbar\omega) - f_v^1(\hbar\omega)$ are mostly responsible for the spectral width of the optical gain. In fact, the inhomogeneous and homogeneous contributions have as main consequence the smoothing of the sharp features of the gain spectrum, which normally is assumed to be staircase-like in a 2D system (see α_0 and $-\alpha_0$ in Fig. 2.3).

It is also worth pointing out the asymmetry in the Fermi-Dirac distributions around $E_{e_1-hh_1}$ that results from the different effective masses. Indeed, the electron effective mass m_e is almost one order of magnitude lighter than the hole one m_{hh} . Note that whatever

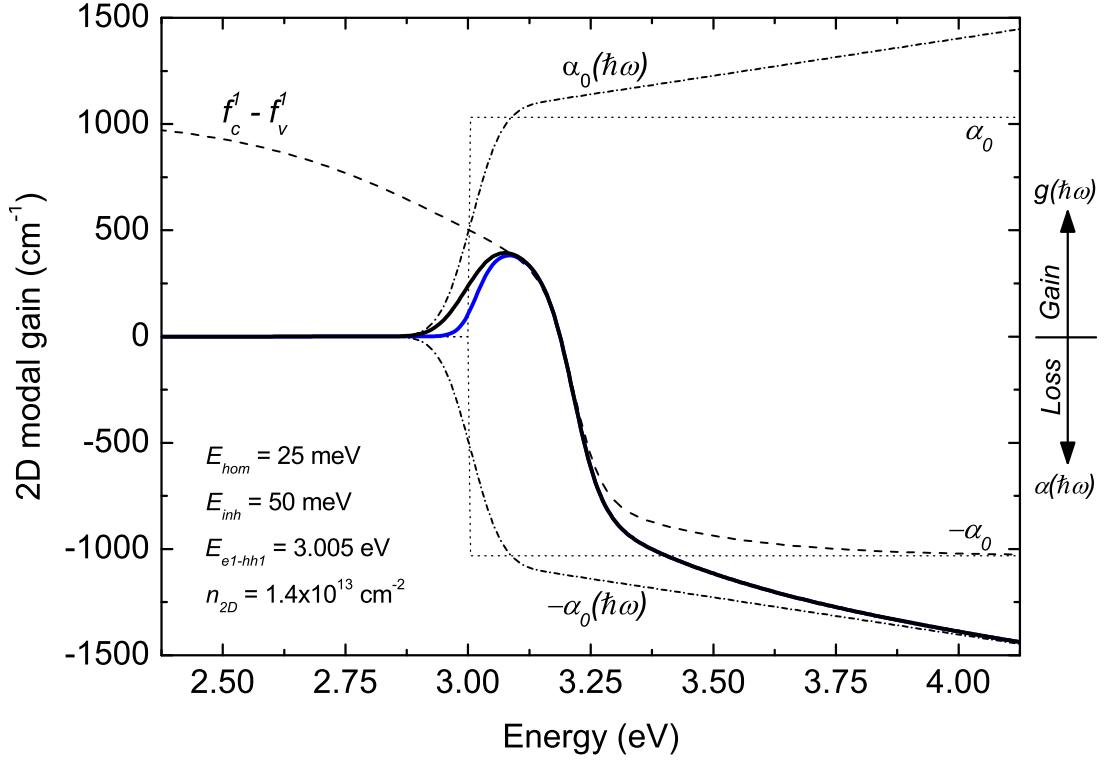


Figure 2.3: Optical modal gain spectra for a single $\text{In}_{0.1}\text{Ga}_{0.9}\text{N}/\text{In}_{0.01}\text{Ga}_{0.99}\text{N}$ QW calculated from eq. 2.13 for $E_{hom} = 0$ (black curve) and from eq. 2.23 for $E_{hom} = 25 \text{ meV}$ (blue curve) at a charge carrier density of $1.4 \cdot 10^{13} \text{ cm}^{-2}$. The QW active layer consists of an $800 \times 2 \mu\text{m}^2$ area per a 4.5 nm large well and the inhomogeneous broadening E_{inh} is set to 50 meV . The dashed black line represents the associated Fermi-Dirac distribution $f_c^1(\hbar\omega) - f_v^1(\hbar\omega)$ for the quasi-Fermi levels in the conduction and valence bands while the dash-dotted black lines $\alpha_0(\hbar\omega)$ (and $-\alpha_0(\hbar\omega)$) represent in turn the associated DOS given by the product $\alpha_0(\hbar\omega) \cdot \theta(\hbar\omega - E_g - e_1 - hh_1)$ in eq. 2.13. The small black dotted lines α_0 (and $-\alpha_0$) depict the classical step-like DOS for a perfect QW (i.e., $E_{inh,hom} = 0$).

the charge carrier density in the heterostructure, the gain curves will always remain limited by the QW DOS given in this case by the product $\alpha_0(\hbar\omega) \cdot \theta(\hbar\omega - E_g - e_1 - hh_1)$ in eq. 2.13 (the dash-dotted black lines $\alpha_0(\hbar\omega)$ and $-\alpha_0(\hbar\omega)$ in Fig. 2.3).

To analyze the QW filling behavior in details, gain spectra for different charge carrier densities are calculated from eq. 2.13 for the QW case and from eq. 2.27 for the bulk one, and are shown in Fig. 2.4. The parameters of the simulations (mostly affecting α_0) have been kept the same for both DOS for the sake of comparison and are listed in Table 2.1. Especially, the effective bandgap E_g is the same in both eqs. 2.13 and 2.27. When increasing the charge carrier density, the gain curves increase. Obviously, the gain rise follows a staircase-like profile for the case of a 2D DOS whereas a $\sqrt{\hbar\omega - E_g}$ profile is seen for a 3D DOS. For sufficiently high carrier densities, gain occurs at photon energy close to the minimum energy possible in the band structures, namely, E_g for a 3D DOS

[Fig. 2.4 (a)] and $E_{e_1-hh_1}$ for a 2D DOS [Fig. 2.4 (b)]. These photons indeed fulfill the Bernard-Durrafourg condition given by eq. 2.6 and can therefore be amplified. The charge carrier number (density) for which $g(\hbar\omega) = 0$ is called *transparency carrier number (density)* N_{tr} (n_{tr}). The calculated value $n_{tr} = 1.5 \cdot 10^{12} \text{ cm}^{-2}$ for a 2D DOS is close, within a factor two, to the experimental values obtained by Scheibenzuber *et al.* [69] and Ryu *et al.* [84]. Note that in the 2D case, gain is not obtained exactly at the transition energy $E_{e_1-hh_1}$ but rather below this value. This is simply ascribed to inhomogeneous broadening as the well thickness and alloy composition fluctuations can allow emission already below the actual transition energy. For photons that are not satisfying eq. 2.6 or for charge carrier densities lower than the transparency one, there is no population inversion: a “negative” gain is experienced and absorption $\alpha(\hbar\omega) = -g(\hbar\omega)$ is obtained. For photon energies smaller than the effective bandgap E_g (or $E_{e_1-hh_1}$ in the 2D case), neither gain nor absorption is observed in the system as in the carrier band structure no such energetic transitions are available.

Regarding the homogeneous broadening contribution, scattering and dephasing effects do not only smooth the gain characteristics but they also reduce substantially the maximum of gain g_{max} (Fig. 2.4). However, when comparing Figs. 2.3 and 2.4 (b), one can infer that this reduction is significant only for small charge carrier densities. Indeed, for higher gains, e.g., for densities ten times larger than that at the transparency (i.e., the $1.4 \cdot 10^{13}$

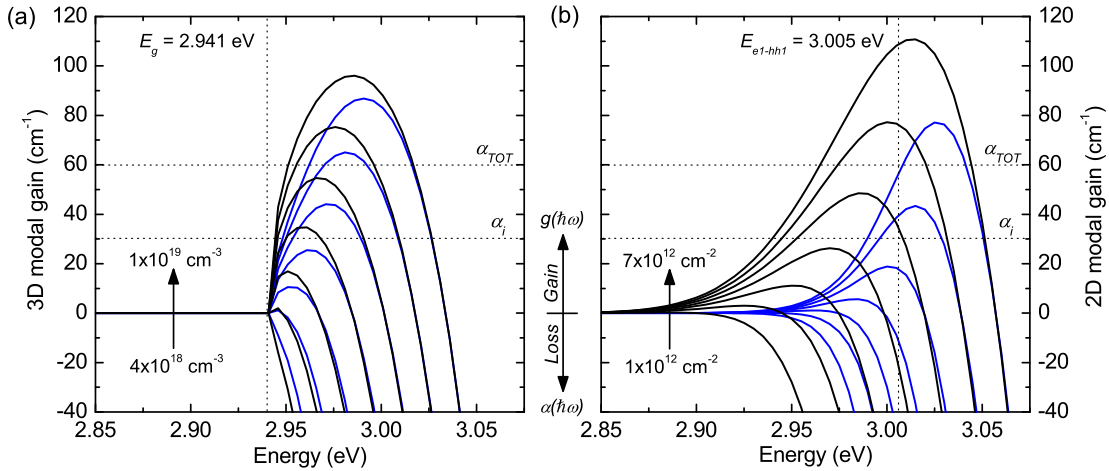


Figure 2.4: Optical modal gain spectra for a bulk $\text{In}_{0.1}\text{Ga}_{0.9}\text{N}$ heterostructure and for a single $\text{In}_{0.1}\text{Ga}_{0.9}\text{N}/\text{In}_{0.01}\text{Ga}_{0.99}\text{N}$ QW calculated (a) from eq. 2.27 for a 3D-DOS and (b) from eq. 2.13 for a 2D-DOS with $E_{inh} = 50 \text{ meV}$, respectively. The homogeneous broadening E_{hom} is set to 25 meV in both cases (blue curves). The charge carrier density ranges from $4 \cdot 10^{18}$ to $1 \cdot 10^{19} \text{ cm}^{-3}$ varying in steps of $1 \cdot 10^{18} \text{ cm}^{-3}$ for (a) and from $1 \cdot 10^{12}$ to $7 \cdot 10^{12} \text{ cm}^{-2}$ varying in steps of $1 \cdot 10^{12} \text{ cm}^{-2}$ for (b). The QW active layer consists of an $800 \times 2 \mu\text{m}^2$ area per a $d_{QW} = 4.5 \text{ nm}$. The horizontal dotted lines represent the internal losses α_i and the total losses α_{TOT} , while the vertical ones represent the energy transitions E_g and $E_{e_1-hh_1}$. The transparency carrier density n_{tr} is about $4.83 \cdot 10^{18} \text{ cm}^{-3}$ for (a) and $1.39 \cdot 10^{12} \text{ cm}^{-2}$ for (b).

cm^{-2} value considered in Fig. 2.3), the homogeneous contribution starts being negligible. The maximum of gain is an extremely important value as only the electromagnetic modes of energy close to $g_{max}(\hbar\omega)$ will be amplified and afterward will lase. These modes are called dominant modes. In the ideal case (i.e., for $E_{inh} = 0$), g_{max} for a QW-based heterostructure is always obtained when $\hbar\omega = E_{e1-hh1}$ (the small blueshift visible on Fig. 2.4 (b) is entirely accounted for by the tail of the DOS due to inhomogeneous broadening). The down-side of QW systems is that the quantization of states implies then a fast saturation of the gain as the carrier density rises as the 2D-DOS is limited by $\alpha_0(\hbar\omega)$ and $-\alpha_0(\hbar\omega)$ (Fig. 2.3). On the contrary, the maximum of gain for a 3D-DOS blueshifts and increases nearly linearly with the carrier density for any inhomogeneous broadening [Fig. 2.4 (a)]. The maximum of gain will be quite useful for the time being to define the laser threshold condition and later on to formulate the absorption saturation mechanism occurring in the AS of a MS-LD.

Let us now suppose that the semiconductor p - n junction is electrically pumped beyond the transparency condition and that the active region amplifies consequently the photons satisfying eq. 2.6. As previously mentioned, the process of amplification is carried out by stimulated emission: an incident photon stimulates the transition of an excited electron to an empty valence band state and thus leading to the emission of a photon of same energy and same phase (leading to coherent emission). The system can then finally exhibit laser oscillations only if it is able to maintain these oscillations, i.e., provided an *optical feedback*. Indeed, to sustain the stimulated emission process it is necessary that each emitted photon will interact as long as possible with the gain region in order to further increase the photon density inside the resonator. This phenomenon of resonance is typical of a laser structure. In the case of edge emitting LDs, the cavity is defined as two perfect facing facets obtained by cleaving the semiconductor crystal along the same crystallographic planes. The semiconductor-air interface then forms a Fabry-Perot resonator with a reflectivity R given by [40]:

$$R = \frac{(n_{eff} - 1)^2}{(n_{eff} + 1)^2}, \quad (2.28)$$

where n_{eff} is the effective refractive index of the semiconductor medium. For GaN, $n_{eff} = 2.45$ at 3 eV [38] and the reflectivity gives $R = 0.17$. The deposition of proper dielectric multilayers on the facets can increase (high-reflection coating) or decrease (anti-reflection coating) the reflectivity.

So, once the inverted active medium is placed in a resonator, laser oscillations can emerge only when the gain in the amplifying medium exceeds the total cavity losses α_{TOT} in the optical resonator. The threshold condition coinciding with the lasing emission at a threshold charge carrier number N_{th} can be written [40]:

$$g_{mod,th}(\hbar\omega) = \Gamma g_{mat,th}(\hbar\omega) = \alpha_{TOT} = \alpha_m + \alpha_i, \quad (2.29)$$

where α_i are the internal losses resulting from free-carrier absorption, roughness scattering, diffraction losses and possibly other processes. The losses α_m result from photon leakage through the mirrors due to the incomplete reflection of the optical wave and read [29]:

$$\alpha_m = \frac{1}{2L_{TOT}} \ln \frac{1}{R_1 R_2}, \quad (2.30)$$

where R_1 and R_2 are the reflectivity of each mirror. Typical values for $\alpha_m + \alpha_i$ are around tens of cm^{-1} in GaN-based LDs.

Using eq. 2.29, the light intensity after one round trip in the cavity can be written as (in a way similar to eq. 2.7) [69]:

$$I(2L) = R_1 R_2 I(0) e^{(g_{mod}(\hbar\omega) + \alpha_i) 2L_{TOT}}. \quad (2.31)$$

Having now introduced the concept of lasing threshold, a few other comments can be made on Fig. 2.4. By looking at the gain curves one can understand that the carrier density required at transparency, i.e., n_{tr} (or also at the laser threshold, i.e., n_{th}) is more or less the same when considering a 3D- or a 2D-DOS (supposing the same amount of cavity losses to compensate). For example, in the case of a 4.5 nm wide QW, one obtains $n_{tr} = 3.09 \cdot 10^{18} \text{ cm}^{-3}$, a value close to that obtained for a bulk layer, i.e., $n_{tr} = 4.83 \cdot 10^{18} \text{ cm}^{-3}$ (see Fig. 2.4). Actually, the interest in exploiting a QW-based heterostructure rather than a bulk material does not originate from the decrease in the transparency (or threshold) *carrier* densities n_{3D} but rather in the decrease in the transparency (or threshold) *current* densities J thanks to the reduction in the active region thickness d via [40]:

$$\frac{\eta_{inj} J}{qd} = \frac{n_{3D}}{\tau} \left(= \frac{\eta_{inj}}{qd} \frac{I}{wL_{TOT}} \right), \quad (2.32)$$

where η_{inj} is the injection efficiency, τ is the total carrier recombination lifetime in the active region (for more details, see eq. 2.39) and I is the current. J and I are usually expressed in $\text{kA} \cdot \text{cm}^{-2}$ and mA , respectively. The impact of a smaller d on J can be emphasized when comparing a homojunction, a heterostructure, and a QW. In the case of a homojunction, d is given by $L_n + L_p$ (see eq. 1.23), which typically amounts to $\sim 1 \text{ } \mu\text{m}$. For a heterostructure, d is already reduced to less than 100 nm while for a QW structure d can even be a few nm thick. Furthermore, the maximum of gain g_{max} (the smallest amount of gain that satisfies both $g(\hbar\omega) > 0$ and eq. 2.29) for an ideal 2D-DOS (i.e., $E_{hom,inh} = 0$) is rapidly obtained and always at the same energy for any carrier number N . Therefore, to decrease the threshold current of a LD, it is really worth decreasing the size of the active region down to the quantum length scale.

For instance, according to the cases depicted in Fig. 2.4, a QW laser structure with a typical total absorption α_{TOT} of 60 cm^{-1} can reach the threshold condition at a population $n_{th} = 5.36 \cdot 10^{12} \text{ cm}^{-2}$ (see Table 2.1). For a QW active layer of $800 \times 2 \text{ } \mu\text{m}^2$ per a $d_{QW} = 4.5 \text{ nm}$, in 3D notation n_{th} is about $1.19 \cdot 10^{19} \text{ cm}^{-3}$, in good agreement with other theoretical values as reported in Ref. [85]. Assuming a typical carrier lifetime

of 2 ns and an injection efficiency of 0.68 [68], this gives a threshold current density of $0.63 \text{ kA}\cdot\text{cm}^{-2}$ and a current of 10 mA. Generally in III-nitrides, a well of about 10-15 nm (i.e., one order of magnitude larger than the de Broglie wavelength) is largely enough to be considered as to bulk and such a thickness is indeed expected to increase the lasing threshold. From tests carried out at LASPE, it seems that the threshold current for InGaN layer thickness of 4.5, 15 and 25 nm are 30 (1.88), 50 (4.17) and 70 (5.83) mA (kA/cm^2), respectively.

Unfortunately, there are also some drawbacks to use QWs. Although g_{max} is obtained *earlier* in terms of injected current and for higher amplitude of gain, it also saturates quickly due to the quantization of states [Fig. 2.4 (b)]. Moreover, given the small dimensions of the active layers, only a fraction Γ of the gain region will overlap with the optical mode and thus experience amplification (see eq. 2.1 and Fig. 2.2). For this reason, the actual gain necessary to reach the threshold condition in a laser structure is a factor $\frac{1}{\Gamma}$ higher: $g_{mat} = \frac{\alpha_m + \alpha_i}{\Gamma}$ (see eq. 2.29). On the contrary, in a bulk heterostructure, the confinement factor Γ is assumed to be ~ 1 and the gain simply continues to rise and to blueshift in energy due to the larger and not quantized DOS. Concerning the optimum number of QWs, the high transparency charge carrier density (inherited from the high effective hole mass) and the low hole mobility in III-nitrides preclude the use of a high number of QWs. However, a single QW in the active region would involve a very high charge carrier density. Determining the optimal number of QWs would therefore be interesting in order to overcome the limiting effect of a reduced active region thickness and at the same time to minimize the threshold current. In III-nitrides, the number of QWs is commonly chosen between one and three [69]. The optimum QW number can be obtained by considering the simple ratio between the cavity losses $\alpha_m + \alpha_i$ and the gain per QW Γg_{QW} [40]. Typically, as stressed in Sec. 2.1.1, this number ranges between 1 and 3. Then, in the case of a multiple-QW (MQW) structure, the quantities considered for single QW (e.g., g_{mod} , N_{tr} , N_{th}) simply scale with N_{QW} according to [40]:

$$g_{MQW,mod} = N_{QW} g_{mod}, \quad N_{MQW,tr} = N_{QW} N_{tr}, \quad N_{MQW,th} = N_{QW} N_{th}. \quad (2.33)$$

In summary, once the Bernard-Duraffourg condition is satisfied, a laser needs a sufficient amount of gain leading to the laser oscillation condition for which $gain = loss$. In this case, the carrier number in the junction (as well as the gain) is clamped to the threshold value N_{th} as all additional carriers injected into the laser heterostructure are converted into photons under the effect of stimulated emission. Actually, the process is not instantaneous as the populations of carriers and photons experience mutual oscillations before reaching the steady-state. This phenomenon will be treated in more details in Sec. 2.2.2. In the case of perfect equilibrium between the total recombination/emission rates, the optical output power P_{out} can be written as [29, 40]:

$$P_{out} = \eta_{ext} \frac{\hbar\omega}{q} (I - I_{th}), \quad (2.34)$$

where I_{th} is the threshold current that, according to eq. 2.32, is equal to $\frac{qdwL_{TOT}n_{3D,th}}{\tau_{th}}$ $= \frac{qN}{\tau_{th}}$ and η_{ext} is the differential external quantum efficiency (*differential* as it considers the current above the threshold and not the total current flowing through the LD). In the lasing regime, η_{ext} is the slope of the P_{out} curve as function of the current and is given by:

$$\eta_{ext} = \frac{q}{\hbar\omega} \frac{dP_{out}}{dI} = \eta_{inj}\eta_i \frac{\alpha_m}{\alpha_m + \alpha_i}, \quad (2.35)$$

where η_i is the internal quantum efficiency and the ratio $\frac{dP_{out}}{dI}$ is referred to as the slope efficiency. The efficiency value η_i means that not all the inverted carriers are depleted by stimulated emission as part of them are trapped by non-radiative channels, some ballistic carriers travel across the cavity without recombining or some others simply recombine spontaneously.

The wall-plug efficiency η_{WP} then measures the optical performance of a device and is given by:

$$\eta_{WP} = \frac{P_{out}}{P_{el}} = \eta_{ext} \left(1 - \frac{I_{th}}{I}\right), \quad (2.36)$$

where $P_{el} = IV$ is the electrical power with V the applied voltage. For a semiconductor LD, η_{WP} is about 30-40% whereas for a gas-based laser it is only about 1% [29].

2.2.1 L - I - V characteristics

In this section, the typical characteristics of a standard edge-emitting single-section LD will be described.

As shown in Fig. 2.5 (a), a standard LD consists of a forward-biased p - n junction working under continuous wave (cw) operation. Devices have been processed as index-guided structures in the ICMP clean rooms (see Sec. 2.4.2). Light-current-voltage (L - I - V) curves of a $800 \times 2 \mu\text{m}^2$ LD from sample A2109 are shown in Fig. 2.5 (b) under cw driving conditions at RT. When increasing the injected current, the I - V curve exhibits an exponential behavior (see eq. 1.23): once the applied voltage V equals the built-in voltage Ψ_{bi} (in this case around 3 V), i.e., once the depletion region W_D completely collapses, a current starts flowing exponentially through the p - n junction. On the other side, the L - I curve shows a kink followed by a linear rise in the output power as the injected current is rised. The kink means that at a current I_{th} the laser cavity has reached the laser oscillation threshold as described in eq. 2.34. Typically, the operating voltage is around 5-6 V and the best values we obtained for I_{th} and the slope efficiency are equal to 40 mA (i.e., 2.5 kA cm^{-2}) and 0.6 W/A, respectively, without facet coatings and substrate thinning. This corresponds to an injection efficiency of $\sim 70\%$ that could indicate an inefficient blocking action of the EBL.

The typical emission wavelength is in the blue-violet range [e.g., 415 nm in Fig. 2.5 (c)]. Note that in Fig. 2.5 (c) the emission exhibits only a single peak as we do not dispose enough spectral resolution to resolve the longitudinal cavity modes. If this is the case,

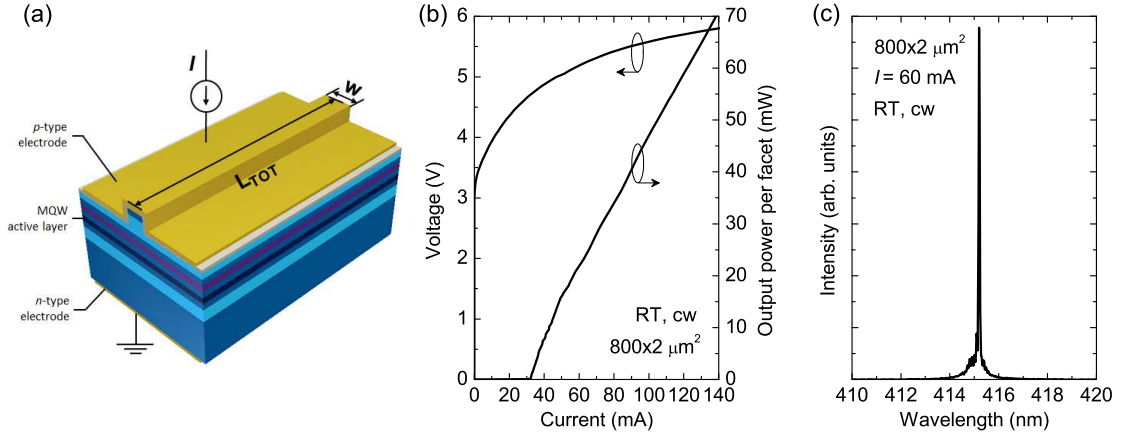


Figure 2.5: (a) Schematic structure of a LD with a standard single-section p -side electrode. The detailed layer structure is depicted in Fig. 2.2. (b) Experimental L - I - V curves for an $800 \times 2 \mu\text{m}^2$ LD as a function of the injected current under cw operation at RT. (c) Optical spectrum at $I = 60 \text{ mA}$ for the same LD.

the spectral dependence of the emission would exhibit a comb-like structure according to the allowed Fabry-Perot resonator modes in the cavity for which the mode spacing $\Delta\lambda$ for a peak emission wavelength λ is given by [29]:

$$\Delta\lambda = \frac{\lambda^2}{2n_{eff}L_{TOT} \left(1 - \frac{\lambda}{n_{eff}} \frac{dn_{eff}}{d\lambda}\right)}. \quad (2.37)$$

The dispersion $dn_{eff}/d\lambda$ can sometimes be neglected. For a GaN-based $800 \mu\text{m}$ -long cavity, the cavity mode spacing is about 0.04 nm . Below threshold, the spectral emission follows the gain curve of the medium whereas above it the cavity modes in the vicinity of the maximum of gain $g_{max}(\hbar\omega)$ undergo laser oscillations, possibly resulting in single longitudinal mode operation at high injection. The wavelength selectivity of the cavity is then due to the mirrors that possess a preferential feedback for certain modes corresponding to the resonant modes (also called dominant modes). This discrimination is ascribed to the quality factor of the cavity given by $Q = \omega/\Delta\omega = \lambda/\Delta\lambda$. Only a small range of frequencies can thus be amplified and exit the device. For this reason, the light emitted from a laser structure is generally mono-frequencial (cavity modes) and coherent (stimulated emission).

State of the art edge-emitting InGaN/GaN MQW LDs operating cw in the violet spectral range are mastered by only a few entities, e.g., Nichia Corp. in Japan, Samsung in South Korea and OSRAM Opto Semiconductors in Germany. Nichia is the world leading company for the production of III-nitride-based commercial devices. They reported a threshold current density of $\sim 2 \text{ kA cm}^{-2}$ ($\sim 30 \text{ mA}$), a slope efficiency of 1.4 - 1.6 W/A and an operating voltage of 4.5 - 5 V at 100 mA for a LD with 96%-reflection-coating on both facets emitting at 400 - 450 nm (values taken from <http://www.nichia.co.jp/>).

2.2.2 Single-section LD dynamics

As stated in Sec. 2.2, under steady-state condition, the total carrier recombination rate R_{TOT} in the heterojunction corresponds to the flow of excess carriers J entering the p - n junction. According to the ABC-model (i.e., a phenomenological model accounting for the dependency of the charge carrier lifetime τ on N), this condition can be written as [40]:

$$\eta_{inj} V \frac{J}{qd} = R_{TOT}(N) = \underbrace{AN}_{R_{SRH}} + \underbrace{BN^2}_{R_{spont}} + \underbrace{CN^3}_{R_{Auger}} + \underbrace{g v_g S}_{R_{st}}, \quad (2.38)$$

where V is the volume of the active region (see eq. 2.5), J is the non-equilibrium current density given by eq. 2.32, N and S are the population of carriers and photons, respectively, $v_g = c/n_g$ is the group velocity, R_{SRH} is the rate of Shockley-Read-Hall (SRH) recombination on defects (deep levels, surface states, etc.), R_{spont} is the spontaneous radiative recombination rate, R_{Auger} is the Auger recombination term and R_{st} is the stimulated recombination rate. The total recombination lifetime τ can be separated in radiative (τ_r) and non-radiative (τ_{nr}) time contributions:

$$\frac{1}{\tau} = \frac{1}{\tau_{nr}} + \frac{1}{\tau_r} = \underbrace{A + CN^2}_{non-radiative} + \underbrace{BN}_{radiative}. \quad (2.39)$$

Note that at threshold (eq. 2.29), the photon lifetime in the cavity τ_{ph} is equal to [29]:

$$\frac{1}{\tau_{ph}} = g_{mod,th} v_g = (\alpha_i + \alpha_m) v_g. \quad (2.40)$$

Before reaching the steady-state described by eq. 2.38, the charge carrier population in the active region and the photon field in the resonator interact mutually and rapidly at the temporal scale. At this point, each microscopic generation process is not balanced by its reciprocal recombination process. Note that in this simplified model, the parameters are spatially independent thus assuming a point operation. The coupled dynamic equations for a semiconductor laser cavity in number notation then read:

$$\frac{dN}{dt} = \frac{\eta_{inj} I}{q} - \frac{N}{\tau(N)} - g(\hbar\omega, N, S) v_g S, \quad (2.41)$$

$$\frac{dS}{dt} = \Gamma g(\hbar\omega, N, S) v_g S + \beta B N^2 - (\alpha_i + \alpha_m) v_g S, \quad (2.42)$$

where g is the material gain and β is the fraction of spontaneous emission coupled into the laser modes as not all the photons emitted in the active region are released into the guided modes. Typically, for Fabry-Perot lasers, β is in the order of 10^{-4} - 10^{-5} but a properly designed microcavity can increase this value by several orders of magnitude up to ≈ 0.1 [86]. In general, the term $\beta B N^2$ (independent of S) in eq. 2.42 reflects the rate of spontaneous emission that provides additional photon generation in the

cavity. The factor Γ appearing in the first term on the right-hand side of eq. 2.42 (the stimulated emission rate R_{st}) reflects the fact that photons are necessarily generated into the waveguide mode and that only the fraction of the wave interacting with the gain medium will play a role to generate new stimulated photons. Note that Γ is not present in the stimulated emission term in eq. 2.41 as carriers are injected in the QWs.

A saturation effect similar to spectral hole burning should also be taken into account in eqs. 2.42 and 2.41. The material gain g is indeed subject to a competition mechanism between the pump rate I and the depopulation rates resulting from stimulated emission and carrier recombination. As the number of photons in the cavity keeps rising, the depopulation mechanism starts to take over (mostly due to the enhancement of the stimulated contribution R_{st}) and as a results the gain gets *compressed* [87]:

$$g(\hbar\omega, N, S) = \frac{g(\hbar\omega, N)}{1 + \varepsilon_{sat}S}, \quad (2.43)$$

where ε_{sat} is the gain compression factor that acts as a damping term and is given by the inverse of the photon saturation density $s_{sat} = \frac{1}{v_g t_{inter} dg_{mod}/dN}$ with dg_{mod}/dN the differential modal gain and t_{inter} the interband recombination time [40]. For usual experimental values such as $dg/dN = 4.3 \cdot 10^{-7} \text{ cm}^{-1}$ and $t_{inter} = 1 \text{ ns}$, we derive an ε_{sat} value equal to $3.36 \cdot 10^{-6}$, which is two orders of magnitude higher than the experimental value found by Scheibenzuber for III-nitrides [69]. When considering instead intraband relaxation, t_{intra} is of the order a picosecond leading to a gain compression factor ε_{sat} of $3.36 \cdot 10^{-9}$. Typically, for the sake of comparison, in a GaAs QW-based LD ε_{sat} is around $\sim 1 \cdot 10^{-8}$ [70, 88]. Therefore, it seems that, at least in principle, intraband transitions more than interband ones are responsible for gain saturation.

Before solving the rate equations 2.41 and 2.42, some considerations should be formulated concerning the material gain $g(\hbar\omega, N)$.

- The homogeneous linewidth contribution will not be taken into account during the analytic resolution of eqs. 2.41 and 2.42. Its implementation in the differential equations would complicate the problem and is beyond the scope of this thesis.
- In a laser system, the transparency and threshold conditions are always obtained at the energy for which the gain is maximum, i.e., g_{max} . Therefore, an approximation taking only into account $g_{max}(\hbar\omega_{max})$ can be developed to “represent” the different characteristics of the gain. This kind of assumption would then be *wavelength independent* (i.e., meaning a so-called single-mode operation) and it would be expressed only in terms of the carrier population N . The method for calculating the gain in that way stands as follows. First, the maximum of gain is given by: $g_{max}(\hbar\omega_{max}) = \alpha_0(\hbar\omega_{max}) [f_c^1(\hbar\omega_{max}) - f_v^1(\hbar\omega_{max})] \theta(\hbar\omega_{max} - E_g - e_1 - \hbar h_1)$ (eq. 2.13). The first assumption consists in considering the ideal case of perfect wells, $E_{inh} = 0$ and therefore $\hbar\omega_{max} = E_{e_1 - \hbar h_1}$. This leads to a maximum of gain given by $g_{max}(E_{e_1 - \hbar h_1}) = \alpha_0(E_{e_1 - \hbar h_1}) [f_c^1(E_{e_1 - \hbar h_1}) - f_v^1(E_{e_1 - \hbar h_1})]$ where the Heaviside

function is taken equal to 1. Then, thanks to eqs. 2.14-2.19, one can formulate the last expression only in terms of carrier number N [40]:

$$g_{max}(N) = \alpha_0(E_{e1-hh1}) \left[1 - \exp\left(-\frac{N}{N_c^e}\right) - \exp\left(-\frac{N}{R_m N_c^e}\right) \right], \quad (2.44)$$

where the critical density N_c^e is given by eq. 2.20 and $R_m = m_{hh}/m_e$ is the ratio of the valence and conduction band effective masses. By supposing $N \approx N_c^e$ (later, we will discuss the validity of this approximation), it is possible to expand the exponential terms in eq. 2.44 to the first order in N/N_c^e , and one obtains:

$$g_{max}(N) \approx \frac{\alpha_0(E_{e1-hh1})}{\frac{m_r}{m_e} N_c^e} \left(N - \frac{m_r}{m_e} N_c^e + O\left[\left(\frac{N}{N_c^e}\right)^2\right] \right). \quad (2.45)$$

This equation is quite interesting as it allows to formulate a *linear* relationship between the gain and the carrier population. Moreover, it implies that the gain is proportional to the population difference between the critical density and that corresponding to the present flowing current. Indeed as explained in Sec. 2.2, within a laser, the gain continuously increases with increasing injected carrier population (see Fig. 2.4) and above threshold the actual gain is clamped or optically saturated under the growing effect of the stimulated emission (R_{st} rate in eq. 2.38). Many authors rather prefer to express eq. 2.45 in terms of the transparency carrier number N_{tr} [87, 88, 89]:

$$g(N) = \frac{dg_{mod}}{dN} (N - N_{tr}), \quad (2.46)$$

where dg_{mod}/dN is the differential modal gain per carrier number and characterizes the strength of the light-matter interaction. Comparing this linear assumption to eq. 2.45, the transparency carrier number N_{tr} seems to correspond to the critical density N_c^e corrected by a factor of m_r/m_e , e.g., in our case 0.88 (see Table 2.1). This factor is in good agreement with the factor equal to 0.69 obtained by dividing the transparency current density n_{tr} resulting from Fig. 2.4 (b) (i.e., $1.39 \cdot 10^{12} \text{ cm}^{-2}$) with the critical carrier density n_c^e given by eq. 2.20 (i.e., $2.02 \cdot 10^{12} \text{ cm}^{-2}$). Anyhow, n_{tr} is always related to n_c^e by a numerical factor close to 1 [40]. Moreover, eqs. 2.45 and 2.46 seem to link the differential gain to a theoretical value given by $dg_{mod}/dN \approx \frac{\Gamma \alpha_0(E_{e1-hh1})}{\frac{m_r}{m_e} N_c^e}$, where Γ is added to eq. 2.45 as the gain in eq. 2.46 is the modal gain. For typical nitride materials parameters (see Table 2.1), this relation leads to a theoretical value for dg/dN of $5.9 \cdot 10^{-10} \text{ cm per QW}$ (in 2D notation), which is less than forty times higher than the experimentally determined value. The experimental value, which has been evaluated at the laser threshold and at the laser emission wavelength, amounts to $8.6 \cdot 10^{-7} \text{ cm}^{-1}$ in number notation or $1.5 \cdot 10^{-11} \text{ cm}$ in 2D notation [69]. To explain this discrepancy one has to keep in mind that eq. 2.45 has been obtained following different approximations: inhomogeneous and

homogeneous broadenings have not been considered and terms beyond the first order have been neglected during the expansion of the exponential function. The discrepancy can also likely be ascribed to the flat-band approximation used for calculating $\alpha_0(E_{e_1}-\hbar h_1)$ whereas the presence of an unscreened internal field would have caused a reduction in the wavefunction overlap in eq. 2.21. Furthermore, the presence of another quantized level in the QW (e.g., $E_{e_2}-\hbar h_1$) would have in turn increased the critical carrier number N_c^e thus reducing further the theoretical value of the differential gain. Moreover, N_c^e has been calculated from eq. 2.20 for the perfect 2D case whereas a more realistic fractional dimensionality of the DOS would lay between 2 and 3, thus further increasing the critical carrier number. Other growth and process related imperfections could also have an impact on the performance of the lasers compared to the theoretically predicted one.

- If one instead does not want to suppress the wavelength dependency and thus wants to continue considering the impact of inhomogeneous broadening, eqs. 2.14-2.19 also allow to formulate a rather complicated expression for the broad material gain $g(\hbar\omega, N)$ given by eq. 2.13. This expression (that we will not write here) would allow to calculate the value of the gain not only in terms of carrier population but also for any given $\hbar\omega$. The rate equations 2.41 and 2.42 would thus allow to describe the dynamical behavior of the carrier and photon populations for a specific lasing mode $\hbar\omega$ also far from $\hbar\omega_{max}$.

Hereafter, we will refer to as the *linear* model in case of gain approximated linearly with the carrier population (eq. 2.46) contrariwise to the *wavelength-dependent* model for which the spectral extension of the gain is preserved (eqs. 2.13-2.19).

ABC model

To the author's knowledge only one exhaustive study has been carried out on the ABC coefficients in the case of III-nitride-based LDs. As stated in Ref. [69], LDs rather than LEDs are more convenient to study the recombination mechanisms as the B and C coefficients are determined close to and above threshold, i.e., where a constant injection efficiency can be assumed as the carrier population in the active region is clamped. Scheibenzuber *et al.* in 2011 have developed a model to experimentally determine the ABC coefficients and the measurements were carried out on the InGa_N-based LDs processed during this thesis [68]. This model is based on the linear approximation of the gain described in eq. 2.46. Unfortunately, if we wished to implement a wavelength-dependent gain, as described in the previous subsection, the ABC coefficients would have to be adapted. Here, we will follow the same method for calculating new ABC coefficients.

First, as stated in Ref. [68], three constraints fix the parabola of the recombination rate

per carrier $r(N) = \frac{1}{\tau(N)} = A + BN + CN^2$ (see eq. 2.38) and they can be written as:

$$r(0) = A = \frac{1}{2\tau_{EL}}, \quad (2.47)$$

$$r(N_{th}) = A + BN_{th} + CN_{th}^2 = \frac{1}{\tau_{th}} = \frac{\eta_{inj}I_{th}}{qN_{th}}, \quad (2.48)$$

$$\frac{dr}{dN}(N_{th}) = B + 2CN_{th} = \left(\frac{\eta_{inj} \frac{dg_{mod}}{dN}}{q \frac{dg_{mod}}{dI}} - \frac{1}{\tau_{th}} \right) / N_{th}. \quad (2.49)$$

Equation 2.47 states that in the low excitation regime ($N \rightarrow 0$), the charge carrier lifetime is immutable and the recombination rate can be well approximated by an exponential with a decay time equal to A^{-1} , which is correlated to the spontaneous emission decay time τ_{EL} within a factor two. After a 50 ns current pulse at 2 mA, Scheibenzuber *et al.* measured a non radiative coefficient of $4.2 \cdot 10^7 \text{ s}^{-1}$ in number notation [68]. This A coefficient falls within the experimental range $1\text{-}6 \cdot 10^7 \text{ s}^{-1}$ reported by other groups [90, 91, 92, 93].

Equation 2.48 is a simple application of eq. 2.32 whereas details concerning the expression given by eq. 2.49 can be found in Ref. [68]. The values for the differential gain per current dg_{mod}/dI , the differential gain per carrier dg_{mod}/dN and the injection efficiency η_{inj} at threshold have been determined experimentally [68]. The carrier number at threshold has been instead calculated according to eq. 2.13 [see Fig. 2.4 (b)], i.e., $N_{th} = 8.58 \cdot 10^7$ in number notation. Then, the only missing quantities, except for the B and C coefficients, are the carrier lifetime at threshold τ_{th} and the threshold current I_{th} . We thus have four unknowns and three equations (two from 2.48 and one from 2.49): another constraint is therefore missing.

The turn-on delay time for lasing τ_{TOD} can provide important information concerning the last equation. The fact that B and C have to be positive, imposes a maximum value for B when $C = 0$ and for C when $B = 0$. This in turn implies an upper limit for the delay time and, respectively, a lower limit. For the present sample, the upper limit is characterized by $C = 0$, $B = 6.845 \text{ s}^{-1}$, $I_{th} = 12.72 \text{ mA}$ and $\tau_{th} = 1.59 \text{ ns}$ whereas the lower limit is obtained for $B = 0$, $C = 5.319 \cdot 10^{-8} \text{ s}^{-1}$, $I_{th} = 8.76 \text{ mA}$ and $\tau_{th} = 2.31 \text{ ns}$. Afterward, the resulting values for A , B and C are inserted in the rate equations 2.41 and 2.42 and the model is solved numerically as a function of the injected current (Fig. 2.6). Note that it is not possible to set 0 for the B -coefficient in eq. 2.42 as the structure can only emit with a non-zero spontaneous emission noise. For this reason the maximum value has been chosen, i.e., $B = 6.845 \text{ s}^{-1}$. Note also that the wavelength-dependent model has been evaluated at the maximum of gain for N_{th} , i.e., for 2.995 eV [see Fig. 2.4 (b)]. Unfortunately, contrary to Ref. [68], we do not have any experimental value to fit the delay time as we are considering an “ideal” device that works according to the complete formula for the gain rather than the linear approximation. Therefore, in

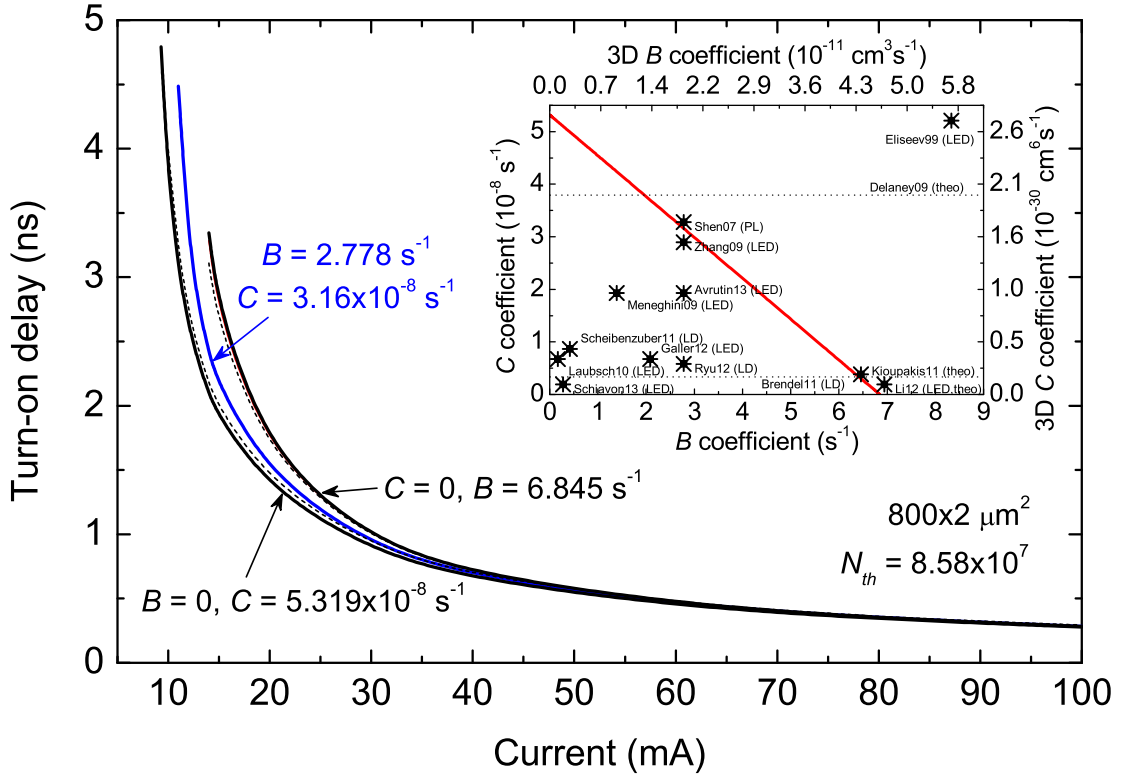


Figure 2.6: Simulated turn-on delay time as a function of the injected current. The black lines are the delay time calculated for the upper limit case ($C = 0$) and the lower limit case ($B = 0$). The blue curve corresponds to the best fit to theoretical and expected values. The dashed lines represent a C -dominant model (lower curve, $B = 0.068 \text{s}^{-1}$, $C = 5.133 \cdot 10^{-8} \text{s}^{-1}$) and a B -dominant model (upper curve, $B = 6.145 \text{s}^{-1}$, $C = 4.712 \cdot 10^{-9} \text{s}^{-1}$). The inset shows the relationship between B and C coefficients calculated according to eqs. 2.48 and 2.49 at threshold (red curve) while the star-like points are the reported values in the literature.

principle, any values for B and C that fulfill the upper and the lower limit are valid: a small B value would correspond to a more Auger-dominant model, i.e., the C coefficient would converge to its maximal value (lower dashed line in Fig. 2.6); at the same time a small C value would correspond to a more spontaneous-emission-dominant model where now the B coefficient would converge to its maximal value (upper dashed line in Fig. 2.6). We thus have to turn our attention on what has been reported on III-nitrides in the literature.

At high injected carrier densities, nitride-based LEDs exhibit a monotonic droop in the quantum efficiency that limits their performances when operating at high power [73]. This effect is even more pronounced with increasing emission wavelength. To explain this efficiency reduction several mechanisms have been proposed such as Auger recombination [90, 94], carrier leakage [95], non-radiative recombination occurring at dislocations [96], high plasma carrier temperatures [97] and junction heating effects [98]. Among these,

numerous experimental and theoretical studies attribute to Auger recombination the real primary cause for the efficiency droop but a strong debate on this subject is still in progress [99]. Very recently, Iveland and co-workers have reported a direct measurement of Auger electrons by electron emission spectroscopy from a cesiated InGaN/GaN LED under electrical injection thus establishing for the first time a straightforward correlation between the high energy emitted electron current and the “droop current” (the missing component of the injected current for light emission) [100]. Nevertheless, in that sense, many important studies have been performed to determine the ABC coefficients in III-nitride materials and especially the C one. Note that ABC coefficients are in fact “shaped” by the device properties (mostly those that characterize the active region) and thus it is really difficult to determine a set of coefficients for the ABC model that fits with all the experimental data.

The inset of Fig. 2.6 displays the relationship between the B and C coefficients according to eqs. 2.48 and 2.49 (red curve). On the same graph the star-like points represent the values for B and C reported in different studies on III-nitrides (labeled for each reference). Auger recombination is a non-radiative process in which an electron recombines with a hole and transfers the resulting energy gained by the recombination to another electron (or hole) in the form of kinetic energy [40]. The impact of the Auger process decreases with increasing bandgap energy and is expected to be negligible in wide-bandgap materials (see graphs for conventional alloys in Refs. [90] and [101]). In this sense, some theoretical calculations indicate an Auger parameter in the range of $10^{-32} - 10^{-34} \text{ cm}^6\text{s}^{-1}$ [102, 103]. However, experimental measurements performed on III-nitride diodes (mostly on LEDs) have shown a much higher C coefficient around $10^{-30} - 10^{-32} \text{ cm}^6\text{s}^{-1}$ (see inset Fig. 2.6) [68, 90, 91, 93, 104, 105, 106, 107, 108, 109, 110]. Indeed, simulations of the internal quantum efficiency based on the ABC model shows that only Auger parameters in this range cause a significant efficiency droop [90, 93, 101]. Note that obtaining reliable C coefficients from experimental measurements is really challenging as one has to rely on other calculated parameters (such as, e.g., the A and B coefficients) and furthermore the Auger contribution has to be carefully decoupled from other possible non-radiative processes. Delaney *et al.* using first-principle density-functional and many-body-perturbation theory reported a theoretical value for the Auger parameter of $2 \cdot 10^{-30} \text{ cm}^6\text{s}^{-1}$, closer to what has been obtained from experiments (dotted line in the inset of Fig. 2.6) [111]. To get rid of polarization effects when growing along the c -axis, Shen *et al.* investigated the Auger coefficient in quasi-bulk InGaN layers using PL and reported values ranging from $1.4 \cdot 10^{-30}$ to $2 \cdot 10^{-30} \text{ cm}^6\text{s}^{-1}$ [92]. These values are in good agreement with our predictions for the B and C coefficients. As the simulations carried out in this section for the wavelength-dependent model rather consider an ideal heterostructure it is more convenient to refer to the values reported in the paper of Shen instead of those for real diodes. Moreover, Ref. [92] is one of the most cited on the subject of Auger recombination in III-nitrides. Note that also the values reported by Kioupakis *et al.*, in which an indirect Auger recombination is considered (i.e., a mechanism mediated by phonon-assisted scattering), are in good agreement with our wavelength-dependent

model (see inset in Fig. 2.6) [76]. However, as previously discussed, such high B and low C coefficients would lead to a more spontaneous-emission-dominant model. Therefore, we decided to use the values reported by Shen *et al.* as these coefficients represent a more weighted spontaneous and Auger recombination mechanisms. According to Ref. [92] we have chosen to implement in the wavelength-dependent model a B coefficient of 2.778 s^{-1} ($2 \cdot 10^{-11} \text{ cm}^3 \text{ s}^{-1}$ in 3D notation) and a C coefficient of $3.16 \cdot 10^{-8} \text{ s}^{-1}$ ($1.638 \cdot 10^{-30} \text{ cm}^6 \text{ s}^{-1}$ in 3D notation). This implies a threshold current I_{th} of 10.4 mA and a carrier lifetime at threshold τ_{th} of 1.95 ns. Note that the delay curve calculated with those B and C coefficients (blue curve in Fig. 2.6) seems to lay well half-way between the two limit cases. A cross-study on the internal quantum efficiency of the diode would allow to assign a more reliable and more precise value to the coefficients of the ABC model. The bimolecular radiative recombination coefficient B within the context of Kane's theory can be expressed as [40]:

$$B = \frac{1}{\tau_r} \frac{N_c^r}{N_c^e N_c^h} = \frac{1}{\tau_r N_c^e} \left(\frac{m_r}{m_h} \right)^a, \quad (2.50)$$

where τ_r is the radiative recombination carrier lifetime, N_c^i is the critical carrier number for the reduced mass (r), the electrons (e) and the holes (h), respectively. In case of a 3D DOS, the coefficient a is equal to $3/2$ and N_c^e is given by eq. 2.25 whereas for a 2D DOS, a is equal to 1 and N_c^e is given by eq. 2.20. For instance, for a typical radiative lifetime τ_r of 1 ns and a critical number N_c^e of $3.23 \cdot 10^7$ (see Table 2.1), the B -coefficient is equal to 3.595 s^{-1} (in number notation), in good agreement with our calculated value.

As stated in Sec. 2.2, the steady-state solution of eqs. 2.41 and 2.42 allows to study the output characteristics of the laser structure as a function of the different internal parameters whereas the dynamic solution allows to inquire the time-dependent behavior of the LD especially close to the threshold where the carrier and the photon population try to stabilize themselves. In Figs. 2.7 (a) and 2.8 (a), the time evolution of the charge carrier number N and photon number S around turn-on is shown for a current of $1.1 \cdot I_{th}$ for the linear and the wavelength-dependent models, respectively. Note that the wavelength-dependent model has been evaluated at the maximum of gain for N_{th} , i.e., at 2.995 eV [see Fig. 2.4 (b)]. First the carrier population builds up in the laser structure. Typically, a turn-on delay τ_{TOD} of a few nanoseconds is needed to create the carrier number necessary to fill the DOS of the gain medium and it can be modeled by the following expression [29]:

$$\tau_{TOD} = \tau \ln \left(\frac{I}{I - I_{th}} \right). \quad (2.51)$$

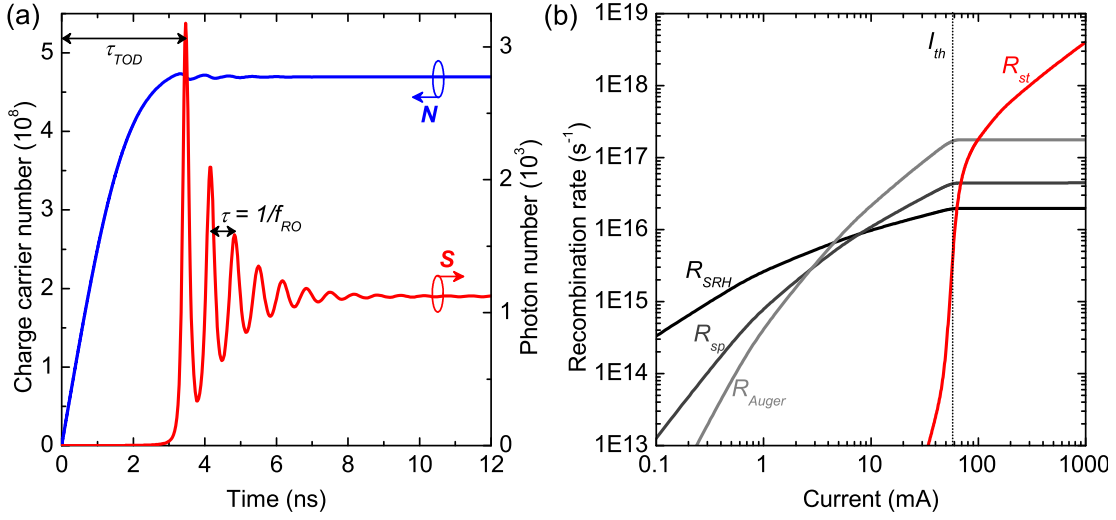


Figure 2.7: Linear model. (a) Dynamic solution of the rate equations 2.41-2.42 for a charge carrier population N (blue) and for a photon population S (red). The injected current I is $1.1 \cdot I_{th}$, i.e., 63 mA. The arrows indicate the turn-on delay time τ_{TOD} and the inverse oscillation frequency $1/f_{RO}$. (b) Recombination rates R_{SRH} (black), R_{spont} (dark grey), R_{Auger} (grey) and R_{st} (red) described in eq. 2.38 as a function of pump current. The vertical dotted line represents the threshold current (i.e., $I_{th} = 57.5$ mA).

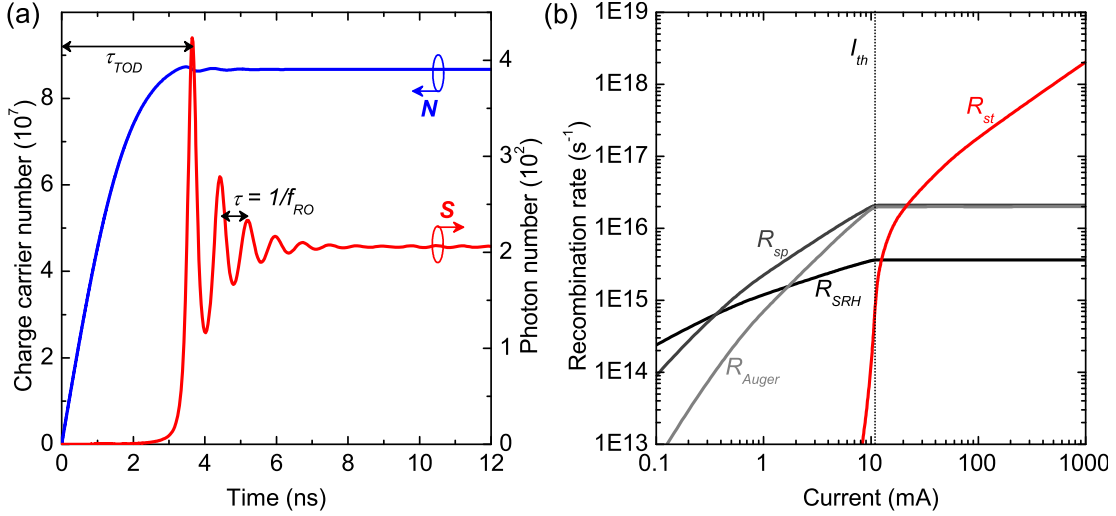


Figure 2.8: Wavelength-dependent model. (a) Dynamic solution of the rate equations 2.41-2.42 for a charge carrier population N (blue) and for a photon population S (red). The injected current I is $1.1 \cdot I_{th}$, i.e., 11.41 mA. The arrows indicate the turn-on delay τ_{TOD} and the inverse oscillation frequency $1/f_{RO}$. (b) Recombination rates R_{SRH} (black), R_{spont} (dark grey), R_{Auger} (grey) and R_{st} (red) described in eq. 2.38 as a function of pump current. The vertical dotted line represents the threshold current (i.e., $I_{th} = 10.37$ mA).

Note that the higher the pump current, the shorter the turn-on delay time τ_{TOD} (see Fig. 2.6). Finally, once the carrier population N overpasses the threshold, the photon population S can build up too and the optical output starts. At this stage, the carrier number N is depleted below threshold by the laser pulse. The continuous supply of carriers given by the pump current is not sufficient to counteract the effect of stimulated emission triggered by the rising optical pulse and as a consequence the photon population S falls in turn below the cw level due to insufficient gain. This mutual interaction between the two populations is repeated until the steady-state (cw) regime is reached (typically, after several nanoseconds) and it takes the form of unstabilized or damped *relaxation oscillations* (ROs) with a frequency f_{RO} given by [88]:

$$f_{RO} = \frac{1}{2\pi} \sqrt{\eta_{inj} \frac{dg}{dN} \frac{v_g}{q} (I - I_{th})}. \quad (2.52)$$

This equation is obtained in the small signal dynamic-response limit for population modulations of δN and δS inserted in eqs. 2.41 and 2.42. Worth pointing out is the square root dependency of the oscillation frequency f_{RO} on pump current I . Moreover, the dependency $\propto \sqrt{dg/dN}$ of the relaxation frequency shows the superiority of QW-based lasers over bulk heterojunction lasers since they possess a higher differential gain. Figures 2.7 (b) and 2.8 (b) display the contribution of each specific recombination mechanism given by eq. 2.38 as a function of the pump current for the linear and the wavelength-dependent models, respectively. In both models, the spontaneous emission rate R_{sp} dominates over the stimulated emission one R_{st} below threshold (vertical dotted line) and the LD is in the so-called LED regime. Whereas above threshold, so when the total cavity losses α_{TOT} are fully compensated by the modal gain according to eq. 2.29, the medium can sustain laser oscillations and the stimulated emission rate R_{st} dominates the spontaneous emission rate R_{sp} . Once the system reaches the steady-state regime, the charge carrier number N is clamped to its threshold value and, more importantly, is now independent of the pump current: any excess of carriers is immediately converted into photons via stimulated emission. In fact, at threshold the stimulated emission process fully compensates the total cavity losses (see eq. 2.42) and any excess carriers produce a stimulated photon (i.e., carriers that are not recombining following transition paths considered in the ABC model). This is displayed in Figs. 2.7 (b) and 2.8 (b) where we see that the stimulated emission rate R_{st} continues to rise as the current is increased beyond threshold whereas the other recombination mechanisms (i.e., R_{SRH} , R_{sp} , and R_{Auger}) remain constant (or clamped). In Fig. 2.7 (a) the carrier population is clamped to $4.69 \cdot 10^8$ in good agreement with the population of $4.4 \cdot 10^8$ reported in Ref. [69]. In Fig. 2.8 (a) the carrier population is clamped to $8.57 \cdot 10^7$ in perfect agreement with the carrier population, which allows the gain to compensate the total cavity losses, i.e., $N_{th} = 8.58 \cdot 10^7$ [see Fig. 2.4 (b)]. This demonstrates the consistency of the wavelength-dependent model.

Note that in the case of the linear model the Auger recombination rate R_{Auger} dominates

over the other recombination mechanisms close to threshold whereas in case of the wavelength-dependent model the spontaneous and Auger contributions have nearly the same rate [Figs. 2.7 (b) and 2.8 (b)]. Obviously, if we could manage to “switch off” the Auger contribution, the threshold current for lasing would decrease significantly. Proportionally, this reduction would be stronger in the case of the linear model. For instance, by keeping any other parameter constant and by setting $C = 0$, the threshold current for such a hypothetical LD would be 15.50 and 5.83 mA instead of 57.50 and 10.37 mA for the linear and the wavelength-dependent models, respectively. However, by keeping any other parameter constant and by setting instead $B = 0$, the new threshold current would be 46.50 and 5.71 mA for the linear and the wavelength-dependent models, respectively. This means that the values that we have chosen for B and C coefficients in the wavelength-dependent model have nearly the same impact on the threshold (they almost double it) whereas in case of the linear model the Auger parameter is the dominant recombination mechanism. In this case, it increases the threshold current by more than a factor of four.

2.3 Multi-section laser diodes

2.3.1 Motivation

The driving concept and the overall target of the FemtoBlue project was to achieve a semiconductor LD capable of producing ultrafast optical pulses in the blue-violet spectral range. Semiconductor LDs featuring a saturable absorber are promising for obtaining extremely short pulses, high peak optical powers, and extremely fast repetition rates [8]. The principle of a saturable absorber material is to absorb electromagnetic radiations up to a certain intensity level beyond which the material becomes transparent [8]. A saturable absorber would then allow the opening of a short net gain window that supports and stabilizes the pulse and at the same time discriminates against the noise that accidentally may grow in between the pulses. However, the traditional direct modulation of the diode parameters (such as, e.g., the driving current in the gain-switching regime) is not able to supply the necessary ultrafast output properties, mostly because of the limited frequency capability, which for a standard LD system is typically around a few tens of GHz [112]. Indeed, the charge carrier dynamics limits the response to a modulation in standard single-section LDs whereas a saturable absorber placed inside the cavity would depend only on the interplay of the internal fields and applied external voltage. Transient heating effects due to the high driving currents also limit the operation of directly modulated LDs [12]. Moreover, especially during the first attempts to obtain a pulsed emission in the 80's, these devices were typically placed inside an external cavity that had the function to set the cavity length (thus the repetition frequency) and to stabilize the pulse train. Unfortunately, if one wants to increase the repetition frequency, the fabrication of shorter and shorter external cavities becomes really difficult. Furthermore, uncontrolled

multiple pulses may arise because of reflections on the non-perfect anti-reflection coated facets of these external cavities [113]. A *monolithic* system that directly integrates a saturable absorber in the waveguide of the heterostructure would in turn solve the limited modulation frequency and at the same time would overcome the need for an external cavity increasing the achievable repetition frequency even up to hundreds of GHz in the mode-locking regime. This monolithic technology would lay the foundation for miniature portable femtosecond lasers combining the well known advantages of semiconductor LDs such as their easy manufacturing, the absence of mechanical alignments, their low cost, compactness and high potential for integrability. It could therefore allow the replacement of the well-developed but bulky and expensive solid-state Ti:sapphire lasers.

Monolithic mode-locking is one of the best techniques for obtaining short-pulsed emission. Thanks to the presence of an intracavity saturable absorber, mode-locking can produce nearly transform-limited pulses *directly*, which means without any external modulation or any further compensation methods as for example for limiting dynamic wavelength chirpings in the gain-switching regime [114]. In the specific case of group-III nitrides, the development of such an ultrafast compact source would then be of special interest for applications in the blue-violet wavelength range such as the next-generation of high-density optical storage systems [115, 116], ultraprecise nanoprocessing [117], optical coherence tomography [118], bio-medical diagnostics and trace detection of hazardous substances [8].

In the last decades, monolithic semiconductor lasers have been extensively exploited for generating short optical pulses thanks to their high efficiency and stability. For instance, semiconductor saturable absorbers can be integrated into a mirror structure as an intracavity layer, the so-called semiconductor saturable absorber mirror (SESAM) concept [119]. The SESAM operates in reflection mode, this means that the more intense the pulse, the higher the reflectivity. The fact that the absorbing layer is placed parallel to the active layer makes the SESAM a good candidate for the design of a VCSEL for ultrafast operation [120]. However, at the same time, as the SESAM is integrated in the heterostructure during the growth, the absorption properties are permanent once the growth is finished. This way, it is not possible to modulate *a posteriori* the saturable absorber pattern.

Another possible approach to achieve ultrafast regimes consists in implementing a monolithic multi-section (MS)-LD, for which a reverse bias voltage is applied to a specific absorber section (AS) [12, 121, 122]. This concept consists in a ridge-waveguided Fabry-Perot-based cavity processed into multiple electrically isolated sections. The longer gain section (GS) is biased at a constant forward current and acts as an amplifier, whereas the shorter reverse-biased AS acts as an intracavity saturable absorber that can be controlled as an optical modulator through electro-absorption effects (i.e., QCFK effects) [12]. With such a design, the sections of the LDs are optically coupled but electrically separated and share the same MQW active region. For instance, once the GS is pumped above transparency, absorption occurs in the AS and a reverse current flows through it, just as in a photodetector [123]. This reverse-applied bias enables a further degree of freedom for

adjusting the internal absorption mechanism of the MS-LD, affecting both the static and the dynamic characteristics of the device, as it will be shown later in this thesis. Indeed, thanks to the dynamical behavior of the absorber, optical pulses much shorter than a gain-switched LD can be generated. The interest in the exploitation of such monolithic multiple-contacted ridge waveguide cavities originates from the possibility to concentrate the energy of the LD, via an internal modulation, in very short pulses with the highest possible repetition rate, thus allowing to reach very high output peak powers. Under appropriate modulation conditions for the AS, the MS-LD would then operate in the dynamic regimes of self-pulsation (SP), Q-switching and active/passive mode-locking.

2.3.2 State of the art

Nine years after the first laser theorized by Townes and Schawlow, DeMaria *et al.* achieved Q-switching and mode-locking with pulses of a few picoseconds by using a Nd^{3+} -doped glass laser [124]. The saturable absorber was made by a reversible bleachable dye solution, which allowed to obtain for the first time mode-locking emission without any critical adjustment of the mirror spacings. In 1991 the first multiple-contacted QW-based laser was fabricated by Sanders and co-workers using a GaAs/AlGaAs heterostructure coupled to an external cavity [125]. They demonstrated passive mode-locking with a round-trip frequency of 1.17 GHz and pulses shorter than 10 ps on a bi-section device. The biased section allowed to control and adjust the saturable absorption in the device. Concerning III-nitrides, more than ten years later, in 2002, Kneissl and co-workers published the first study on a monolithic two-section InGaN MQW-based LD with an integrated electro-absorption modulator [12]. Compared to other materials, non-linear absorption changes as large as 5000 cm^{-1} were already shown with a moderate reverse bias of 7.2 V. This highly tunable absorption was promising for the establishment of a very stable passive mode-locking regime. In 2004, gain-switching operation with high peak powers up to 0.4 W was reported for the first time in an InGaN MQW LD [9]. Only recently, in 2009, the first report on pulsed emission in a monolithic bi-section GaN-based LD was finally published by the Laboratory of Advanced Materials at Sony Corporation [11]. Miyajima and co-workers reported stable SP on an InGaN/GaN double QW separate-confinement heterostructure laser with pulses of 30 ps, an optical peak output power of 2.4 W and a repetition frequency of 0.9 GHz. In this paper the influence of the reverse-biased AS on the dynamic output characteristics is stressed in terms of decrease of the carrier lifetime and increased absorption in the absorber QWs. One year later the same group reported the first mode-locked bi-section InGaN-based LD placed in an external cavity configuration (the mirrors were spaced by about 15 cm) [126]. 3 ps long optical pulses with a peak power of 3 W have been produced under passive and hybrid mode-locking at a 1 GHz repetition rate. Afterward, they reported peak powers of 10 W with a self-pulsating triple-section device with pulses of 15 ps at a repetition rate of 1 GHz [127] and of 100 W with a mode-locked bi-section LD with pulses of 3 ps at 1 GHz [128]. These last record peak power values were obtained thanks to the implementation of a semiconductor

optical amplifier in the external cavity geometry. Consequently, in parallel, the same group working in collaboration with Sony Corporation has carried out studies on one of the main applications concerning such III-nitride based ultrafast lasers: high density optical data storage. In 2010 void-based volumetric optical recording on a rotating disk was demonstrated at 404 nm exploiting multi-photon absorption in an organic material [129]. Later in 2011, 200 Gbytes under dynamic recording was demonstrated in a three dimensional optical disk using a Ti:sapphire laser with femtosecond pulse emission [116]. Since the beginning of the FemtoBlue project in September 2009 many important steps have been made in the field of group-III nitride MQW-based ultrafast lasers. For a better control of mode-locking and SP regimes, it was crucial to understand how the current injected in the GS and the applied bias on the AS influence the performance of the MS-LDs. For this reason, two exhaustive studies have been carried out on the static characteristics of MS-LDs, one by Scheibenzuber *et al.* in 2011 [130] and another one by our group in 2012 [131]. Both emphasize the role of modal absorption features and the high tunability of the AS MQWs under reverse bias conditions stressing the potential of MS-(Al,In)GaN-LDs for applications demanding compact pulsed light sources operating in the blue-violet range. One year later, Scheibenzuber *et al.* demonstrated SP with a frequency ranging from 1.5 to 4.5 GHz when increasing the pump current on the monolithic MS-LDs fabricated during this thesis [132]. The optical pulses were as short as 18 ps and with a peak power of 0.6 W. Interestingly, stable SP is already obtained at zero absorber bias mainly because of the intrinsic internal polarization field of III-nitride materials that ensures good absorption between the two sections already at moderate values of the applied voltage. This characteristic is extremely suitable for applications as no additional bias sources would be required. The first ever mode-locking operation in a monolithic GaN-based cavity was demonstrated by Vasil'ev in 2013 using our devices [133]. Passive mode-locked pulses on a bi-section LD at repetition frequencies in the range from 40 to 93 GHz were observed with pulse widths of 3-5 ps and at a peak power of 0.32 W. Finally, in 2013 Olle *et al.* also demonstrated hybrid mode-locking with a round-trip frequency of 28.6 GHz on the same monolithic cavities [134]. Passive mode-locking with pulses of 8 ps and a peak power of 37 mW has been observed whereas under hybrid mode-locking the pulses shortened down to 4 ps and the peak power increased up to 72 mW.

2.3.3 L - I - V characteristics

In this section, the typical characteristics of an edge-emitting multiple-contacted LD are described. As for single-section LDs, these devices have been processed as index-guided structures in the ICMP clean rooms (see Sec. 2.4.2).

As depicted in Fig. 2.9 (d), the MS-LD consists of an AS on which a constant bias voltage V_{AS} is applied and a GS working under cw operation. The p -type electrodes of the gain and absorber sections are separated by a 15 μm wide contactless gap that ensures electrical isolation while maintaining optical coupling. The leakage series resistance is

as high as 500 k Ω . Devices with different AS section lengths L_{AS} and different cavity lengths L_{TOT} have been fabricated with the absorber located at the edge or at the center of the cavity [left and right panels in Fig. 2.9 (d), respectively]. In Fig. 2.9 (a) the far field pattern of a MS-LD above lasing threshold is shown (in the inset, the AS in the center of the device can be distinguished).

L - I - V curves of an $800 \times 2 \mu\text{m}^2$ LD with $L_{AS} = 100 \mu\text{m}$ from sample A2109 are displayed in Fig. 2.9 (b) as a function of the cw current I_{GS} injected in the GS. The I - V and L - I characteristics of MS-LDs are similar to those of standard single-section lasers whereas the threshold current I_{th} is slightly higher at $V_{AS} = 0$ due to the absorption occurring in the AS. Indeed, when connecting together gain and absorber sections, i.e., when recovering a single-section-like device, the L - I curves are almost linear above the lasing threshold. Interestingly, in the case of a MS-LD the threshold current for lasing I_{th} is not constant and shifts with the bias V_{AS} applied to the AS. The charge carrier lifetime and the absorption in the AS are mostly responsible for this shift, as it will be explained

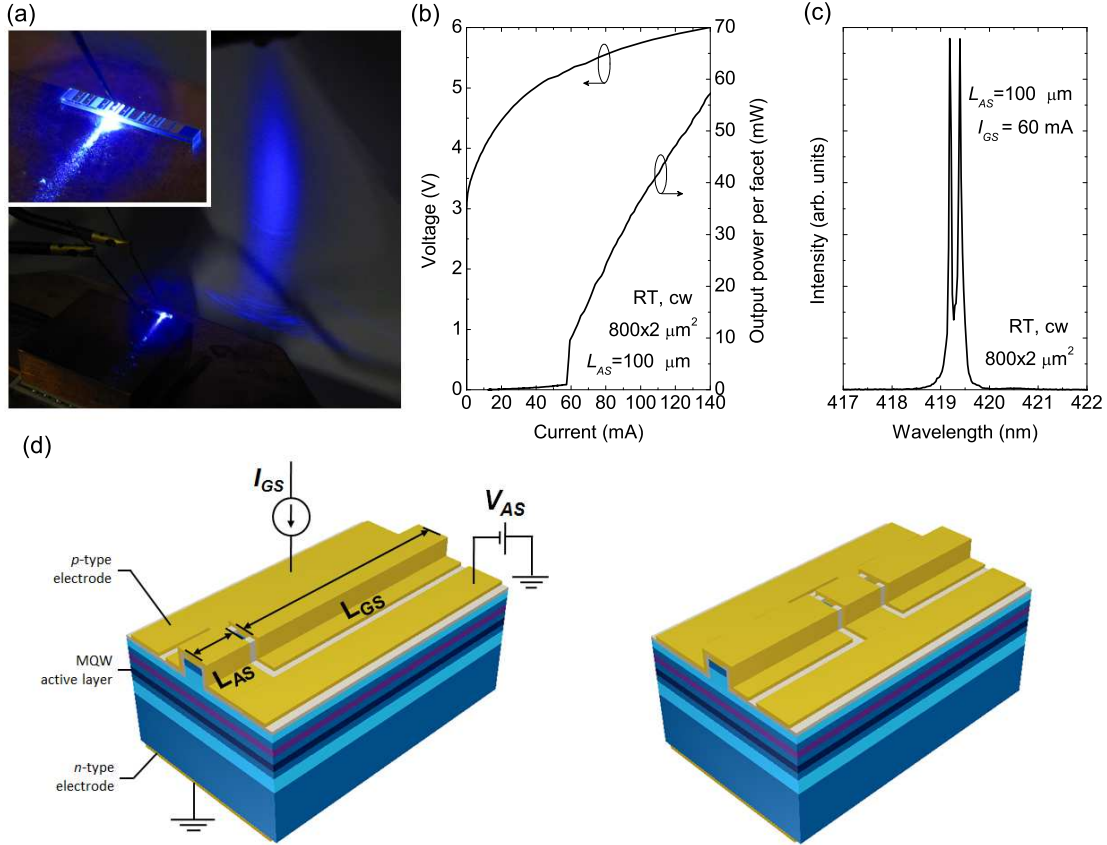


Figure 2.9: (a) Far field pattern of a MS-LD in the lasing regime. (b) Experimental L - I - V curves for an $800 \times 2 \mu\text{m}^2$ MS-LD with $L_{AS} = 100 \mu\text{m}$ as a function of the injected current in the GS under cw operation at RT. (c) Optical spectrum at $I_{GS} = 60 \text{ mA}$ for the same MS-LD. (d) Schematic structure of a MS-LD with bi-section (left) and triple-section (right) p -side electrode. The detailed layer structure is depicted in Fig. 2.2.

in more details in Sec. 3. Moreover, within a specific absorber bias range [e.g., $V_{AS} = 0$ in Fig. 2.9 (b)], the MS-LD exhibits a non-linear behavior, which leads to a “kink” at threshold in the L - I curves and also in the photocurrent extracted from the AS [135]. Note that the L - I curves are acquired by adiabatically increasing the pump current in the GS. The kink is ascribed to a sharp increase in the carrier density in the AS within the build-up of lasing emission in the cavity. The rising optical field bleaches the absorber yielding a further increase in the emission power. This non-linear transient process results in a characteristic switching-on jump in the output power characteristic [136]. After, when reducing adiabatically the pump current, the structure then exhibits a hysteresis of the switching-on and switching-off threshold [137]. The optical bistability around the threshold will be treated more exhaustively in Sec. 3.6. These features (i.e., the shift of I_{th} , the bistability of the L - I and photocurrent curves) attest that the absorber well operates as a saturable absorber.

The typical emission wavelength of MS-LDs fabricated during this thesis lies in the blue-violet (e.g., ~ 420 nm). It is worth noticing that for specific V_{AS} and I_{GS} values the emission spectra show multiple peaks. For example, the peak wavelength separation in Fig. 2.9 (c) is about 0.25 nm. This value is too large to be explained as originating from the longitudinal-mode splitting for an 800- μm long cavity, i.e., 0.04 nm according to eq. 2.37. The peak separation more likely corresponds to the free spectral range induced by the 100 μm -long absorber intracavity, i.e., 0.32 nm, due to refractive index changes caused by the electrical polarization [131]. This phenomenon should not be confused with the so-called mode spectral substructures or also mode clustering effects observed in InGaN semiconductor lasers that instead are mostly governed by both the inhomogeneous broadening of the gain and by the mode-width variations due to antiguiding lens effects [138, 139]. Anyway, hereafter, only the intensity-weighted average wavelength is reported as lasing wavelength λ_{lasing} since we focus on the cw, gain switching, and self-pulsation regimes.

2.3.4 Multi-section LD dynamics

To operate a MS-LD in the pulsed regime, the GS is driven under forward bias to act as an amplifier while the AS is biased to act as a saturable absorber or an electromodulator. In principle, as the two sections share the same active region, the gain for the GS and AS MQWs is exactly the same. However, as the two sections are operated under different conditions, it is convenient to distinguish between two gains. Hereafter, we refer to $g_{GS}(\hbar\omega, N_{GS}, S)$ as the GS gain according to which the carrier population in the GS N_{GS} fills the GS bands and to $g_{AS}(\hbar\omega, N_{AS}, S, V_{AS})$ as the AS gain according to which the carrier population in the AS N_{AS} fills on the contrary the AS bands. As usually the AS is driven well below I_{th} (in most cases it is reverse-biased), there is no electrical injection in the absorber MQWs. Therefore, rather than gain, the absorber bias V_{AS} introduces an additional absorption in the cavity, i.e., $\alpha_{AS}(V_{AS}) = -g_{AS}(V_{AS})$, that the system should compensate to reach laser oscillations. In principle, an increase in the

photon population S in the cavity leads to a decrease in the electron population N_{GS} and thus also in the gain g_{GS} in the GS whereas in the AS it induces an increase of the electron population N_{AS} and thus a decrease in the absorption α_{AS} [136]. Note that for an accurate treatment, the gain parameters g_{GS} and g_{AS} ($-\alpha_{AS}$) should be weighted with the respective section length, i.e., $L_{AS,GS}/L_{TOT}$. So, the threshold condition given by eq. 2.29 can be re-written as follows [130, 140, 141]:

$$\Gamma \left[\frac{L_{GS}}{L_{TOT}} g_{GS,th}(\hbar\omega, N_{GS}, S) - \frac{L_{AS}}{L_{TOT}} \alpha_{AS,th}(\hbar\omega, N_{AS}, S, V_{AS}) \right] = \alpha_i + \alpha_m \quad (2.53)$$

Thus, $\alpha_{AS}(V_{AS})$ allows a further degree of freedom on the internal absorption mechanism of the LD, that affects both the static and the dynamic characteristics of the device (see Chapters 3 and 4). On the other side, under steady state condition, the flow of carriers J entering the GS continues to be compensated by the total recombination rate R_{TOT} according to the ABC model and the stimulated emission process (see eq. 2.38).

In a similar way to a standard single-section LD, as the system starts to be pumped, the charge carrier population in both active regions and the photon field in the cavity interact mutually and rapidly at the temporal scale. However, the steady-state is no longer the desired condition. The interest in the exploitation of a multiple-contacted resonator cavity actually lies in balancing the reciprocal recombination processes that are going on in the active region in order to stabilize the ROs. If the device parameters successfully meet certain stability criteria, the oscillation process repeats itself continuously without dissolving leading to SP or even to mode-locking [142]. The coupled dynamic rate equations 2.41 and 2.42 extended to a multiple-contacted semiconductor laser cavity then read (in number notation):

$$\frac{dN_{GS}}{dt} = \overbrace{\frac{R_{inj}}{q}}^{\eta_{inj} I_{GS}} \overbrace{-AN_{GS} - BN_{GS}^2 - CN_{GS}^3}^{-N_{GS}/\tau_{GS} = R_{TOT}^{GS}} - \overbrace{\frac{L_{GS}}{L_{TOT}} g_{GS}(\hbar\omega, N_{GS}, S) v_g S}^{R_{st}^{GS}}, \quad (2.54)$$

$$\frac{dN_{AS}}{dt} = -\overbrace{\frac{N_{AS}}{\tau_{AS}}}^{R_{TOT}^{AS}} + \overbrace{\frac{L_{AS}}{L_{TOT}} \alpha_{AS}(\hbar\omega, N_{AS}, S, V_{AS}) v_g S}^{R_{st}^{AS}}, \quad (2.55)$$

$$\begin{aligned} \frac{dS}{dt} = \Gamma \left[\frac{L_{GS}}{L_{TOT}} g_{GS}(\hbar\omega, N_{GS}, S) - \frac{L_{AS}}{L_{TOT}} \alpha_{AS}(\hbar\omega, N_{AS}, S, V_{AS}) \right] v_g S \\ + \beta B N_{GS}^2 - (\alpha_i + \alpha_m) v_g S, \end{aligned} \quad (2.56)$$

where R_{inj} is electrical injection rate in the GS, R_{st}^{GS} and R_{st}^{AS} are the stimulated emission rates in the gain and absorber sections, respectively, R_{TOT}^{GS} and R_{TOT}^{AS} are the total carrier recombination rates in the gain and absorber sections, τ_{GS} and τ_{AS} are the charge carrier lifetimes in the gain and absorber sections, respectively. The absorber lifetime τ_{AS} is an important parameter in the dynamics of a MS-LD and can be significantly smaller than

τ_{GS} as it strongly depends on how the applied V_{AS} modifies the absorber band structure. Moreover, as in principle the AS is always reverse-biased, the absorber carrier lifetime τ_{AS} mostly depends on the escape rate of carriers from the active region (as we will see) and therefore the ABC model implemented in the case of τ_{GS} would not apply. A specific section 4.1 is dedicated to the evolution of τ_{AS} . A detailed analysis of the AS gain g_{AS} is carried out instead in Sec. 3.3. As the dependency of the absorber gain on the applied bias (in terms of transition energies and wavefunction overlaps, see eq. 2.21) is fairly complicated, in this section we will refer to the carrier-free absorption value $\alpha_0(V_{AS})$ as an intrinsic value α_0 , then without taking into account that this value may correspond to a specific band structure.

In the case of the linear model, we will use the equation for the saturation of gain 2.43 for both $g_{GS}(\hbar\omega, N_{GS}, S)$ and $\alpha_{AS}(\hbar\omega, N_{AS}, S, V_{AS})$. Then, we will employ the linear approximation of gain given by eq. 2.46 for g_{GS} whereas for α_{AS} this equation can not be straightforwardly employed as the AS differential absorption $d\alpha_{AS}/dN_{AS}$ is not known *a priori*. Moreover, a quantity such as $d\alpha_{AS}/dN_{AS}$ would not only depend on the AS charge carrier population N_{AS} but also on how the band structure is modified by the applied bias V_{AS} . As instead the quantity α_0 is known, Scheibenzuber in Ref. [69] proposes a slightly different linear approximation for α_{AS} :

$$\alpha_{AS}(\hbar\omega, N_{AS}, V_{AS}) = \alpha_0 (1 - \kappa N_{AS}) \quad (2.57)$$

where κ is a fitting parameter and is estimated to $1 \cdot 10^{-12} \text{ cm}^2$ (in 2D notation). Basically this is the same linear approximation of eq. 2.46 where the transparency population N_{tr} corresponds to $1/\kappa$ and $d\alpha_{AS}/dN_{AS}$ to $\alpha_0 \cdot \kappa$. Here, we prefer to follow the procedure described in Sec. 2.2.2 by employing the gain approximation proposed by Rosencher and Vinter in Ref. [40] (see eq. 2.44):

$$\alpha_{AS}(\hbar\omega, N_{AS}, V_{AS}) = -\alpha_0(V_{AS}) \left(1 - e^{-\frac{N_{AS}}{N_{AS,c}^e}} - e^{-\frac{N_{AS}}{N_{AS,c}^{hh}}} \right). \quad (2.58)$$

where $N_{AS,c}^e$ and $N_{AS,c}^{hh}$ are the critical carrier numbers given by eq. 2.20 for the electrons and holes, respectively. Note that this gain approximation can be traced back to the linear gain approximation described by eqs. 2.46 and 2.57 as shown in eq. 2.45.

Regarding the wavelength-dependent model, we do not need any further approximation for g_{GS} and α_{AS} as we are considering the whole gain expression given by eq. 2.13 for both the gain and absorber sections. As for the linear model, we will also use the equation for the saturation of gain 2.43. Nevertheless, the energy at which the gain is evaluated has to be chosen carefully. Note that the rate equation models proposed here, as far as we can make them effective, are inadequate for a quantitative study of the experiments. Nonetheless, they allow to analyze qualitatively the dynamic behavior of a MS-LD.

Figure 2.10 depicts the solutions of eqs. 2.54-2.56 in the case of the linear model. All the parameters have been kept constant except for the absorber carrier lifetime τ_{AS}

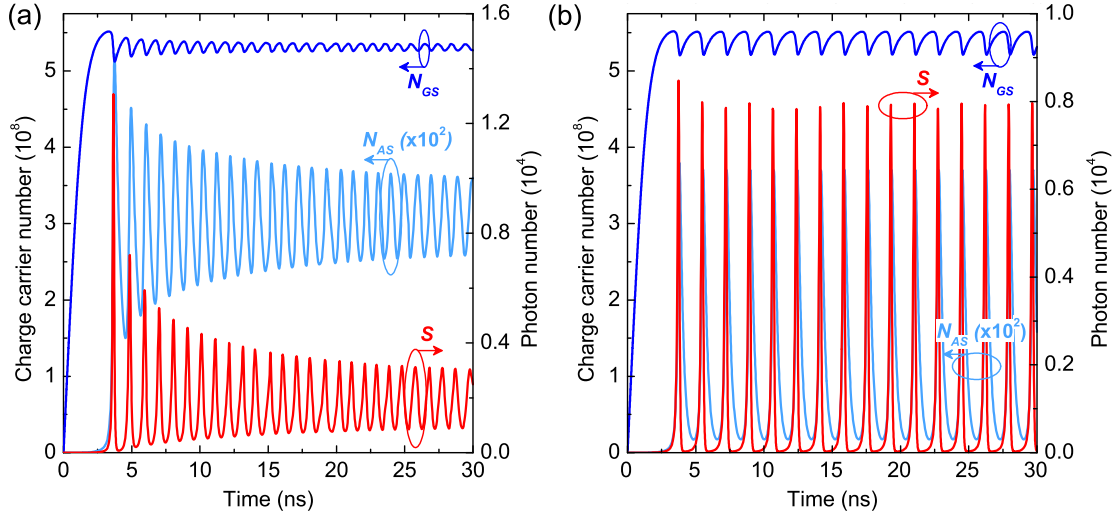


Figure 2.10: Linear model. Dynamic solution of the rate equations 2.54-2.56 for a GS charge carrier population N_{GS} (blue), an AS charge carrier population N_{AS} (light blue) and for a photon population S (red). SP takes the form of (a) stabilized ROs and (b) Q-switching. The parameters are: $I_{GS} = 1.04 \cdot I_{th} = 90$ mA, $L_{AS}/L_{TOT} = 0.2$, $\alpha_0 = 82$ cm $^{-1}$, $\tau_{AS} = 0.5$ ns for (a) and $\tau_{AS} = 0.25$ ns for (b).

which for (a) is twice that for (b). Thus, the self-pulsating emission takes the form of (a) stabilized ROs and (b) Q-switching. In Ref. [143], it is underlined how the amount of spontaneous photon emission (which is proportional to the pump current) in a cavity with an absorbing medium allows discriminating between two distinct regions in the SP frequency regime in a very general case. For a low spontaneous emission rate (e.g., low pump current), a longer time is required to bleach the absorption. Once the system gets lasing, the absorption will recover to its initial carrier-free state. This leads to a maximum amplitude between on-lasing and off-lasing states and thus low-frequency Q-switching. On the other hand, for a higher spontaneous emission rate (e.g., higher pump current), the absorber can rapidly reach transparency. In this case, the absorption section can no longer be fully depopulated between two pulses and weak amplitude undamped oscillations are observed. As in Fig. 2.10 (describing the specific case of a multiple-contacted cavity) the pump current is the same, what discriminates between two different SP regimes is the absorber lifetime τ_{AS} . The reasoning is very similar: the lower the interpulse intensity becomes, the longer it takes for the absorber to reach transparency [143]. Therefore, for a short lifetime τ_{AS} the absorber empties more easily and a longer time is needed to reach transparency thus leading to low-frequency Q-switching. Indeed, in case of Q-switching, the absorber carrier population N_{AS} goes back nearly to 0 and it has to start all over again for the next pulse [Fig. 2.10 (b)]. Whereas in the case of undamped ROs, the absorber carrier population N_{AS} is never completely depleted and this increases the rate at which a new pulse is generated [Fig. 2.10 (a)]. Note that the name “Q-switching” comes after the fact that the quality factor Q of the cavity (i.e., the energy stored over the energy lost per cycle) is indeed modulated via absorption changes

(in case of a MS-LD this is done passively in the AS that acts as an electroabsorption modulator).

Note that contrary to standard single-section LDs, the onset of SP oscillations prevents the usual clamping of the carrier population (in the GS) and the subsequent steady-state. Nevertheless, a quasi-steady-state cw operation can be obtained if the absorber “is not working properly”. By this expression, we mean a situation in which given a GS electrical injection rate, the absorber does not possess enough carrier-free absorption to generate stable SP. The system is thus able to continuously compensate any further absorption in the cavity. This is the case for a low carrier-free absorption value α_0 , for a small absorber/cavity length ratio L_{AS}/L_{TOT} , or also for a long absorber carrier lifetime τ_{AS} that hinders the depletion of the AS (i.e., the absorber remains partly saturated). The result is the damping of the SP oscillations (see also the theoretical analysis shown in Ref. [142]). This will be intensively discussed in Fig. 2.14 in which we see that the range of pump currents for stable SP shrinks for lower α_0 , lower L_{AS}/L_{TOT} and longer τ_{AS} (compare the distance in terms of current between the circles and the crosses). In the same way, under very high injected current, the strong optical pump of the GS will prevent the absorber from recovering an adequate value of carrier-free absorption to establish SP oscillations. Nevertheless, small residual oscillations are always present in the simulations (hence the notation quasi-steady-state) but their amplitude is less than 0.01% of the total population.

As the wavelength-dependent model considers the whole gain expression given by eq. 2.13, it is fairly accurate and thus it can help us to determine *a priori* how much carrier population is needed for the quasi-steady-state. Nevertheless, the energy at which g_{GS} and α_{AS} should be evaluated has to be chosen carefully. According to eq. 2.53, a modal gain medium $\Gamma \frac{L_{GS}}{L_{TOT}} g_{GS,th}$ should compensate a modal absorbing region $\Gamma \frac{L_{AS}}{L_{TOT}} \alpha_{AS,th}$ and total cavity losses $\alpha_i + \alpha_m$ to make the MS-LD reach threshold conditions. Following the same approach described in Fig. 2.4 for a 2D DOS, the modal gain medium $\Gamma \frac{L_{GS}}{L_{TOT}} g_{GS,th}$ must compensate, e.g., an carrier-free absorption α_0 of 200 cm^{-1} (i.e., $\Gamma \frac{L_{AS}}{L_{TOT}} \alpha_{AS,th} = 40 \text{ cm}^{-1}$) and total cavity losses α_{TOT} of 60 cm^{-1} to reach the threshold condition. Therefore, 100 cm^{-1} of modal gain correspond to a population N_{GS} of $9.459 \cdot 10^7$ (in number notation) [black curve in Fig. 2.11 (a)]. As explained in Sec. 2.2, we do not need that the whole gain spectrum lies beyond the threshold condition as it is sufficient that only the optical modes around the maximum of gain experience amplification. In the case of Fig. 2.11 (a), $g_{GS,max}$ is reached at an energy $E_{g_{max}}$ of 3.021 eV. Then, the rate equations 2.54-2.56 have been solved according to the wavelength-dependent model for $g_{GS}(\hbar\omega = E_{g_{max}})$ and for a reasonably high amount of pump current that inhibits the absorbing ability and enables the establishment of a quasi-steady-state emission [e.g., $I_{GS} = 1.7 \cdot I_{th} = 22.24 \text{ mA}$ in Fig. 2.11 (b)]. The photon population S reaches a cw emission after a few tens of nanoseconds while the GS carrier population N_{GS} is clamped to $8.871 \cdot 10^7$. This value is lower than what is predicted by eq. 2.53 (i.e., $N_{GS} = 9.459 \cdot 10^7$) but if we also take into account the AS carrier population (i.e., $N_{AS} = 0.36 \cdot 10^7$), the total carrier population in the cavity is $9.231 \cdot 10^7$, a value which is in

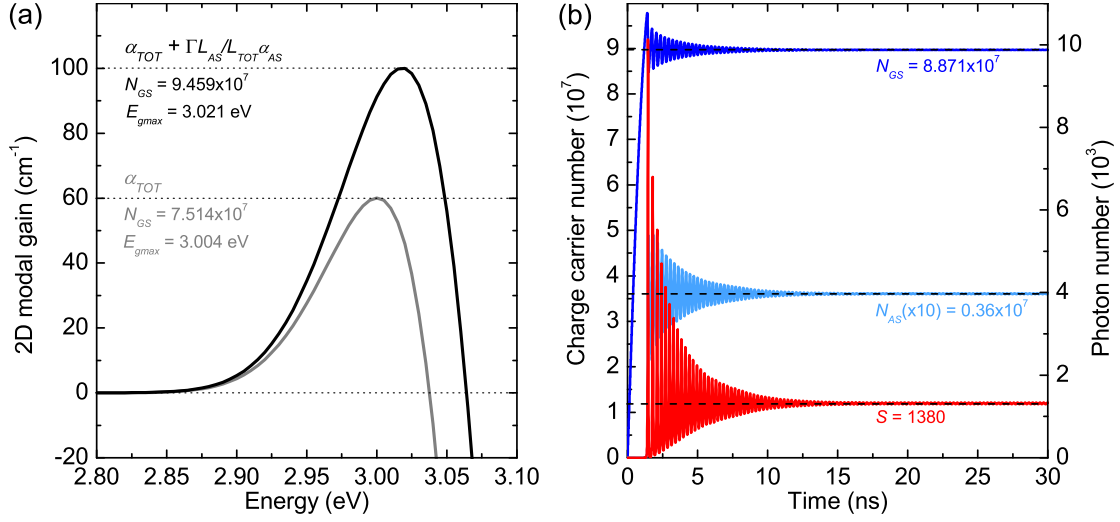


Figure 2.11: Wavelength-dependent model. (a) Optical modal gain spectra $\Gamma \frac{L_{GS}}{L_{TOT}} g_{GS}$ for a single $\text{In}_{0.1}\text{Ga}_{0.9}\text{N}/\text{In}_{0.01}\text{Ga}_{0.99}\text{N}$ QW calculated from eq. 2.13 for a 2D-DOS with $E_{inh} = 50$ meV. The horizontal dotted lines represent the total cavity losses α_{TOT} and absorber losses $\Gamma \frac{L_{AS}}{L_{TOT}} \alpha_{AS,th}$, respectively. (b) Dynamic solution of the rate equations 2.54-2.56 for a GS charge carrier population N_{GS} (blue), an AS charge carrier population N_{AS} (light blue) and for a photon population S (red). The gain g_{GS} has been evaluated at the energy $E_{gmax} = 3.021$ eV. The parameters are: $I_{GS} = 1.7 \cdot I_{th} = 22.24$ mA, $L_{AS}/L_{TOT} = 0.2$, $\alpha_0 = 200$ cm⁻¹, $\tau_{AS} = 0.25$ ns.

good agreement with the predictions. Indeed, it can be understood that a small amount of the population had to grow in the AS to compensate for the losses $\Gamma \frac{L_{AS}}{L_{TOT}} \alpha_{AS,th}$ of this section. The small residual difference between the predicted population and the actually clamped one results from the assumption that the carrier population compensating for the losses remains in the GS whereas the absorber in the AS interacts within the process and also fills itself accordingly. Therefore, the population N_{GS} for $\Gamma \frac{L_{GS}}{L_{TOT}} g_{GS,th}$ is slightly overestimated and E_{gmax} is slightly blueshifted. This overestimation is also supported by the fact that the discrepancy between the populations slightly increases with the carrier-free absorption α_0 . Note also that when shortening the absorber lifetime τ_{AS} , the respective amounts of N_{GS} and N_{AS} change (the AS filling process is slowed down thus N_{GS} gets higher and N_{AS} smaller) but $N_{GS} + N_{AS}$ remains constant. These results confirm the consistency of the wavelength-dependent model.

Figure 2.12 depicts the solutions of eqs. 2.54-2.56 in the case of the wavelength-dependent model at the energy $E_{gmax} = 3.021$ eV. All the parameters have been kept constant except for the absorber carrier lifetime τ_{AS} and thus the self-pulsating emission takes the form of (a) stabilized ROs and (b) Q-switching. The dynamic behavior is basically the same as for the linear model. Note that a shorter absorber carrier lifetime τ_{AS} has to be considered as the wavelength-dependent model possesses faster dynamics compared to the linear one. As the ABC-coefficients are higher, the gain carrier lifetime τ_{GS} is shorter and it is thus reasonable to take into account also a shorter τ_{AS} . On the other

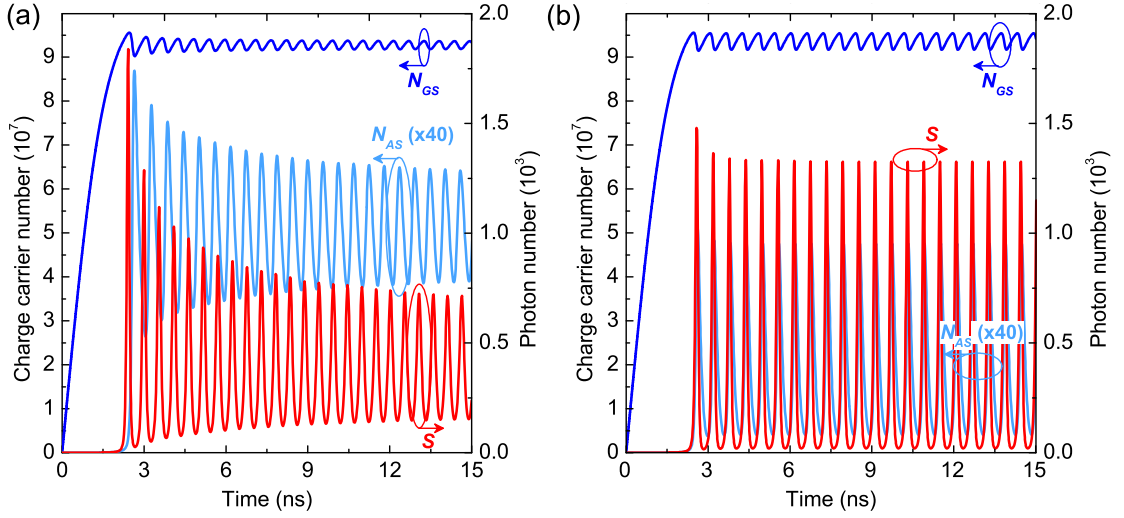


Figure 2.12: Wavelength-dependent model. Dynamic solution of the rate equations 2.54-2.56 for a GS charge carrier population N_{GS} (blue), an AS charge carrier population N_{AS} (light blue) and for a photon population S (red). SP takes the form of (a) stabilized ROs and (b) Q-switching. The gain g_{GS} has been evaluated at the energy $E_{g_{max}} = 3.021$ eV. The parameters are: $I_{GS} = 1.2 \cdot I_{th} = 15.7$ mA, $L_{AS}/L_{TOT} = 0.2$, $\alpha_0 = 200$ cm $^{-1}$, $\tau_{AS} = 0.25$ ns for (a) and $\tau_{AS} = 0.1$ ns for (b).

hand, in the wavelength-dependent model applied to MS cavities, the threshold current appears to be lower than in single-section cavities as we are considering a smaller gain cavity (by a factor L_{GS}/L_{TOT}) and consequently a smaller critical density. Note also that the carrier-free absorption α_0 considered here is higher than the one considered in the linear model. This is due to the smaller differential gain dg/dN implemented in the linear model compared to the wavelength-dependent one (see discussion concerning eq. 2.45).

To understand in details how populations interact within the cavity, Fig. 2.13 (top) displays a temporal magnification of Fig. 2.10 (a) around the first SP peak. On the other hand, Fig. 2.13 (bottom) represents the calculated recombination rates for each parameter in eqs. 2.54 and 2.55. In the same way as for the single-section LD described in Figs. 2.7 and 2.8, a constant electrical injection rate R_{inj} gradually fills the GS with charge carriers N_{GS} (blue curve). Of course, the carrier population in the GS is higher than the one in the single-section LD as the gain medium has to compensate for a higher absorption α_{AS} to reach the threshold. Once the threshold condition is reached, a photon population S (red curve) builds up in the cavity mainly due to the stimulated recombination process R_{st}^{GS} (red dotted curve). Then, the emitted pulse starts to deplete the GS carrier population N_{GS} and at the same time to optically pump the AS. Therefore, as the absorber is not electrically pumped, the absorber population N_{AS} (light blue curve) rises due to absorption as the stimulated recombination rate R_{st}^{AS} (orange dotted curve) is indeed negative. This partly saturates the absorber. After the pulse, so when the optical pumping provided by the GS is interrupted, the absorber stimulated process

R_{st}^{AS} starts to lose strength (e.g., around 3.75 ns in Fig. 2.13) and the photo-generated carrier population N_{AS} reaches its maximal amplitude. At this point, recombination processes R_{TOT}^{AS} , such as radiative recombinations and tunneling, deplete the absorber (the exponential decay of N_{AS} is indeed imposed by the value of τ_{AS} , e.g., 0.5 ns in Figs. 2.10 (a) and 2.13). The process then starts over again and again with a frequency of several GHz. If the absorber lifetime τ_{AS} is short enough to allow the absorber to recover its initial empty state (i.e., a fully carrier-free absorption), the emission takes the character of Q-switching. On the contrary, if the absorber is not completely depleted by R_{TOT}^{AS} , the absorber QW states remain partially filled and the subsequent pulse poses a lower photon population as the system can exploit more favorable (less absorption) threshold conditions. Then, self-pulsating emission takes the form of undamped ROs (see the case of Fig. 2.13).

When analyzing the SP curves, the most important characteristics are the turn-on delay time τ_{TOD} occurring to activate the pulsed emission, the photon population in the first

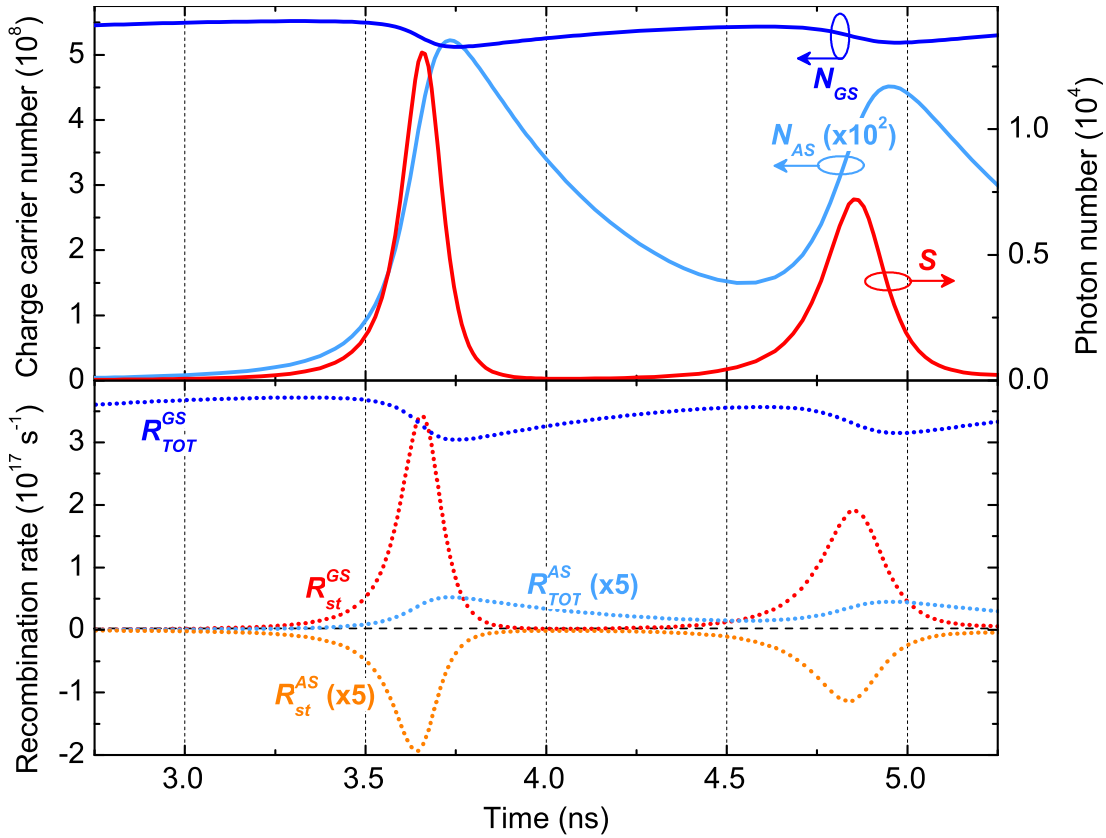


Figure 2.13: Linear model. (top) Temporal magnification of the stabilized ROs plotted in Fig. 2.10 (a). (bottom) Recombination rates R_{TOT}^{GS} (blue), R_{st}^{GS} (red), R_{st}^{AS} (orange) and R_{TOT}^{AS} (light blue) given in eqs. 2.54 and 2.55 as a function of time. The horizontal dashed black line represents a null recombination rate. The constant injection rate R_{inj} provided by a pump current $I_{GS} = 90$ mA amounts to $3.85 \cdot 10^{17} \text{ s}^{-1}$.

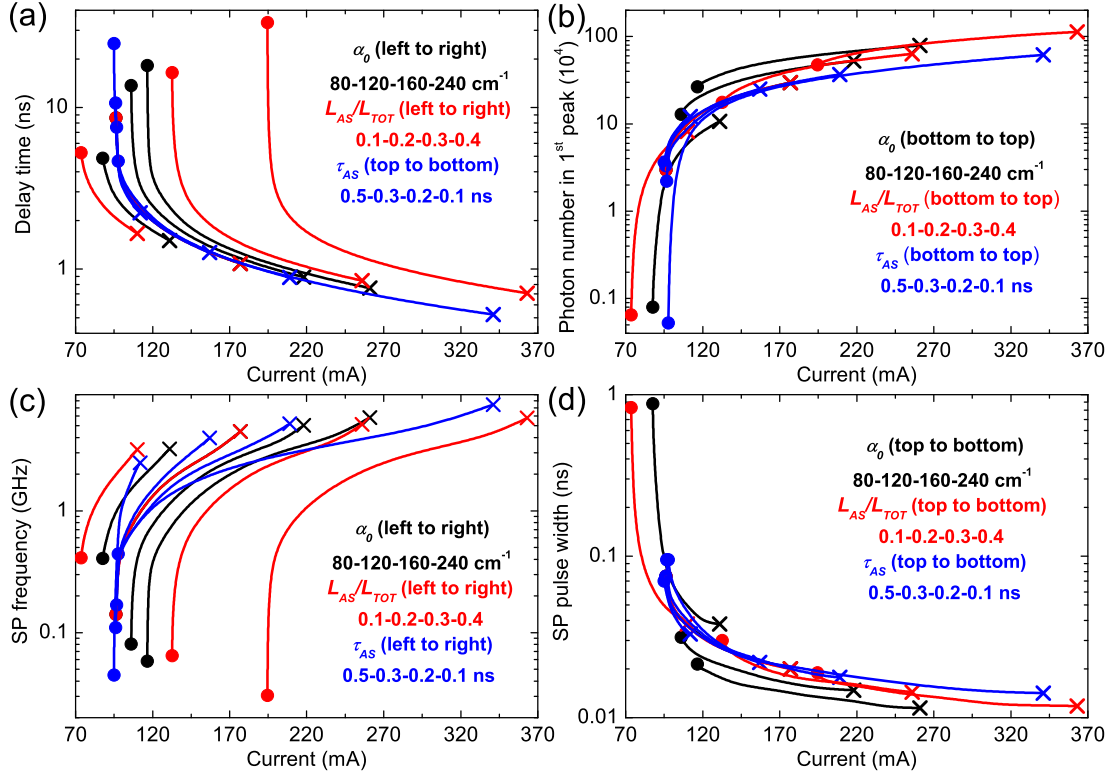


Figure 2.14: Linear model. (a) Turn-on delay time, (b) photon population of the first SP peak, (c) SP frequency and (d) pulse width of the first SP peak vs pump current and as a function of the carrier-free absorption α_0 (black), the ratio L_{AS}/L_{TOT} (red) and the absorber carrier lifetime τ_{AS} (blue). α_0 is evaluated for 80, 120, 160 and 200 cm^{-1} by keeping constant $L_{AS}/L_{TOT} = 0.2$ and $\tau_{AS} = 0.25$ ns; L_{AS}/L_{TOT} is evaluated for 0.1, 0.2, 0.3 and 0.4 by keeping constant $\alpha_0 = 120$ cm^{-1} and $\tau_{AS} = 0.25$ ns; τ_{AS} is evaluated for 0.5, 0.3, 0.2 and 0.1 ns by keeping constant $\alpha_0 = 120$ cm^{-1} and $L_{AS}/L_{TOT} = 0.2$. The circles represent the threshold condition while the crosses the quasi-steady-state.

peak of the self-pulsating oscillations (that can be easily related to the output power), the SP oscillation frequency f_{SP} and the temporal width of the first SP peak τ_{SP} . These quantities are plotted in Figs. 2.14 (a), (b), (c) and (d), respectively, as a function of the pump current in the case of the linear model. Note that the wavelength-dependent model gives qualitatively similar results. In Fig. 2.14 the circles represent the current at which the MS-LD reaches the threshold condition for the parameters considered whereas the crosses display the current for which the SP oscillations disappear and the quasi-steady-state is established. To control the SP emission we dispose then of three parameters in eqs. 2.54-2.56: the carrier-free absorption α_0 in α_{AS} , the absorber carrier lifetime τ_{AS} and the ratio L_{AS}/L_{TOT} between the absorber and the total cavity length. Hereafter, we will try to provide some short explanations on how each of these three parameters influences the SP. Note that during the simulations, α_0 and τ_{AS} have been considered as free parameters that can be arbitrarily changed. In fact, as we will see in

the next chapters, α_0 and τ_{AS} strongly depend on the absorber applied bias V_{AS} and therefore should not be considered independently. Nonetheless, thanks to the applied bias V_{AS} , we can adapt them *a posteriori* or “live” during the device operation. On the contrary, the ratio L_{AS}/L_{TOT} is decided *a priori* by the device geometry (see Sec. 2.4). First, *when increasing the pump current, the turn-on delay time decreases, the photon population rises, the SP frequency increases and the pulse width shortens* (Fig. 2.14). Concerning the turn-on delay time, it is obvious that the higher the injected current the sooner the threshold condition and the higher the emission intensity. Then, as previously discussed, for a higher pumping rate the absorber can rapidly reach transparency leading to a minimum amplitude between on-lasing and off-lasing states and thus to high-frequency undamped ROs [143]. The same holds for the pulse width as a high injection rate implies faster dynamics. On the other hand, as mentioned above, a too high GS injection rate prevents the establishment of SP as the absorber would be so highly optically pumped that it could not recover even a small amount of absorption (cf. crosses in Fig. 2.14).

Rate equations are solved for a *carrier-free absorption* α_0 of 80, 120, 160 and 200 cm^{-1} and by keeping constant the other parameters, i.e., $L_{AS}/L_{TOT} = 0.2$ and $\tau_{AS} = 0.25$ ns (black curves in Fig. 2.14). We see that for a given pump current, *a higher absorption corresponds to a longer turn-on delay time, a higher emission intensity, a lower SP frequency, and a shorter pulse width*. We can understand this as follows. To reach the threshold condition (eq. 2.53), a higher amount of absorption in the AS to be compensated delays the onset of lasing. At the same time, this leads to higher carrier and photon populations in the cavity, which slows down the train of pulses that is possible to develop with the same amount of pump current. Finally, as the leading and the trailing edges of the pulse are the most absorbed parts, a higher α_0 corresponds to a sharper pulse and thus to a shorter pulse width. Note that a higher absorption also implies a higher threshold current (circles) and at the same time it considerably broadens the range of pump currents where stable SP can be achieved (crosses).

Then, rate equations are solved for an *absorber/cavity length ratio* L_{AS}/L_{TOT} of 0.1, 0.2, 0.3 and 0.4 and by keeping constant the other parameters, i.e., $\alpha_0 = 120$ cm^{-1} and $\tau_{AS} = 0.25$ ns (red curves in Fig. 2.14). We see that for a given pump current, *a higher ratio corresponds to a longer turn-on delay time, a smaller SP frequency and a higher threshold current but the emission intensity and the pulse width remain almost unchanged*. In particular the threshold current rises with the ratio L_{AS}/L_{TOT} . By increasing the absorber ratio, a larger portion of the cavity experiences the same carrier-free absorption α_0 given in α_{AS} whereas a shorter portion of the cavity exhibits the same amount of gain given by g_{GS} (see eq. 2.53). The absorption and gain densities are changed accordingly and the system has to compensate for a larger absorbing region with a shorter amplifying one to reach the threshold condition. This delays the lasing emission and slows the dynamics. However, it is the effective ability to absorb light imposed by α_0 that allows later the intensity to rise and the pulse width to shorten. No matter how long is the absorbing region, at all times the absorbing reservoir is imposed by α_0 and not by

L_{AS}/L_{TOT} .

Finally, rate equations are solved for an *absorber carrier lifetime* τ_{AS} of 0.5, 0.3, 0.2 and 0.1 ns and by keeping constant the other parameters, i.e., $\alpha_0 = 120 \text{ cm}^{-1}$ and $L_{AS}/L_{TOT} = 0.2$ (blue curves in Fig. 2.14). We see that for a given pump current, *a shorter carrier lifetime corresponds to a lower SP frequency whereas the turn-on delay time, the emission intensity, the pulse width and the threshold current remain almost unchanged*. A shorter absorber lifetime allows the AS to faster recover its initial carrier-free state leading to slower dynamics. Otherwise, the absorber lifetime mainly stabilizes the pulsed emission over a wider range of pump currents.

It is worth noticing that a very high amount of carrier-free absorption (given by a high α_0 or a high L_{AS}/L_{TOT}) would even inhibit lasing although the gain medium in the cavity is beyond the transparency condition. The amount of losses is so high that the gain could never compensate for them and the device is in the optical amplification regime or the so-called superluminescent regime. Such devices called superluminescent LEDs (SLEDs) are obtained by either tilting the ridge waveguide at a certain angle with respect to the cleavage plane thus killing the optical feedback [144, 145] or by inserting in the cavity a passive section that acts as a strong absorber [40]. Especially, the latter is particular interesting for our subject as it implies that a MS-LD operating under high carrier-free absorption rates can be used as an SLED.

2.4 Microfabrication process

The processing of the GaN-based devices fabricated during this thesis is carried out in the class 10000 clean room of the ICMP at EPFL. In this section, the design of the photolithography masks and the technological steps involved in the microfabrication process of the devices are briefly described.

2.4.1 Design mask layers

Three generations of photomasks have followed in the course of this thesis (Fig. 2.15). Devices with an absorber in the center or at the edge of the cavity have been both designed. Typically 600 and 800 μm -long devices are the most common. Thus if mode-locked, these LD devices would show very large cavity round-trip frequencies, in the range of hundreds of GHz [89]:

$$\omega_{cav} = \frac{Mv_g}{2L_{TOT}} \quad (2.59)$$

where M is the number of multiple pulses in the cavity. Longer devices have been considered in order to lower the emission frequencies and thus to facilitate data acquisition. The absorber length L_{AS} is the technological parameter that influences the most the dynamic characteristics of a MS-LD, therefore careful attention should be paid when

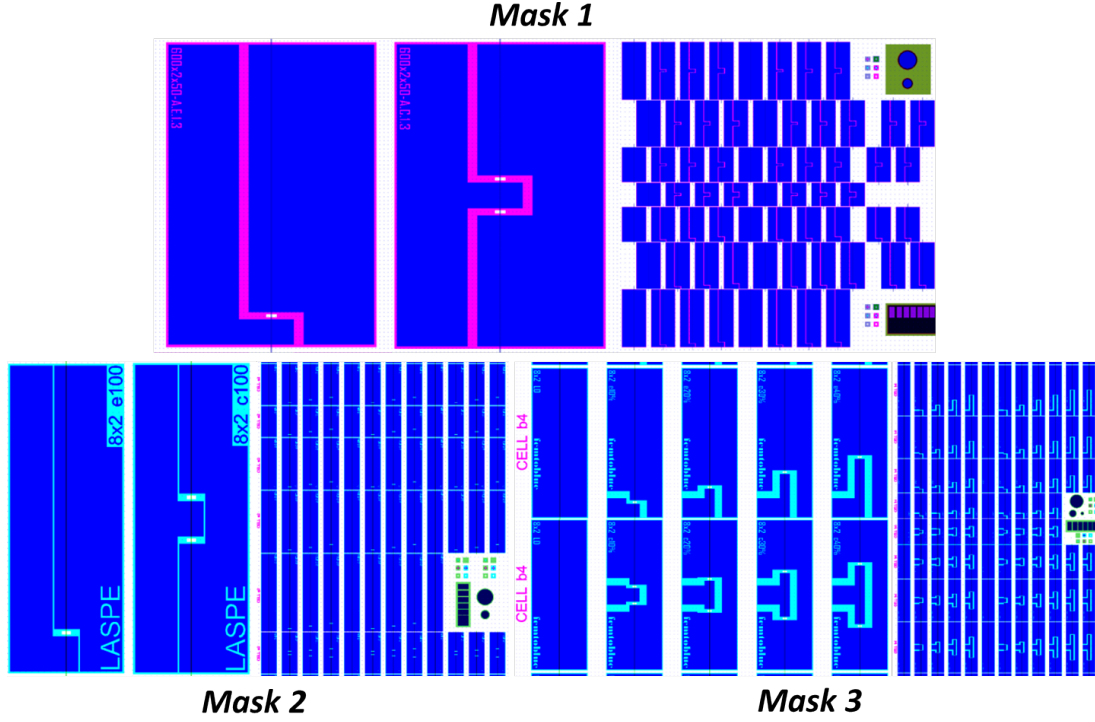


Figure 2.15: Layout of the photolithography quartz masks employed during the microfabrication process of the devices. On the left-hand side the layout of a single device (with edge/center-absorber geometry) and on the right-hand side the design of a unit cell are displayed. The size parameters for each set of masks are listed in Table 2.3.

designing its size. At the beginning of this thesis we decided to keep this parameter not too long ($< 100 \mu\text{m}$, see Mask 1 in Table 2.3). Afterward, improvements in the growth quality, optimizations in the microfabrication process and the better understanding of InGaN-based MS-LDs allowed us to increase L_{AS} even up to half of the cavity length (see Mask 3 in Table 2.3). Indeed, a longer absorber would enable to reach higher values of the differential absorption coefficient. Moreover, starting from Mask 2, the absorber contact area is decreased to a $100 \mu\text{m}^2$ square pad. This modification has been introduced to reduce parasitic resistance noise during high-frequency operation under active and hybrid mode-locking.

Concerning the ridge width w , too narrow laser stripes may encounter photolithography resolution limits (the AZ5214 photoresist used has a resolution of $\sim 1 \mu\text{m}$) and increase light scattering while too large stripes may cause a multi-(transverse) mode emission [146]. For this reason, laser ridges of $2\text{-}10 \mu\text{m}$ wide have been designed.

2.4. Microfabrication process

	Mask 1	Mask 2	Mask 3
L_{TOT} [mm]	0.4, 0.6, 0.8, 1	0.6, 0.8, 1, 1.2, 1.5	0.6, 0.8, 1, 1.2
L_{AS} [μm]	25, 50, 75	50, 100, 150	10%,20%,30%,40%,50% of L_{TOT}
w [μm]	2, 4, 6, 10	2, 3, 5	2, 3
<i>Geometry</i>	edge/center	edge/center	edge/center

Table 2.3: Characteristics of the different sets of masks employed during this thesis.

2.4.2 Clean room process

In this section the different techniques used during the microfabrication process in the clean rooms are briefly listed and described.

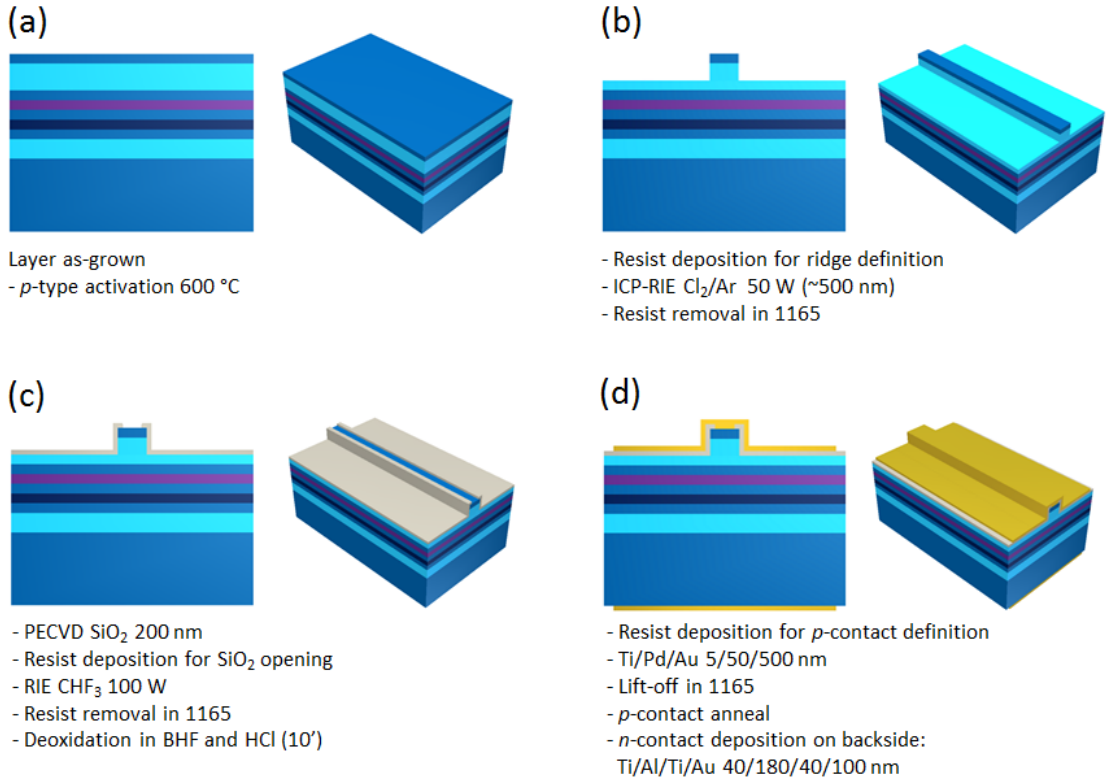


Figure 2.16: Step by step index-guided process of a standard single-section LD. The detailed layer structure is depicted in Fig. 2.2.

Sample cleaning

The surface of the sample may be contaminated by exposition to air and/or various chemicals deposited during each processing step, such as photoresist, dust,... A cleaning treatment is therefore required in order to re-establish a clean and residue-free surface. These treatments are not listed in Fig. 2.16 as they are continuously repeated before and after each processing step. Typical cleaning procedures are:

- rinse for several minutes in AMI solvents (acetone, methanol, isopropanol in this order) in an ultrasonic bath at moderate vibration power;
- N₂ blow drying;
- oxygen plasma at 100 W for several minutes (removal of organic particles).

Photolithography

Photolithography is the most common and basic processing step to define specific geometries during the fabrication of a semiconducting device and it is used to open particular windows in the photoresist, i.e., a thin organic polymer sensitive to UV light. Each photomask belonging to a set of masks (described in the previous section) is related to a single photolithography step of the whole process procedure, such as, e.g., the definition of an etching pattern or a metal contact.

The photolithography step consists in the deposition on the sample surface of a photoresist. The thickness of this resist layer is controlled using a rotation spinner that also ensures good homogeneity. Then, the sample is placed in contact with the photomask and exposed to UV light. In the case of a positive resist, the illuminated areas (uncovered by the photomask) become soluble and are removed by means of a specific solvent (the developer). On the contrary, in the case of negative resist, the soluble areas are the ones not exposed to UV light.

The photoresist used during this thesis is the Shipley AZ5214. It can act as a positive resist or also as a negative one after an image reversal at 115 °C and can be easily removed by acetone or by the 1165 remover. Typically, a spinning rotation of 5000 rpm gives a 1.4 μm thick layer and a lithography resolution of $\sim 2 \mu\text{m}$. The developer used for the development is MF319 and the mask-aligner is a Karl Süss MJB-3 with an alignment precision of $\sim 1 \mu\text{m}$. The adherence of the resist is improved by the use of a primer (e.g., hexamethyl-dizane, HMDS) before spinning the photoresist on dielectric layers such as SiO₂.

III-nitride etching

During the microfabrication process, III-nitrides must be etched for several reasons: for horizontal carrier confinement, for optical confinement, for accessing the underlying layers or for the removal of specific layers. For the development of index-guided LDs, dry etching in a Sentech inductive coupled plasma-reactive ion etching (ICP-RIE) SI 500 is performed under Cl₂ and Ar gas flow. Typical etching rates are 80 nm/min for a 50 W source power. The *p*-type layers are partially etched (only a narrow ridge is left intact) almost down to the interface of the AlGaN top cladding layer and the InGaN waveguide layer [Fig. 2.2 and 2.16 (b)], which corresponds to a so-called *shallow etch*. This etching is particularly important in index-guided lasers as it defines the structure of the optical waveguide as discussed in Sec. 2.1.2. Note that wet etching of GaN is extremely difficult as III-nitrides are quite chemically inert (at least on Ga polar face, which is the growth face of the layers).

Dielectric deposition and etching

Dielectric films can be used for the realization of SiO_2 masks for process steps requiring a sharp and precise etching of the nitride alloys. Indeed, abrupt and smooth sidewalls are very difficult to obtain with standard photoresist masks due to imperfect UV illumination and development of the resist. However, the most important and common employment of dielectric layers is to provide electric isolation between the p -type layers and the metallic contacts when required. This application is called *passivation*. In this thesis, the dielectrics are deposited by means of an Oxford PlasmaLab 100 plasma-enhanced chemical vapor deposition (PECVD) reactor. To form the SiO_2 -based insulating layer, plasma-activated gaseous precursors such as SiH_4 and NO_2 are used. CHF_3/Ar -based RIE is employed to open the isolation layer and thus to form an access for the contact pads [Fig. 2.16 (c)]. Wet etching (e.g., using BHF) is sometimes preferred to dry etching as it is a much simple and rapid procedure although it does not allow to obtain very abrupt sidewalls.

Metal deposition

The deposition of metallic layers such as p -type and n -type contacts/pads is realized by means of an electron beam deposition system in an ultra high vacuum chamber and is extremely homogeneous. Concerning the p -contact, the metal evaporation is preceded by a photolithography step so that, after the metal deposition, the resist, and hence also the unwanted metal covering it, is removed by acetone or 1165 by a procedure called *lift-off*. As a result, the metal layer only remains in the areas where the resist has been removed during the development [Fig. 2.16 (d)].

In the particular case of MS-LDs, the p -type electrodes of the gain and absorber sections are separated by a $15\text{ }\mu\text{m}$ wide contactless gap [Fig. 2.17 (b)]. A specific metal etch step has been performed to ensure electric isolation between the sections by using both a wet ($3\text{HCl}:1\text{HNO}_3$) and a dry (RIE plasma Ar) etch. Note that other groups have performed also an etch of the underlying semiconductor layers to obtain an even better electrical isolation [12]. In fact, such a separation is not necessary and risks to damage the optical waveguide.

Finally, facets are obtained by cleaving the wafer along crystallographic planes. No additional coatings have been added. Standard single-section LDs are fabricated together with MS-LDs during the same process flow and from the same epiwafer for the sake of comparison [Fig. 2.17 (a)].

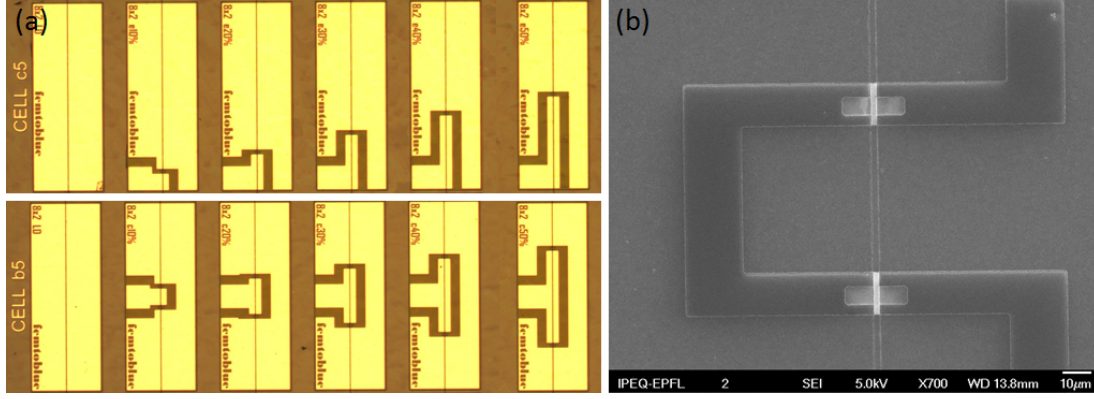


Figure 2.17: (a) Top-view of an $800 \times 2 \mu\text{m}^2$ index-guided MS-LDs processed with Mask 3 (top: edge-absorber; bottom: center-absorber). (b) Scanning electron microscope (SEM) image of the $15\text{-}\mu\text{m}$ long regions separating the gain and the absorber sections in the case of a triple-section device.

Summary of the results

In this chapter, we reviewed the main characteristics of the active region of a III-nitride-based epitaxial growth. To simulate the dynamic evolution of a MS-LD, we modified the standard laser rate equations. A theoretical model that also takes into account the spectral dependency of the gain in the active region (the wavelength-dependent model) has been developed with a particular attention paid to the *ABC*-coefficients accounting for the dependency of the charge carrier lifetime τ on the carrier population N . The theoretical values considered (in 3D notation) are $4.2 \cdot 10^7 \text{ s}^{-1}$ for A , $2 \cdot 10^{-11} \text{ cm}^3 \text{ s}^{-1}$ for B and $1.638 \cdot 10^{-30} \text{ cm}^6 \text{ s}^{-1}$ for C . As we will see in the next chapters, this model is in excellent agreement with experimental results. The special configuration of MS-LD cavities allows then to control and explore different pulsation mechanisms via tuning of the absorber/cavity length ratio L_{AS}/L_{TOT} , the carrier-free absorption α_0 and the carrier lifetime τ_{AS} in the AS. SP under the form of stabilized ROs and Q-switching have been reproduced. Simulations predict higher output powers and shorter pulse widths when increasing both the carrier-free absorption α_0 and/or the pump current I_{GS} . Low-frequency but more stable pulsation regimes are expected for a higher L_{AS}/L_{TOT} ratio, a stronger carrier-free absorption α_0 , a shorter lifetime τ_{AS} and a lower pump current I_{GS} . Depending on the driving conditions, the turn-on delay time τ_{TOD} amounts to several nanoseconds, the SP oscillation frequency f_{SP} to several gigahertz and the temporal width of the first SP peak τ_{SP} to several tens of picoseconds. SP is eventually lost and quasi-steady-state cw operation is established if the absorber cannot recover an adequate value for carrier-free absorption to generate stable pulsations, i.e., corresponding to low α_0 , small L_{AS}/L_{TOT} , long τ_{AS} and high I_{GS} values.

3 Multi-section laser diodes: static characteristics

In this chapter, the main “static” characteristics of III-nitride-based MS-LDs are presented. We will show that due to the built-in polarization field \mathbf{F}_{int} (unavoidable in InGaN heterostructures grown along a c -plane), the shift of the optical absorption edge in the absorber can be largely tuned via the QCSE. The absorption behavior is detailed vs. an external applied voltage that modifies the net-field \mathbf{F}_{QW} across the heterojunction. Then, the impact of the applied bias on the macroscopic static characteristics such as the threshold current, the lasing wavelength, and the lasing bistability is described.

3.1 Epi-wafer mapping

Before describing the main static characteristics of the LDs processed during this thesis, it is worth presenting how these characteristics spatially evolve across the wafer in order to check the data dispersion and see how reliable will be the data analysis.

In Fig. 3.1, mappings of the most important properties of sample A1902 are shown. Before the process, RT PL images have been taken around the QW emission energy with an He:Cd laser emitting at 325 nm and with a spot size of 100 μm . The peak intensity [Fig. 3.1 (a)] and the emission wavelength [Fig. 3.1 (b)] show a clear radial symmetry, with a low intensity and short wavelength region located close to the center of the wafer. Both growth and substrate quality can influence the homogeneity of the sample characteristics. As previously mentioned, contrary to silicon or even GaAs, it is challenging to grow bulk GaN substrates. So far, one of the best techniques providing good quality wafers consists in growing GaN on another material (for example sapphire or GaAs) and then to remove it to obtain a so-called FS GaN substrate. In most cases, FS GaN substrates exhibit slightly different crystal plane orientations, which impact the surface morphology and therefore the indium incorporation. Another important source of inhomogeneities is the bowing of the substrate, which develops during the growth. In fact, when growing materials with different lattice parameters and different thermal expansion coefficients than GaN (such as, e.g., AlGaN or InGaN, see Table 1.1) on top of a GaN

substrate, the wafer tends to bow due to elastic energy that develops. Then, the bow changes the thermal contact between the substrate and the reactor susceptor. This will in turn induce temperature inhomogeneities across the wafer during the growth, which can influence the indium incorporation in the MQWs (the impact of growth temperature variations arising from barrier composition is much smaller).

Unfortunately, the wafer inhomogeneities do not only affect the morphological and optical properties of the sample but also the electrical characteristics. Figures. 3.1 (d)-(f) show the mappings of specific properties of the L - I - V curves such as the voltage at 100 mA, the current at the lasing threshold and the slope efficiency, respectively, for an $800 \times 2 \mu\text{m}^2$ single-section LD. When comparing (d)-(f) to (a)-(b), there is a good correlation between L - I - V and PL mappings: the high-voltage, high-threshold and low-slope-efficiency regions (poor electrical characteristics) are related to the low-intensity and low-wavelength regions (poor optical characteristics), and *vice-versa* for the “good” ones. Note that the wafer quality and the resulting bowing also hinder the proper cleavage of the laser bars along the right crystallographic planes thus reducing the number of devices available for testing. Of course, this inhomogeneity of the characteristics over the whole wafer goes to the expense of the reproducibility of the growth conditions from one sample to another. On the other hand, it allows to study on a single wafer devices showing very different characteristics.

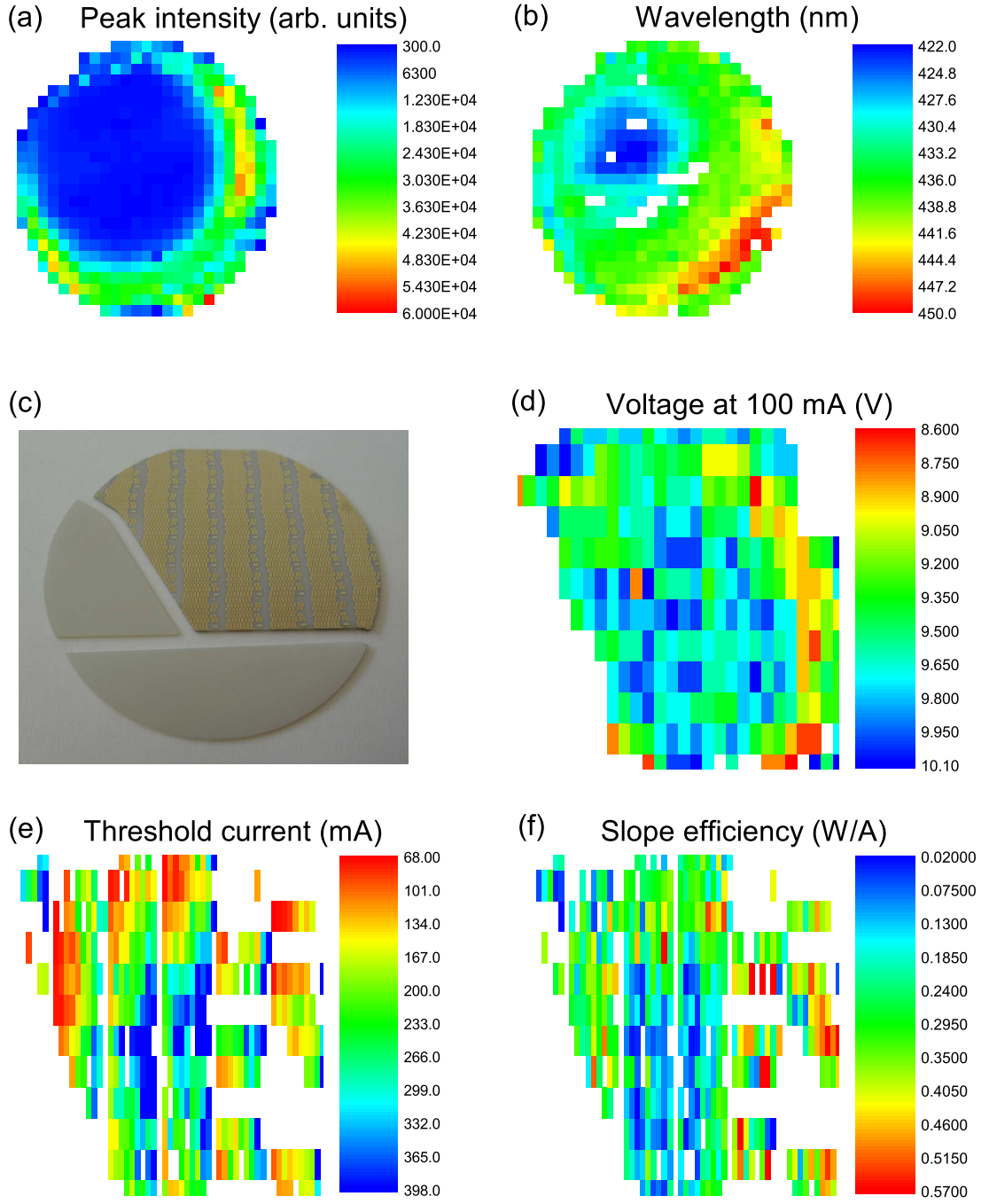


Figure 3.1: PL mappings of sample A1902 for (a) the peak intensity and (b) the peak wavelength at the QW emission. (c) Picture of the unprocessed (bottom) and processed (top) pieces of sample A1902. The photolithographic steps have been performed using Mask 1. (d) Measured voltage at 100 mA, (e) current at the lasing threshold and (f) slope efficiency for an $800 \times 2 \mu\text{m}^2$ single-section LD.

3.2 Internal polarization field

Usually, under dynamic operations, a MS-LD is driven with a forward bias on the GS whereas the AS is reverse-biased. In the next two sections, we will concentrate our attention on how the external field F_{ext} applied to the absorber modifies the internal polarization field F_{int} and how this will impact the absorption features of the AS.

To better understand the absorption features in reverse-biased InGaN MQWs, we computed the lowest interband transition energy and wavefunction overlap of electron-hole pairs in the well as a function of the AS applied bias V_{AS} . As shown by our analysis, the carrier density in the absorber under lasing operation (bleached absorber) is relatively high. Therefore, we can safely neglect any excitonic absorption contribution [137]. The electric field in the MQWs comes partly from the p - n junction field F_{ext} , which depends on the built-in potential Ψ_{bi} , and on the external applied bias V_{AS} (see eq. 1.21). The width of the intrinsic region d_u was assumed to only originate from the width of the last barrier on the p -side (see Table 2.2). In addition, as discussed in Chap. 1 in the particular case of III-nitride materials grown along the polar c -axis, one should also consider an additional field F_{int} arising from the piezoelectric and spontaneous polarization mismatch at the heterointerfaces (see eq. 1.13). Thus, the total net internal electric field in the MQW structure is obtained by summing all these contributions (eq. 1.22). Since under reverse bias the current is small, we neglect the voltage drop in the strongly p - and n -doped cladding regions of the laser heterostructure. To evaluate the contributions from the different terms in eqs. 1.4 and 1.13, we followed the approach described in Ref. [26] and we use the general assumption that the InGaN/InGaN QWs are pseudomorphically strained on the GaN epilayer.

As shown in Fig. 3.2 for sample A2109, a reverse bias V_{AS} modifies the internal electric field F_{int} across the band structure thus tilting the QW potential profile. At a bias

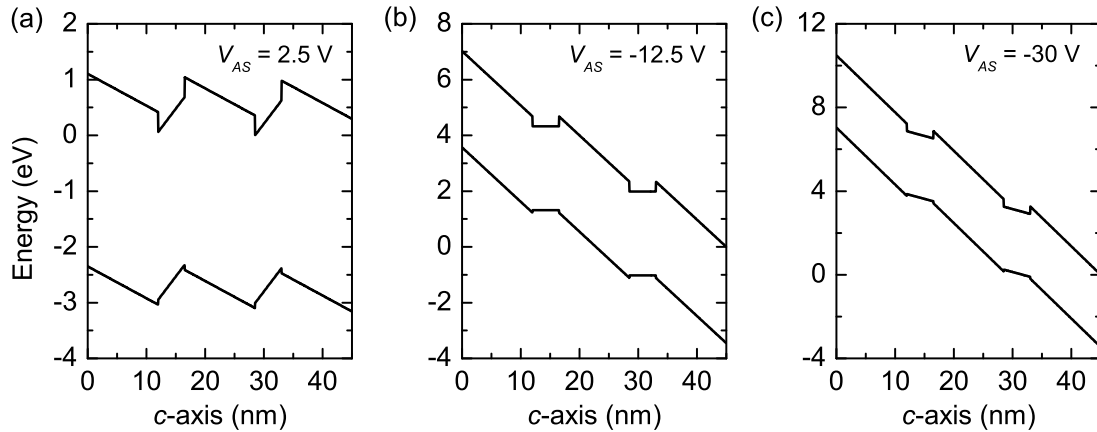


Figure 3.2: Band profile calculations at (a) 2.5 V, (b) -12.5 V and (c) -30 V absorber bias voltage V_{AS} for the active region of sample A2109. For the sake of simplicity, only the active region has been simulated. Note that in the figures, the p -side of the heterojunction is on the left.

voltage of about -12.5 V the QWs recover their rectangular-shaped profile indicating that flat-band conditions, for which the external field F_{ext} fully compensates F_{int} , are achieved [Fig. 3.2 (b)]. The bias V_{AS} at which this compensation occurs strongly depends on the design of the active region. The most sensitive parameters are, e.g., the doping concentrations of the heterojunction and those of the active layers, the intrinsic width d_u , the QW width, the indium content of the QWs and that of the barriers. Note that for $V_{AS} = -30$ V the QW band profile is tilted in the opposite direction compared to the initial situation [see Fig. 3.2 (a) and (c)]. Driving the device under large negative voltages V_{AS} would thus highly reduce the potential barriers that confine the carriers in the well, denoted E_{CBO} and E_{VBO} for the conduction and valence band offsets, respectively [see Fig. 2.1 (a)]. This will shorten the carrier lifetime, as we will see in Sec. 4.1. Note that the strong potential drop in Fig. 3.2 (c) (about 10 eV over nearly 45 nm) is due to the very high field F_b experienced by the well barriers at such large bias voltages (e.g., $F_b = 2.7$ MV/cm at $V_{AS} = -30$ V for sample A2109).

The evolution of the electric field, transition energy, and wavefunction overlap as a function of the absorber bias V_{AS} are plotted in Fig. 3.3 for sample A2109 and C128. Note that all the calculations have been carried out in the case of a single QW instead of two as the simulation of confined states that we have developed is not reliable in the case of a MQW system. As expected, sample A2109 with a higher indium contrast between the MQWs and the barriers (see Table 2.2) exhibits stronger polarization effects. In Fig. 3.3 (a), the net internal electric field F_{QW} in the active region as a function of V_{AS} is reported. With increasing negative absorber bias V_{AS} , F_{QW} increases from an initial negative value imposed by the built-in polarization field F_{int} (dotted lines). The calculated built-in fields are about $F_{int}^{A2109} = -1.57$ MV/cm and $F_{int}^{C128} = -0.88$ MV/cm, for the two MQW laser heterostructures with low and high barrier indium content, respectively. The net electric field in the MQWs F_{QW} vanishes at an external bias of -12.5 V and -2.5 V for samples A2109 and C128, respectively, indicating that flat-band conditions are achieved [Fig. 3.3 (b)] [12, 131]. At these biases, the oscillator strength is maximal. By shifting the bias away from these values, the QCSE separates the electron and hole wavefunctions on opposite sides of the well thus causing a reduction in the overlap and in the transition energy [131, 147]. Note that the thickness of the depletion region calculated by using eq. 1.20 amounts to 20 nm at 2.5 V and to 260 nm at -30 V. For biases lower than 1.5 V, its extension entirely drops in the active layers (i.e., 45 nm), thus allowing to discard the presence of free-carriers in the QW region under reverse bias conditions.

As we will see in the next sections, by adjusting the net-field F_{QW} in the AS it is possible to change the internal absorption of the device and hence the laser output characteristics.

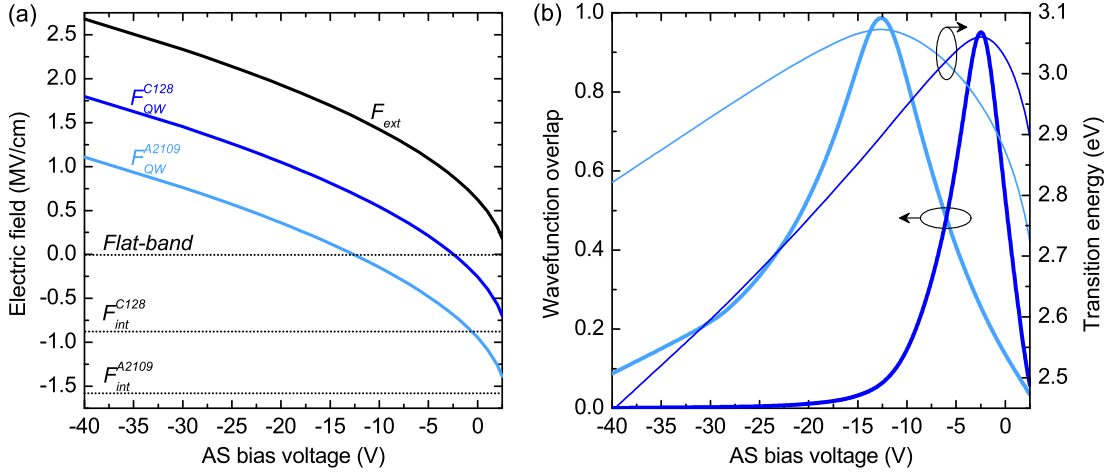


Figure 3.3: (a) Calculated electric fields in the MQWs, (b) wavefunction overlap (thick lines) and transition energy of the electron-hole transition (thin lines) as a function of absorber bias V_{AS} for samples A2109 (light blue) and C128 (dark blue). The dotted horizontal lines in (a) correspond in turn to the flat-band field ($F_{QW} = 0$) and to the polarization fields for samples A2109 and C128 (F_{int}^{A2109} and F_{int}^{C128} , respectively). Note that transition energies of the two structures for flat-band conditions differ by 10 meV.

3.2.1 Electro-reflectance on standard LED structures

To further inquire how the external field modifies the internal polarization field, we performed electro-reflectance (ER) spectroscopy on standard InGaN/GaN structures processed as LEDs. A study on the InGaN QW properties based on ER spectroscopy technique is presented in more details in Appendix A. ER is an external modulation spectroscopy technique in which a modulated electric field including a possible DC offset is applied to the sample [148]. In the ER setup that we have developed the presence of an electric field applied perpendicularly to the surface of the sample lifts degeneracies inside the energy band structure. Then, the spectra obtained by modulation spectroscopy are the superposition of the lineshapes corresponding to each critical point of the sample under investigation. To extract the position of each critical point, an advanced fitting procedure is required and details can be found in Ref. [148]. By looking at the reflectance changes $\Delta R/R$ one can understand how the sample responds to a moderate excitation by means of a quasi-monochromatic source [149]. The transmission changes can then be correlated to absorption changes via the complex dielectric function $\varepsilon(\omega)$ [150].

Fig. 3.4 (a) shows the ER spectra of an $\text{In}_{0.13}\text{Ga}_{0.87}\text{N}/\text{GaN}$ LED structure with 3 2.3-nm wide QWs and 11-nm wide barriers (sample C182) for biases ranging from 1 V down to -23 V. In order to analyze the optical transition of the sample, the ER spectra are fitted as 2D confined Lorentzian-broadened band-to-band transitions for several critical points (i.e., the main transition energies): QWs, well barriers, and GaN cap layer transitions. The highest energy critical point does not depend on the applied bias as can be seen from Figs. 3.4 (a) and 3.4 (b) (blue circles). This transition energy at 3.4 eV corresponds

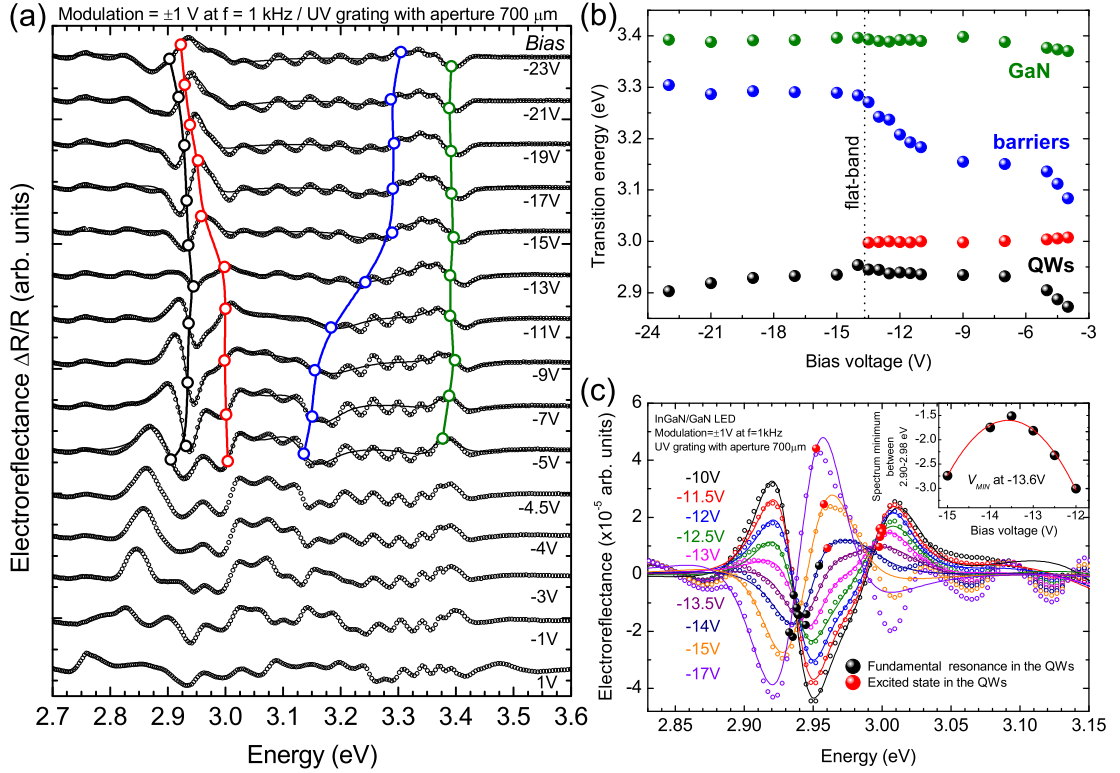


Figure 3.4: (a) ER spectra of an InGaN/GaN MQW LED structure for different applied biases (sample C182). (b) Critical points extracted from (a). The critical point with the highest energy does not depend on the applied bias and is associated to transitions occurring in the GaN cap layer (green circles). The two critical points of lower energy are related to the fundamental resonance of the QWs and its first excited state (black and red circles, respectively). The critical points of intermediate energy are more likely related to well barrier emission (blue circles). Critical points of ER spectra for biases larger than -5 V have not been extrapolated as the fitting procedure is not reliable anymore around the fundamental resonance mainly because of the weaker phase oscillations. (c) Determination of the flat-band voltage of the InGaN/GaN MQWs LED structure. The phase of the fundamental resonance in the MQWs switches sign between -13 V and -15 V [see (a)], which indicates that the flat-band voltage lies within this range. The inset shows the extrapolated V_{MIN} . [148]

to optical transitions occurring within the GaN cap layer as the applied bias is expected to have a stronger impact on the energies of the confined states [49]. The second highest energy critical point could then be ascribed to a transition somehow related to the GaN well barriers but its behavior with respect to the applied bias remains unclear [blue circles in Figs. 3.4 (a) and 3.4 (b)]. It may be that different critical points correspond to this transition [148]. The two remaining critical points represent the confined states in the MQWs. It is very likely that the lowest one corresponds to the fundamental resonance (black circles) while the highest one corresponds to an excited state within the QWs (red circles).

A maximal blueshift of the fundamental resonance energy is observed when approaching -13.5 V [black circles in Fig. 3.4 (b)]. Moreover, when looking at the ER spectra around the fundamental resonance it is obvious a phase flip for biases between -13 V and -15 V [Fig. 3.4 (a)]. Figure 3.4 (c) shows detailed ER spectra around the fundamental resonance (2.94 eV) in this bias range and a bias of -13.6 V is then extrapolated from the ER spectrum minima [inset in Fig. 3.4 (c)]. These features indicate that the MQWs are under flat-band conditions around this bias (hereafter referred to as V_{MIN}). Away from this bias, the MQWs start to be tilted into a triangular-shaped potential thus leading to a redshift of the emission [see also the simulated curves of the transition energy in Fig. 3.3 (b)] and to a phase flip in the ER signal.

3.3 Internal absorption coefficient

To interpret the absorption behavior of the AS under different bias conditions, absorption coefficient simulations in the effective mass approximation for a LD heterostructure have been performed following eq. 2.13 and setting the number of QWs (N_{QW}) to 1. As the carrier population for a specific bias V_{AS} is unknown, we only consider a “carrier-free” ($N = 0$) modal absorption for the first confined state according to eq. 2.21. Note that sometimes the charge carrier population is simply neglected for negative bias voltages as carriers are more easily swept out the active region [69]. We will analyze in more details this aspect in the upcoming sections dedicated to the dynamic behavior of MS-LDs. Otherwise, the DOS of the laser structure is approximated following eq. 2.22 and an inhomogeneous broadening of 50 meV is considered.

Figure 3.5 shows calculated modal absorption spectra in the case of a single QW ($N_{QW} =$

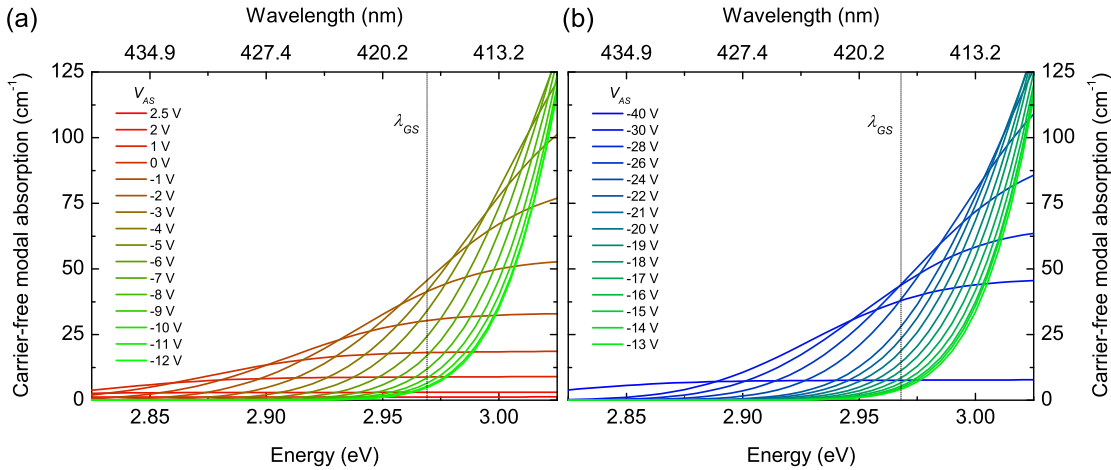


Figure 3.5: Simulated carrier-free modal absorption α_0 of sample A2109 for different absorber bias voltages and $N_{QW} = 1$: (a) from 2.5 V to -12 V and (b) from -13 V to -40 V. The inhomogeneous broadening is set to 50 meV. The dotted vertical line represents the typical wavelength (417 nm or 2.97 eV) at which the GS emits.

1) with the characteristics of sample A2109 for an inhomogeneous broadening of 50 meV. As shown in Fig. 2.2, the confinement factor Γ of the photon mode in the laser waveguide for sample A2109 is equal to 0.0148. The values for the wavefunction overlap and the transition energy at different absorber bias voltages have been calculated in the previous section and they are shown in Fig. 3.3. The absorption $\alpha_0(\hbar\omega)$ starts from a value of 0 for energies below the first permitted interband transition of the QWs and suddenly increases for higher energies, as depicted in Fig. 2.3 (dash-dotted black lines). A clear blueshift in the absorption edge is observed when approaching the flat-band conditions at $V_{AS} = -12.5$ V [Fig. 3.5 (a)] whereas a redshift is experienced by further increasing the reverse bias down to $V_{AS} = -40$ V [Fig. 3.5 (b)]. When extrapolating the absorption at the energy at which the GS emits, e.g., 2.97 eV, a rather complex behavior is observed (Fig. 3.6). As the absorber bias is reduced, the absorption first reaches a local maximum around -3.3 V and then a local minimum around -12.5 V for sample A2109. Note that the decrease in the absorption for biases larger than -26 V is an artifact. In such tilted structures, no stable confined states for carriers (especially holes) can be sustained as the apparent barrier width is comparable to the extension of the carrier wavefunction in the barrier thus leading to strong tunneling [see Fig. 3.2 (c)]. In reality, the absorption would continue to rise. Though, the calculated absorption minimum at $V_{AS} = -12.5$ V (hereafter referred to as V_{MIN}) corresponds to a maximum energy difference between the AS absorption edge and the GS energy emission E_{GS} [12, 131]. Indeed, at this bias, the absorption edge exhibits the strongest blueshift since flat-band conditions are achieved (Fig. 3.5) [130, 131, 140]. In other words, the maximal energy detuning is the dominant effect in eq. 2.13 as it strongly reduces the absorption between the absorber and the gain section despite maximal wavefunction overlap. We restrict this absorption study to the bottom of the absorption spectrum since the GS emission is located in this energy range (see also Hakki-Paoli gain spectroscopy measurements in Ref. [69]). On the contrary, the calculated absorption maximum at $V_{AS} = -3.3$ V (hereafter referred to as V_{MAX}) corresponds to a complicated trade-off between a stronger absorption when a negative bias is applied, due to a larger electron-hole wavefunction overlap and a moderate energy detuning between the GS emission and the AS absorption edge, respectively [see Figs. 3.3 (b) and 3.5] [131]. In other words, these two counteracting phenomena will have a maximum impact around V_{MAX} . As expected, V_{MIN} and V_{MAX} for sample C128 are shifted to lower biases. This shift is ascribed to a lower internal polarization field F_{int} [see Fig. 3.3 (a)] due to the higher indium content in the QW barriers: $F_{int}^{A2109} = -1.57$ MV/cm and $F_{int}^{C128} = -0.88$ MV/cm (see Table 2.2). Different internal fields result in different flat-band compensations. The inset of Fig. 3.6 depicts the band structure of the two samples.

To study the optical gain spectra in semiconductor materials, several methods have been employed, e.g., the variable stripe length method [151], the Hakki-Paoli technique [152] and cw transmission gain spectroscopy [153]. Among them, the most precise and widely used is the Hakki-Paoli method. Scheibenzuber working in the group of Prof. Schwarz at the Fraunhofer Institute in Freiburg has performed Hakki-Paoli gain spectroscopy

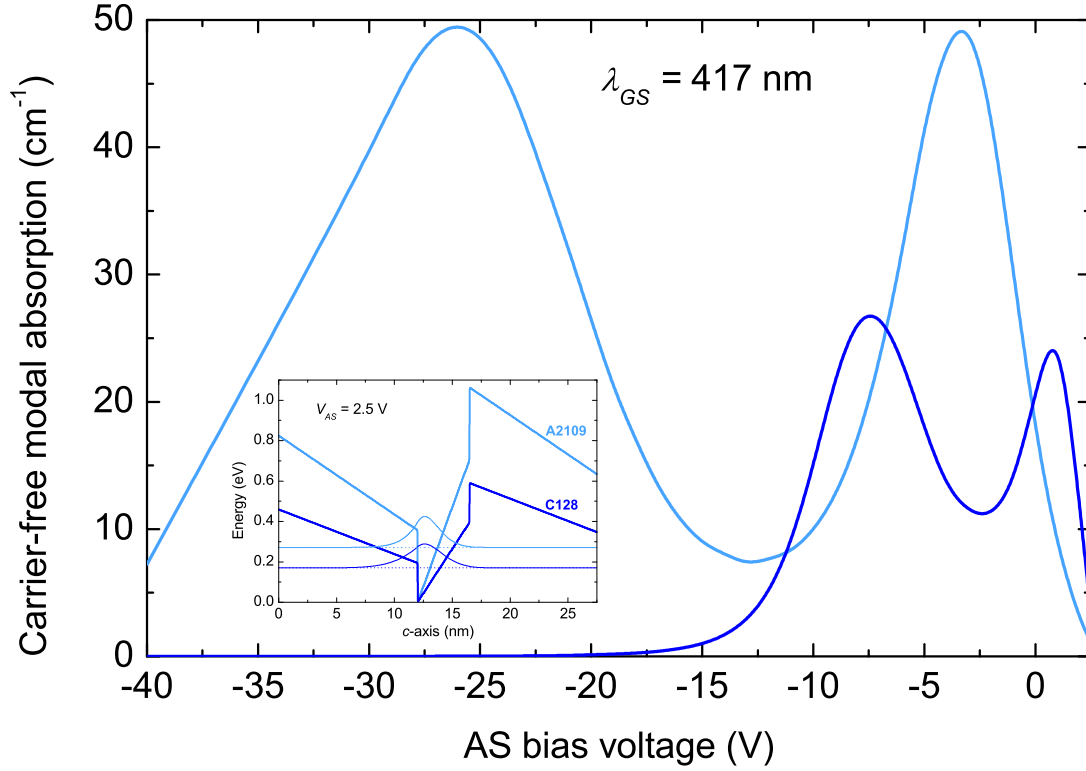


Figure 3.6: Calculated absorption at $E_{GS} = 2.97$ eV ($\lambda_{GS} = 417$ nm) as a function of V_{AS} for sample A2109 (light blue) and C128 (dark blue). The inhomogeneous broadening is set to 50 meV and the number of QWs N_{QW} to 1. The inset shows the conduction band structure for one QW of samples A2109 (light blue) and C128 (dark blue) with the respective electron wavefunction at an absorber bias voltage V_{AS} of 2.5 V.

measurements on several of our LDs during the Femtoblue project. The measurements have been published in Refs. [69] and [130] for sample A1902. The experimental values are in good agreement with the previously calculated absorption spectra as well as with the calculated maximum and minimum values of the absorption at the laser emission wavelength (see Fig. 3.7). Indeed, in Ref. [130], it is shown that the measured modal absorption exhibits a maximum at small negative bias while for larger negative bias it decreases.

The modal absorption given by Hakki-Paoli gain spectroscopy measurements reaches a peak value at V_{MAX} of 250 cm^{-1} , a factor four times higher than the simulated one (compare with Fig. 3.6). Note that the measurements depicted in Fig. 3.7 deal with sample A1902, i.e., $N_{QW} = 2$ and $d_{QW} = 3$ nm. The simulated curves obtained from eq. 2.13 for such parameters lead to an absorption of 200 cm^{-1} , much closer to the experimental case. The remaining discrepancy could then be ascribed to an imperfect way to simulate the InGaN band structure and the references used in the calculations.

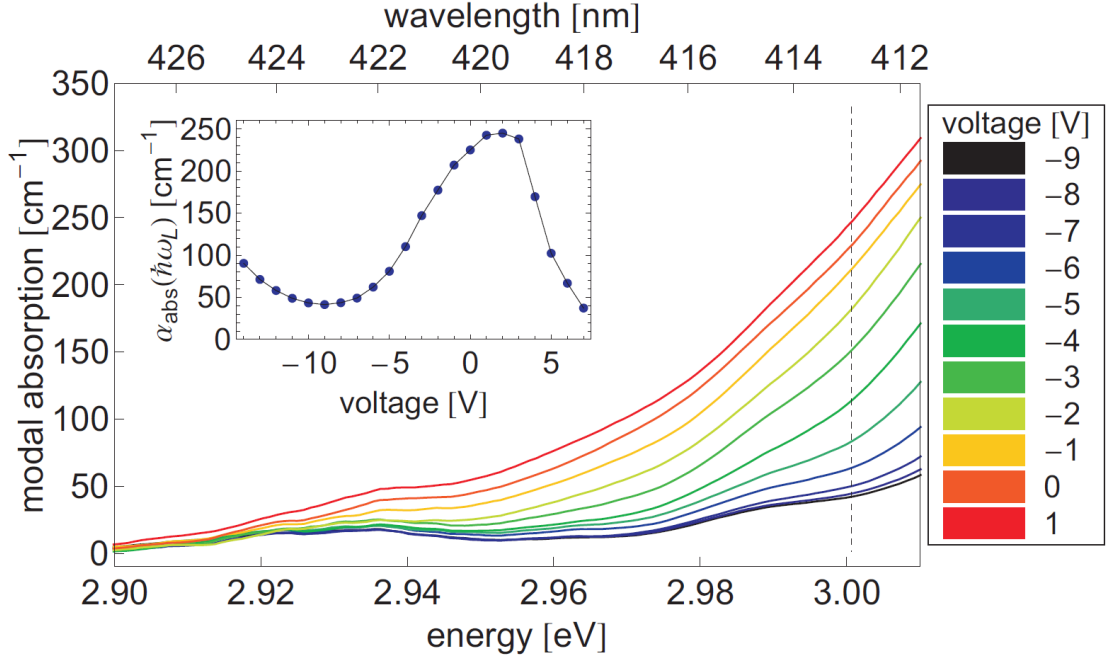


Figure 3.7: Measured absorption spectra at absorber bias voltages ranging from -9 to 1 V for sample A1902. The inset shows the absorption at the lasing wavelength of 413 nm as a function of the absorber voltage from -14 to 7 V. The picture is taken from Ref. [69].

3.4 L - I - V curves and threshold current

The typical L - I - V curves of MS-LDs fabricated from sample A2109 and C128 and measured under direct-current (dc) driving conditions for different absorber biases V_{AS} are shown in Figs. 3.8 (a) and (b) [131]. Around threshold, optical bistability is observed on the L - I - V curves. This feature will be described in more details in Sec. 3.6. It is obvious from Fig. 3.8 that the threshold current for lasing I_{th} is clearly not constant and shifts with V_{AS} . Also the slope efficiency is affected by V_{AS} and starts to decrease already at moderate negative bias voltages [e.g., $V_{AS} = -3$ V for sample A2109 in Fig. 3.8 (a)]. Samples C133 (3 QWs) and C134 (5 QWs) behave in the same way as a function of V_{AS} . In particular, sample C133 exhibits nearly the same characteristics than sample C128 (same I_{th} , slope efficiency and emission wavelength) whereas sample C134 shows worse properties because the electrical injection is not homogeneous across all QWs.

Figure 3.9 (a) displays the impact of V_{AS} on I_{th} for samples A2109 and C128. For sample A2109, when the AS is forward-biased, I_{th} decreases from 60 mA down to 37 mA since the device then behaves as a single-section LD. Conversely, for reverse-biased AS, I_{th} increases and reaches a maximum at $V_{AS} = -3$ V. A further increase in the reverse bias voltage causes I_{th} to decrease. A minimum I_{th} is obtained for $V_{AS} = -9.5$ V. For larger negative biases ($V_{AS} < -9.5$ V), I_{th} starts to increase again and becomes much larger than its value at $V_{AS} = 0$. Sample C128 exhibits similar features but shifted to smaller biases. Note that the induced photocurrent flowing in the AS, which amounts to several

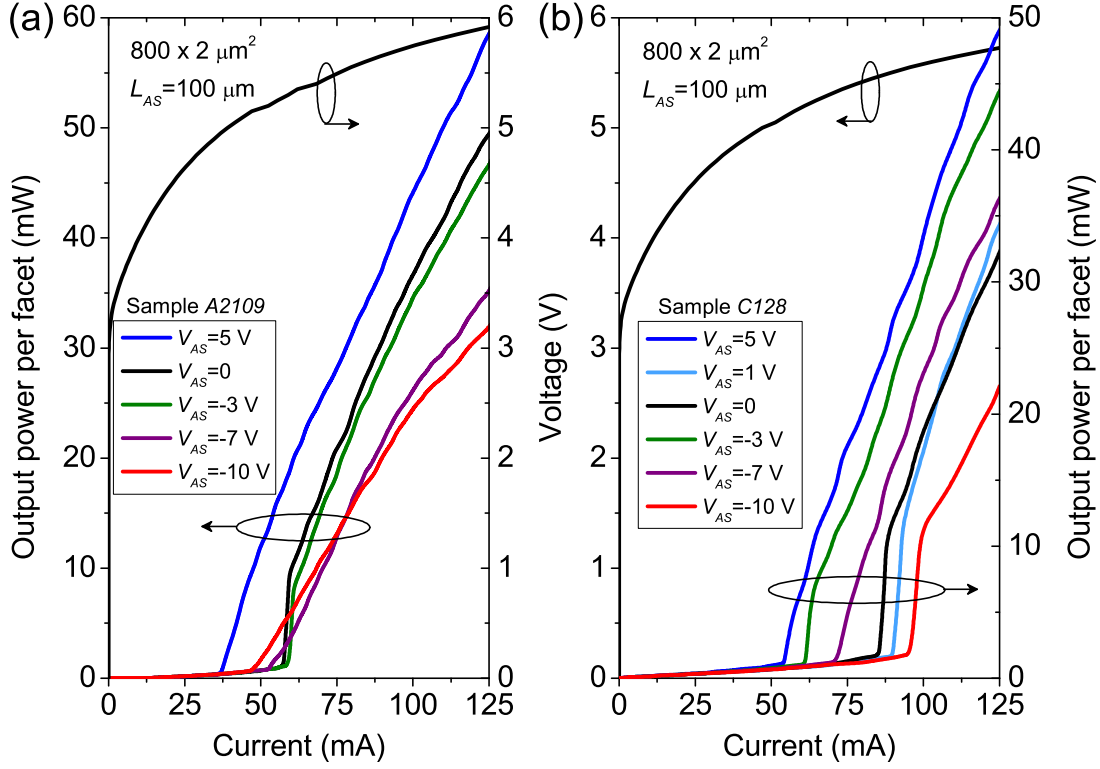


Figure 3.8: Experimental L - I - V curves for a MS-LD from sample (a) A2109 and (b) C128 biased at different V_{AS} and I_{GS} under cw operation at RT.

100 μ A, varies similarly to I_{th} . Interestingly, when comparing the threshold current curves in Fig. 3.9 (a) to the absorption curves in Fig. 3.6, we clearly see the same trend for both samples. It is likely that the non-monotonic variation of I_{th} (i.e., V_{MAX} and V_{MIN}) is mainly determined by the absorption of the AS under different bias conditions. Therefore, as expected, the maximum threshold observed at V_{MAX} is the consequence of a trade-off between a stronger absorption when negative bias is applied, due to a larger electron-hole wavefunction overlap, and a limited energy detuning between GS emission and AS absorption edge, respectively. In turn, the minimum I_{th} (occurring at V_{MIN}) should correspond to a maximum energy detuning between the AS absorption edge and the peak of the GS curve emission. Actually this situation is achieved for flat-band conditions.

This is in contrast with the behavior observed in strain-free GaAs LDs reported in Ref. [154] and in InGaN-based lasers from Ref. [126]. For instance, Miyajima *et al.* report a monotonic increase in the absorption coefficient in InGaN-based MS-LDs when the reverse-bias increases [155]. However, as emphasized in Sec. 3.3, the internal absorption coefficient strongly depends on the epitaxial structure. In fact, the MS-LDs of Ref. [155] emit at 405 nm. Most likely, this translates into very small internal polarization fields F_{int} and thus in low V_{MAX} and V_{MIN} values (see the wavelength-dependent trend in Fig. 3.10). For this reason, the devices measured in Refs. [126, 155] should exhibit a

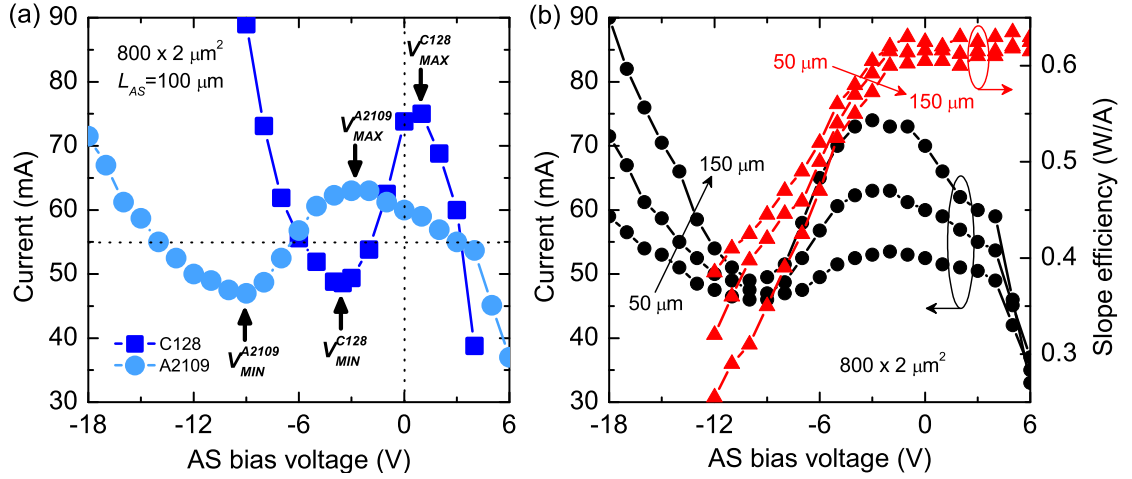


Figure 3.9: (a) I_{th} as a function of V_{AS} under cw operation for sample A2109 with low indium content barriers (light blue circles) and sample C128 with high indium content barriers (dark blue squares). The dotted lines correspond to $V_{AS} = 0$ (vertical) and to $I_{GS} = 55$ mA (horizontal). (b) I_{th} (black circles) and slope efficiency (red triangles) for $800 \times 2 \mu\text{m}^2$ MS-LDs from sample A2109 with different absorber lengths (Mask 2, i.e., $L_{AS} = 50, 100$ and $150 \mu\text{m}$).

monotonic behavior similar to “polarization-free” materials. Moreover, the well barriers of their devices are intentionally n -doped, which also reduces the magnitude of the internal field [49]. In our case, when applying a fixed I_{GS} close to threshold at $V_{AS} = 0$ (e.g., 55 mA), it is possible to turn on and off the lasing regime by simply changing V_{AS} . This indicates that in multiple-section devices implemented in III-nitride alloys, the lasing regimes can be tailored via electrical control of the absorber. However, in contrast with conventional III-V devices, variations in the absorption with the applied negative bias are not monotonic, therefore rendering the observation of periodic pulse regimes (e.g., self-pulsation, Q-switching, or mode-locking) a challenging task [12, 156].

Figure 3.9 (b) shows the impact of the saturable absorber length L_{AS} on I_{th} and on the slope efficiency for sample A2109. At first sight and not surprising, a longer absorber corresponds to higher threshold currents. But having a closer look, one can see that the threshold current for lasing is nearly the same around V_{MIN} , the absorber bias at which flat-band conditions occurs [$V_{AS} = -9.5$ V in Fig. 3.9 (b)]. On the other hand, the impact of a larger L_{AS}/L_{TOT} ratio is stronger only for biases away from V_{MIN} .

As can be seen in Figs. 3.8 and 3.9 (b), the slope efficiency starts to decrease beyond $V_{AS} = -3$ V for both samples. This droops cannot be ascribed to any behavior related to V_{MAX} or V_{MIN} . Actually, this decrease is the result of fast carrier tunnelling induced by strongly reverse-biased barriers [e.g., $V_{AS} < -3$ V in Fig. 3.9 (b)] [131]. Thus, the carrier density in the absorber cannot sufficiently rise up to reach the gain regime reducing thereby the slope efficiency [e.g., $V_{AS} = -7$ V and $V_{AS} = -10$ V in Fig. 3.8 (a)]. The tunneling time will be treated in more details in Sec. 4.1. Moreover, the slope efficiency is reduced when increasing L_{AS} [Fig. 3.9 (b)]. As for the threshold current, this is due to

a larger L_{AS}/L_{TOT} ratio that enhances the absorption effects in reverse-biased MS-LDs. The larger threshold current, the increased photocurrent, and the discontinuities of the output power as the reverse bias voltage is raised, indicate that the AS operates as a saturable absorber [157].

It is worth to notice that the local maximum of I_{th} at V_{MAX} (and local minimum of I_{th} at V_{MIN}) slightly varies for each tested laser bar made from the same epiwafer due to temperature inhomogeneities. In Fig. 3.10, the bias voltages V_{MAX} and V_{MIN} for different devices fabricated from the sample A2109 wafer are plotted as a function of the lasing wavelength measured at zero bias ($V_{AS} = 0$). The lasing wavelength varies between 407 and 430 nm on this epitaxial wafer. Both V_{MAX} and V_{MIN} decrease with the lasing wavelength while their difference slightly increases. In Fig. 3.10, shorter lasing wavelengths correspond to lower indium content in the MQWs, leading to smaller strain and hence a lower built-in field F_{int} . As a result, the flat-band condition occurs at smaller reverse bias in devices exhibiting a shorter emission wavelength. No particular dependencies on L_{AS} have been observed for V_{MAX} and V_{MIN} in terms of lasing wavelength. Note that compared to triple-section devices, the values of V_{MAX} for bi-section devices are more scattered (see light blue full circles in Fig. 3.10). Most likely this is due to a less stable absorption profile in bi-section devices. In fact, with a center-absorber geometry,

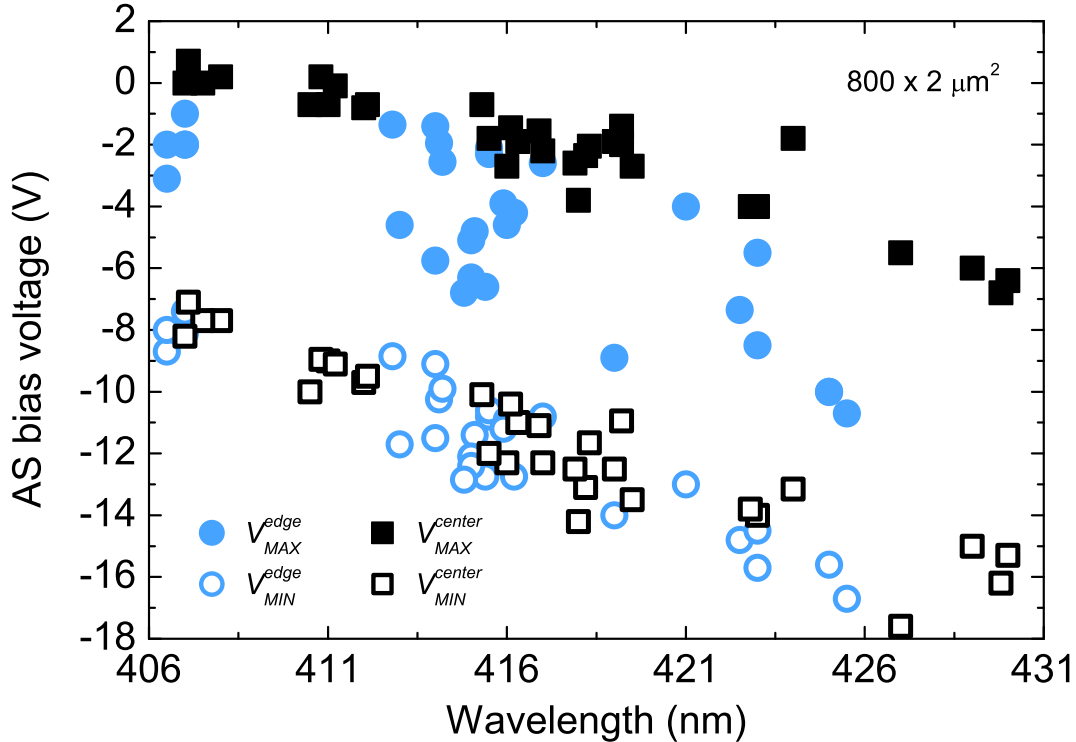


Figure 3.10: V_{MAX} (full symbols) and V_{MIN} (hollow symbols) as a function of lasing wavelength (taken at $V_{AS} = 0$) for $800 \times 2 \mu\text{m}^2$ MS-LDs from sample A2109 with central absorber (black squares) and edge-absorber (light blue circles) geometries.

the light emission of two GSs placed on both sides of the absorber is more suitable to fill uniformly (in terms of space along L_{AS}) the DOS of the absorber MQWs and thus to set up a more balanced absorption profile in the AS.

3.5 Spontaneous and lasing emission

To better understand the absorption behavior of the absorber for different bias conditions, emission spectra from the AS and GS facets have been recorded well below the lasing threshold [see the experiment sketch in Fig. 3.11 (a)]. The experimental conditions are adjusted so as to keep the carrier density in the GS MQWs near transparency.

As a comparison, Figure 3.11 (b) shows the absorption spectra calculated from eq. 3.1 for sample A2109 and C128 at $V_{AS} = 2.5$ V and at V_{MIN} . The pump current is in both cases 5 mA ($\sim 0.08 \cdot I_{th}$). As previously discussed for the simulated absorption and for the threshold current, sample A2109 exhibits a minimal absorption at larger negative voltages and a more important QCSE between the case of 0 net-field ($V_{MIN} = -11$ V) and the highest applied bias ($V_{AS} = 2.5$ V) as compared to C128.

Figures 3.12 (a) and 3.12 (b) show in more details the emission spectra recorded in sample C128 structure for different V_{AS} . Figures 3.12 (a) and 3.12 (b) distinguish spectra recorded for a biased absorber above and below V_{MIN} . As the GS is driven near transparency (well below I_{th}), we can neglect the optical gain and build up a simple model with the following assumptions: (1) the spontaneous emission is uniform across the GS; (2) due to the low reflectivity of the facets, a single pass in the cavity can be considered; and (3) the number of photogenerated carriers in the AS is negligible owing

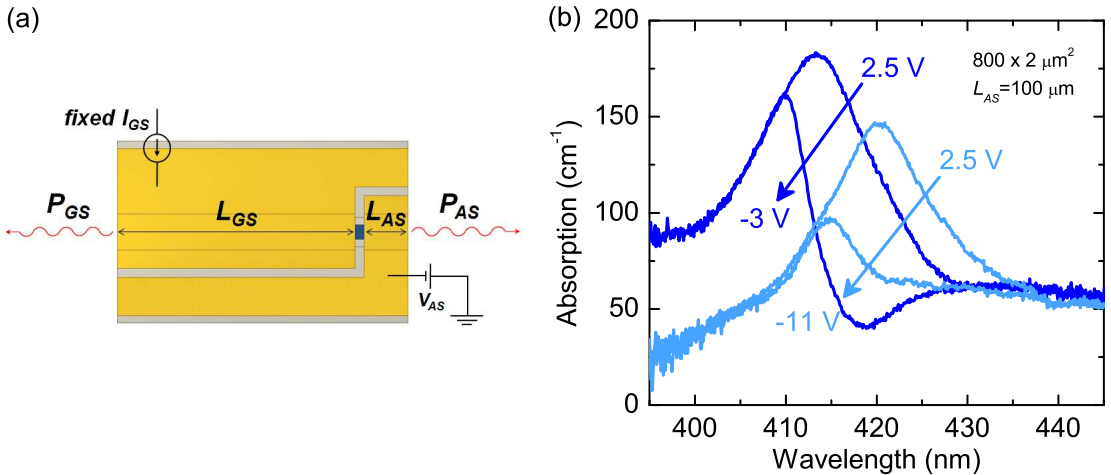


Figure 3.11: (a) Schematic top view of a bi-section device driven at fixed cw I_{GS} and constant V_{AS} . The emission of the electrically injected GS is collected from both sides of the MS-LD, i.e., from the gain and absorber facets. (b) Absorption spectra at $V_{AS} = 2.5$ V and at V_{MIN} extracted from the AS emission properties using eq. 3.1 for sample A2109 (light blue) and C128 (dark blue).

to the very low photocurrent (e.g., screening of F_{int} is determined by the applied external bias). Therefore, the relative AS absorption spectra can be extracted from the following power ratio (based on eq. 2.7) [131, 154]:

$$\frac{P_{AS}(\hbar\omega)}{P_{GS}(\hbar\omega)} = \frac{e^{-\alpha_{AS}(\hbar\omega, V_{AS}, I_{GS})L_{AS}} (1 + R)}{1 + R \cdot e^{-2\alpha_{AS}(\hbar\omega, V_{AS}, I_{GS})L_{AS}}}, \quad (3.1)$$

where $P_{AS}(\lambda)$ and $P_{GS}(\lambda)$ are the spectral power densities of the light emission from AS and GS facets, respectively. Here we have supposed $R = 0.17$ for uncoated facets. The absorption spectra $\alpha(\lambda)$ deduced from eq. 3.1 are plotted in Figs. 3.12 (c) and 3.12 (d). Notice that this approach does not allow to observe the entire absorption band taking place at energies above the GS spontaneous emission (Fig. 3.5). For this reason, in the case of a MS-LD, the absorption measured using eq. 3.1 is often expressed *in relation to* the emission of the GS. Note that this absorption is indicative and cannot be fully compared to the *absolute absorption* measured by Hakki-Paoli gain spectroscopy.

The emission spectrum recorded from the GS facet at $V_{AS} = 0$ (black curve) does not change appreciably when varying V_{AS} . In contrast, the emission spectra recorded from the AS facet shift towards higher energies when decreasing the bias from 2.5 V to -3 V [Fig. 3.12 (a)]. This blueshift is caused by the QCSE shift of the AS absorption edge, yielding a decrease in the absorption coefficient when approaching the flat-band conditions ($V_{AS} = -3$ V) [130]. As previously mentioned, at V_{MIN} , the AS absorption is minimal for the low energy side of the GS emission since the bandgap energy offset between the GS emission and the AS absorption edge is maximum [131].

The situation is reversed when further reducing the bias (from -3 V to -16 V): the emission intensity decreases and the emission peak shifts towards lower energies [Fig. 3.12 (b)]. The absorption edge redshifts together with an increase in the absorption coefficient [Fig. 3.12 (d)]. The absorption at the lasing wavelength (e.g., 419 nm, vertical dotted line in Fig. 3.12) can thus be electrically adjusted between the flat-band conditions (V_{MIN}) and the largest absorber applied bias (-16 V in this case), enabling us to tailor the dynamics of the lasing regimes in polar GaN-based MS-LDs. Afterwards, the observed changes in the recorded spectra for different absorber biases due to QCSE are then used to calculate the change in the absorption in the QWs ($\Delta\alpha$) [150]. The emission at 2.5 V (the highest applied bias) is used as a reference value. As a first approximation, the recorded emission on the absorber facet P_{AS} is proportional to $e^{-\alpha_{AS}(V_{AS})L_{AS}}$. The induced absorption change can be calculated using [12, 149, 158]:

$$\begin{aligned} \Delta\alpha_{AS}(\hbar\omega, V_{AS}, I_{GS}) &= \alpha_{AS}(V_{AS}) - \alpha_{AS}(V_{AS} = 2.5V) = \\ &= -\frac{1}{L_{AS}} \ln \frac{P_{AS}}{P_{AS}(V_{AS} = 2.5V)}. \end{aligned} \quad (3.2)$$

The principle behind this approach is very similar to the modulation spectroscopy technique described in Sec. A, i.e., electro-reflectance (ER), in which a lamp with a continuous spectrum is used as source/probe beam and the sample parameters are modulated by an

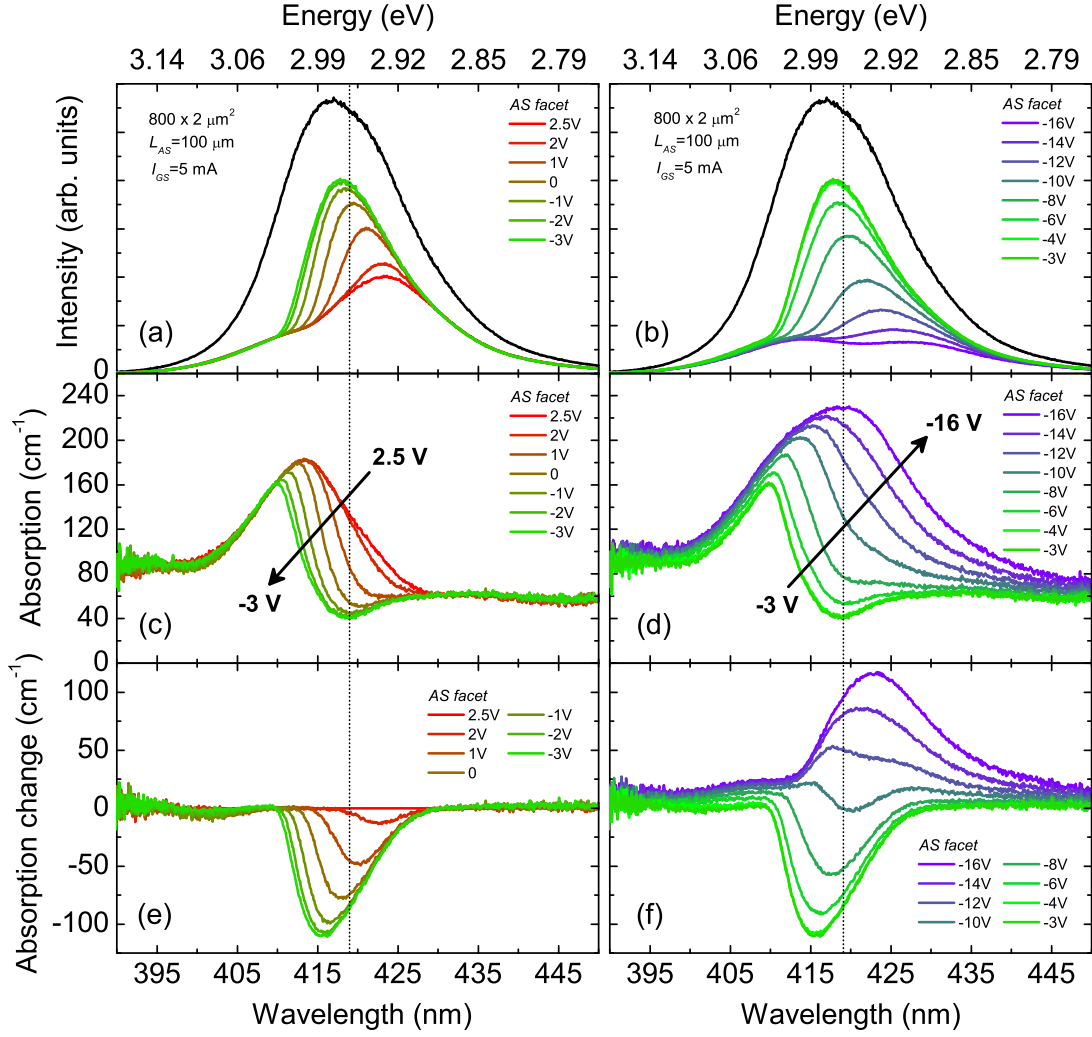


Figure 3.12: Spontaneous emission spectra (recorded on sample C128 device below lasing threshold, e.g., $I_{GS} = 5$ mA) for different negative biases: (a) from 2.5 to -3V and (b) from -3 V to -16 V. The black curve corresponds to the emission spectrum recorded from the GS facet at $V_{AS} = 0$. (c)-(d) display the absorption spectra extracted from AS emission properties using eq. 3.1. (e)-(f) display the absorption changes relative to the absorption spectrum for the highest applied bias ($V_{AS} = 2.5$ V) according to eq. 3.2. The dotted vertical line corresponds to the lasing wavelength (taken at $V_{AS} = 0$).

external applied bias that induces changes in the reflection or transmission coefficient of the sample [148]. Figures 3.12 (e) and 3.12 (f) show the field-induced absorption changes for the emission recorded from the absorber facet above and below V_{MIN} (i.e., -3 V), respectively. The absorption change at $V_{AS} = 2.5$ V is obviously flat as its emission is used as reference value. Absorption changes as large as 100 cm^{-1} at the lasing wavelength have been observed by modulating V_{AS} . Kneissl *et al.* reported induced absorption changes of 5000 cm^{-1} on InGaN-based MQW MS-LDs but they were considering the material absorption and not the modal absorption [12]. Supposing a confinement factor Γ

of 0.02, the two values are in very good agreement. Sari *et al.* also reported an absorption change of 6000 cm^{-1} (material absorption) in InGaN/GaN-based LEDs [159]. Such large absorption changes demonstrate the possibility to use III-nitride materials as efficient quantum electro-absorption modulators [12].

Note that the constant absorption background on the low energy side ($\sim 60 \text{ cm}^{-1}$) can be ascribed to cavity material losses [see Figs. 3.12 (c) and 3.12 (d)]. Indeed, Hakki-Paoli gain spectroscopy indicates internal losses of about 30 cm^{-1} [130]. Interestingly, at $V_{AS} = -3 \text{ V}$, the absorption around the lasing wavelength is lower than this value [Figs. 3.12 (c) and 3.12 (d)]. This apparent decrease in the absorption could be attributed to re-emission from low energy states in the AS MQWs, which exhibit a significant Stokes shift between absorption and luminescence. This effect is enhanced around flat-band conditions mainly because of the higher recombination rate (see, e.g., eq. 1.16) [137]. It is worth to notice that the MS-LD lases at 419 nm (vertical dotted line in Fig. 3.12), on the long wavelength side of the GS spontaneous emission spectrum [Fig. 3.12 (a)]. This shows that the threshold condition is achieved not at the GS emission peak, where the absorption is too high but in the wavelength range where the AS absorption is lower [154].

Above the lasing threshold, no difference has been observed between the spectral shape of the emission recorded from the gain and absorber facets as the device behaves as a single laser entity. In fact, the lasing wavelength varies with both I_{GS} and V_{AS} . A two dimensional color map of the lasing wavelength and average output power (dashed-dotted lines) as a function of I_{GS} and V_{AS} are displayed in Fig. 3.13 for sample C128. The device is driven at 1% duty cycle with a current pulse width of $1 \mu\text{s}$ in order to minimize the impact of self-heating effects on the measured lasing spectra. Notice that the lasing wavelength at large V_{AS} (below -9 V) and high I_{GS} (above 100 mA) has not been investigated due to the risk of absorber breakdown by avalanche-like carrier generation under strong reverse bias.

Around V_{MIN} , we observe the shortest lasing wavelength, the highest average output power and the lowest I_{th} (Fig. 3.13). At this bias, the AS MQWs are under flat-band conditions and the AS absorption edge is strongly blueshifted in respect to the gain curve and the energy difference between the two sections is maximal [Fig. 3.12 (c)]. Any variations in the reverse absorber bias will cause a redshift in the absorption edge. This will increase the absorption coefficient, thereby increasing the threshold current I_{th} , redshifting the lasing wavelength and reducing the output power [see also Figs. 3.8 (b) and 3.9 (a)]. Note that the maximum of the output power under flat-band conditions shifts towards larger negative biases with increasing pump current I_{GS} (see hollow black circles in Fig. 3.13). This slight shift can be explained by partial screening of the built-in potential Ψ_{bi} due to photogenerated carriers in the reverse-biased absorber. Therefore, a higher V_{AS} is needed to reach the flat-band conditions according to eq. 1.22.

The situation is reversed around V_{MAX} where the longest lasing wavelength is observed together with the lowest average output power and the highest I_{th} (Fig. 3.13). Indeed, as V_{AS} is progressively decreased (from 4 V down to V_{MAX}) at constant current (larger

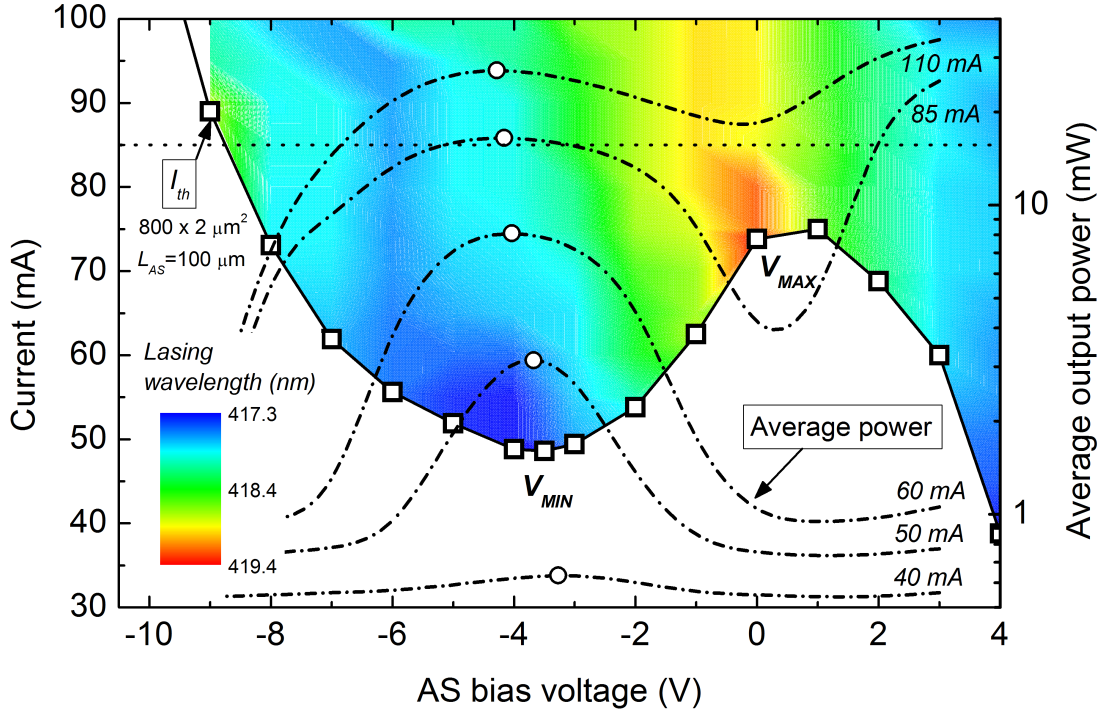


Figure 3.13: Emission wavelength (2D color map), threshold current (hollow squares) and average output power (dash-dotted lines) recorded at different I_{GS} as a function of V_{AS} for sample C128. The dotted horizontal line corresponds to $I_{GS} = 85$ mA. The hollow black circles correspond to the respective maxima in the average output power curves.

than I_{th} , e.g., 85 mA, horizontal dotted line in Fig. 3.13), the AS absorption strength increases. But contrary to the situation observed at V_{MIN} , the energy detuning between the two sections is minimum since the AS absorption edge still matches the GS emission [Fig. 3.12 (c)].

Figure 3.14 (a) displays a 2D color map of the lasing wavelength as a function of I_{GS} and V_{AS} for sample A2109. The observed behavior is similar to that of sample C128, V_{MAX} and V_{MIN} are just shifted to larger biases due to the higher internal polarization field. Note that, as mentioned in Sec. 2.3.3, for specific V_{AS} and I_{GS} values the emission spectra show multiple peaks due to internal reflections on the reverse-biased AS intracavity. In Figs. 3.13 and 3.14 (a) only the intensity-weighted average wavelength is reported. However, the impact of the absorption as a function of V_{AS} is also visible on the lasing peaks [Fig. 3.14 (b)]. For biases near V_{MAX} the lasing mode pattern (not considering the longitudinal mode splitting) exhibits a single-peak while for larger (or smaller) negative biases the spectra consist of multiple-peaks whose separation is fixed by L_{AS} . This indicates that for low absorption in the cavity, additional lasing modes can build up.

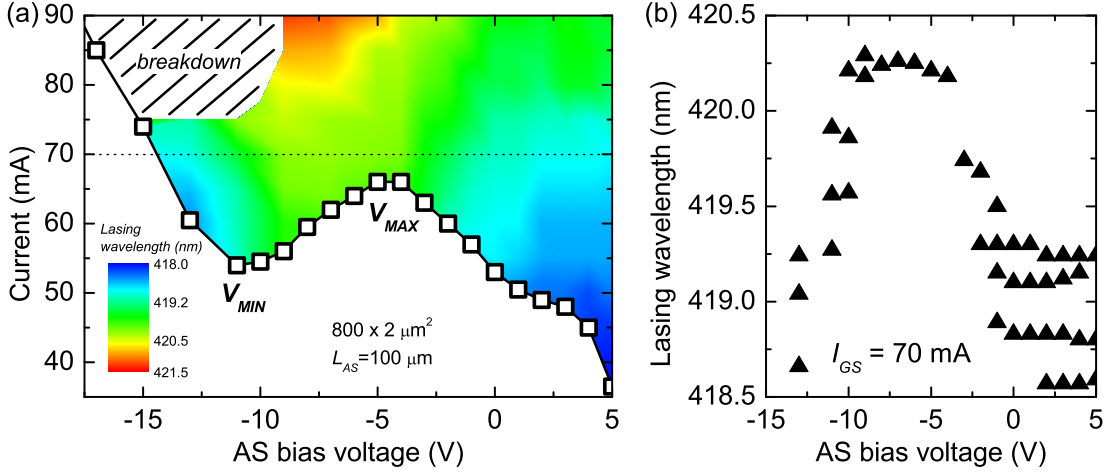


Figure 3.14: (a) Emission wavelength (2D color map) recorded at different I_{GS} and threshold currents (hollow squares) as a function of V_{AS} for sample A2109. The dotted horizontal line corresponds to $I_{GS} = 70$ mA. (b) Lasing wavelength as a function of V_{AS} for a 70 mA forward-biased GS. Note the peak separation (~ 0.25 nm) for a given bias induced by the $100 \mu\text{m}$ -long absorber intracavity (see discussion in Sec. 2.3.3).

3.6 Optical bistability

Under certain conditions, the photon density in the cavity and the level of saturation of the absorber MQWs cause a hysteresis loop in the L - I characteristics of the MS-LD. Two stable optical states are thus available for the same injected current, the so-called *on* and *off* states. This phenomenon is called *optical bistability* and it is a desirable property for all-optical switching and signal processing applications [160]. In the context of the Femtoblue project bistability enables the assessment of several important device parameters. For this reason, the dependence of the hysteresis on the absorber length L_{AS} and absorber bias V_{AS} has been investigated. The reader can explore in more details this aspect in Ref. [137].

The bistability study published in Ref. [137] is based on MS-LDs from sample A2109 processed with Mask 2 [note that the acronym SA (saturable absorber) has been substituted in this thesis by AS (absorber section)]. Figure 3.15 (a) displays the cw L - I - V curves of a MS-LD with $L_{AS} = 100 \mu\text{m}$ for different absorber biases V_{AS} . A hysteresis loop is observed for $V_{AS} = 2, -2, -21$ and -23 V while for $V_{AS} = -8$ and -17 V the hysteresis disappears. This behavior is more evident in the inset of Fig. 3.15 (a) in which the hysteresis width (in term of injected current) is plotted as a function of the absorber bias. Moreover, the longer the absorber the larger the hysteresis width [Fig. 3.15 (b)]. Thus, the applied bias V_{AS} and absorber length L_{AS} control the occurrence and also the width of the L - I hysteresis. Photocurrent is extracted from the AS as a function of I_{GS} [inset in Fig. 3.15 (b)]. This current arises from photogenerated carriers created in the absorber MQWs because of the optical pumping from the GS. Hysteresis loops in the photocurrent curves are perfectly correlated to the switching-on and switching-off

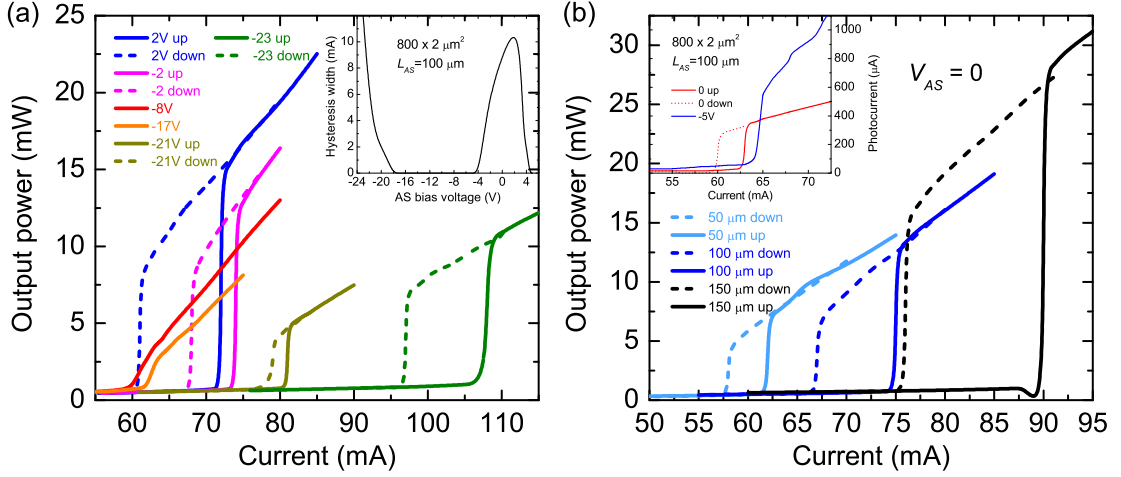


Figure 3.15: (a) L - I - V characteristics of a MS-LD with $L_{AS} = 100 \mu\text{m}$ for different absorber biases V_{AS} . The notation up and down refer to an adiabatic increase and decrease in the injected current, respectively. The inset shows the hysteresis width vs V_{AS} for the present device. (b) L - I - V characteristics of a MS-LD at $V_{AS} = 0$ for different absorber lengths L_{AS} . The inset shows the detected photocurrent flowing through the AS as a function of I_{GS} for $V_{AS} = 0$ and -5 V .

currents of the L - I curves. Note that the photocurrent extracted for $V_{AS} = 0$ is lower than the one at -5 V . This is a signature of saturation in the absorber MQWs under reverse bias conditions [135].

The following model has been developed by Dmitri L. Boiko in Ref. [137]. Standard rate equations for a bi-section LD are used to model the data with the following assumptions: linear gain and absorption approximations, single mode operation, no spontaneous emission and no current leakage from the gain to the absorber section. A dimensionless parameter V_a is introduced to describe the change in the transparency carrier density n_{tr} via $n_{tr}(1 - V_a)$. Analytical expressions can thus be calculated for the normalized switching-on threshold $J_{n,th}$ and the hysteresis loop width $\Delta J_{n,th}$ using the Lyapunov exponent method [137, 161]:

$$J_{n,th} = \frac{2L_{TOT}\alpha_i - 2\ln R}{g_0 n_{tr} \tau_{GS} \Gamma(1 - \alpha)} + \frac{T_{cav}}{\tau_{GS}} \left[1 + \frac{\alpha\sigma(1 - V_a)}{1 - \alpha} \right], \quad (3.3)$$

$$\Delta J_{n,th} = \left[\sqrt{\frac{\alpha(1 - V_a)}{1 - \alpha} \left(\frac{T_{cav}}{\tau_{GS}} \sigma - \frac{T_{cav}}{\tau_{AS}} \right)} - \sqrt{\frac{2L_{TOT}\alpha_i - 2\ln R}{g_0 n_{tr} \tau_{AS} \Gamma(1 - \alpha) \sigma}} \right]^2, \quad (3.4)$$

where α in this case is the length ratio of the absorber to the cavity, T_{cav} is the cavity roundtrip time, g_0 is the differential material gain and σ is the ratio of differential absorption to differential gain.

Figure 3.16 (a) shows the measured and calculated switching-on threshold current as a function of V_{AS} . V_{MAX} and V_{MIN} are about -3 and -12 V , respectively (sample A2109

device). As observed in the L - I - V curves, bistability only occurs in specific voltage ranges: from 3 V to -5 V and below -20 V [green areas in Fig. 3.16 (a)]. Then, a simultaneous fit of the switching-on and switching-off threshold given by eq. 3.3 for the three absorber lengths (available on Mask 2) enables us to define the relation between the biasing parameter V_a and the reverse bias V_{AS} [137]. Around flat-band conditions, the resulting simulated threshold current curve is in good agreement with the experimental one [compare the dashed and continuous black lines in Fig. 3.16 (a)]. The obtained value for V_a can now be included in eq. 3.4 where the only remaining unknown parameter is the absorber carrier lifetime τ_{AS} . As for the switching-on threshold currents, the width of the hysteresis loop was measured for different absorber lengths. Then, the hysteresis width is plotted as a function of the ratio α for each reverse applied bias and numerically fitted in eq. 3.4 using τ_{AS} as a free parameter. The inset in Fig. 3.16 (b) shows the fitted parameters in the case of $V_{AS} = 0$. This way, we are now able to estimate the dependence of the carrier lifetime on applied bias. Note that a condition on the bias voltage ranges where optical bistability is observed, and thus for which the carrier lifetime can be calculated, is deduced from eq. 3.4 [137]:

$$\tau_{AS} > \frac{\tau_{GS}}{\sigma} \frac{1 - \beta}{-\beta}, \quad \beta = -\frac{g_0 \sigma T_{cav} \Gamma n_{tr} (1 - V_a)}{2L_{TOT} \alpha_i - 2 \ln R} \alpha, \quad (3.5)$$

where β is the ratio of the carrier-free modal absorption to the cavity loss.

Figure 3.16 (b) shows the estimated carrier lifetime as a function of V_{AS} . Carrier lifetime starts from a value of 1.9 ns at $V_{AS} = 0$ and rapidly decreases towards a minimum value reached at flat-band where bistability disappears (and the carrier lifetime can no longer be extracted). Nevertheless, a carrier lifetime of 400 ps can be extrapolated at flat-band. These experiments can be qualitatively understood as follows. Let us suppose that we adiabatically increase the current in the GS. Once the additional absorption losses induced by the intracavity absorber is compensated, the MS-LD can lase (switching-on threshold). In fact, these additional losses are not only compensated but rather saturated

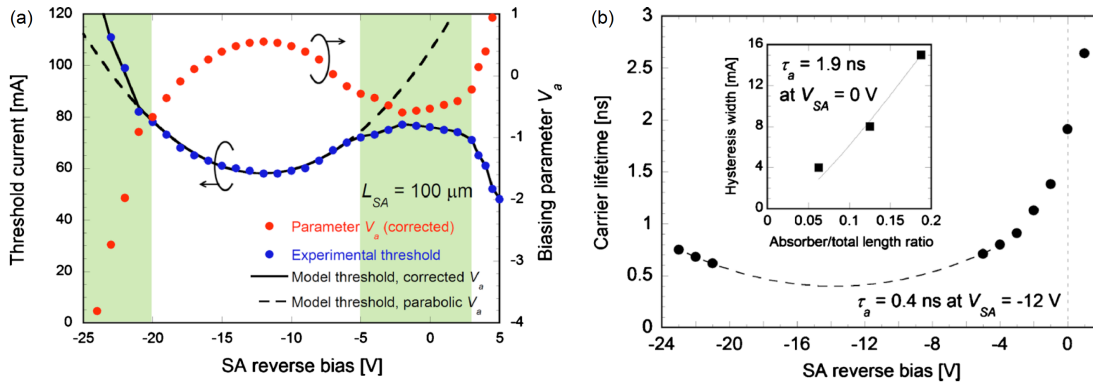


Figure 3.16: (a) Measured and simulated threshold currents for $L_{AS} = 100 \mu m$ and corrected bias parameter V_a . (b) Estimated carrier lifetime vs V_{AS} . The inset shows the fit of the hysteresis width at $V_{AS} = 0$. [137]

(as opposed to internal and mirror losses that are never saturated). Therefore, the induced absorption drops to 0 and a typical kink at threshold is observed. The MS-LD recovers its “absorption-free-like” L - I curves but at higher current. If now the current is decreased the photon population in the cavity is still high enough to maintain lasing emission and additional losses are kept saturated. Once the injected current is not able to maintain this saturation, the lasing emission turns off (switching-off threshold). It is thus likely that optical bistability develops when the carrier-free absorption and/or the carrier lifetime in the AS are significant, so when the absorber is hardly depleted. A similar behavior has also been observed for InGaN-based LDs featuring a SESAM [162] and for InGaAs/InAlAs-based MS-LDs [163]. In the particular case of III-nitride MS-LDs, optical bistability develops:

- in the case of *strong carrier-free absorption*, that means the ability for the AS MQWs to absorb. As previously discussed (see Fig. 3.10), absorption is stronger away from the flat-band bias V_{MIN} , e.g., around V_{MAX} and for very large biases [green areas in Fig. 3.16 (a)]. Around V_{MIN} , we expect that the absorber requires a higher photon density to be saturated and hence bistability disappears. Moreover, the hysteresis width increases with L_{AS} indicating a stronger absorption also for longer absorbers [Fig. 3.15 (b)]. Indeed, bistability at very large reverse bias has not been observed for short absorber lengths (i.e., $L_{AS} = 50 \mu\text{m}$).
- in the case of *long carrier lifetime*, that means the ability of the AS MQWs to remain filled (with photogenerated carriers) as long as possible. The carrier lifetime evolution will be treated in more details in Sec. 4.1. Its main dependencies are radiative and non-radiative recombinations (proportional to the carrier-free absorption), tunneling effects (proportional to the reverse applied bias) and thermionic escape (proportional to the temperature). Radiative recombination is the predominant contribution under flat-band conditions whereas tunneling effects are strongly enhanced for large reverse bias. The carrier lifetime measured by the EL decay after a current pulse is in good agreement with bistability measurements except for one feature: the measured carrier lifetime monotonically decreases and does not rise up again for very large bias as the estimated one. In fact, Scheibenzuber measured the carrier lifetime on the same device (A2109 sample) and also obtained a lifetime decreasing from about 2 ns at $V_{AS} = 0$ down to 400 ps at $V_{AS} = -15$ V (the expected V_{MIN}) when increasing the reverse bias [132]. No minimum value seems to appear from the curves. Further electroluminescence-decay measurements performed on sample C128 MS-LDs (reported in Ref. [133]) and other InGaN-based MS-LDs (reported in Ref. [164]) showed the monotonic decrease in the carrier lifetime. It is thus likely that the “real” carrier lifetime monotonically decreases due to strong tunneling effects at large biases. The lifetime rise extrapolated from bistability measurements is an artifact. Lifetime simulations that will be described in Sec. 4.1 support this argument.

Here, we propose that bistability reappears for biases larger than -20 V because of the stronger absorption that allows the absorber to saturate despite the decrease in the carrier lifetime and NOT because of a lower recombination rate that allows the absorber to remain saturated [137]. Unfortunately, when solving eqs. 3.3, 3.4 and 3.5, an increase in the absorption for biases larger than V_{MIN} is interpreted as an increase in the carrier lifetime as the model is based on radiative recombinations and neglects tunneling effects. The fact that absorption is the predominant condition for bistability rather than the carrier lifetime is also supported by the increase in the hysteresis width with L_{AS} [Fig. 3.15 (b)]. Moreover, triple-section devices exhibit more stable hysteresis loops than bi-section ones as AS MQWs placed in the middle of the cavity are more uniformly pumped.

In conclusion, conditions for bistable and unstable regimes notably depend on the carrier lifetime and the absorption coefficient in the AS. The remarkable feature of the model presented in Ref. [137] consists in that the carrier lifetime values are extracted only from electrical measurements without any kind of streak camera or autocorrelator (as opposed to Refs. [132, 133, 164])!

Summary of the results

In this chapter, we have demonstrated how the non-monotonic evolution observed in the main static characteristics of MS-LDs (threshold current, output power, lasing wavelength, hysteresis width of the optical bistability,...) is governed by the unique absorption pattern of the InGaN-based MQWs located in the AS. The minimum in the absorption at V_{MIN} is reached for flat-band conditions, i.e., when the external applied field F_{ext} fully compensates the internal polarization field F_{int} . The maximum in the absorption at V_{MAX} and the minimum at V_{MIN} strongly depend on the layer structure and especially on the indium content in the barriers and in the wells. The shift in the absorption edge and the respective calculated internal absorption coefficients obtained from simulations of the band structure carried out in the effective mass approximation further confirm this interpretation. Hakki-Paoli gain measurements indicated an induced modal absorption change up to 300 cm^{-1} in the absorber MQWs.

4 Multi-section laser diodes: dynamic characteristics

In this chapter, the main “dynamic” characteristics of a III-nitride-based MS-LD are presented. The bias V_{AS} applied to the AS modifies the total net-field F_{QW} across the MQWs leading to absorption and carrier lifetime changes. The impact on self-pulsation (SP) and mode-locking is discussed.

4.1 Carrier lifetime

The absorber charge carrier lifetime τ_{AS} is a key parameter that controls the dynamic processes in MS-LDs. As the carrier-free absorption α_0 , it strongly depends on V_{AS} . A detailed understanding of the carrier emission from the active region is thus crucial to optimize the device parameters. In particular, a very short absorber carrier lifetime would be desirable for the generation of stable mode-locked pulses. Indeed, the absorption can then recover between each cavity round trip of the pulse. In this respect, a long carrier lifetime would limit the operational frequency of the device. On the other hand, a short lifetime would inhibit multiple output pulse formation in external-cavity mode-locked lasers due to parasitic retroreflections caused by an imperfect anti-reflection coating [165]. Note that the use of a reverse-biased section rather than a forward-biased one makes the absorber lifetime dynamics considerably differing from the behavior of the GS lifetime τ_{GS} (that we have described by means of the ABC model in Sec. 2.2.2). In fact, the total absorber carrier lifetime τ_{AS} can be written as the result of multiple contributions via:

$$\frac{1}{\tau_{AS}} = \frac{1}{\tau_{nr}} + \frac{1}{\tau_r} + \overbrace{\frac{1}{\tau_{therm}} + \frac{1}{\tau_{tun}}}^{1/\tau_{esc}}, \quad (4.1)$$

where τ_{nr} is the non-radiative carrier lifetime, τ_r is the radiative carrier lifetime, τ_{therm} is the thermionic carrier lifetime, and τ_{tun} is the tunneling carrier lifetime. The non-radiative contribution is mainly due to defect-related SRH recombinations and is thus commonly expressed as the inverse of the A -coefficient (see eq. 2.47). For instance, for

$A = 4.2 \cdot 10^7 \text{ s}^{-1}$, the non-radiative lifetime τ_{nr} amounts to 24 ns. Scheibenzuber *et al.* reported a carrier lifetime at very low carrier injection rates (i.e., $N \rightarrow 0$) of 2.8, 25 and 7.1 ns for violet, blue and green GaN-based LDs, respectively [166]. In principle, the longer τ_{nr} (or the smaller A), the higher the crystalline quality of the active region. Note that other non-radiative recombination processes, such as Auger recombination (see eq. 2.39), can substantially lower this value, especially in the high injection regime.

In a similar way to what was calculated in Sec. 2.2 for the absorption/gain in a QW and according to Fermi's golden rule (see eq. 2.3), the spontaneous optical transition rate is proportional to the probability for a state in the conduction band to be occupied and for a state in the valence band to be empty. Given the distribution of carriers at quasi-thermodynamic equilibrium in a semiconductor as described by the position of their respective quasi-Fermi levels, the total spontaneous emission rate R_{sp}^{AS} is then obtained by integrating over the entire spectrum [40, 167]:

$$R_{sp}^{AS} = \int_{E_{e1}-\hbar h_1}^{\infty} \frac{q^2 n_g}{c^3 d_{QW} \varepsilon_0 \pi^2 \hbar^4} \frac{m_r}{m_0} (\hbar \omega)^3 \frac{E_p}{E_g^2} |\langle i | f \rangle|^2 \cdot \theta(\hbar \omega - E_{e1}-\hbar h_1) \cdot f_c^1(\hbar \omega) [1 - f_v^1(\hbar \omega)] d\hbar \omega, \quad (4.2)$$

where θ is the Heaviside function approximated by eq. 2.22 that describes the DOS, f_c^1 and f_v^1 are Fermi-Dirac distributions in the first subband given by eqs. 2.14 and 2.16.

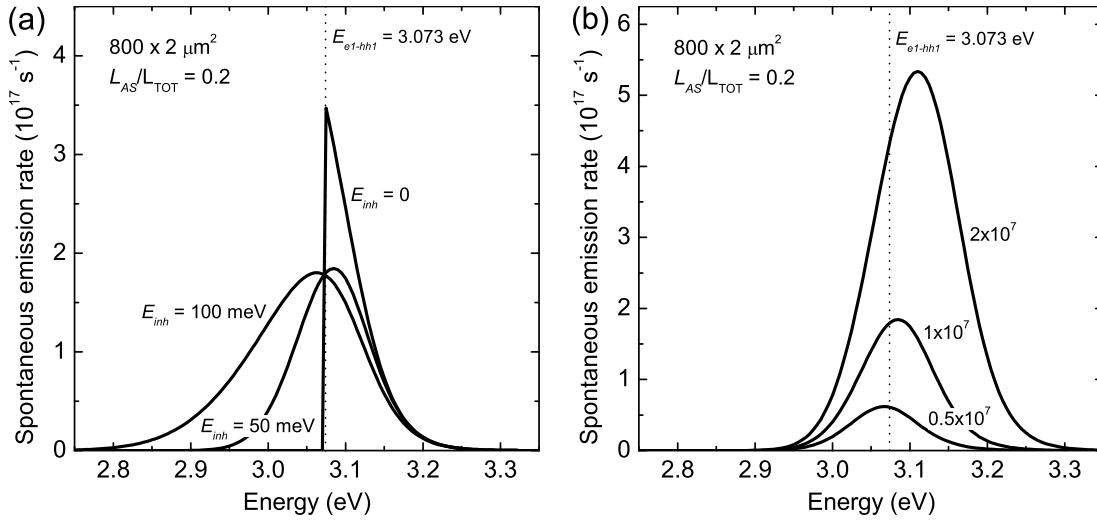


Figure 4.1: (a) Spectral distribution of the spontaneous emission rate $R_{sp}^{AS}(\hbar\omega)$ at different inhomogeneous broadening E_{inh} , i.e., 0, 50 and 100 meV from top to bottom, respectively, for $N_{AS} = 1 \cdot 10^7$. The sample considered is A2109 and the spectra are evaluated for flat-band conditions ($E_{e1}-\hbar h_1 = 3.073 \text{ eV}$, dotted vertical line). (b) Spectral distribution of the spontaneous emission rate $R_{sp}^{AS}(\hbar\omega)$ at different AS carrier populations N_{AS} , i.e., $0.5 \cdot 10^7$, $1 \cdot 10^7$ and $2 \cdot 10^7$ from bottom to top, respectively, for an inhomogeneous broadening E_{inh} of 50 meV.

To finally obtain the radiative carrier lifetime τ_r one still has to divide eq. 4.2 by the total carrier population in the absorber N_{AS} , i.e., $\tau_r = N_{AS}/R_{sp}^{AS}$. Figure 4.1 shows the spectral behavior of the spontaneous emission rate as a function of the photon energy for (a) different E_{inh} and for (b) different N_{AS} . As expected, in the case of an ideal QW [i.e., $E_{inh} = 0$ in Fig. 4.1 (a)], the spontaneous emission rate exactly starts at the transition energy $E_{e_1-hh_1}$ and then decreases exponentially following the population energy distribution. As expected, in the case of a non-zero inhomogeneous broadening, the spontaneous emission rate shows an important emission below the bandgap. Note also how the spontaneous emission rate increases with the carrier population N_{AS} due to the filling of the QW states that pushes the quasi-Fermi levels to higher energies [Fig. 4.1 (b)].

On the other hand, a carrier can escape the MQW and potentially contribute to the AS photocurrent. Two processes can be distinguished: a flow i) tunneling *through the well barrier* (tunneling emission) and ii) emitted *above the well barrier* (thermionic emission). These two mechanisms can be accounted for by the escape carrier lifetime τ_{esc} . Under the assumption of a 3D DOS close to the top of the well barrier and assuming a Boltzmann-like carrier statistics, Schneider and von Klitzing express the thermionic carrier lifetime τ_{therm} in a MQW structure as [168, 169]:

$$\tau_{therm} = \sqrt{\frac{2\pi m_{e,QW} d_{QW}^2}{k_B T}} \cdot \exp\left(\frac{E_b}{k_B T}\right), \quad (4.3)$$

where $m_{e,QW}$ is the electron effective mass in the MQW and E_b is the barrier energy, which must be overcome by the carriers. The product between the barrier collision frequency and the transmission probability through such a barrier leads to an expression for the carrier escape rate via tunneling emission. When applying the zero-order Wentzel-Kramers-Brillouin (WKB) approximation, the tunneling carrier lifetime τ_{tun} can then be estimated and we get [170, 171, 172, 173, 174]:

$$\begin{aligned} \tau_{tun} &= T_{coll}^{[170]} \cdot \exp \int_0^{L_b} 2\sqrt{\frac{2m_{e,b}}{\hbar^2}(E_{c,max} - E_{e_1-hh_1})} dz = \\ &= \sqrt{\frac{2m_{e,QW}}{e_1}} d_{QW} \cdot \exp\left(\frac{4}{3} \frac{\sqrt{2m_{e,b} E_b^3}}{\hbar q F_b}\right), \end{aligned} \quad (4.4)$$

where $T_{coll}^{[170]} = 2d_{QW}/v(z)$ is the oscillation period of an electron in the QW region with $v(z)$ the particle velocity approximated according to $e_1 = \frac{1}{2}m_{e,QW}v(z)^2$ [170], L_b is the well barrier thickness, $E_{c,max}$ is the maximum potential in the effective well barrier, $m_{e,b}$ is electron effective mass in the barrier and F_b is the electric field in the barrier.

Figure 4.2 (a) depicts the calculated carrier lifetime for each emission mechanism described in eq. 4.1 as a function of V_{AS} . Typically, at V_{MIN} we have $E_b = 295.4$ and 137.8 meV, $e_1 = 60.6$ and 57.2 meV and $F_b = 1.98$ and 1.15 MV/cm for samples A2109 and C128, respectively. The non-radiative lifetime τ_{nr} is set for both samples to 5 ns and

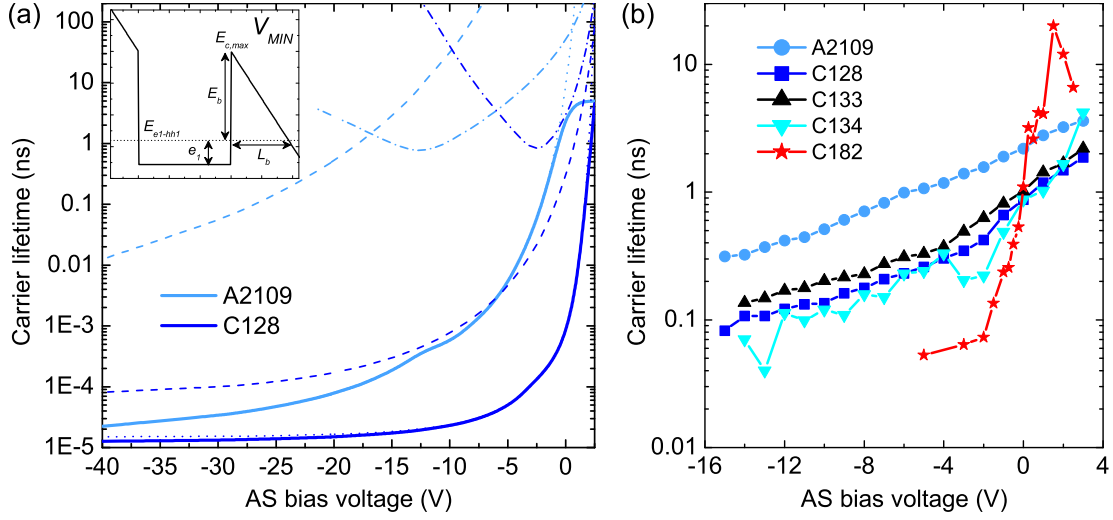


Figure 4.2: (a) Calculated absorber carrier lifetime for sample A2109 (light blue curve) and C128 (dark blue curve) as a function of V_{AS} . The dash-dotted lines correspond to the radiative contribution, the dashed ones to the thermionic one, the dotted ones to the tunneling one and the continuous lines to the total absorber lifetime τ_{AS} . The inset shows a schematic representation of the band structure involved in the escape mechanisms for flat-band conditions. (b) Absorber carrier lifetime τ_{AS} for $800 \times 2 \mu\text{m}^2$ MS-LDs determined for samples A2109 (light blue curve), C128 (blue curve), C133 (black curve) and C134 (cyan curve) measured by pulsed electroluminescence decay. The red stars represent the carrier lifetime measured on a $500 \times 500 \mu\text{m}^2$ LED made from sample C182.

influences the total carrier lifetime only at low forward bias voltages. As expected the radiative lifetime τ_r (dash-dotted lines) reaches a minimum value of about 1 ns when the reverse-biased band structure is under flat-band conditions (i.e., at V_{MIN} , -12.5 V for sample A2109 and -2.5 V for sample C128). This happens because at this specific bias the QW oscillator strength is the strongest [cf. Fig. 3.3 (b)]. The calculated carrier lifetime around flat-band conditions is in good agreement with the one reported in Ref. [175], where an experimental radiative lifetime of about 0.6 ns is measured on a reverse-biased InGaN-based LEDs using time-resolved PL. On the contrary, the calculated lifetime for the carrier escape rates (thermionic and tunneling ones, dashed and dotted lines, respectively) monotonically decreases with V_{AS} . This droop is ascribed to the strong tilt experienced by the band structure under reverse bias conditions that causes a reduction in the potential barrier E_b that the carriers (electrons and holes) experience [see inset of Fig. 4.2 (a)]. Thus, the absorber carrier lifetime τ_{AS} (continuous lines) starts to be shorter than 1 ps already at $V_{AS} = -5$ V and seems to reach a plateau in the range of a few tens of femtoseconds at very large negative biases (e.g., $V_{AS} = -40$ V). One can therefore conclude that tunneling emission is the dominant effect at large V_{AS} .

For comparison, in Fig. 4.2 (b) the absorber carrier lifetime measured on different heterostructures processed during this thesis is reported as a function of V_{AS} . The

lifetime measurements have been carried out on the IAF set-up and streak camera images have been integrated over numerous shots. The absorber lifetime is investigated by applying a constant bias voltage superimposed to a square current pulse to the AS and by observing the decay of the EL after the weak current pulse [132, 176]. τ_{AS} amounts to several nanoseconds under forward and low negative voltages whereas it decreases down to several hundreds of picoseconds for larger negative voltages. Interestingly, the absorber carrier lifetime measured on samples C128, C133 and C134 are about a factor of three shorter than in sample A2109. As sample A2109 nominally presents the same indium content in the MQWs but a lower indium composition in the well barriers (see Table 2.2), the shorter lifetime of samples C128, C133 and C134 can be likely ascribed to a lower barrier E_b [169, 176, 177]. Band structure simulations give indeed an E_b for sample A2109 higher than for the other structures. The shortest measured lifetime is about 40 ps at $V_{AS} = -13$ V (sample C134).

According to Fig. 4.2 (b), the carrier lifetime saturates for large V_{AS} around 100 ps whereas simulations seem to suggest a much shorter lifetime (~ 10 fs). The charge carrier lifetime in a reverse-biased GaN-based MQW active region placed within a p - n junction has been measured in most studies on LED structures. In Fig. 4.3, the experimental (diamonds) and simulated (crosses) reported in the literature are depicted as a function of the applied bias. We can make a distinction between bluish and greenish structures. Note that as expected, the difference in the sweep-out processes between blue and green structures is attributed to the larger barrier height and barrier width that carriers have to overcome in green structures compared to blue ones. Therefore, the main decay pathways are the thermionic and radiative emission ones for low internal field structures whereas tunneling is the dominant process in high fields ones. In 2002, Jho *et al.* carried out an interesting and exhaustive study on the carrier lifetime in blue and green InGaN/GaN LED structures using pump-probe reflectivity [169, 178]. The carrier lifetime decreases with the reverse applied bias voltage and they reported about 10 ps and 2 ns at -16 V (2 ps and 200 ps at -30 V) for blue and green structures, respectively. Even if it was done for a really different kind of structure and material system, Malins *et al.* measured an absorption recovery time shortening from 62 ps down to 700 fs when the applied voltage is reduced from 0 to -10 V on InAs p - i - n QD structure [179]. They attributed this lifetime reduction to ultrafast thermionic and tunneling emissions. Pinos *et al.* reported a PL decay time of 580 ps for an applied bias voltage of -5 V by exciting an AlGaIn/AlGaIn LED structure with a mode-locked Nd:YAG laser [180]. This value is in good agreement with the one measured on our InGaIn/InGaIn MS-LDs (i.e., 300-1000 ps in Fig. 4.3 and values reported in Refs. [132, 133]). Park *et al.* reported a minimum PL lifetime of 125 ps for both an InGaIn/GaN LED structure (at $V_{AS} = -9$ V) and an InGaIn/InGaIn one (at $V_{AS} = -8$ V) [181]. Studying an InGaIn/GaN LED structure, Sizov *et al.* observed a decrease in the carrier lifetime associated with carrier tunneling from the active region when increasing the reverse applied bias [174]. They reported a carrier lifetime of about 200 ps at -10 V. For InGaIn/GaN-based MQW solar cells, Choi *et al.* using time-resolved PL also measured a reduction in the carrier lifetime by increasing the reverse applied

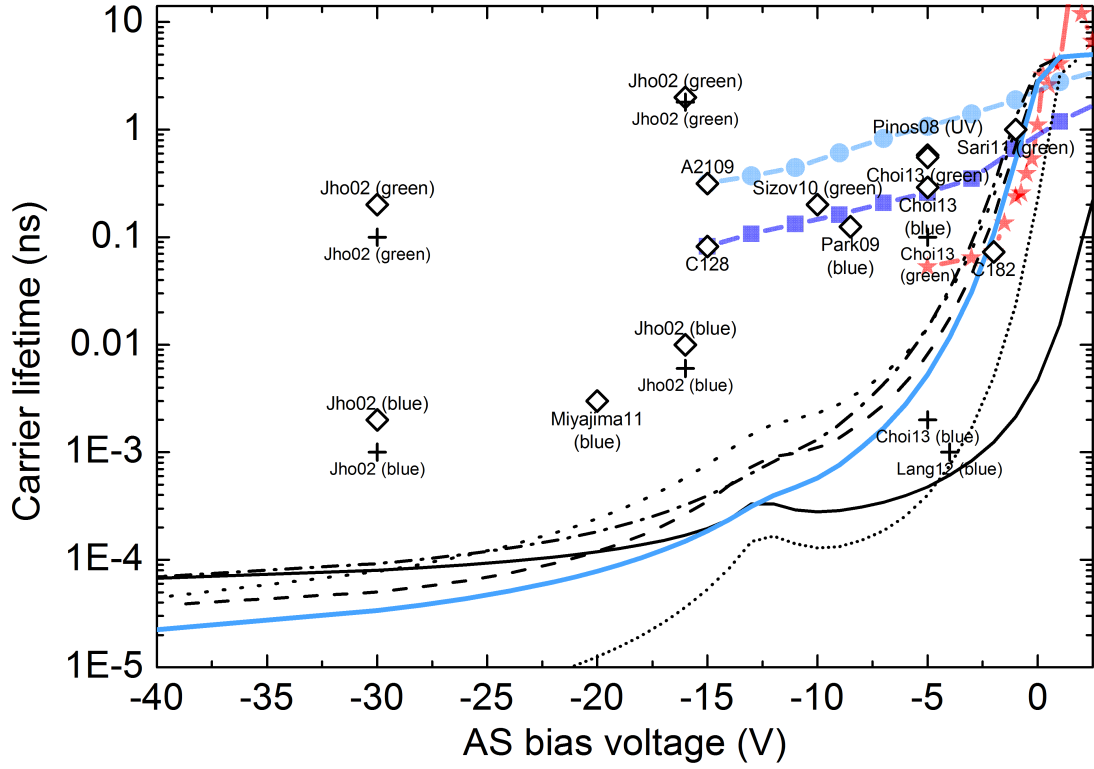


Figure 4.3: Absorber carrier lifetime τ_{AS} of sample A2109 as a function of V_{AS} calculated according to Shankar correction $T_{coll}^{[170]}$ (light blue continuous line), the hole correction (black continuous line), the excitonic correction (black dotted line), the Larsson correction $T_{coll}^{[182]}$ (black dash-dotted line), the Goldman correction $T_{coll}^{[183]}$ (black short-dotted line) and the Larkin correction $T_{coll}^{[184]}$ (black dashed line). The scattered points depict the experimental (diamonds) and the simulated (crosses) lifetimes reported in the literature.

bias voltage [177]. They reported 290 ps at -5 V for InGaN/GaN MQW structure with 17% of indium and 550 ps with 25% indium. More recently, Miyajima *et al.* measured an absorption recovery time of 3 ps at $V_{AS} = -20$ V by means of a pump-probe technique in which the absorber of an InGaN-based MS-LD is optically saturated [155]. The authors stated that the decrease in the absorption recovery time under reverse bias corresponds to the change in the carrier escape speed from the QWs [155].

For the sake of comparison we also carried out time-integrated and time-resolved PL experiments in collaboration with the group of Prof. B. Deveaud-Plédran at LOEQ-EPFL (PhD student Mehran Shahmohammadi and Dr. Gwénolé Jean Jacopin). We used the third harmonic ($853/3 \simeq 280$ nm) of a Ti:Al₂O₃ mode-locked laser (pulse width and repetition rate of 2 ps and 80.7 MHz, respectively) to excite an LED structure with a transparent ITO top *p*-contact. Sample C182 is also studied by ER spectroscopy (see Appendix A). The laser beam was focused down to a 5-10 μm spot on the sample surface. We estimate that the photogenerated carrier density was about $5 \cdot 10^{12} \text{ cm}^{-2}$ in the QW. The PL was analyzed with a 1200 grooves/mm grating followed by a streak camera

working in synchroscan mode. In Fig. 4.4 the streak camera traces for different applied biases and the respective extrapolated carrier lifetimes are shown. We observe a sharp quenching of the decay time around 0 bias as the applied bias is reduced from 2.5 down to -5 V. At the same time the peak emission wavelength blueshifts with applied bias. Unfortunately, we were limited to -5 V as the measured carrier lifetime falls well below the streak camera resolution, i.e., ~ 20 ps. Nevertheless, at -2 V the measured carrier lifetime is already below 80 ps, roughly a factor of 5 lower than the ones measured for sample C128 and 20 times lower than sample A2109 for the same bias. Note that these values are in good agreement with simulations (Fig. 4.3). Thus, according to our measurements on LED structures and those reported in the literature (Refs. [132, 133, 176]), we believe that the carrier lifetimes measured on the MS-LDs are overestimated by at least one order of magnitude [see Fig. 4.2 (b)]. In fact, in Ref. [133] it is proposed that the measured carrier lifetime is an upper limit of the actual lifetime due to trigger jitter limitation and the decay time of the electrical pulse. In order to sustain mode-locked emission that has been indeed observed in Ref. [133], the actual carrier lifetime is expected to be much shorter than 100 ps, approximately equal to the cavity roundtrip time (i.e., 20 ps). Hereafter, we propose several carrier emission corrections that can slow down the emission rates and provide a more reliable estimation for the actual carrier lifetime (see Fig. 4.3). Until now, only the electrons have been considered as the carriers that sweep out from the active region by tunneling and/or thermionic emission and that therefore contribute to the total carrier lifetime. According to what has been proposed in Refs. [174, 185], the calculated absorber lifetime when considering holes instead of electrons as charge

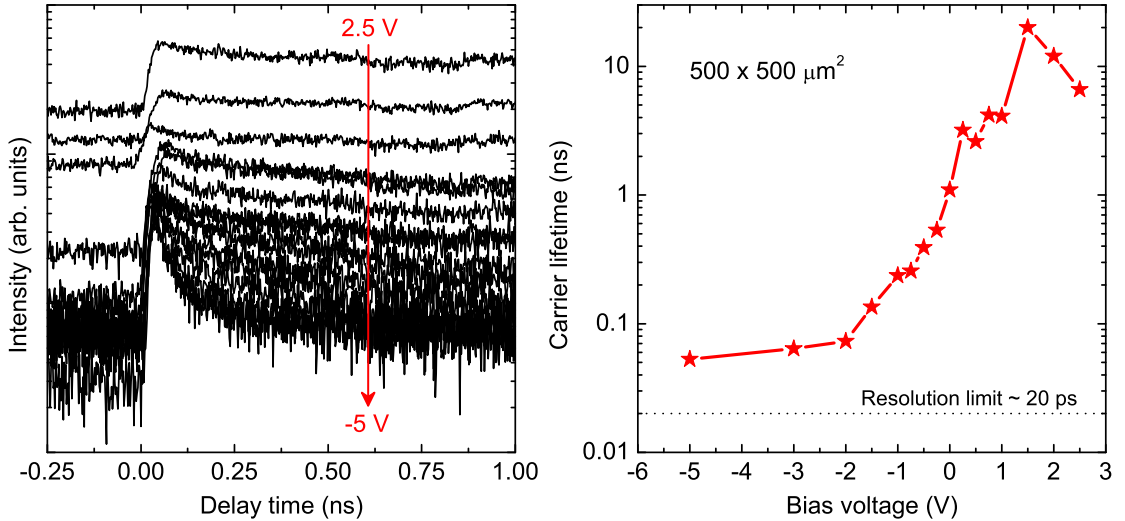


Figure 4.4: (a) Spectrally integrated streak camera traces for a $500 \times 500 \mu\text{m}^2$ LED from sample C182 at different bias conditions (semi-log scale). (b) Bias-dependent carrier lifetimes extrapolated from the electroluminescence decay traces shown in (a). These experiments have been carried out in collaboration with the group of Prof. B. Deveaud-Plédran at LOEQ-EPFL.

carriers is shown in Fig. 4.3 for sample A2109 (dashed line). The hole effective mass m_h is $1.423 m_0$ (Table 2.1) and typically, at V_{MIN} we have $E_b = 74$ meV and $h_1 = 13$ meV. Note that the hole effective barrier E_b has been calculated simply by applying the common anion rule that governs the band offsets of most semiconductors. In the specific case of an InGaN heterostructure the ratio E_{CBO}/E_{VBO} is fixed to 80:20. As can be seen in Fig. 4.3 (black continuous line), the calculated lifetime for holes is shorter than the one of electrons only before the flat-band condition (i.e., $V_{MIN}^{A2109} = -12.5$ V). In principle, the lower escape barrier E_b experienced by holes should shorten their carrier lifetime while the heavier effective mass m_h and their lower confinement energy h_1 would instead increase it. If we compare the hole lifetime with that calculated for electrons, we can thus state that there are two counteracting contributions when reducing the applied bias: the reduced escape barrier E_b implies a shorter lifetime for holes before flat-band conditions due to larger thermionic and tunneling emission rates whereas the heavier effective mass m_h and the lower confinement energy h_1 become of greater importance and increase accordingly the lifetime for larger negative voltages. Therefore, we can conclude that the sweep out mechanisms have a complex character and that one may consider both types of carriers [174].

In order to explain why the experimental carrier lifetimes are much longer than the calculated tunneling and thermionic emission times, Pinos *et al.* proposed to consider excitonic effects for the carrier dynamics in AlGaIn QWs [180]. This means to set aside the free carrier model and consider the impact of Coulomb interaction between electrons and holes. The exciton binding energy E_X^b in an InGaIn QW has been calculated according to the method described in Ref. [186] in which the binding energy is given by an integral (over the electron and hole coordinates perpendicular to the confining layers) of a prescribed function weighted by the squares of the electron and hole subband wavefunctions. Typically, E_X^b reaches the highest value for flat-band conditions (i.e., V_{MIN}) as the oscillator strength is maximum and values equal to 40 and 37 meV for samples A2109 and C128, respectively. For the sake of comparison, at $V_{AS} = 0$ the calculated exciton binding energy is 19 and 27 meV for samples A2109 and C128, respectively. The excitonic contribution is then simply multiplied to the escape emission terms (tunneling and thermionic) in eq. 4.1 as:

$$\tau_{therm,tun}^{ex} = \tau_{therm,tun} \cdot \exp\left(\frac{E_X^b}{k_B T}\right), \quad (4.5)$$

where $\tau_{therm,tun}$ are the thermionic and tunneling carrier lifetimes in the free carrier model. The exponential term represents the extra energy that has to be given to the system to dissociate the exciton and to allow the carriers escaping from the active region. The black dotted curve in Fig. 4.3 displays the corresponding carrier lifetime τ_{AS} for sample A2109. The excitonic lifetime is about a factor 2-4 longer than the one calculated for the free carrier model (light blue curve). For instance, at $V_{AS} = -15$ V the lifetime calculated according to the free carrier model τ_{AS} is equal to 185 fs whereas τ_{AS}^{ex} amounts to 769 fs. Clearly, the greatest impact is experienced for flat-band-conditions (simulated

$V_{MIN}^{A2109} = -12.5$ V), i.e., at the bias for which the carrier wavefunction overlap is maximum. Then, the higher the applied field the lower the exciton binding energy and the higher the probability to dissociate the exciton. Note that for a given external field, a narrow QW would imply excitons more difficult to dissociate.

Finally, as τ_{tun} is the most important contribution in eq. 4.1, one further remark can be made concerning the tunneling time. In the literature, the authors systematically consider the simple quasi-classical WKB approximation to analyze and to interpret the experimental data (see the exponential term in eq. 4.4). However, several alternative expressions can be found in the literature concerning the pre-exponential factor T_{coll} . Basically, these expressions represent different ways to describe how carriers trapped in the QWs “feel” the barrier through which they will tunnel. Generally, the classical expression that can be found in many quantum mechanics text books assumes that carriers in the QW region oscillate according to their energy e_1 via $T_{coll}^{[170]} = 2d_{QW}/v(z) = \sqrt{\frac{2m_{e,QW}}{e_1}}d_{QW}$ (see eq. 4.4). The higher the carrier energy the higher the oscillation frequency and hence the higher the tunneling rate [170]. Unfortunately, this expression overestimates the oscillation period of the carriers in the QW, especially for small d_{QW} , as it does not take into account the wave penetration in the barrier: at each oscillation the carriers collide with the barrier and may tunnel. For the sake of clarity and to facilitate comparisons, Larkin *et al.* proposed to split the tunneling lifetime into two contributions, i.e., a carrier collision time term T_{coll} and a carrier transmission probability term $|t|^2$ [184, 187]:

$$\tau_{tun} = T_{coll} \cdot \frac{1}{|t|^2} = T_{coll} \cdot \frac{\frac{m_{e,QW}}{m_{e,b}}E_b + e_1}{\sqrt{\frac{m_{e,QW}}{m_{e,b}}e_1E_b}} \cdot \exp\left(\frac{4}{3} \frac{\sqrt{2m_{e,b}E_b^3}}{\hbar q F_b}\right), \quad (4.6)$$

where the transmission term $|t|^2$ is calculated employing the formalism of propagating waves and reflection/transmission coefficients, and then approximated using the asymptotic behavior of the Airy functions assuming a sufficiently wide and high barrier [187]. Immediately we see that the actual tunneling lifetime obtained in eq. 4.6 differs from the quasi-classical WKB value by a non-trivial pre-exponential factor, usually larger than unity. Then, concerning the other pre-exponential factor T_{coll} , the expressions that can be found in the literature, in addition to the one used in eq. 4.4, are:

$$T_{coll}^{[182]} = \frac{2m_{e,QW}d_{QW}^2}{\hbar\pi} \quad [182, 185, 188, 189], \quad (4.7)$$

$$T_{coll}^{[183]} = \frac{1}{16} \left(\frac{E_{c,max}}{e_1}\right)^2 \frac{\hbar}{E_b} \quad [183], \quad (4.8)$$

$$T_{coll}^{[184]} = \frac{\frac{m_{e,QW}}{m_{e,b}} E_b + e_1}{2E_b e_1} \left(\frac{d_{QW} \sqrt{m_b E_b}}{\sqrt{2}\hbar} + \frac{E_{c,max}}{\frac{m_{e,QW}}{m_{e,b}} E_b + e_1} \right) \quad [184]. \quad (4.9)$$

$T_{coll}^{[182]}$ is widely used to interpret the experiments and basically it assumes a carrier confined in the well that oscillates back and forth with a corresponding velocity $v(z) = \frac{\hbar k_z}{m_{e,QW}}$ (as opposed to $e_1 = \frac{1}{2} m_{e,QW} v(z)^2$ for $T_{coll}^{[170]}$ in eq. 4.4) and with a perpendicular carrier wavevector $k_z = \frac{\pi}{d_{QW}}$ (perpendicular to the layers) in the case of an infinite potential barrier [182]. Using the same collision rate as for $T_{coll}^{[170]}$, i.e., $2d_{QW}/v(z)$, this leads to the expression given in eq. 4.7. However, as for $T_{coll}^{[170]}$, $T_{coll}^{[182]}$ still overestimates the collision rate because, especially for small d_{QW} values, most of the wavefunction extends in the barrier. $T_{coll}^{[183]}$ may also not be an accurate expression for the collision rate as it takes into account a rectangular barrier shape to evaluate the transmission coefficient. Larkin *et al.* consider the solution of the Schrödinger equation in the QW and adjust the WKB wave function to this solution [184]. This model ($T_{coll}^{[184]}$) provides a more accurate description for the carrier lifetime behavior since it considers the real extension of the carrier wavefunction inside the barrier (for more details see Refs. [184, 187]). However, as shown in Fig. 2 of Ref. [184], the accuracy of $T_{coll}^{[184]}$ compared to other expressions is tangible only for QW widths smaller than the Bohr radius (i.e., $d_{QW} \leq a_B$).

Figure 4.3 shows the carrier lifetime calculated according to the different correction factors for sample A2109. With the sole exception of $T_{coll}^{[183]}$, the $T_{coll}^{[182]}$ and $T_{coll}^{[184]}$ corrections predict a slightly longer carrier lifetime compared to $T_{coll}^{[170]}$. As previously mentioned, the discrepancy would have been more important for narrower wells ($d_{QW}^{A2109} = 4.5 \text{ nm} \simeq 1.36 \cdot a_B$). Nevertheless, we can conclude that by taking into account different contributions such as, e.g., the hole lifetime, excitonic effects, and/or improved collision expressions, the calculated carrier lifetime can be increased by more than one order of magnitude. This way, it can approach the picosecond range, which is expected for a GaN-based QW under a high reverse external bias.

Several ways to further reduce the carrier lifetime in the AS are worth mentioning. Staggered QWs are used in III-nitrides to enhance the spontaneous recombination rate especially for structures emitting in the green wavelength range [190]. Such a design can substantially increase the carrier escape rate from the reverse-biased AS by several orders of magnitude while, at the same time, maintaining high carrier localization in a deep QW in the forward-biased GS [191]. An intentionally *n*-doped active region (generally only the well barriers) is also found to further enhance the recombination rate in the QWs thus shortening the carrier lifetime [49, 192]. The growth of a poor quality layer (especially well barriers) would also decrease the carrier lifetime.

4.2 Self-pulsation

During the Femtoblue project, the lasing dynamics in MS-LDs have been mainly investigated in collaboration with Dr. Dmitri L. Boiko at CSEM in Neuchatel and with Prof. Ulrich Schwarz at IAF in Freiburg. In Boiko's laboratory, the output lasing emission is detected with a 50 GHz photodetector and analyzed with a sampling oscilloscope triggered with pump current pulses. At IAF, a streak camera system with a temporal resolution better than 1% of the set time range (~ 2 ps) and a spectral resolution of 0.2 nm is used.

We observed regimes of gain switching and relaxation spiking as well as periodic regimes of SP and Q-switching with a repetition frequency ranging from 1 to 5 GHz when increasing I_{GS} and varying the absorber bias V_{AS} (Fig. 4.5). Although the pulsed emission regime is fairly complicated, we will develop a qualitative picture of the overall underlying physical mechanisms according to the simulations carried out in Sec. 2.3.4.

First, it is important to specify in which conditions the MS-LD is operated. In Sec. 2.3.4, we have emphasized how the carrier-free absorption α_0 , the absorber/total cavity length ratio L_{AS}/L_{TOT} , and the absorber carrier lifetime τ_{AS} govern the lasing dynamics of the device (see Fig. 2.14). However, during those simulations, α_0 , L_{AS}/L_{TOT} and τ_{AS} have been considered as free parameters that can be arbitrarily changed. In fact, this is not completely the case. With the exception of L_{AS}/L_{TOT} , which is imposed by the process (see Sec. 2.4), α_0 and τ_{AS} strongly depend on the absorber applied bias V_{AS} via the QCSE that take place in the AS MQWs. Indeed, as shown in Sec. 3.3, when the reverse bias is increased, the carrier-free absorption α_0 exhibits a maximum at V_{MAX} and then a minimum at V_{MIN} before increasing again for very large negative voltages (see Fig. 3.6). Moreover, we have seen how these V_{MAX} and V_{MIN} values are imposed by the internal field \mathbf{F}_{int} : the higher the field the larger the reverse biases (e.g., $\mathbf{F}_{int}^{A2109} > \mathbf{F}_{int}^{C128}$ hence $V_{MAX,MIN}^{A2109} < V_{MAX,MIN}^{C128}$). Then, in Sec. 4.1, we have shown how the carrier lifetime τ_{AS} monotonically decreases with the applied bias (Fig. 4.2). Thus, it is important to

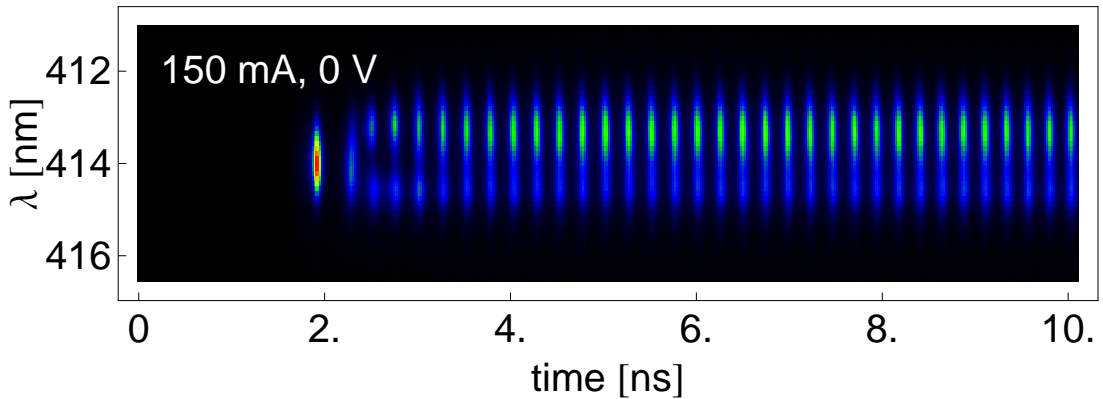


Figure 4.5: Example of a streak camera trace for stable SP at $V_{AS} = 0$ and $I_{GS} = 155$ mA for sample A2109 MS-LD. [132]

keep in mind how each of these parameters behaves individually to understand later on how their complex interplay affects the lasing dynamics of GaN-based MS-LDs for a given bias voltage range.

MS-LDs (sample A2109) have been excited with 100 ns electric pulses at a repetition frequency of 10 kHz. The light output was measured with a streak camera operating in single-shot mode [69]. Note that for this sample V_{MIN} is about -10 V while V_{MAX} around -3 V [see Figs. 3.6 and 3.9 (a)]. Stable SP is observed for absorber biases between 0 and -9 V and for driving current up to twice I_{th} . The oscillation frequency ranges from 1 to 5 GHz [Figs. 4.6 (a) and 4.6 (b)]. For long absorber lengths (i.e., $L_{AS} = 100$ and $150 \mu\text{m}$), a transition to cw emission is experienced for currents already below twice I_{th} . This transition shifts to higher currents when increasing the reverse V_{AS} [dashed curves in Figs. 4.6 (b)]. When increasing the pump current, the pulse width shortens down to a plateau of about 20 ps whereas when the reverse bias gets larger, it becomes longer [Figs. 4.6 (c) and 4.6 (d)]. The peak power increases with the pump current but it decreases if the reverse bias is varied from 0 down to -9. The maximum peak power measured is 1.1

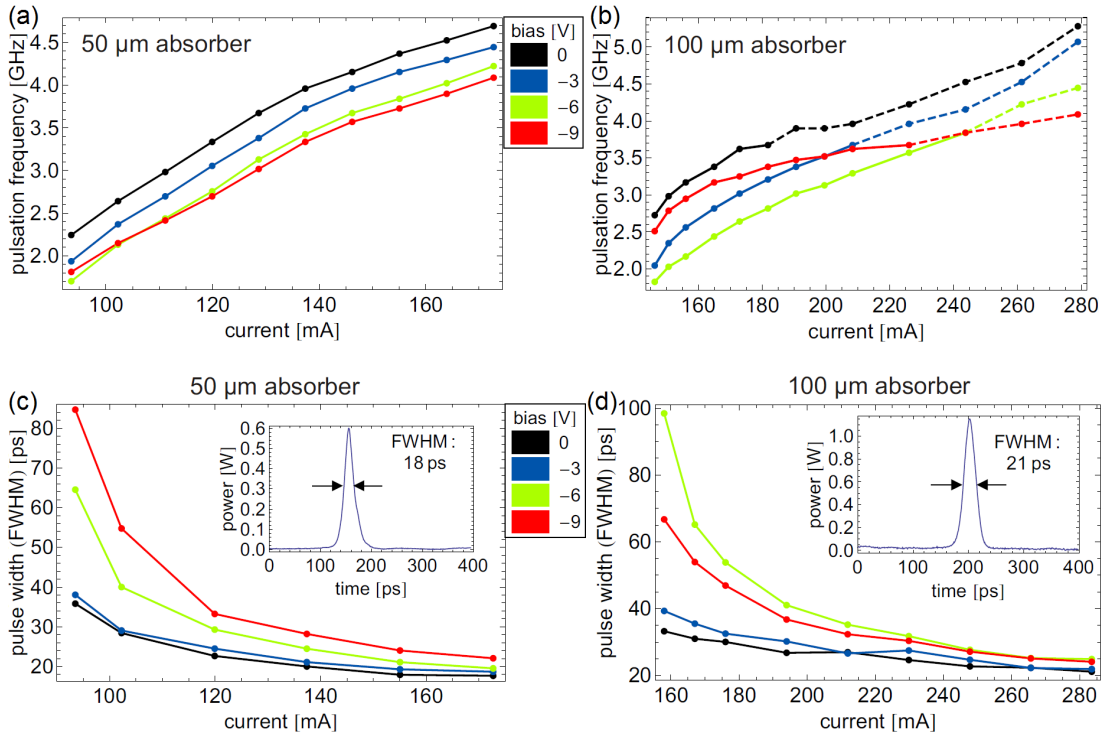


Figure 4.6: Oscillation frequency f_{SP} as a function of I_{GS} at different bias voltages V_{AS} for sample A2109 MS-LD with (a) $L_{AS} = 50 \mu\text{m}$ and (b) $L_{AS} = 100 \mu\text{m}$. The dashed lines in (b) indicate the current range where the oscillations become unstable and a quasi-steady-state emission is obtained. Width of initial pulse τ_{SP} as a function of I_{GS} at different bias voltages V_{AS} for a sample A2109 MS-LD with (c) $L_{AS} = 50 \mu\text{m}$ and (d) $L_{AS} = 100 \mu\text{m}$. The insets show the pulse shape at (c) 173 mA and (d) 283 mA, respectively, at $V_{AS} = 0$. The figure is adapted from Ref. [69].

W at $I_{GS} = 283$ mA and at $V_{AS} = 0$ for $L_{AS} = 100$ μm . The corresponding maximum pulse energy is 23 pJ. Note also that the emission spectrum in self-pulsating operation is broader than a typical cw emission for a standard single-section LD [about 2 nm broad, compare with Fig. 2.5 (c)]. A detailed description of SP pulse parameters occurring in these MS-LDs can be found in Refs. [69] and [132].

The results for sample A2109 can be understood as follows. SP is obtained at $V_{AS} = 0$ while at larger reverse biases ($V_{AS} < -9$ V) pulsations are no longer observed despite shorter carrier lifetime (see Figs. 4.2 and 4.6). When approaching flat-band conditions ($V_{MIN}^{A2109} = -10$ V) AS absorption decreases due to a larger energy detuning between absorber and gain sections [see Fig. 3.3 (b)]. As explained in Sec. 2.3.4, for a given pump current, a smaller α_0 corresponds indeed to a lower emission intensity, a higher SP frequency and a longer pulse width as the absorber “is not working properly”, i.e., a too low absorption in the cavity does not allow the system to stabilize the ROs (see the discussion related to Fig. 2.14). Note that despite a lower absorption, trapping and detrapping of point defects can also help to stabilize the system thus enabling the onset of regular emission of a train of pulses [143]. On the other hand, SP is obtained at $V_{AS} = 0$ despite the long carrier lifetime. Indeed, α_0 is still large enough to sustain self-pulsating oscillations thanks to the proximity of V_{MAX} (i.e., -3 V). This ability to produce stable SP at such moderate absorber bias makes the measurements reported in Ref. [69] particularly interesting.

Now let us turn our attention to sample C128. Recorded sampling optical oscilloscope traces are displayed in Fig. 4.7 (a) for a constant pump current $I_{GS} = 187$ mA and for different V_{AS} biases. Figure 4.7 (b) shows detected traces at a constant absorber bias $V_{AS} = -8$ V and for various currents. The device was driven with 20 ns long current pulses at 1% duty cycle applied to the GS. Note that in Fig. 4.7, the pulse shape is distorted and the SP frequency is chirped during the pump pulse due to retroreflections and interference effects occurring in the RF cable from the current source to the GS.

It can be seen in Fig. 4.7 (a) that SP takes place only for large negative biases (below -7 V). It is proposed that for such a bias range, the absorption in the AS MQWs is strong enough while the carrier lifetime shortens dramatically due to the large electric field present in the barriers, which favors carrier tunneling [131]. In addition, we observe an increase in the SP frequency when decreasing the reverse bias. Actually, two distinct features of SP can be distinguished on the oscilloscope traces: at moderate reverse bias ($V_{AS} = -9$ V), SP has the character of undamped ROs whereas at larger reverse bias ($V_{AS} = -11$ V) self-Q-switching takes place (compare simulated curves in Figs. 2.10 and 2.12). As already mentioned at the end of Sec. 2.3.4, Mirasso *et al.* underlined how the amount of spontaneous photon emission (proportional to the pump current) in a cavity with an absorbing medium allows discriminating between two distinct regions in the SP frequency regime [143]. In the specific case of a MS device, these different SP patterns are related to an increase in the carrier tunneling rate while applying a reverse bias, which leads to a faster depopulation of the AS. For this reason, the MS-LD exhibits a self-Q-switching-like regime at the expense of its undamped RO character at large

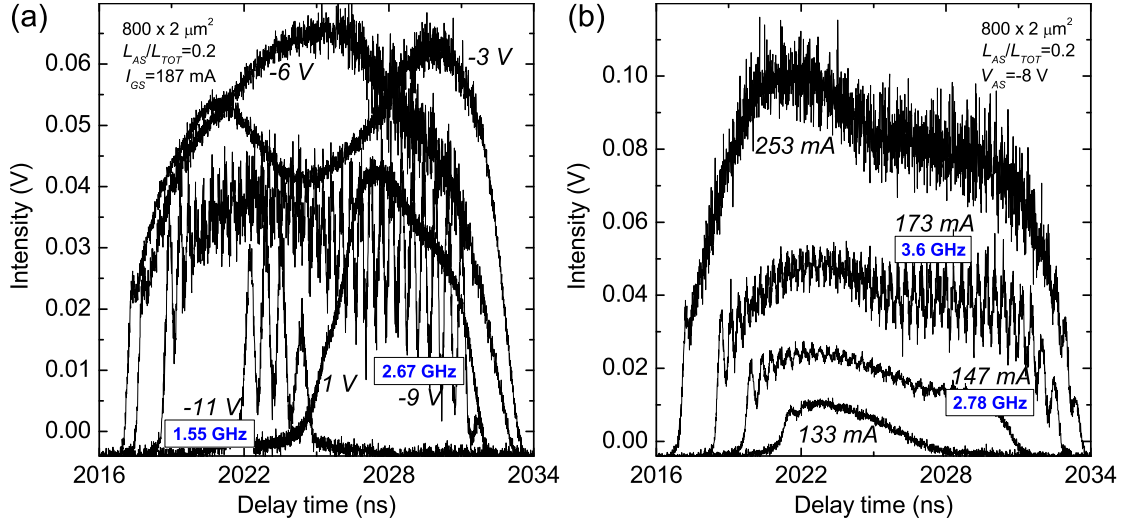


Figure 4.7: Sampling optical oscilloscope traces (a) at constant I_{GS} for different V_{AS} and (b) at constant V_{AS} for different I_{GS} (sample C128).

negative biases and slows likewise the frequency [131]. These findings are in contrast with the results reported in Ref. [127], where an almost constant pulsation frequency around 1 GHz was observed as a function of V_{AS} and I_{GS} . On the other hand, this mechanism is confirmed by the simulations (Fig. 2.14).

Hereafter, we would like to stress the complex interplay between absorption and carrier lifetime in the AS for sample C128. Note that for this sample V_{MIN} is expected around -3 V while V_{MAX} occurs around 1 V [see Figs. 3.6 and 3.9 (a)]. In Figs. 3.12 (c) and 3.12 (d), it can be seen that the amount of absorption at the lasing wavelength (419 nm) is similar for $V_{AS} = -9$ V and $V_{AS} = 1$ V. This is also confirmed by the simulated carrier-free absorption curves for sample C128 plotted in Fig. 3.6. However, SP is observed only at larger reverse biases and not at 1 V. One can thus conclude that in this case the absorber carrier lifetime governs the dynamics of the device. Below a certain absorber bias (e.g., $V_{AS} < -7$ V in Fig. 4.7), neither the carrier-free absorption nor the carrier lifetime are high or short enough to sustain self-pulsating oscillations: at $V_{MAX} = 1$ V the absorption is high but the carrier lifetime is too long whereas at $V_{MIN} = -3$ V the carrier lifetime is short, but the absorption is minimum (compare Figs. 3.6 and 4.2). As previously mentioned, this is in contrast with sample A2109 reported in Ref. [132], where a different internal field leads to a different band structure and hence to a different behavior upon the external applied bias. Therefore, in order to obtain a MS-LD with a stable self-pulsating emission at moderate absorber biases, the indium composition in the active region should be carefully chosen as it will impose on one side the position of V_{MAX} (to be read as available carrier-free absorption) via the total polarization field F_{int} and on the other side the shortening of τ_{AS} via the height of the escape barrier E_b (to be read as absorption recovery time). Special designs of the active region such as, e.g., non-radiative traps in the well barriers or MQW structures that favor carrier

tunneling emission would also allow to further optimize this feature independently from the applied bias V_{AS} .

Figure 4.7 (b) displays an increase in SP frequency together with I_{GS} . Under high current injection, the photon density in the cavity increases as well as the number of photogenerated carriers in the AS. At some point, deep carrier depletion in the absorber can no longer occur between the pulses thereby preventing the establishment of self-Q-switched oscillations [131]. As supported by the simulations [see Fig. 2.14 (c)], this allows for a faster modulation of the SP frequency [143]. These considerations are consistent with the results reported in Ref. [132] where SP excitation is attributed to a stabilization of the ROs by the AS, as confirmed by the square root dependency of the oscillation frequency on the current [88]. Note that SP disappears for very high current injection in the GS (e.g., 253 mA). The large density of photogenerated carriers in the AS hinders the absorber carrier depletion in between the pulses to a level necessary for periodic pulse production. This is also depicted in Figs. 2.11 and 2.14 for the simulated SP traces as the establishment of a quasi-steady-state emission.

To summarize, the SP regime in InGaN-based MS-LDs is inhibited if the device is driven close to a *no-absorber-like* configuration. This could be the case: (i) for a large energy detuning between the MQW ground state in the AS and the lasing wavelength, which is maximum for flat-band conditions [Fig. 3.3 (b)], (ii) at forward and small reverse biases if the AS carrier lifetime is too long (Fig. 4.2), (iii) under high injection current, which prevents sufficient carrier depletion in the absorber [Fig. 2.11 (b)] [131].

4.3 Mode-locking

Besides IAF in Freiburg and CSEM in Neuchatel, the laboratories equipped for ultrafast measurements in the Femtoblue consortium were the group of Profs. I. White and R. Penty at UCAM in Cambridge and the one of Prof. Vasil'ev at the P.N. LPI in Moscow. The former set-up consists in a 35 GHz visible photodiode connected to a 50 GHz bandwidth RF spectrum analyzer and in an in-house collinear autocorrelator or visible monochromator with an estimated resolution bandwidth smaller than 50 pm. The LPI set-up consists in a streak camera with a temporal resolution of about 1.5 ps and an autocorrelator. Depending on the resonator length, we observed pulsed emissions in the mode-locked regime with a repetition frequency of several tens of GHz in our monolithic cavities. Note that sometimes mode-locking is in competition with self-pulsating behavior as the saturable absorber in the cavity should be operated at proper bias and current conditions to emit a clean phase-locked train of pulses [193]. In certain cases this leads to a so-called self-Q-switched mode-locking [176]. Usually, self-starting mode-locking needs a large carrier-free absorption α_0 in the AS, a short absorber carrier lifetime τ_{AS} and also a large bandwidth and a uniform spectral profile of the optical gain [133]. In principle, the larger the spectrum the shorter the mode-locked pulses as more modes are experiencing optical gain and can thus contribute equally to the formation of pulses. Note

that a larger inhomogeneous broadening would inhibit mode competition thus leading to a multimode operation and even a dual color mode-locking [194]. QD-based devices are for instance more suitable to observe such a multi-color pulsed emission thanks to their wide spectral bandwidth due to inhomogeneous broadening as a result of the dot size dispersion [195].

Peter Vasil'ev reported a first study on passive mode-locked monolithic MS-LDs carried out on samples C128, C133 and C134 (see Table 2.2) in Ref. [133]. The repetition frequency is in the range of 40 to 90 GHz with pulses as short as 3-5 ps with peak powers of around 320 mW. In the paper it is shown how the period of these high-speed pulsations corresponds to the cavity round trip time given by eq. 2.37 and is independent of the driving conditions thus indicating a mode-locked regime (as opposed to SP). For instance, a MS-LD with a total cavity length L_{TOT} of 1 mm and an absorber length L_{AS} of 150 μm exhibits a repetition frequency of 48 GHz (21.1 ps) with a pulse width of 6-10 ps and

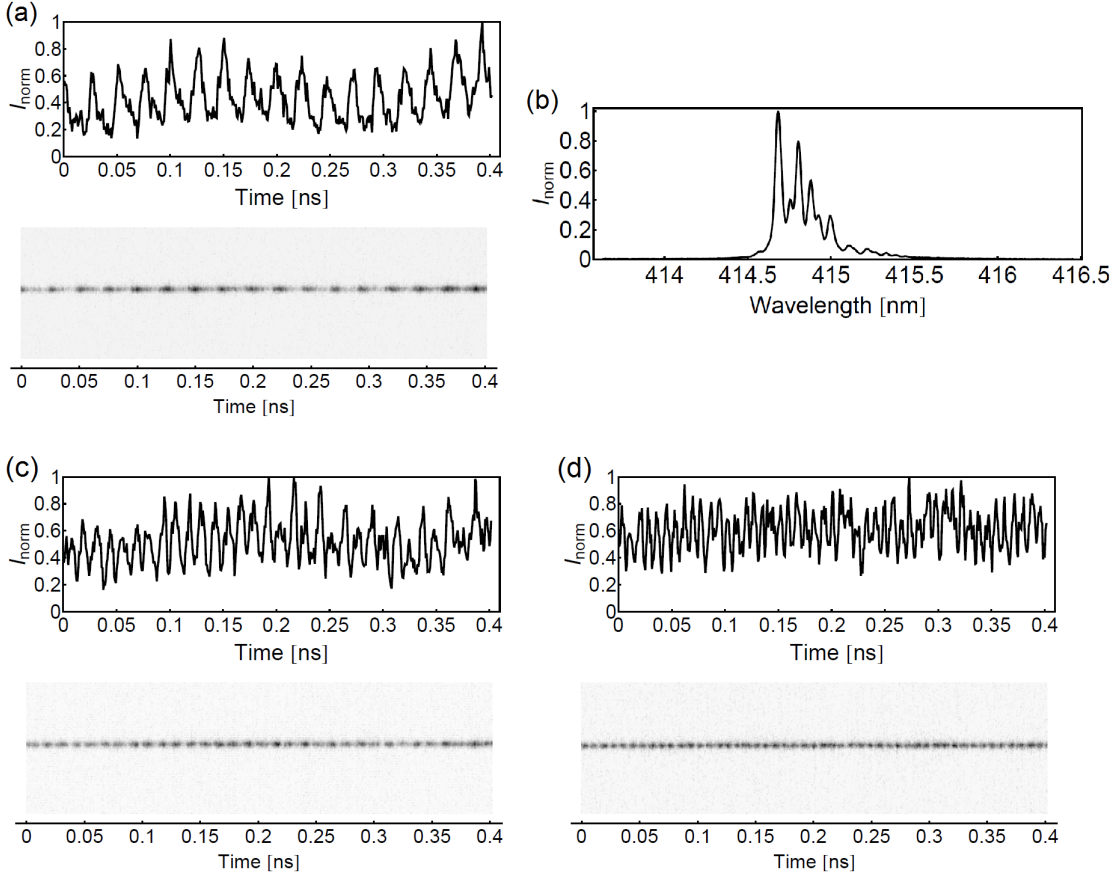


Figure 4.8: Streak camera traces of a center-absorber MS-LD made from sample C128 with $L_{TOT} = 1.2$ mm and $L_{AS}/L_{TOT} = 0.2$ with a pulse repetition frequency of (a) 40 GHz (at $V_{AS} = 0$), (c) 82 GHz (at $V_{AS} = 0$) and (d) 122 GHz (at $V_{AS} = -6$ V). (b) Lasing spectrum of (a) integrated over numerous shots showing several longitudinal modes, which contribute relatively homogeneously to passive mode-locking. [176]

minimum peak powers of 250 mW. Cavities of 600 and 1200 μm are then mode-locked at 92.5 (10.8) and 40.3 (24.8) GHz (ps), respectively. Mode clustering due to low-frequency Q-switching superimposed on mode-locked pulses is pointed out as a possible reason for the relatively large (compared to the theory) time-bandwidth product of the observed pulses (i.e., equal to 2.4). However, as the shortest pulse widths have been observed in the shortest cavities, it seems that group delay dispersion in the QW gain medium is still the main cause for pulse broadening.

Together with Thomas Weig (IAF) and Dr. Jean-Michel Lamy (LASPE-EPFL), we observed on the set-up of Prof. Schwarz passive mode-locking in our MS-LDs (samples C128, C133 and C134) with repetition frequencies ranging between 34 and 92 GHz [176]. At specific driving conditions, a competition between mode-locking and SP is observed, especially for high pump current and large absorber biases. Note that in short cavity length devices in which the cavity round trip is extremely short (~ 10 ps), stable mode-locking has been more challenging to observe as SP might take over. Passive mode-locking at the fundamental repetition frequency of 92 GHz (10.9 ps) for a resonator cavity of $L_{TOT} = 450 \mu\text{m}$ and $L_{AS} = 150 \mu\text{m}$ at $V_{AS} = -8.5$ V and for $I_{GS} = 660$ mA has been obtained. Passive mode-locking at the fundamental repetition frequency of 40 GHz (25 ps) has been also observed for a resonator cavity of $L_{TOT} = 1.2$ mm and $L_{AS} = 240 \mu\text{m}$ at $V_{AS} = 0$ [Fig. 4.8 (a)]. Interestingly, on such cavity lengths and with a center-absorber design, mode-locking at higher harmonics frequencies may occur. Unfortunately, these ultrafast oscillations were unstable along the electric pulse. Figures 4.8 (c) and 4.8 (d) show mode-locked traces at the second harmonic frequency (81 GHz) at $V_{AS} = 0$ and at the third harmonic frequency (122 GHz) at $V_{AS} = -6$ V. Note that the integrated spectrum shows a broad emission (due to the phase-locked modes) but also strong mode clustering 2-3 times larger than the fundamental mode-spacing [Fig. 4.8 (b)]. In Ref. [176] it is proposed that the competition between harmonics leads to large supermode noise under continuous pumping. As for SP, these results are particularly interesting and important as they show how a proper design of the active region can indeed allow to obtain a monolithic mode-locked MS-LD also operating at moderate low absorber bias (e.g., $V_{AS} = 0$) for which the absorber recovery lifetime is still relatively high.

Finally, Vojtech Olle, a PhD student at UCAM, reported passive and hybrid mode-locking on a MS-LD from sample C133 in Ref. [134]. The device is 1.5 mm long with an absorber section L_{AS} of 50 μm and emits at 422 nm. The repetition frequency under passive mode-locking is about 28.6 GHz with a peak power of 37 mW and a pulse width of 8 ps for $V_{AS} = 0$ and $I_{GS} = 138$ mA. On the contrary, under hybrid mode-locking the pulse width is reduced to 4 ps while the peak power is increased to 72 mW. Furthermore, from the autocorrelation trace it is pointed out that most of the laser output power ($\sim 90\%$) is in the main mode-cluster producing perfect mode-locked pulse trains.

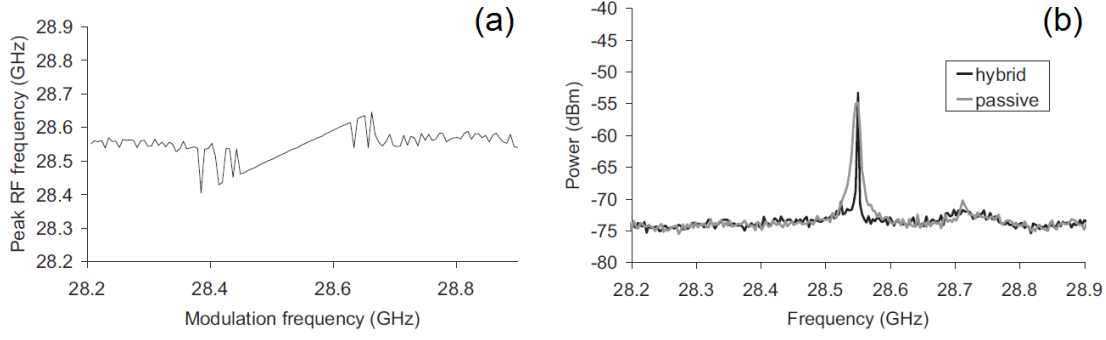


Figure 4.9: (a) Pulse repetition frequency as a function of modulation frequency for hybrid mode-locking and (b) passively and hybrid mode-locked RF spectra. [134]

Summary of the results

Self-pulsation and passive/hybrid mode-locking at different pulsation frequencies have been demonstrated in our InGaN-based MS-LDs in a monolithic configuration without the implementation of an external cavity. In this chapter, we have shown how the complex interplay between the absorption and carrier lifetime in the AS MQWs governs the dynamic features of the devices. Both experiments and modeling predict a monotonic and exponential decrease in the carrier lifetime when increasing the applied reverse bias V_{AS} . The main mechanism responsible for the shortening of the carrier lifetime at large reverse biases is the high carrier tunneling rate through the well barriers due to the strong tilt of the MQW band structure. At $V_{AS} = -15$ V (i.e., above the expected flat-band conditions), the measured lifetime amounts to several tens of picoseconds whereas the simulated one lies in the picosecond range. Different effects that can slow down the escape/emission rates and provide a more reliable estimation for the actual carrier lifetime (e.g., hole contribution, excitonic effects, improved barrier collision expressions) have also been considered. As predicted by the model (see Sec. 2.3.4), we were able to control the self-pulsating parameters by means of the driving parameters, i.e., the applied bias V_{AS} and the pump current I_{GS} . V_{AS} controls the carrier-free absorption α_0 and the carrier lifetime τ_{AS} in the AS while I_{GS} is responsible for the optical pumping degree of the total absorption α_{AS} . Self-pulsed emission is obtained only for strong absorption (i.e., higher than 50 cm^{-1}), short lifetime (i.e., shorter than 1 ns) and low injection regimes (i.e., lower than twice the threshold current). No pulsation is observed for flat-band conditions (V_{MIN}).

5 Superradiance and superfluorescence: application to III-nitride semiconductors

Let us first define what superradiance (SR) and superfluorescence (SF) are.

Superradiance (SR). *Superradiance is the cooperative emission of a system composed of $N \gg 1$ identical stationary emitters that are excited by a coherent pulse into a correlated state possessing a macroscopic electric dipole and that emit a radiation pulse with an intensity proportional to N^2 [196, 197].*

Superfluorescence (SF). *Superfluorescence is the cooperative spontaneous emission of an emitter system that is initially excited with a net zero macroscopic dipole moment and with a uniform population difference between the excited and the fundamental states. It spontaneously creates phase correlations between the N elementary dipoles leading to a combined macroscopic dipole which gives rise to a pulse whose maximum intensity is proportional to N^2 (as for SR) [197].*

Basically, it is possible to distinguish between SR and SF depending on the initial conditions of the emitter ensemble: in the superradiant case the ensemble of emitters are *coherently prepared* in the excited state whereas in the superfluorescent case the system consists in *incoherently prepared* excited emitters. In this sense, SF is intrinsically a quantum process since it is initiated by the “noise” arising from spontaneous emitted photons [197]. In the literature, most of collective spontaneous emission studies deal with SF rather than SR. However, many authors do not make the distinction between the two cooperative phenomena and wrongly refer in a generic way to a “superradiant emission”. It is interesting to see how this general misunderstanding, which sometimes leads even to strong disagreements, involves also the “founding fathers” of the domain, as this excerpt from a discussion, which occurred during the “Cooperative Effects Meeting” at Redstone Arsenal in 1976, shows [198]:

Chapter 5. Superradiance and superfluorescence: application to III-nitride semiconductors

T. A. DETEMPLE: What used to be called a superradiant laser is now called a superfluorescent laser; can we come to some agreement on the words we use to describe these phenomena?

R. BONIFACIO: The physics involved is different: one can distinguish superfluorescence from superradiance by their second moments.

J. H. EBERLY: The physics is different? The distinction should be experimentally feasible.

M. S. FELD: Let me find a place where we agree.

R. BONIFACIO: Nothing.

In this chapter, we will give insights into the superradiant mechanisms that govern the dynamics in semiconductors. In particular, attention will be paid to the case of III-nitrides. First, the motivations and the state of the art for SR and SF heterostructures are highlighted. Then, a brief introduction to the theory behind SR and SF is presented, especially concerning the model developed by Dicke, who studied for the first time the cooperative spontaneous emission from an ensemble of excited emitters interacting with each other via the radiation field. Finally, experimental tests on the possibility to obtain a superradiant emission from III-nitride heterostructures via both optical and electrical pumping are reported.

5.1 Motivation

Since 1954, the year in which R. Dicke published his famous pioneering paper, superradiance, i.e., the cooperative radiative decay of an ensemble of quantum emitters, has been widely investigated both theoretically and experimentally [196]. SR is substantially different from other short pulse emission mechanisms (e.g., SP and mode-locking) in LDs as it should allow us generating ultrashort pulses (hundreds of femtoseconds) with record optical peak powers (hundreds of watts) without even the implementation of a standard laser cavity resonator [199]. Indeed, as opposed to standard LDs, for which such high-power subpicosecond pulses can be achieved only by sophisticated technology and pulse processing techniques, SR is inherent to the semiconductor active medium itself [200].

Possible bio-medical applications that would benefit of the compactness and performances of a SR semiconducting source are coherent anti-Stokes Raman spectroscopy [201], terahertz time domain spectroscopy of DNA [202] and fluorescence lifetime imaging in biological samples [203]. Another interesting application is in ultrahigh stability atomic clock [204]. Then, SR emission could be achieved at any wavelength thanks to wide direct bandgap materials covering a broad spectral range and also in indirect bandgap

semiconductors, like Ge and Si. Indeed, this is what Belyanin *et al.* proposed in Ref. [200]: if we managed to inject a sufficiently large amount of carriers in the direct valley of such materials to initiate SR recombinations, nearly all carriers would contribute to the SR emission of femtosecond pulses since the SR recombination timescale is much shorter than the intraband scattering to the other lower but indirect valleys. In addition to all these practical applications, SR emission in semiconductors is intriguing from a mere physical point of view as it involves many fundamental interesting physical mechanisms such as, e.g., the spontaneous build-up of coherence in a quasi-two-level system.

Concerning the specific case of III-nitrides, they are potentially excellent candidates for observing macroscopically coherent effects in solids especially thanks to their very large exciton binding energy [19] and Rabi coupling constant at low carrier densities, their oscillator strength more than five times higher than in III-arsenides [205], and their robustness to very high current injection. Note that the establishment of SR emission would not be precluded by the harmful efficiency droop experienced by III-nitrides under high injection (see discussion below Fig. 2.6 concerning the ABC model) as the carrier non-radiative recombination timescale is much longer than the cooperative one. However, the fair electrical conductivity of GaN-based devices may induce device heating at very high pumping rate required for SR thus preventing femtosecond pulse emission [206].

5.2 State of the art

The first to describe and give the mathematical basis of SR was R. Dicke in 1954 [196]. In his seminal paper, he described for the first time a phenomenon where the probability to emit a photon depends on the states of other molecules that interact within a common radiation field that are located within a volume whose dimensions are small compared to the optical wavelength λ of interest (i.e., $V \ll \lambda^3$). The single quantum-mechanical system of N two-level atoms radiates with a maximum intensity equal to N^2 and Dicke called it “superradiant gas”. Subsequently to this paper, several theoretical and experimental studies have been carried out on SR mostly in quantum optics.

A few decades later, F. Arecchi and E. Courtens extended the model of Dicke SR by including propagating effects imposed by the finite velocity of light in the system [207]. They showed how the radiation field that mediates the cooperative emission of an ensemble of atoms has to operate at a timescale shorter than the SR pulse one in order to involve the whole atoms in the collective emission. Shortly after, N. Rehler and J. Eberly got rid of the volume limitation imposed by R. Dicke and considered SR for atoms located in an extended sample with various geometrical shapes [208]. In 1973, Skribanowitz *et al.* observed the first SR pulse emitted at RT from an optically pumped HF gas at millitorr pressures [209]. In 1975, according to the experiments of Skribanowitz, R. Bonifacio and L. Lugiato published a general non-perturbative treatment of cooperative emission in systems composed of N two-level atoms [197] and, in a subsequent paper,

Chapter 5. Superradiance and superfluorescence: application to III-nitride semiconductors

a fully quantum-mechanical treatment of the phenomenon known as SF [210]. They showed how generalized Maxwell-Bloch equations for the envelopes of the radiation inside the active volume and the polarization can be reduced to a simple pendulum equation. According to this simple model, two important conditions are required for SF to occur: (i) dephasing processes should occur on a time scale much larger than the characteristic time of the cooperative emission and (ii) cooperative spontaneous emission dominates the stimulated one, which exhibits radiation intensity proportional to N [197]. In 1982, Gross and Haroche reported a long and exhaustive study of SR in which they discussed the case of the coupling of N initially inverted atoms with a fictitious spin of $1/2$ from a quantum-mechanical point of view [211]. They showed that as the system cascades down from the fully symmetrical state (experienced at the beginning of the SR process where all atoms are in the upper excited level) to the ground state, the rate of emitted photons strongly increases due to the emergence of correlation between the dipoles of different atoms (i.e., the formation of a global radiating dipole). Shortly after, Florian *et al.* demonstrated the formation of a SR state in a highly excited KCl:O_2^- crystal [212] while Zinov'ev *et al.* observed SR emission from a diphenyl crystal containing pyrene [213]. In 1989, J. Maki *et al.* reported a quantum-mechanical treatment of the influence of collisional dephasing processes on the statistical properties of SF by varying the temperature of a KCl:O_2^- sample [214]. The authors demonstrated how superfluorescent and amplified spontaneous emission regimes are in competition when the collisional dephasing rate is varied.

Concerning SR in semiconductors, many studies have been published over the last 15 years, mostly theoretical ones and on the GaAs material system. In 1997, and afterward in 2003, Belyanin *et al.* discussed the establishment of SR in an AlGaAs/GaAs structure within a theoretical approach [200, 206, 215]. In agreement with the predictions of J. Maki [214] for a more general quantum system, Belyanin *et al.* pointed out for the first time the main issue when aiming at SR in a semiconductor: the very short incoherent relaxation time T_2 of the polarization (mainly due to scattering processes) that amounts to about 100-300 fs. To prevail the collisions destroying the phase of oscillating dipole moments in a MQW heterostructure, Belyanin *et al.* proposed to use a very low Q -factor cavity, a few tens of micrometers long, under a very high pumping rate, for which lasing was not possible [215].

In the literature, during the past decade, there have been several groups claiming evidence for superradiant emission occurring in semiconductor heterostructures. So far, neither direct evidence for the crucial N^2 -signature nor self-phasing process involved in SF have been provided. For instance, P. Vasil'ev claims to have obtained a femtosecond SR emission in a GaAs/AlGaAs-based MS-LD by analyzing the experimental data on the basis of the formation of non-equilibrium coherent BCS-like states in a system of collectively paired electrons and holes [199]. This author observed a 200 fs pulse width, a narrow far field emission and a record peak power of 230 W. These features *could* be ascribed to SR but not in a certain and unambiguous way as the author itself admits “despite of some very unusual features of the SR in semiconductors, SR has become the

only explanation that accounts reasonably well for the available experimental results” [199]. Concurrently, Jho *et al.* reported the first observation of SF from a dense photo-excited electron-hole plasma in InGaAs/GaAs MQW as evidenced from the resulting spectral, spatial, and statistical features of the luminescence [216, 217]. To promote the formation of a dense electron-hole plasma in the active region they employed intense femtosecond laser pulses combined with a strong perpendicular magnetic field in order to laterally confine the carriers and increase the DOS thanks to Landau quantization. More recently, Timothy Noe II *et al.* reported intense, delayed bursts of coherent radiation from a photo-excited semiconductor in high magnetic fields and interpreted this as SF [218]. They observed a macroscopic coherence decaying superradiantly together with an abrupt decrease in population from full inversion to zero. They demonstrated how the superfluorescent burst characteristics such as the intensity, duration and delay time are tunable by varying the magnetic field, the temperature, and the pump laser power. These results are of particular interest as they show an unprecedented degree of controllability in the formation of SF in solid-state systems.

Concerning III-nitrides, in 2012, D. Boiko and P. Vasil’ev analyzed theoretically SR in MS-LD heterostructures using InGaN/GaN MQW heterostructure as a prototypical system [219]. By employing semiclassical traveling wave Maxwell-Bloch equations, the authors presented a numerical model for SR-like emission in semiconductor LDs and showed the correspondence with the analytical Ginzburg-Landau equation for the BCS-like phase transition. Nonetheless, no phase-locking mechanism responsible for the collective process typical of SR and SF has been introduced in their model. Unlike previous analytical treatments, D. Boiko and P. Vasil’ev only consider a high critical carrier density for the enhancement of a cooperative behavior (hence neither magnetic fields nor low temperatures are required).

5.3 Theory

In order to introduce the coherent amplification of noise via collective scattering that occurs during a SR, Joel Greenberg in his thesis proposed a simple way to describe the phenomenon [220]. He considered the case of a single excited emitter undergoing de-excitation, where the electromagnetic field has an amplitude E_1 , an intensity $I_1 \propto |E_1|^2$, and occurs for a characteristic time τ_1 . First, if the N emitters radiate independently of one another, the fields possess random phases ϕ_n and the system is in the regime of standard fluorescence. This means that the total peak intensity can be written as $I_N \propto |\sum_n E_1 \exp i\phi_n|^2 = NI_1$ and the radiation pattern is completely isotropic. Now, if for any reason the emitters are coherent (we can prepare them in a coherent state or we can let the radiation-mediated interactions to spontaneous phase-lock the ensemble, as we will see later on), they will start to radiate collectively. Coherence implies that the relative phases between the emitters are fixed (i.e., $\phi_n = \phi_1$) thus leading to a total intensity equal to $I_N \propto |\sum_n E_1 \exp i\phi_1|^2 = N^2 I_1$ and to a faster decay proportional

Chapter 5. Superradiance and superfluorescence: application to III-nitride semiconductors

to τ_1/N . Moreover, as opposed to standard fluorescence, the radiation pattern of this superradiant (or superfluorescent, depending on the initial conditions) emission is highly directional as a result of the geometry imposed by the spatial distribution of emitters. Let us turn our attention on the model proposed by Dicke to illustrate the superradiant radiative dynamics of a system of N identical two-level atoms confined to a volume with dimensions small compared to the radiation wavelength [196]. As previously mentioned, Dicke considered an ensemble of $N \gg 1$ atoms that, connected through the common radiation field, modify the spontaneous radiation process. Each atom possesses a ground $|g\rangle$ and excited $|e\rangle$ state separated by an energy $\hbar\omega$ and every single two-level atom state is completely described by the superposition of these two states. For instance, if we postulate that all atoms are initially prepared in the upper level $|e\rangle$, the initial system state can be expressed as $|\Psi(t=0)\rangle = |e, \dots, e\rangle$. Note that as we suppose motionless atoms located within a very small volume V , their coupling (through the radiation field) is symmetrical with respect to the switch of any two atoms in the system. This is due to the indistinguishability imposed by the Heisenberg uncertainty principle for which a photon of wavelength λ cannot be assigned to a specific emitter in the system if $V \ll \lambda^3$ [211].

Such an ensemble of two-level atoms can be formally mapped onto a pseudo-spin system of spin $1/2$ with $|e\rangle$ the spins up and $|g\rangle$ the spin down [196, 211]. According to this representation, all two-level Hermitian operators \mathbf{R}_k with $k=1,2,3$ are analogous to Pauli spin matrices. The total Hamiltonian \mathbf{H}_{TOT} for a N ensemble of atoms can be written as [196, 221]:

$$\mathbf{H}_{TOT} = \mathbf{H}_0 + \mathbf{H}_{int} = -\mathbf{E}d\mathbf{R}_1 + \hbar\omega\mathbf{R}_3, \quad (5.1)$$

where \mathbf{H}_0 is the interaction Hamiltonian operator, \mathbf{H}_{int} is the internal energy Hamiltonian operator, \mathbf{E} is the electric field operator, d is the real part of the dipole moment operator, R_k are the quasi-spin operators for which we have used $\mathbf{R}_k = \sum_{j=1}^N R_{jk}$. Then, the total energy of the system E_{TOT} can be written as [196]:

$$E_{TOT} = E_0 + m \cdot \hbar\omega, \quad (5.2)$$

where E_0 is the energy of motion and mutual interaction of the molecules and for which the relation $\mathbf{R}_3\Psi_{0,m} = m\Psi_{0,m}$ is valid with $\Psi_{0,m}$ the eigenstate of the system. From a physical point of view, m corresponds to the population inversion of the system, which is indeed defined as:

$$m = \frac{1}{2} (N_e - N_g), \quad (5.3)$$

with N_e and N_g are the number of atoms in the excited and ground states, respectively, for which, of course, the relation $N = N_e + N_g$ is valid. Note that, due to symmetry, the energy state E_{TOT} has a degeneracy of $\frac{N!}{(\frac{1}{2}N+m)!(\frac{1}{2}N-m)!}$.

Unfortunately, we are not allowed to write $\mathbf{H}_{TOT}\Psi_{0,m} = E_{TOT}\Psi_{0,m}$ as \mathbf{R}_3 commutes only with \mathbf{H}_{int} and not with \mathbf{H}_0 . On the other hand, $\mathbf{R}^2 = \mathbf{R}_1^2 + \mathbf{R}_2^2 + \mathbf{R}_3^2$ would commute with \mathbf{H}_{TOT} and consequently, stationary states can be chosen to be eigenstates of \mathbf{R}^2

[196]. For this reason, Dicke introduced the “cooperation number” r and he denoted the new eigenstates $\Psi_{0,r,m}$ as [196]:

$$|\Psi_{0,r,m}\rangle = |0, r, m\rangle = \underbrace{|e, \dots, e\rangle}_{r+m} \underbrace{|g, \dots, g\rangle}_{r-m}. \quad (5.4)$$

Note that for r to be valid, we should verify $|m| \leq r \leq \frac{1}{2}N$ and $\mathbf{R}^2\Psi_{0,r,m} = r(r+1)\Psi_{0,r,m}$. The collective behavior does not impact on the total energy of the system E_{TOT} that even for $\Psi_{0,r,m}$ is always given by eq. 5.2, i.e., $\mathbf{H}_{TOT}\Psi_{0,r,m} = E_{TOT}\Psi_{0,r,m}$. However, it does impact on the degeneracy of the state that is now expressed by $\frac{N!(2r+1)}{(\frac{1}{2}N+r+1)!(\frac{1}{2}N-r)!}$ [196]. This way the eigenstate $|\Psi_{0,\frac{1}{2}N,\frac{1}{2}N}\rangle = |e, \dots, e\rangle$ of an ensemble of atoms coherently prepared (i.e., $r = \frac{1}{2}N$) in the excited state (i.e., $m = \frac{1}{2}N$) is nondegenerate as the atoms are indistinguishable. In general, we can affirm that all the states with the same value $r = r_{max} = \frac{1}{2}N$ but with different values of m are also nondegenerate. For this reason, any eigenstate $|\Psi_{0,r_{max},m}\rangle$ is called *fully symmetrical state*. This assumption made by Dicke in 1954 for which all atoms must be prepared in the maximal coherent state has been subsequently questioned by other authors while developing the theory concerning SF [197, 210].

Thanks to this formalism, the transition matrix elements of the interaction energy operator \mathbf{H}_0 joining a given state m with the successive one can now be calculated [196]:

$$\langle\Psi_{0,r,m}|\mathbf{H}_0|\Psi_{0,r,m\mp 1}\rangle = \mathbf{E}d\sqrt{(r\pm m)(r\mp m+1)}. \quad (5.5)$$

Then, the transition probabilities will be proportional to the square of the matrix element thus leading to a spontaneous transition rate of [196]:

$$\Gamma_{m,m-1} = \Gamma_0 (r+m)(r-m+1) \stackrel{r=r_{max}}{=} \Gamma_0 N_e (N_g + 1), \quad (5.6)$$

where Γ_0 is the spontaneous decay rate for a single atom.

From eq. 5.6, we see that the photon emission rate Γ at the beginning (i.e., $t = 0$), so when the N ensemble starts out in a many-body state that is symmetric by atom permutations (i.e., $r = r_{max} = \frac{1}{2}N$) and is in the fully excited state (i.e., $m = \frac{1}{2}N$ or $N_e = N$ and $N_g = 0$), is equal to $\Gamma_0 N$, which is exactly the emission rate expected from a system of N independent dipoles. The largest amount of coherent radiation occurs when r is large but $|m|$ small [196]. Indeed, the system prepared as $|\Psi_{0,r_{max},m=r_{max}}\rangle = |e, \dots, e\rangle$ will cascade, one atom at a time, down to the fully de-excited state $|\Psi_{0,r_{max},m=-r_{max}}\rangle = |g, \dots, g\rangle$ through a “ladder” of $2r_{max} + 1 = N + 1$ symmetric energy levels [Fig. 5.1 (a)] [196, 211]. During this cascade, Γ strongly increases and reaches a maximum emission for $|\Psi_{0,r_{max},m=0}\rangle$ equals to $\Gamma_{max} = \Gamma_0 \frac{N}{2}(\frac{N}{2} + 1)$. This half de-excited state is the largest rate at which an ensemble of N atoms with an even number of molecules can radiate spontaneously and is proportional to the square of the number of atoms N^2 [196]. As the photon emission rate is a factor of N larger than that for independent atoms because

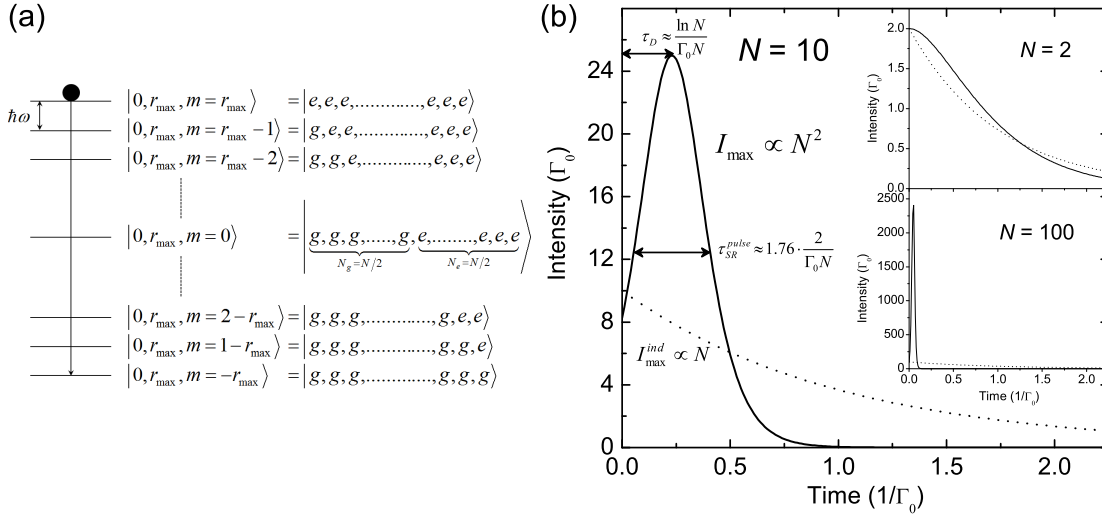


Figure 5.1: (a) The Dicke states $\Psi_{0,r,m}$ in case of full symmetry (i.e., $r = r_{\max} = \frac{1}{2}N$) can be represented as a “ladder” of $2r_{\max} + 1 = N + 1$ energy levels through which the atomic system can cascade by steps of $\hbar\omega$ from the fully inverted state $|\Psi_{0,r_{\max},m=r_{\max}}\rangle = |e, \dots, e\rangle$ down to the ground state $|\Psi_{0,r_{\max},m=-r_{\max}}\rangle = |g, \dots, g\rangle$ [211]. During de-excitation the system passes the state $|\Psi_{0,r_{\max},m=0}\rangle$, which is called superradiant state. (b) Emission intensity for an ensemble of $N = 10$ emitters in the collective regime (solid curves) and for an ensemble of independent emitters (dotted curves) as a function of time. The insets show the cases $N = 2$ and $N = 100$ for comparison. Note that the solid curves for $N = 10$ and 100 have been calculated according to eq. 5.10 whereas the curve for $N = 2$ which does not satisfy the assumption $N \gg 1$, has been calculated according to the more simple formula expressed in eq. 2.29 in Ref. [211]. The discrepancy between the collective and independent emission at $t = 0$ for $N = 10$ is also ascribed to the imperfect approximation introduced by eq. 5.10 for small N , otherwise the initial radiative rate is equal to the one found for a system of N independently radiating dipoles.

of coherence, this state/emission is called *superradiant*. This situation is completely analogous to the emission from a phased array of classical oscillators. Note that on the contrary for a low cooperation number, e.g., $r = m = 0$, the states would no longer radiate since the ensemble would be completely analogous to a classical system of an even number of oscillators swinging in pairs oppositely phased [196]. Once the system ends up in the fully de-excited energy level $|\Psi_{0,r_{\max},m=-r_{\max}}\rangle$, the photon emission rate collapses and the emission stops. For Dicke, a superradiant emission can be achieved according to two possible initial conditions: (i) the ensemble is in the ground state $|\Psi_{0,r_{\max},m=-r_{\max}}\rangle$ and is illuminated by a pulse of radiation directly to the superradiant state $|\Psi_{0,r_{\max},m=0}\rangle$ from which it starts immediately to radiate as a single macrodipole; (ii) the ensemble is in the excited state $|\Psi_{0,r_{\max},m=r_{\max}}\rangle$ (no macroscopic dipole) and starts to radiate via spontaneous emission until it decays into the superradiant state.

Refs. [196, 197, 210] state that the evolution of a Bloch vector can describe the emission mechanism depicted in Fig. 5.1 (a). At the beginning, the Bloch vector points to the

“north” (all dipoles are in the excited state) and at the end to the “south” (all dipoles are in the ground state). During the cascade of states, the ensemble of N dipoles emits all its energy as light. At the superradiant state (i.e., when $m = 0$), a macroscopic dipole moment in the order of N times the atomic dipole moment builds up with $N_e = \frac{1}{2}N$ atoms in the excited state and $N_g = \frac{1}{2}N$ in the ground state. Population inversion is lost and the system is at the transparency. We can then wonder, at which state the radiated light would be the most intense? At the superradiant state, “order” appears in the system: all the dipoles are perfectly macroscopically symmetric because of the equality $m = 0$ and any perturbation of the system would have a strong influence on the emission. The situation is analogous to that of a classical over-damped pendulum for which the evolution of its angle θ under the effect of gravity is proportional to $\sin \theta$ [218]. Prepared at the unstable equilibrium point (“north” pole), the pendulum starts to fall accelerating with θ , becomes fastest at 90° , eventually begins to slow down and finally stops once the stable equilibrium point (“south” pole) is reached. As for SR, this is a totally dissipative process during which all the energy of an initial fully inverted system is emitted as a superradiant burst before reaching its stable ground state. For the pendulum, this means for instance a potential energy dissipated as heat at a release rate proportional to its kinetic energy whereas for the ensemble of atoms, this means an internal energy E_{int} dissipated as light at a release rate proportional to its mutual interaction energy E_0 .

Note that in this simple model, the indistinguishability of the atom with respect to photon emission characterizes SF [211]. Thanks to this indistinguishability, dipole-dipole correlations between the atoms build up, phase-lock their emission and create a macroscopic polarization. This is the physical origin of the collective behavior leading to a emitted intensity proportional to N^2 . Then, the emission of N photons occurs in a timescale a factor of N shorter than the spontaneous emission of a single atom due to energy conservation [211]. Although the emitted light would have a very long coherence length, it should not be called a laser as the coherence is derived from the atom collective behavior rather than from the radiation field like in the case of stimulated emission. In fact, stimulated emission does not play an important role in the whole emission process as the photons exhibit a microscopic occupancy of the cavity [222]. Moreover, as shown by Dicke, the stimulated emission rate during SR is not affected (i.e., comparable to the one for independent atoms) despite the abnormally large spontaneous radiation rate [196]. The stimulated emission rate can be expressed as the rate of spontaneous emission from a state $|\Psi_{0,r,m}\rangle$ minus the rate from the closest higher state $|\Psi_{0,r,m+1}\rangle$ via:

$$(r+m)(r-m+1) - (r+m+1)(r-m) = 2m$$

$$\xrightarrow{r=r_{max}} N_e(N_g+1) - (N_e+1)N_g = N_e - N_g. \quad (5.7)$$

The stimulated emission rate is therefore always equal to the normal incoherent rate, which is proportional to the population inversion $m = \frac{1}{2}(N_e - N_g)$.

Chapter 5. Superradiance and superfluorescence: application to III-nitride semiconductors

The time evolution of the full system can be determined by simply following the motion of its “inverted” center $\langle m(t) \rangle$ via the expression [211]:

$$\frac{d\langle m(t) \rangle}{dt} = \Gamma_0 (r + \langle m(t) \rangle) (r - \langle m(t) \rangle + 1). \quad (5.8)$$

Starting from $m_0 = r_{max}$ at $t = 0$, the solution of this equation is [211]:

$$\langle m(t) \rangle \approx -\frac{N}{2} \tanh \left[\Gamma_0 \frac{N}{2} (t - \tau_D) \right], \quad (5.9)$$

where $\tau_D = \frac{\ln N}{\Gamma_0 N}$ is the delay time.

The mean time-dependent intensity produced by the atom ensemble can then be approximated (under the assumption that $N \gg 1$) [211, 221]:

$$I(t) \approx -\frac{d\langle m(t) \rangle}{dt} \approx \Gamma_0 \frac{N^2}{4} \operatorname{sech} \left[\Gamma_0 \frac{N}{2} (t - \tau_D) \right]. \quad (5.10)$$

Figure 5.1 (b) shows the average rate of emitted intensity calculated according to eq. 5.10 for $N = 2, 10$ and 100 . For the sake of comparison, on the same graph we have also plotted the emission in the case of N independently emitting atoms (dotted curves) according to the formula $\Gamma_0 N \exp -\Gamma_0 t$ [211]. As can be seen in the top inset of Fig. 5.1, the difference between a superradiant (solid curve) and an independent emission (dotted curve) for $N = 2$ is not prominent as the collective behavior is more perceptible for $N \gg 1$. We see that the collective system emits a single short radiation burst containing the full excitation energy of the ensemble and that scales with N^2 as opposed to the exponential decay constant Γ_0 proper of a system of independently radiating dipoles. Typically, the superradiant emission is centered around a delay time $\tau_D = \frac{\ln N}{\Gamma_0 N}$ and its pulse duration τ_{SR}^{pulse} is equal to $1.76 \cdot 2\tau_{SR} = 1.76 \frac{2}{\Gamma_0 N}$ where 1.76 is the FWHM of a sech^2 function and τ_{SR} is the characteristic superradiant time-scale. Thanks to these N -dependencies, we can now see the asset of SR: a larger number of atoms in an ensemble spontaneously radiates much faster and stronger compared to standard fluorescence and in a well specific direction depending on the sample geometry.

5.3.1 Large sample superradiance

A superradiant medium can be seen as a mirrorless laser pumped in a percussional way at time $t = 0$ [211]. However, some of the assumptions used in the precedent section to describe the onset of superradiant emission should be revised. The fact that atoms are confined in a very small volume (i.e., $V \ll \lambda^3$) and that interactions are fully symmetrical by permutation, is quite unrealistic or, at least, it is valid only for very specific symmetric arrangements of atoms. Moreover, we have also neglected the pumping and relaxation mechanisms that may occur during the evolution of the system as we were exclusively focusing our attention to atoms only interacting with their own

radiation field. In fact, SR experiences dipole dephasing due to Van der Waals interaction between atoms, spontaneous emission on other transition levels, Doppler dephasing and, more importantly, atomic collisions and scattering [211]. All these dephasing effects perturb the highly correlated dipole-dipole states and lead to levels of lower symmetry that weaken the cooperative character of SR.

In order to “generalize” the SR emission, first, Bonifacio *et al.* and afterward, Gross and Haroche proposed the theory of *large sample SR* (i.e., $V \gg \lambda^3$), as opposed to small or point sample SR [197, 210, 211]. This theory is closely related to SF as it takes into account the case of an arbitrary dipole arrangement (with a few limitations concerning the spatial dimension of the distribution) that, after a period of time, develops a macroscopic dipole moment. At time $t = 0$ no optical dipole is present in the sample as the system starts from a complete disordered state. Then, the quantum fluctuations of the electromagnetic field make the system evolving and correlations between the dipoles build up due to phase-locking. Furthermore, the particular N -dependencies typical of SR (i.e., $I \propto N^2$, $\tau_D \propto \ln N/N$ and $\tau_{SR} \propto 1/N$) are conserved also in case of SF. Note that some authors introduce a so-called “superradiant or superfluorescent threshold” resulting from the competition between the dipole phase-locking and the aforementioned dephasing effects. Indeed, the more atoms are correlated at the initial stage $t = 0$, the faster the system reaches the superradiant state and strongly radiates proportionally to N^2 . This implies a minimum amount of initially inverted atoms for the superradiant emission to prevail.

In most SR experiments so far, the conditions realized correspond to large sample SR as this configuration is closer to a real situation. To describe in a simple way such a system it is convenient to introduce the concept of a *pencil-shape sample* [197, 210, 211]. This sample consists in a long cylinder of length L and radius w so that the radiation can expand within two small cones defined by the cylinder longest dimension. The idea is to have a convenient shape for a superradiant medium and for which we can neglect the spontaneous emission off-axis with respect to the cooperative emission along the propagation axis (by convention, the longitudinal Oz axis). This single-direction propagating field is likely to develop when the Fresnel number of the emitting cylinder $F = \frac{\pi w^2}{L\lambda}$ is close to unity. In this case, SR could be treated qualitatively as a one-dimensional problem [211]. Since the radiation field differs at various points along the propagation axis, the evolution of the emitters at various points is different. Then, according to the pencil-shaped arrangement, only the photons that have been spontaneously emitted in the diffraction angle ($F \sim 1$) can indeed *actively* participate to the onset of the superradiant emission process.

To describe the evolution of such 1D pencil-shaped sample SR, one can use Maxwell-Bloch equations within the rotating-wave and slowly-varying envelope approximation [211]. For slowly varying amplitudes of the population inversion $N_{inv}(z, t)$ (note that $N_{inv} = N_e - N_g$) of the electromagnetic field $\mathbf{E}(z, t)$ and of the material polarization $\mathbf{P}(z, t)$, these equations take the following form (in the case of plane waves) [200, 206, 211, 223]:

$$\frac{dN_{inv}}{dt} = -\frac{N_{inv} - N_{pump}}{T_1} + \frac{i}{\hbar}(\mathbf{E}\mathbf{P}), \quad (5.11)$$

$$\frac{d\mathbf{E}}{dt} = -\frac{\mathbf{E}}{T_E} + \Gamma \frac{i\omega}{2\pi\epsilon_0} \mathbf{P}, \quad (5.12)$$

$$\frac{d\mathbf{P}}{dt} = -\frac{\mathbf{P}}{T_2} - \frac{i\mu^2}{\hbar} N_{inv} \mathbf{E}, \quad (5.13)$$

where N_{pump} is the amount of population inversion supported by pumping, T_1 is the population inversion relaxation time (also called spontaneous recombination time of the electron-hole pairs), T_E is the decay time of the field in the cavity (sometimes referred to as the photon lifetime in the cavity τ_{ph}), T_2 is the polarization relaxation time (sometimes referred to as polarization dephasing time) and μ^2 is the square of the dipole moment of interband transitions with $\mu = q \cdot a_B$. Note that one common simplification is to consider only one arbitrary direction of field propagation even though both emission directions are equivalent. Nonetheless, this approximation does not impact qualitatively on the problem. Note also that most of the time, the spatial dependencies of the population inversion and of the polarization are neglected. Of course, this is not the case for the radiating field for which we need to know the spatial distribution. The new set of coupled eqs. 5.11-5.13 is then expressed as $\frac{\partial N_{inv}}{\partial t}$, $\frac{\partial P}{\partial t}$ and $\frac{\partial}{\partial t} + c \frac{\partial}{\partial z} E$.

To obtain the evolution of the field in the medium, the superradiant emission has been compared to an over-damped pendulum trajectory in a viscous liquid with an initial tipping angle θ_0 (with the “north” pole) at $t = 0$ and going down to $\theta = \pi$ (“south” pole) [211, 223, 224]. Eqs. 5.11-5.13 have then been modified and solved by introducing a Bloch vector $\theta(z, t)$ such as:

$$\frac{\partial^2 \theta}{\partial z \partial t} = \frac{\sin \theta}{L \tau'_{SR}} \xrightarrow{\text{dimensionless}} \frac{\partial^2 \theta}{\partial (z/L) \partial (t/\tau'_{SR})} = \sin \theta, \quad (5.14)$$

where τ'_{SR} is the characteristic superradiant time defined as [211, 214]:

$$\tau'_{SR} = \frac{\overbrace{1}^{\tau_{SR}}}{\Gamma_0 N} \frac{8\pi^2 w^2}{3\lambda^2}. \quad (5.15)$$

Equation 5.14 is known as the sine-Gordon equation [211, 223]. When neglecting propagation effects at all times (assuming the homogeneity of the initial conditions), eq. 5.14 can be rewritten in a more convenient form [197]:

$$\frac{\partial^2 \theta}{\partial t^2} + \left(\kappa + \frac{1}{2T_2} \right) \frac{\partial \theta}{\partial t} - \frac{e^{-\frac{t}{T_2}} \sin \theta}{\tau_c^2} = 0, \quad (5.16)$$

where τ_c is the correlation time (i.e., the time at which the field and the system exchange energy) and κ is the damping coefficient. For an atomic system, this damping parameter represents the field dissipation, i.e., the irreversible leakage of the field propagating through the medium [197]. The term $\kappa + \frac{1}{2T_2}$ represents then the friction experienced by the system subjected to damping and dephasing effects. Note that for very large κ and

T_2 , eq. 5.16 describes the evolution of the overdamped, dephasing-free “pure” Dicke SR, discussed in the previous section.

As for the damped pendulum case, eqs. 5.14 and 5.16 predict the irreversible evolution of the ensemble from the excited state $[\theta(t = 0) = \theta_0]$ down to the ground state $[\theta(t = \infty) = \pi]$ including a damping term κ and a dephasing time T_2 . In both equilibrium states (north and south poles) no net dipole moment is present in the ensemble. Note that we impose a small $\theta_0 \neq 0$ (which means a polarization $P(t = 0) \neq 0$) as otherwise eq. 5.14 would not start without any perturbation. Indeed, the onset of the superradiant process strongly depends on quantum noise (or quantum initiation) at the very early-stage [211]. Typically, the tipping angle θ_0 is assumed to be equal to $\sqrt{\frac{2}{N}}$. However, its phase (the azimuthal angle of the Bloch vector θ) is completely random; this is the distinct feature between SF and SR. Successively, the evolution of SF will eventually lock the inverted dipoles to a common phase. The latter are initially incoherent at various points of the ensemble, thus leading to a macroscopic intensity pulse radiation proportional to N^2 ($\propto \left(\frac{\partial \theta}{\partial t}\right)^2$ in the case of eqs. 5.14 and 5.16), as for the small sample SR. The common radiation field is responsible for this dipole-dipole coupling and its locking efficiency evolves during the emission process with a maximum action at the superradiant state (i.e., $m = 0$). This maximum emission occurs after a finite delay time τ'_D (much larger than τ'_{SR}) that can be written as [211, 223, 225]:

$$\tau'_D \propto \tau'_{SR} \ln \sqrt{\pi N}^2. \quad (5.17)$$

Especially in the dimensionless form, eq. 5.14 also shows how L is the natural length of the superfluorescent evolution and τ'_{SR} the natural time [211]. Note that the characteristic superradiant time τ'_{SR} expressed in eq. 5.15 is a factor close to the superradiant time $\tau_{SR} = \frac{1}{\Gamma_0 N}$ found in the previous section in the case of “pure” Dicke SR. Unfortunately, in real systems, this superradiant time τ'_{SR} should also face dephasing effects. The term $\frac{\mathbf{P}}{T_2}$ in eq. 5.13 is related to the inhomogeneous broadening of SF as it takes indeed into account the relaxation processes experienced by the polarization \mathbf{P} , mostly due to collisions or scattering between the dipoles. Some authors also take into account other dephasing effects such as, e.g., the Doppler shift of atoms with different velocities. However here we will only focus our attention on polarization relaxation due to scattering (T_2). Bonifacio *et al.* showed how the incoherent polarization decay term $\frac{\mathbf{P}}{T_2}$ temporally broadens the superfluorescent pulse and at the same time reduces the intensity pulse amplitude by a factor equal to $\exp \frac{-t}{T_2}$ (see eq. 5.16) [197]. The relaxation mechanism would have a minor impact on the cooperative buildup of the polarization only if the following condition is fulfilled [197, 200, 206, 210, 211]:

$$\tau'_{SR}, \tau'_D \ll T_2, \quad (5.18)$$

which essentially means that *the superradiant emission should occur faster than any other dephasing processes*. If the condition 5.18 is not fulfilled, dephasing effects will destroy

Chapter 5. Superradiance and superfluorescence: application to III-nitride semiconductors

the cooperative behavior that tries to phase-lock the dipoles thus leading to an ensemble of independent emitters with an emission intensity proportional to N [197]. Compared to the “pure” Dicke SR, the presence of a finite dephasing time T_2 can be seen as a loss of symmetry by the atom ensemble, which weakens consequently the superradiant emission. In fact, any physical process that induces a symmetry breaking between the dipoles makes the atoms distinguishable thus reducing the superradiant emission rate [211].

When setting eqs. 5.11-5.13 we have assumed slow varying envelopes for the observables N_{inv} , \mathbf{E} and \mathbf{P} so that their time and space variations are very small compared to the wavefrequency ω_0 and the wavevector k_0 of the respective plane waves [i.e., $\propto \exp i(\omega_0 t - k_0 z)$]. We have then seen that the superradiant time-scale of these observables is expressed in terms of a characteristic superradiant time $\tau_{SR} = \frac{1}{\Gamma_0 N}$ (τ'_{SR} is proportional to τ_{SR}) that is inversely proportional to N . The question is: how much can we increase the population N before breaking the slow variation approximation? Indeed, by merely increasing N we will get to a point in which the superradiant time-scale is so fast that the slow variation assumption is no longer valid. For this reason, in eqs. 5.11-5.13, the correlation time τ_c of the emission process has to be shorter than the characteristic superradiant time τ_{SR} . This is known as the Arecchi-Courtens condition [207, 211]:

$$\tau_c < \tau_{SR}, \tau'_{SR} \xrightarrow[F = \frac{\pi w^2}{L\lambda} \sim 1]{\text{large sample SR}} N < \frac{8\pi c}{3\lambda\Gamma_0}, \quad (5.19)$$

where τ_c , which is the intrinsic duration of each photon process, is of the order of $\frac{\lambda}{c}$ and $\frac{L}{c}$ for the small and large sample SR, respectively. If the condition 5.19 is not fulfilled (i.e., the light propagation through the whole medium is slower compared to the superradiant time-scale τ_{SR}), the cooperative emission of the whole ensemble is lost since the emission occurs before the different points of the ensemble may interact, just as in the case of independent single emitters. Thus, the maximum number of atoms that are able to emit cooperatively are given by the right-hand side condition of eq. 5.19. Sometimes, eq. 5.19 is replaced by the more restrictive Born-Markov condition for which $N\tau_c < \tau_{SR}$ and we call this case microscopic SR [211, 226].

As opposed to small sample SR, the superfluorescent emission shows several emission maxima called SR ringings. This multiple-peak emission is a consequence of the damping term κ in eq. 5.16 that exhibits an oscillating behavior around $\theta = \pi$. Note that κ should be equal to $\frac{c}{2L}$ for $\theta = 0, \pi$ [197]. The damping parameter does not only depend on the fixed constraints of the sample (such as, e.g., the shape L and w) but also on the dynamic and spatial distribution of the ensemble. Indeed, due to propagation, the various parts of the sample evolve at different speed as they see a different field also depending on their position z . For instance, a smaller sample (narrower L or w) implies a bigger damping coefficient κ as the correlation time τ_c is shorter and the system becomes more “cooperative” as the dipole-dipole coupling is stronger. On the other hand, placing the sample in a resonator cavity inhibits the field dissipation thus decreasing κ [197]. In the

case of “pure” Dicke SR, we have assumed a completely dissipative system (i.e., $\kappa = \infty$) which leads, according to the damped pendulum analogy, to a superradiant emission for $\theta = \pi/2$ before the radiation eventually vanishes at $\theta(t = \infty) = \pi$. This means that the system stops radiating when all dipoles are in the ground state so all de-excited. On the contrary, a finite damping term κ (independently on how you want to express it) would imply a system that oscillates around its stable equilibrium state at $\theta = \pi$. As long as some dipoles remain in the excited state (i.e., $\theta \neq 0$), the ensemble possesses a net total optical dipole and there is a non-zero probability for the ensemble to still radiate. This means that at each oscillation the system has a chance to superradiantly emit light for a state θ restrained between the ground state $\theta = \pi$ and the maximum state θ_{max} reached during the oscillation. Hence, the multiple pulse emission or superradiant ringing. Obviously, because of damping, θ_{max} is intended to inexorably diminish from its initial value $\theta(t = 0) = \theta_0$ down to its minimum value $\theta(t = \infty) = \pi$ reached at the equilibrium. When all the energy of the system has been emitted, the radiation eventually stops and this happens when all the dipoles are finally in the ground state [211].

Bonifacio *et al.* proposed to distinguish different values of $\kappa\tau_c$ in order to discriminate between the different radiating regimes of the cooperative emission that can be obtained [197]:

- $\kappa\tau_c \gg 1$ is the case of large damping. This regime is analogous to the “pure” Dicke SR described in the previous section and its emission consists in a single burst of radiation modeled by eq. 5.10. The emitted photons can not act back on the system as their escape rate from the active volume is too fast (no stimulated emission/absorption processes) [197]. The Arecchi-Courstens condition is automatically satisfied as $\tau_c < \tau_{SR}$.
- $\kappa\tau_c \sim 1$ is the case of oscillatory superfluorescence (finite damping term). The emission is in the form of multiple pulses (ringing) with decreasing amplitude. This situation is achieved in Ref. [209]. In this regime the emitted photons can act back on their emitters thus leading to competition between the stimulated absorption/emission and the cooperative spontaneous emission [197]. The Arecchi-Courstens condition is nearly satisfied as $\tau_c \sim \tau_{SR}$ and SF-like pulse can be obtained only if $\tau_c, \tau_{SR} \ll T_2$ is still satisfied (see eq. 5.18).
- $\kappa = 0, T_2 = \infty$ is the homogeneous case (no damping). This regime consists in a train of identical pulses of intensity proportional to N , i.e., no more SF is observed as the stimulated and cooperative processes are equally important [197]. The system behaves in a more laser-like operation.

In summary, we can distinguish between four different time-scales in the description of the superfluorescent process: a dephasing time T_2 , a dissipation/decay time $\propto \frac{1}{\kappa}$, a correlation time τ_c , and a characteristic superradiant time τ_{SR} . According to Bonifacio

Chapter 5. Superradiance and superfluorescence: application to III-nitride semiconductors

et al., the conditions for SF are [197]:

$$\frac{1}{\kappa}(\tau_c) \leq \tau_{SR}, \tau'_{SR} \ll T_2. \quad (5.20)$$

The left-hand side says that to achieve SF the cooperative spontaneous emission must dominate the stimulated emission process. The right-hand side indicates that to have SF the cooperative spontaneous emission must dominate the polarization relaxation process. On the other hand, $\frac{1}{\kappa}(\tau_c) \ll T_2$ implies that the emitted photons should cover the entire length of the sample before the dipoles dephase to promote the cooperative behavior. The right-hand side of eq. 5.20 is an obvious condition if we want the collective radiation to occur rapidly with respect to the incoherent decay but it also implies that the system should be well above the threshold as $\tau_{SR} \propto \frac{1}{N}$. Some authors prefer the equivalent condition $\alpha L \gg 1$ with α the gain per unit length [199, 209, 223]. Therefore, the left-hand side of eq. 5.20 is necessary to prevent the system to lase. Typically, a laser system satisfies:

$$\tau_{SR}, \tau'_{SR} \leq T_2 \ll \frac{1}{\kappa}(\tau_c). \quad (5.21)$$

Thus, for SF it is mandatory to have not only an excellent amplifier medium but also a highly dissipative (low Q -factor) system.

5.3.2 Superradiance and superfluorescence in multi-section laser diodes

SR and SF in semiconductors are very controversial subjects. As discussed in the previous sections, under specific conditions, a coherent superradiant pulse with intensity proportional to N^2 is emitted after a delay time τ'_D from an ensemble of N inverted dipoles initially excited in an incoherent state. We have called this phenomenon SF. To obtain such a superfluorescent emission, the mutual phasing of the dipoles via the radiation field should happen in a time-scale τ_c shorter than τ'_D . However, while creating the macrodipole in the system, this self-phasing mechanism must face other counteracting phenomena such as the incoherent spontaneous emission acting at a time-scale T_1 (see eq. 5.11) and the collisional relaxation time T_2 (see eq. 5.13). To generate SF, it is thus necessary that the characteristic superradiant time τ'_{SR} and the delay time τ'_D are much shorter than these harmful mechanisms, i.e., $\tau'_{SR}, \tau'_D \ll T_1, T_2$. This is the distinctive feature of SR and SF as opposed to standard lasing [215].

Unfortunately, SF in solids is very challenging due to their very short polarization dephasing time T_2 , i.e., ~ 200 fs at RT [200, 206, 214, 215]. As to obtain SF the mutual phasing of the dipoles via the common radiation field must happen in a time-scale τ_c shorter than the mechanisms that destroy the cooperative effects, the short dephasing time T_2 of semiconductors makes even more problematic the condition $\tau'_{SR}, \tau'_D \ll T_1, T_2$ to be satisfied. Moreover, the strong inhomogeneous broadening and the energy dispersion within the bands, typical of semiconductors, further prevents the cooperative mutual self-phasing necessary for SF, especially in bulk materials. To enhance the cooperative

rate $1/\tau_c$, one should create a singularity in the energy space thus reducing the effective dimension of the electron-hole ensemble in the real space [206]. Possible strategies are excitonic SR [227], QDs [228] or magnetoplasmas [229]. For this reason, many groups have started to work on semiconductor magneto-plasmas in which the QWs are placed in a high magnetic field that enhances the transition dipole moment μ and hinders dephasing effects thus leading to a longer T_2 [218, 229]. For instance, G. Timothy Noe II *et al.* reported the first observation of SF in an InGaAs/GaAs semiconductor magneto-plasma [218]. Other promising semiconductor structures are quantum dots, which, thanks to their quasi zero-dimensional highly localized states, exhibit longer dephasing times [228]. Recently, Ding *et al.* observed SR of excitons in a single ZnO tetrapod nanostructure [230].

Another possible strategy is to dispose of a MQW heterostructure placed in a cavity with high photon losses and under very high pumping rate [206]. The abnormally high population N of inverted dipoles (in the case of semiconductors we can refer to as electron-hole pairs) shortens so much the characteristic superfluorescent time τ'_{SR} that its time-scale falls below the dephasing one imposed by T_2 thus satisfying the condition 5.20 [215]. However, reaching such a high population regime, necessary for SR and SF to occur, is very difficult as compared to standard lasing. Moreover, for such a gain medium above transparency, stimulated emission may dominate the recombination processes thus preventing further any collective behavior. For these reasons, Belyanin *et al.* proposed the use of a very low Q -factor cavity (i.e., of very short T_E), a few tens of micrometers long, under a very high pumping rate, for which conventional lasing is strongly inhibited [206, 215]. Indeed, to keep the escape time of the photons T_E as short as possible, the reflectivities R at each facet and the cavity length L_{TOT} must be very short [206]. We will present the results of this approach in Sec. 5.4 in which we investigate InGaN- and GaN-based MQW samples processed as short stripes for superfluorescent emission. MS-LDs may also be a practical solution to reach such high carrier densities (much higher than conventional lasing threshold densities) and at the same time to prevent the stimulated emission from taking over: we have seen in the previous chapters that such structures with built-in absorber sections prevent lasing in the cavity for a sufficiently long time and therefore may allow coherent cooperative state to occur. The results of high injection in MS-LDs will be presented in Sec. 5.5.

But how can we describe the dynamical evolution of such a highly pumped system? In principle, at least from a macroscopic point of view, the Maxwell-Bloch semiclassical equations 5.11-5.13 presented in the previous section can describe any dynamical system involving a two-level medium with an inverted population N_{inv} , an internal polarization \mathbf{P} and a cavity field \mathbf{E} . Normally, in the standard lasing regime (corresponding to lasers of class A and B), the incoherent polarization relaxation time T_2 is so fast compared to the field decay time T_E , i.e., $T_2 \ll T_E$, that the medium polarization \mathbf{P} adiabatically follows the electromagnetic field \mathbf{E} and can thus be eliminated from the set of Maxwell-Bloch eqs. 5.11-5.13. This way, only N and \mathbf{E} possess spatiotemporal dynamics and they can be easily described by the standard rate equations 2.41 and 2.42 treated in Sec. 2.2.2.

Chapter 5. Superradiance and superfluorescence: application to III-nitride semiconductors

On the contrary for lasers of class C (or even D), the incoherent polarization relaxation time T_2 is of the same order or even greater than the field decay time T_E , i.e., $T_2 \geq T_E$ (the case of a highly dissipative system or a low Q -factor cavity), and the polarization can no longer be adiabatically eliminated [231]. The standard rate equation model is no longer valid. Fast polarization dynamics in the system have to be considered and SR and SF regimes belong to this last category. For this reason, we have developed a set of equations based on the Maxwell-Bloch semiclassical ones 5.11-5.13 in order to describe the fast emission processes involved in superfluorescent emission for the specific case of a multiple-contacted cavity. The set of equations presented can be easily generalized in the case of both an optically and electrically pumped structure. In the case of slow radiation dynamics (i.e., $T_2 \ll T_E$), these equations would bring back to the standard rate equations 2.54-2.56 discussed in Sec. 2.3.4 for the conventional dynamics involved in a MS-LD [215, 219]. In our model, the GS (AS) carrier populations n_{GS} (n_{AS}) [in 3D notation], the GS (AS) polarization \mathbf{P}_{GS} (\mathbf{P}_{AS}) and the electromagnetic field in the cavity \mathbf{E} are expressed as follows:

$$\frac{dn_{GS}}{dt} = \frac{\eta_{inj} I_{GS}}{qV_{GS}} - An_{GS} - BV_{GS}n_{GS}^2 - CV_{GS}^2n_{GS}^3 - \frac{1}{\hbar}(\mathbf{E} \cdot \mathbf{P}_{GS}), \quad (5.22)$$

$$\frac{dn_{AS}}{dt} = -\frac{n_{AS}}{\tau_{AS}} - \frac{1}{\hbar}(\mathbf{E} \cdot \mathbf{P}_{AS}), \quad (5.23)$$

$$\frac{d\mathbf{E}}{dt} = \frac{1}{2}\Gamma\frac{2\omega}{\varepsilon V}(V_{GS}\mathbf{P}_{GS} + V_{AS}\mathbf{P}_{AS}) + \frac{1}{2}\beta BV_{GS}n_{GS}^2\frac{2\hbar\omega}{\varepsilon|\mathbf{E}|^2}\mathbf{E} - \frac{1}{2}(\alpha_i + \alpha_m)v_g\mathbf{E}, \quad (5.24)$$

$$\frac{d\mathbf{P}_{GS}}{dt} = -\frac{\mathbf{P}_{GS}}{T_2} + K\frac{\mu^2}{\hbar\omega^2V_{GS}T_2}\frac{L_{GS}}{L_{TOT}}g_{GS}(\hbar\omega, n_{GS}, E)v_g\mathbf{E} + \Lambda, \quad (5.25)$$

$$\frac{d\mathbf{P}_{AS}}{dt} = -\frac{\mathbf{P}_{AS}}{T_2} - K\frac{\mu^2}{\hbar\omega^2V_{AS}T_2}\frac{L_{AS}}{L_{TOT}}\alpha_{AS}(\hbar\omega, n_{AS}, E, V_{AS})v_g\mathbf{E} + \Lambda, \quad (5.26)$$

where $V = d_{QW}wL_{TOT}$ is the active volume with $V_{GS} = \frac{L_{GS}}{L_{TOT}}V$ and $V_{AS} = \frac{L_{AS}}{L_{TOT}}V$ the gain and absorber active volumes, respectively. K is a constant non-dimensional term (set to $4.94 \cdot 10^8$). Its physical origin will be explained shortly after (see eqs. 5.30 and 5.31). The Langevin force term Λ accounts for the polarization noise and is set to $1 \cdot 10^{-15} \text{ Cm}^{-2}\text{s}^{-1}$. Its impact on the dynamic evolution of the system is negligible and it is introduced only for the sake of completeness. Note that for $\frac{L_{AS}}{L_{TOT}} = 0$ (i.e., no AS), the model describes the fast dynamics of a standard single-section LD for which only eqs. 5.22, 5.24 and 5.25 hold. Moreover, for $\frac{L_{AS}}{L_{TOT}} = 0$, the field decay time T_E corresponds to $\frac{1}{(\alpha_i + \alpha_m)v_g}$ that in our case (see Table 2.1) is equal to ~ 2 ps. The interest in the exploitation of a MS-LD relies on the fact that the term $\frac{1}{2}\Gamma\frac{2\omega}{\varepsilon V}V_{AS}\mathbf{P}_{AS}$ in eq. 5.24 shortens further the total T_E due to the AS absorption α_{AS} in eq. 5.26. Basically, we could write the new total T_E as $\frac{1}{(\alpha_i + \alpha_m + \alpha_{AS})v_g}$. Note also that, in the absence of

pumping term, the population relaxation time T_1 in eq. 5.11 corresponds now to the population relaxation time in each section, i.e., it corresponds to the GS charge carrier lifetime τ_{GS} in eq. 5.22 (expressed via the ABC model) and to the AS charge carrier lifetime τ_{AS} in eq. 5.23.

The cooperative frequency ω_c ($\propto \frac{1}{\tau_c}$) is defined from the coupling coefficient between the polarization \mathbf{P} and the electric field \mathbf{E} in eqs. 5.25 (and consequently in eq. 5.26) and in our case it reads (for the GS) [215, 232]:

$$\frac{\omega_c^2}{4\pi} = K \frac{\mu^2}{\hbar\omega^2 V_{GS} T_2} \frac{L_{GS}}{L_{TOT}} g_{GS}(\hbar\omega, n_{GS}, S) v_g. \quad (5.27)$$

This expression is extremely important for the analysis of the establishment of a superfluorescent emission. Indeed, as previously mentioned, in case of SF regime it holds $T_E^{-1} \gg \omega_c \geq \tau_{SR}^{-1}, \tau'_{SR}{}^{-1} \gg T_2^{-1}$ (see discussion regarding the condition 5.20 and for fast dynamics fulfilling $T_2 \gg T_E$).

The steps that transform the Maxwell-Bloch eqs. 5.22-5.26 into the former rate eqs. 2.54-2.56 are the following. In case of slow radiation dynamics, the medium polarization adiabatically follows the electromagnetic field thus implying $\frac{d\mathbf{P}}{dt} \ll \frac{\mathbf{P}}{T_2}$ and $\frac{d\mathbf{P}_{GS}}{dt}, \frac{d\mathbf{P}_{AS}}{dt} = 0$. Eqs. 5.25 and 5.26 then become:

$$\begin{aligned} \mathbf{P}_{GS} &= K \frac{\mu^2}{\hbar\omega^2 V_{GS}} \frac{L_{GS}}{L_{TOT}} g_{GS}(\hbar\omega, n_{GS}, E) v_g \mathbf{E} + \Lambda, \\ \mathbf{P}_{AS} &= -K \frac{\mu^2}{\hbar\omega^2 V_{AS}} \frac{L_{AS}}{L_{TOT}} \alpha_{AS}(\hbar\omega, n_{AS}, E, V_{AS}) v_g \mathbf{E} + \Lambda, \end{aligned} \quad (5.28)$$

This way, the polarization \mathbf{P} can be eliminated from the set of eqs. 5.22-5.26 (we neglect for the moment the Langevin term Λ). Finally, within the corpuscular model, we know that the total energy carried by the photons $s_{3D}\hbar\omega$ is equal to the total electromagnetic energy of the wave $\frac{\varepsilon}{2}|\mathbf{E}|^2$ [40, 81]. So, the following equations relate the photon population density s (in 3D notation) to the electromagnetic field \mathbf{E} :

$$s_{3D}\hbar\omega = \frac{\varepsilon}{2}|\mathbf{E}|^2 \rightarrow \frac{ds_{3D}}{dt} = \frac{\varepsilon}{2\hbar\omega} \cdot 2\mathbf{E} \frac{d\mathbf{E}}{dt}. \quad (5.29)$$

with $s_{3D} = \frac{S}{V}$. The distinction between photon and carrier active volumes is made in eq. 5.24 where the confinement factor Γ is inserted in the first term.

Therefore, starting from eqs. 5.22-5.26 and within the adiabatic approximation of the polarization, by using eqs. 5.28 and 5.29, the well-known standard rate equations 2.54-2.56 for a GS charge carrier population N_{GS} , an AS charge carrier population N_{AS} and a photon population S , typical of lasers of class A and B, can be derived. However, during these algebraic substitutions, one condition should be satisfied in order to obtain exactly the same set of equations. This condition reads:

$$\frac{\mu^2}{\hbar\omega} = \frac{\varepsilon V}{2} \frac{1}{K}, \quad (5.30)$$

Chapter 5. Superradiance and superfluorescence: application to III-nitride semiconductors

where K , as previously mentioned is a constant non-dimensional parameter. To justify the relation expressed in eq. 5.30 we propose the following reasoning. The polarization \mathbf{P} can be expressed as a function of the dipole moment of each electron-hole pair via $\mathbf{P} = \frac{N}{V}\mu$ but also as a function of the electric field via $\mathbf{P} = (\epsilon_r - 1)\epsilon_0\mathbf{E} \approx \epsilon\mathbf{E}$. Thanks to the relationship between the photons and the electric field in the cavity stated in eq. 5.29, the following expression can then be derived:

$$\frac{\mu^2}{\hbar\omega} \approx \frac{\epsilon V}{2} \frac{4S}{N^2}. \quad (5.31)$$

Eq. 5.30 and 5.31 are equivalent provided $K \approx \frac{N^2}{4S}$ holds. As in our case the carrier population N and the photon one S change mutually over each instant, we do not know how to exactly interpret this last relationship. Nevertheless, eq. 5.31 seems to state that somehow the assumption given by eq. 5.30 can be justified even if its exact interpretation is still not understood.

In order to demonstrate the consistency of our new formalism, we computed the dynamic evolution of a system using eqs. 5.22-5.26 for the linear model (cf. Chap. 2). Note that we consider only the norms of the medium polarization \mathbf{P} and the electric field \mathbf{E} . For the GS and AS material gain, we implement the expressions given in eqs. 2.46 and 2.58, respectively. Fig. 5.2 depicts the dynamic solutions of eqs. 5.22-5.26 in the case of Q-switched emission. For the sake of comparison, the parameters are exactly the same as for Fig. 2.10 (b): a pump current I_{GS} of 90 mA, an absorber carrier lifetime τ_{AS} of 0.25 ns and a carrier-free absorption α_0 of 82 cm⁻¹. The polarization dephasing time T_2 is equal to 200 fs. All other parameters are listed in Tables 1.1 and 2.1. The calculated pulsed emission is in very good agreement with the one calculated with standard rate equations [compare Figs. 5.2 (a) and 5.2 (b) with Fig. 2.10 (b)]. For instance, the calculated turn-on delay times τ_{TOD} are equal to 3.74 and 3.75 ns, the photon populations in the first peak are equal to 8476 and 8235, the self-pulsating frequencies f_{SP} are equal to 0.58 and 0.57 GHz for the standard and the new Maxwell-Bloch rate equations model, respectively. This excellent agreement is not surprising. Indeed, the case treated in Fig. 5.2 [and consequently in Fig. 2.10 (b)] is in the regime of slow radiation dynamic as $T_2 \ll T_E, \tau_{GS}, \tau_{AS}$ and therefore, according to our discussion, the medium polarization could have been adiabatically eliminated.

During the analysis of the dynamic evolution described by eqs. 5.22-5.26 (or by the standard semiclassical Maxwell-Bloch eqs. 5.11-5.13), a simple question spontaneously arises: in which term have we introduced the self-phasing mechanism typical of a superfluorescent emission? Or how can we identify in the equations the collective behavior occurring between the dipoles in case of SF? In fact, we do NOT have introduced any cooperating term and thus we should NOT expect that our equations describe the underlying physical mechanism typical of SF. Semi-classical Maxwell-Bloch equations are macroscopic equations and so they do not allow to demonstrate the self-phasing process generating dipole-dipole correlations. Only a theory based on a microscopic quantum approach will allow to do this. One can argue that even if, at present, SF can not be

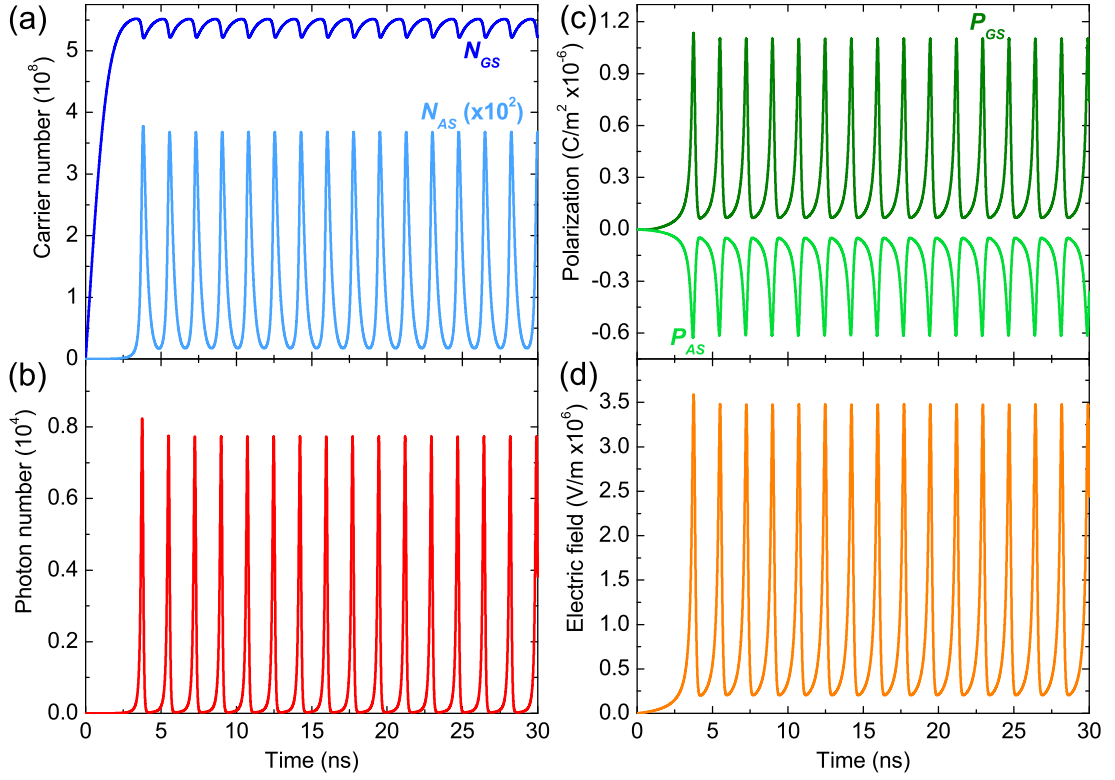


Figure 5.2: Linear model. Dynamic solution of the Maxwell-Bloch semiclassical equations 5.22-5.26 for a GS charge carrier population N_{GS} (blue), an AS charge carrier population N_{AS} (light blue), a photon population S (red), a GS polarization P_{GS} (dark green), an AS polarization P_{AS} (light green) and an electric field in the cavity E (orange). The pulses take the form of a Q-switched emission. As for Fig. 2.10 (b), the parameters are: $I_{GS} = 1.04 \cdot I_{th} = 90$ mA, $L_{AS}/L_{TOT} = 0.2$, $\alpha_0 = 82 \text{ cm}^{-1}$ and $\tau_{AS} = 0.25$ ns. The polarization dephasing time T_2 is set to 200 fs.

properly described by the conventional Maxwell-Bloch equations, at least SR should be. Indeed, in the case of pure Dicke SR, the ensemble is initially prepared in an excited state by a coherent pulse into an already correlated state possessing a macroscopic electric dipole. In this sense, an ensemble of indistinguishable electron-hole pairs should be considered as highly correlated and thus its decay should result in the emission of a superradiant pulse. However, this is not the case. Only a microscopic quantum approach would allow to describe the “ladder” of $2r_{max} + 1 = N + 1$ energy levels through which the system can cascade from the fully inverted state down to the ground state passing by the superradiant state [see Fig. 5.1 (a)]. For this reason, we should also not expect that the emitted intensity calculated from eq. 5.24 shows the superlinear behavior typical for a collective emission as opposed to the emission of an ensemble of independent dipoles. In 1989, Zheleznyakov *et al.* in the introduction of their paper on “Polarization waves and super-radiance in active media” explain this issue very clearly [232]:

“(In contrast to slow processes (i.e., $T_2 \ll T_E$) such coherent processes cannot be described by rate equations with time-dependent radiation intensity and time dependent stimulated transition probability. In this respect, collective processes are particularly interesting. Dicke SR was among the first processes involving a large number of particles of the medium to be predicted and discovered experimentally.

The microscopic method, which starts with the quantum electrodynamics of cold field modes and individual molecules in vacuum, can in principle take into account all the effects of the interaction between molecules and the field. In particular, this applies to effects due to the spatial inhomogeneity of radiation and the internal energy of particles in the active medium. However, considerable difficulties are encountered in the transition from micro to macro characterization of the relevant processes, and a number of simplifications and approximations have had to be resorted to. The direct numerical method of investigation is difficult to use as a basis for developing physical ideas capable of describing and explaining these phenomena. Neither approach can reveal the place of different collective coherent processes in quantum radiophysics and optics in the overall picture of unstable wave processes, or point to analogous processes in other branches of physics.

The macroscopic approach of continuum electrodynamics simplifies the solution of these problems and often provides a unified physical interpretation of the phenomena under consideration. ”

We can also understand the problem concerning SF with the following simple point of view. As explained at the beginning of Sec. 5.3, if the N emitters independently radiate one another, the emitted fields possess random phases ϕ_n and the system is in the regime of fluorescence. The random phases ϕ_n make the dipoles distinguishable from each other. On the other hand, coherence between the dipoles implies that the relative phases between the emitters are fixed thus leading to a total intensity proportional to N^2 . When solving the Maxwell-Bloch equations, we take into account only the modulus of each quantity (i.e., $|\mathbf{E}|$ and $|\mathbf{P}|$) and the modulus of a vector is always independent of its phase. In other words, the electron-hole pairs that we have introduced in our formalism are *indistinguishable* and thus automatically in phase with one another. For a proper and precise description of the onset of SF, at least from a phenomenological point of view, somehow we should introduce the phase terms $\exp i\phi_n$ in our equations and explain how these terms would interact with the populations and the polarizations (especially with the gain terms) to develop the collective behavior expected in the case of SF. Nonetheless, even in case of success, such set of equations would not still be able to describe SR as only a microscopic quantum approach would solve this issue. Moreover, the carrier spectral dependency typical of semiconductors should also be taken into account when developing the gain term in eqs. 5.22-5.26. In this sense, the wavelength-dependent

model introduced in the second chapter should help us in the establishment of a more rigorous dynamic model. So far in the literature, the self-phasing mechanism necessary for the establishment of SF has not been introduced in the Maxwell-Bloch rate equations. However, this does not mean that the macroscopic electrodynamics described by the Maxwell-Bloch equations are useless for the analysis of SR or SF. The dynamic evolution obtained by solving eqs. 5.22-5.26 can indeed be seen as the evolution of a macrodipole of completely indistinguishable dipoles at each instant. The macrodipole is in fact the charge carrier population N that can be seen as an ensemble of N electron-hole pairs, which interact within the common radiation field \mathbf{E} in the cavity and the medium polarization \mathbf{P} . In this sense, the dephasing time T_2 describes more the lifetime of the macrodipole rather than the relaxation of the coherence between the dipoles. In other words, the calculated dynamic traces would give information concerning the evolution of the amplitude of the macrodipole rather than its coherence. Eqs. 5.22-5.26 may therefore rather be used as an indication on the range of parameters for which the chances to obtain a collective emission are maximized.

According to the condition 5.20, SF is more likely to occur when the dephasing time T_2 is much longer than the characteristic superradiant time τ'_{SR} or the cooperative one τ_c . One way to obtain such a situation is to dispose of a MQW heterostructure placed in a very low Q -factor cavity under a very high pumping rate, for which conventional lasing is inhibited [206, 215]. The idea is that the abnormally high population N of electron-hole pairs rises so much the cooperative frequency ω_c given by eq. 5.27 that the condition 5.20 is easily fulfilled. In case of MS-LDs, the escape time of the photons T_E is kept as short as possible thanks to large absorption in the AS. For these reasons, we computed eqs. 5.22-5.26 for a high pumping rate ($I_{GS} = 1$ A), very large carrier-free absorption ($\alpha_0 = 1000 \text{ cm}^{-1}$) and very short absorber carrier lifetime ($\tau_{AS} = 1$ ps) for the linear model (Fig. 5.3). In order to favor a superfluorescent-like emission, the polarization relaxation time T_2 is arbitrarily increased by a factor of 5 compared to its nominal value for semiconductors, i.e., $T_2 = 1$ ps. As it can be seen in Fig. 5.3, the emission is Q-switched. However, during each pulse the carrier population N_{GS} falls below its transparency threshold $N_{tr} = 3.3 \cdot 10^8$. In other words, the gain g_{GS} in the GS becomes negative (absorption occurs). In standard lasing regimes (even if pulsed) this is strictly forbidden as the gain is always positive or at least close to zero (e.g., in case of strong Q-switching) due to a simple conservation law.

Belyanin *et al.* in Ref. [200] interpret this behavior as a signature of a coherent process in which the SR pulse absorbs almost all the energy stored in the active medium (as expected for a superradiant emission). As no superradiant/collective term has been added in the equations (see the discussion concerning macroscopic and microscopic approaches), we strongly disagree with this interpretation. No superradiant-like mechanism can be invoked if one is not considering any self-phasing dipole-dipole process nor any quantum collective behavior in the Maxwell-Bloch equations. Here, we propose a simpler explanation for this negative gain that takes into account only what is really in the eqs. 5.22-5.26. Compared to the conventional regimes described by the standard rate equations 2.54-

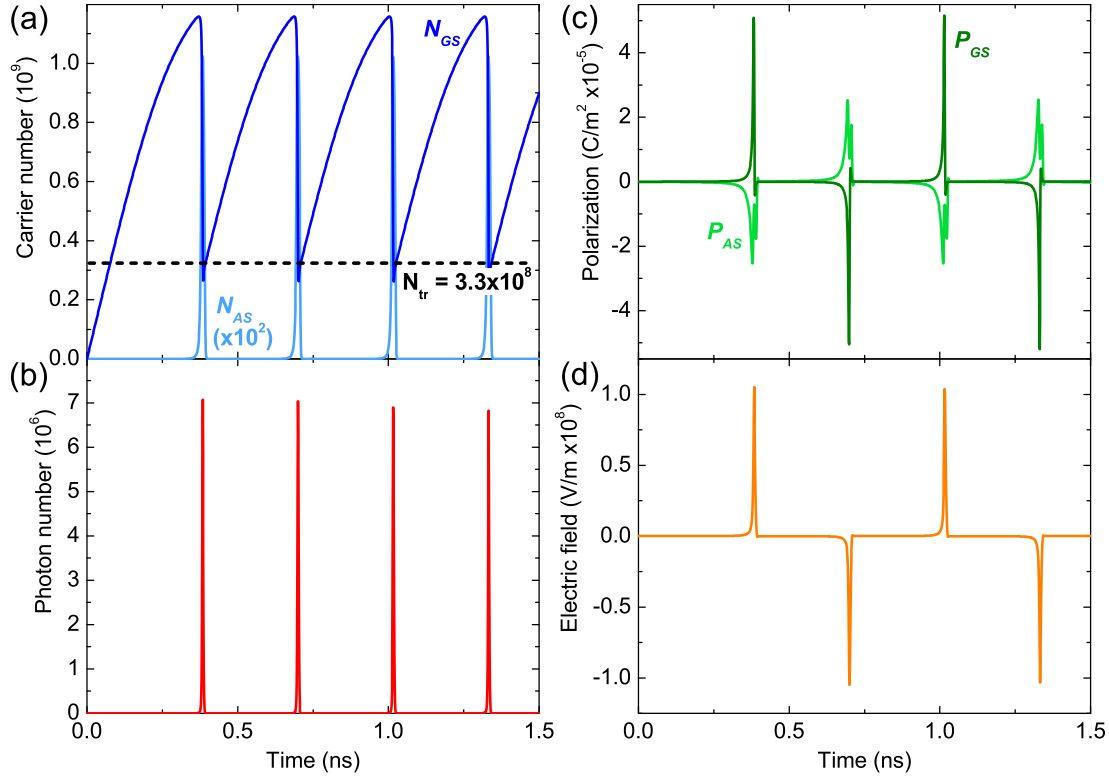


Figure 5.3: Linear model. Dynamic solution of the Maxwell-Bloch semiclassical equations 5.22-5.26 for a GS charge carrier population N_{GS} (blue), an AS charge carrier population N_{AS} (light blue), a photon population S (red), a GS polarization P_{GS} (dark green), an AS polarization P_{AS} (light green) and an electric field in the cavity E (orange). The parameters are: $I_{GS} = 11.55 \cdot I_{th} = 1$ A, $L_{AS}/L_{TOT} = 0.2$, $\alpha_0 = 1000 \text{ cm}^{-1}$ and $\tau_{AS} = 1$ ps. The polarization dephasing time T_2 is set to 1000 fs. The dotted black line in (a) represents the carrier population N_{GS} at the transparency, i.e., $N_{tr} = 3.3 \cdot 10^8$.

2.56, the Maxwell-Bloch equations possess two more relations that concern the medium polarization \mathbf{P} in the respective sections. Eqs. 5.25 and 5.26 impose the system a further time-scale proportional to T_2 . We believe that the system has thus a further degree of freedom to “store” its energy in the form of a high polarization and that is then used to deplete the GS below its transparency threshold. This picture is supported by the evolution of the gain in the GS with respect to the dephasing time value T_2 . For relatively short dephasing times (i.e., $T_2 \leq 500$ fs), the gain remains always positive as expected for a standard lasing emission. On the contrary, once T_2 is increased (i.e., $T_2 \geq 1$ ps), the population starts to fall below its transparency threshold during each pulse. The observed negative gain for such drastic operating conditions can thus be referred to as a normal energy storage during the pulse (in the form of electric field and polarization) that once emitted strongly depletes the carrier population.

5.4 Optically-pumped superfluorescence

In this section we report the experimental tests that we have carried out to investigate the possibility of a superfluorescent emission from a semiconductor confined to a small volume by optical pumping. Basically, we followed the approach proposed by Belyanin and Kocharovsky in Refs. [215, 206, 200]. According to what is explained in Sec. 5.3.2, a semiconductor structure must fulfill the condition 5.20 based on the Arecchi-Courtens condition 5.19 for which $\tau_c \leq \tau'_{SR} \ll T_2$ [197]. We can thus extract an upper limit for the sample length via $\tau_c < T_2$, i.e., to promote the cooperative behavior the emitted photons should cover the entire length of the sample before the dipoles dephase. τ_c is the intrinsic duration of each photon process and is of the order of $\frac{L}{c}$ for the large sample SR. This means that for a dephasing time T_2 of 200 fs and an effective refractive index n_{eff} of 2.5 (at 3 eV for GaN [38]), the critical stripe length is $\sim 24 \mu\text{m}$.

5.4.1 Samples, design and microfabrication process

Unfortunately, direct measurements of the microscopic dipole magnitude are not possible. Therefore, the idea is to fabricate waveguide-like structures (according to the pencil-shaped sample in the case of large sample SR) with various lengths and to study the temporal dynamics of a non-resonantly excited electron-hole plasma in these structures as a function of length. This practical approach has been already investigated by Lars Kappei in GaAs/AlGaAs MQW heterostructures [221]. The spatial confinement was provided by the definition of etched mesa structures in one case and in another by a metal mask that allows the selective excitation of waveguide-like stripes. According to the theoretical studies of Belyanin and Kocharovsky [200], Kappei proposed to investigate the behavior of the lifetime of the photoexcited carriers as a function of the sample length in order to identify the transition to a superradiant-like emission. In practice, if the carrier lifetime shortens when increasing the stripe length, this can be ascribed to a more important amplified spontaneous emission as the photons traveling along the cavity favor the stimulated emission process thus enhancing the carrier depletion mechanism in the MQWs. On the contrary, if the carrier lifetime shortens when decreasing the stripe length, this is more likely ascribed to a superradiant transition mode as the cooperative time scale τ_c is expected to be smaller than the dephasing time T_2 . Therefore, as previously mentioned, a superradiant emission may occur when the sample dimensions get below a critical value and the condition 5.20 is satisfied.

The samples grown for optically-pumped SR experiments are C1094, C1095, C1217 and C1233 (see Table 2.2). The respective layer compositions are shown on the left-hand side of Figs. 5.4 and 5.5. A specific photolithography quartz mask has then been realized for the microfabrication process of superradiant structures. To meet the criteria reported by Belyanin and Kocharovsky, mesa structures with lengths ranging from 1 to 30 μm with steps of 1 μm and widths of 2, 5 and 10 μm have been designed (Fig. 5.6). To further frustrate the optical feedback of the cavity, a set of mesa structures with the

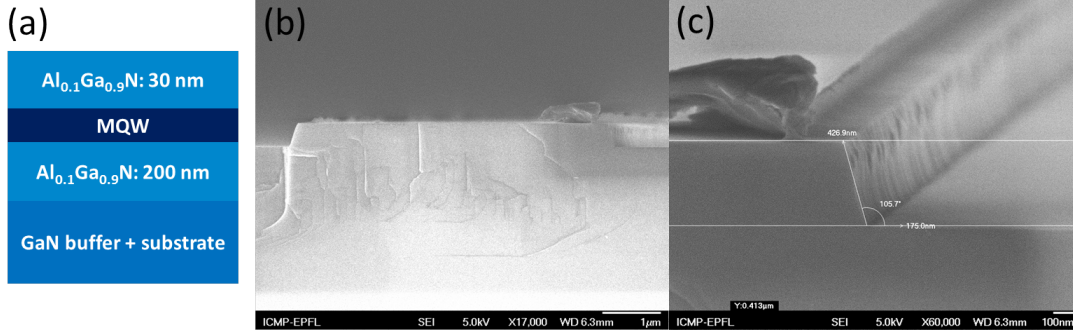


Figure 5.4: (a) Layer compositions of the structures along the vertical c -axis. The MQW active region consists in 7 $\text{In}_{0.08}\text{Ga}_{0.92}\text{N}/\text{GaN}$ and $\text{GaN}/\text{Al}_{0.1}\text{Ga}_{0.9}\text{N}$ well/barrier layers for samples C1094 and C1095, respectively (see Table 2.2). (b) SEM images of a $10 \times 5 \mu\text{m}^2$ stripe taken from the cleaved facet. (c) Detail of the dry etched stripe walls.

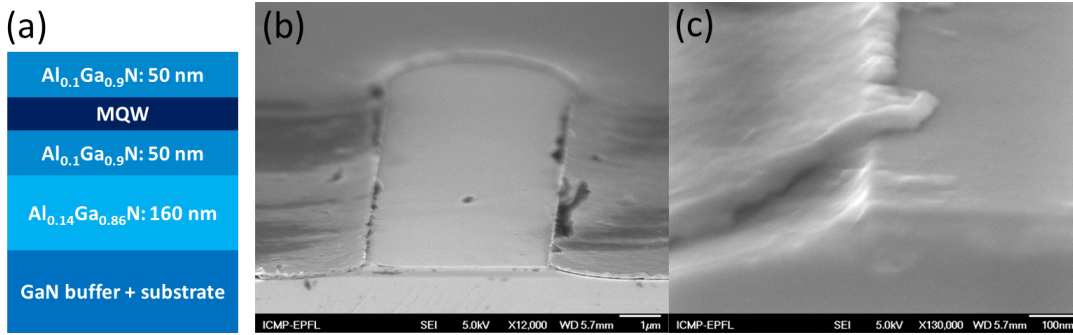


Figure 5.5: (a) Layer compositions of the structures along the vertical c -axis. The MQW active region consists in 1 and 5 $\text{GaN}/\text{Al}_{0.1}\text{Ga}_{0.9}\text{N}$ well/barrier layers for samples C1217 and C1233, respectively (see Table 2.2). (b) SEM images of a $10 \times 5 \mu\text{m}^2$ stripe taken from the cleaved facet. (c) Detail of the dry etched stripe walls.

same dimensions but tilted by 7° with respect to the cleavage planes have also been fabricated on the same mask. One photolithography step has been realized to define the mesa structures. The etching depth was larger than 250 nm so as to remove the MQW anywhere else than in the mesa [Figs. 5.4 (c) and 5.5 (c)]. Time-integrated and time-resolved experiments have then been carried out on the same setup as described in Fig. 4.4. We used the third harmonic of a $\text{Ti}:\text{Al}_2\text{O}_3$ mode-locked laser ($\sim 280 \text{ nm}$, repetition rate of $\sim 4 \text{ ns}$, pulse width of $\sim 2 \text{ ps}$) to excite non-resonantly the stripe. The excitation spot FWHM is estimated to be $5 \mu\text{m}$.



Figure 5.6: Layout of the photolithography quartz masks employed during the microfabrication process of superradiant structures. After cleavage, the mesa structures range from 1 to 30 μm long and 2, 5 and 10 μm wide. Note that longer structures (50, 100, 200, 400 and 800 μm) have been also implemented in the mask to better discriminate a possible lasing regime.

5.4.2 Experimental results

These following experiments have been carried out in collaboration with the group of Prof. B. Deveaud-Plédran at LOEQ-EPFL (PhD student Mehran Shahmohammadi and Dr. Gwénolé Jean Jacopin).

First, we processed samples C1094 and C1095 by dry-etching mesa structures with different lengths according to the mask depicted in Fig. 5.6 (see Fig. 5.4). Unfortunately, it was not possible to distinguish between the signal coming from the etched stripes and the one coming from the GaN layers surrounding the stripes. No evident trend has been observed by changing the stripe length. Indeed, the excitation spot size is not limited to the mesa area but it also extends over the neighboring regions thus making the signal collection difficult to discriminate.

For the second attempt, we decided to combine the spatial confinement provided by etched mesa structures with the selective excitation provided by a metallic mask. Thus, samples C1217 and C1233 have been dry-etched to form mesa structures (about 200 nm deep) according to the mask described in Fig. 5.6 and subsequently a gold layer (about 60 nm thick) has been deposited on the etched regions (Fig. 5.5). This way, the metal coating ensures that the collected signal solely comes from the mesa structures and not from the surrounding etched layers. Furthermore, in samples C1217 and C1233 a bottom AlGaIn cladding layer has been inserted to enhance the optical confinement in the MQW active region. The simulated optical confinement factor amounts to $\sim 1\%$.

Figure 5.7 displays a summary of the optical experiments carried out on sample C1233 (5 QWs with $d_{\text{QW}} = 2.5$ nm). All the spectra have been recorded at 4 K and have been collected from the top of the sample due to difficulties in collecting the light coming from the stripe facet at cryogenic temperature and high injection at the same time. Figure 5.7 (a) shows the PL spectra of the unprocessed sample under cw excitation at 244 nm and for increasing excitation powers (from bottom to top). The spectra show several

Chapter 5. Superradiance and superfluorescence: application to III-nitride semiconductors

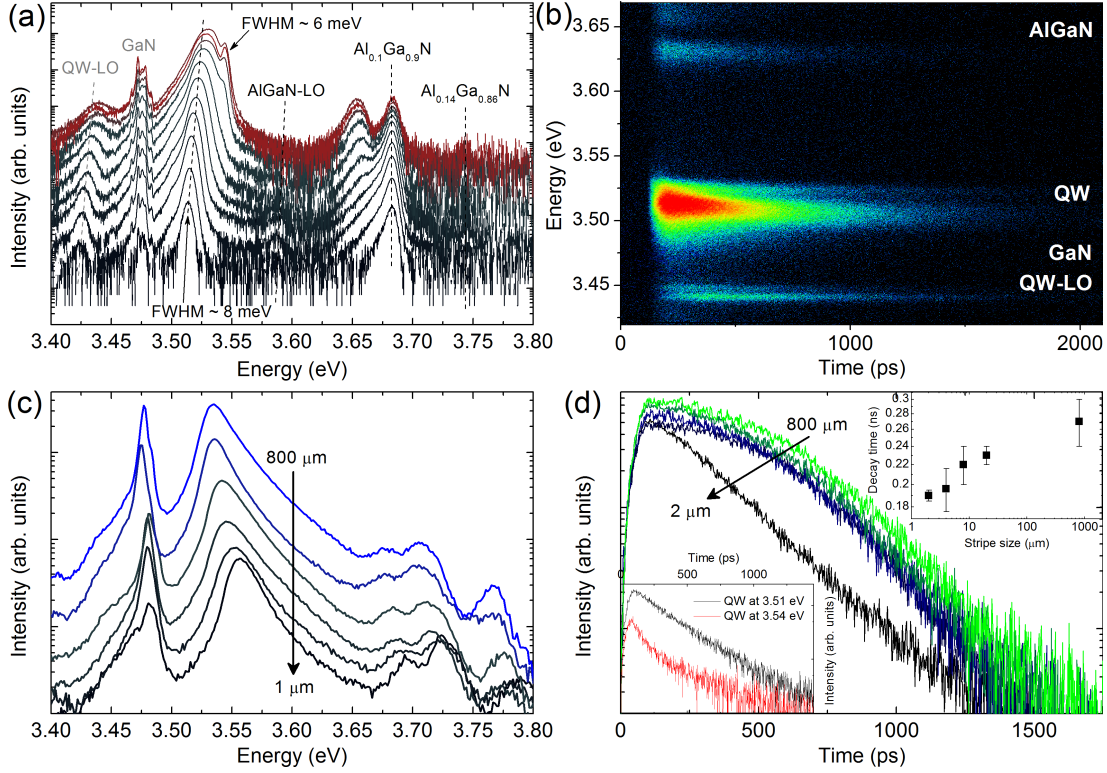


Figure 5.7: Sample C1233. (a) PL spectra for the unprocessed sample measured at 4 K for varying excitation powers. (b) Streak camera trace measured at 4 K for a $2 \times 2 \mu\text{m}^2$ stripe. (c) Time-integrated PL spectra measured at 4 K from mesa structures with varying lengths. The respective dimensions are (from bottom to top): 1×2 , 2×2 , 4×2 , 8×2 , 20×2 and $800 \times 2 \mu\text{m}^2$. (d) Normalized PL intensity at the lower well transition (3.51 eV) as a function of time measured at 4 K for varying lengths. The respective dimensions are (from bottom to top): 2×2 , 4×2 , 8×2 , 20×2 and $800 \times 2 \mu\text{m}^2$. The bottom inset shows the time-resolved PL intensity for the well transition energies at 3.51 (black) and 3.54 (red) eV, respectively, whereas the top inset shows the decay time with respective error bars as a function of the stripe size.

pronounced peaks ascribed to: the longitudinal optical (LO) phonon replica of the QWs at 3.42 eV, the bulk GaN at 3.47 eV, two distinct QW transitions at 3.51 and 3.54 eV, the LO-phonon replica of the AlGaN layers at 3.59 eV, the AlGaN barrier layer at 3.68 eV and the AlGaN cladding layer at 3.75 eV. The remaining peak at 3.66 eV may be ascribed to the bi-exciton of the AlGaN barrier layer. Note that the QW transition at 3.51 eV exhibits an extremely narrow linewidth of 8 meV at low excitation power indicating the high quality of the sample. The QW transition at 3.54 eV exhibits an even narrower linewidth of 6 meV but only at higher excitation power. We interpret this transition to be related to amplified spontaneous emission occurring in the QWs. In Figs. 5.7 (b)-(d) time-resolved PL spectra are plotted by collecting the emission from the sample surface. When decreasing the mesa size, the emission peaks of the time-integrated spectra blueshift whereas the spectral shape remain unchanged [Fig. 5.7

(c)]. The blueshift can likely be ascribed to strain relaxation that modifies the total polarization field in the QWs thus shifting the transition energies. At the same time, the temporal evolution also seems to depend on the mesa length [Fig. 5.7 (d)]. Indeed, the decay time shortens from about 270 ps down to 190 ps when the stripe length is decreased from 800 μm down to 2 μm [see top inset in Fig. 5.7 (d)]. Due to the sample holder drift during the measurements, we may assume to be in the high excitation density regime only for mesa stripes larger than $4 \times 2 \mu\text{m}^2$. Note that the QW transition at 3.54 eV also exhibits a faster component at short delay time that may be ascribed to relaxation occurring in the ground state [see bottom inset in Fig. 5.7 (d)]. As previously mentioned, a shortening of the decay time with the stripe length could be ascribed to the onset of a superradiant-like emission. However, an alternative explanation, as proposed by L. Kappei in Ref. [221], could be surface recombinations occurring at the dry-etched mesa side walls or diffusion from the excitation spot. On one side, suppressing the etching step in the fabrication process of the mesa structure could favor the identification of the surface recombination contribution but this could be done at the expense of a lower spatial confinement. On the other side, collecting the emission from the stripe facet instead of the sample surface should allow to rule out the diffusion contribution [221]. In fact, when collecting the light from the sample surface, the detection region coincides with the excitation spot. Therefore, the photogenerated carriers can diffuse out of the excitation area thus leading to an erroneously (from a radiative point of view) shorter lifetime. Nonetheless, III-nitrides are expected to exhibit a slower initial diffusion of carriers out of the detection region and to be less sensitive to surface recombinations. Given the moderate decrease in the carrier lifetime (100 ps until a 2 μm long stripe), it is very likely that the shortening is mainly due to diffusion/surface recombinations rather than to a SR related collective behavior of carriers. Indeed, the superradiant time-scales are expected to be in the range of femtoseconds.

In summary, no evidence of a fast superradiant-like emission has been observed in our samples. One possible reason for the absence of collective effects is the excitation power limitation. In fact, to excite the GaN/AlGaIn MQW active regions, we must operate the Ti:Al₂O₃ mode-locked laser at the third harmonic ($\sim 280 \text{ nm}$), which implies a significant loss of power. Indeed, the estimated excitation power at the third harmonic is expected to be $\sim 20\%$ of the second harmonic (in Ref. [221] the GaAs/AlGaAs samples are excited with this second harmonic) and $\sim 5\%$ of the fundamental one. As emphasized in the previous sections, the chances for a cooperative behavior to occur are directly proportional to the number N of available inverted dipoles. Anyway, SF in semiconductors is very challenging due to the large inhomogeneous broadening, the strong energy dispersion within the bands and the high polarization dephasing rate. Especially concerning the latter, the right-hand side of condition 5.20 (i.e., $\tau_{SR} \ll T_2$) is fairly difficult to satisfy in semiconductors due to the high scattering and collision rates of carriers in the valence and conduction bands. As mentioned in section 5.3.2, to overcome all these problems, the rising idea is to “help” the cooperative self-phasing behavior by creating a singularity in the DOS by means of excitons, QDs, or even magnetoplasmas.

5.5 Electrically-pumped MS-LDs for SF purpose

In this section we report the experimental tests that we have carried out to investigate the possibility of SF from a GaN-based MS-LD. SF in semiconductors is a very controversial subject. Especially the dephasing time seems to be the major drawback for obtaining SF under electrical pumping. Indeed, in a forward-biased diode, the carriers are electrically injected in the active region, which means in a complete incoherent way. Moreover, they are also injected in the excited states thus immediately experiencing a very high dephasing rate that drastically prevents any collective behavior.

Assuming that all other parameters expressed in the cooperative frequency ω_c given by eq. 5.27 are optimized, the key strategy to enhance a collective behavior is to increase as much as possible the population N of inverted dipoles in a small volume. In a LD, this means reaching a high number of electron-hole pairs in the active region by increasing the injected current. However, in a common LD the number of carriers is clamped to a certain value once the system reaches the lasing threshold condition. On the contrary, a MS-LD possesses the unique feature to postpone the threshold condition to larger current values. Indeed, as shown in Fig. 2.14, the threshold condition can be shifted to higher currents for a larger carrier-free absorption α_0 in the cavity and consequently also for a higher absorber/cavity length ratio L_{AS}/L_{TOT} . This way, for a reasonably high amount of absorption in the cavity, the system can never satisfy the threshold condition and the carrier population in the active region can be heavily raised. As depicted in Figs. 3.6 and 3.9 (a), this situation is met for large negative bias voltages applied to the AS. Moreover, at this bias range, the carrier lifetime is so short that the absorber can easily recover its initial carrier-free state thus preventing any absorption saturation (Fig. 4.3). For all these reasons, it is thus convenient to investigate the potential superradiant emission of a MS-LD driven at high I_{GS} , biased at large V_{AS} and with a long L_{AS} (i.e., with a high L_{AS}/L_{TOT}). In other words, it is mandatory to avoid situations leading to condition 5.21 otherwise lasing will take over. Therefore, SR and SF are likely to occur just below the lasing threshold, i.e., a phase-like transition occurring between amplified spontaneous emission (i.e., superluminescence in the case of a LD) and Q-switching (due to the large reverse bias). In principle, SR and SF should show extremely high peak powers, a distinct temporal evolution and an extremely narrow pulse leading to a severe spectral broadening, characteristics which strongly differ from conventional spontaneous emission and lasing.

While we were looking for superradiance-like emission in our MS-LDs, we observed some unexpected and strange features. Unfortunately, none of them have demonstrated the superlinear peak power growth with injected carrier density typical of SR and SF. Hereafter, we will list these unexpected behaviors and provide, if possible, a simple explanation to interpret them. Note that as we are investigating regimes at large reverse bias V_{AS} , the duty cycle of the pump current is kept below 1% during the experiments to avoid absorber breakdown.

Figure 5.8 (a) shows the pulse wave form using an optically triggered sampling scope

while driving the MS-LD close to threshold at very large negative biases and high pump current. Apparently, the pulse intensity is one order of magnitude higher than a typical self-pulsating emission (compare with Fig. 4.7). According to the experiments of Scheibenzuber *et al.* described in Ref. [132], this means a peak power of several watts. Passive mode-locking could explain these values but can be ruled out since the emission consists in the generation of a single pulse. Conventional lasing can also be excluded as the recorded spectrum is very broad [~ 1 nm in the inset of 5.8 (a)]. Figure 5.8 (b) shows an overexposed streak camera image for the same device but biased at a larger negative voltage and driven at higher pump current ($V_{AS} = -23$ V and $I_{GS} = 417$ mA). As in the previous case, the MS-LD is driven close to the lasing threshold. Interestingly, we see that after a delay time of 0.35 ns the amplified spontaneous emission is quenched and a giant burst of light is emitted. Moreover, after the light burst no amplified spontaneous emission is observed. This temporal evolution can not be ascribed to conventional lasing. In fact, after Q-switched pulse the carrier density in the GS is just above the transparency threshold (in the case of stabilized ROs it would be just below the lasing threshold) and therefore amplified spontaneous emission should be observed. On the other hand, in the case of a superfluorescent burst, the carrier density entirely drops to zero since the majority of the carriers must participate to the pulse emission thus leading the system to reach the fully deexcited state [see Fig. 5.1 (a)]. So, it would not be possible to observe any further spontaneous emission. Finally, if we assume that the measured pulse width is resolution limited, the deconvoluted pulse width is below 1.1 ps, approaching the superradiant time-scale (femtoseconds). Although some features might be compatible

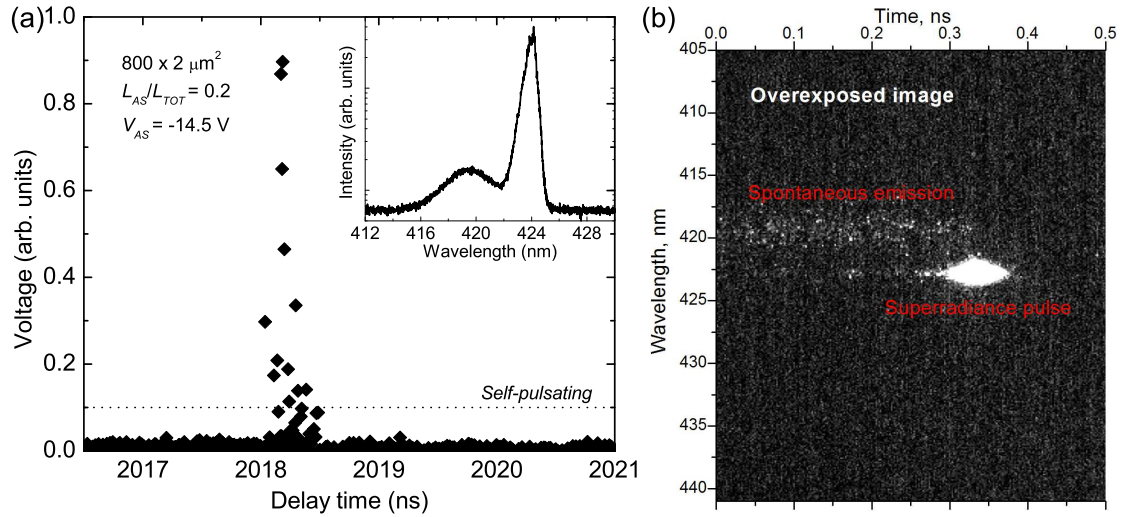


Figure 5.8: (a) Pulse wave form detected using an optically triggered sampling scope with sampling head of 70 GHz and 50 GHz bandwidth. The inset shows the emitted spectrum at $V_{AS} = -14.5$ V. (b) Overexposed streak camera image of a superfluorescent-like pulse emission. The device is an $800 \times 2 \mu\text{m}^2$ MS-LD with a $150 \mu\text{m}$ long central absorber biased at $V_{AS} = -23$ V and driven at $I_{GS} = 417$ mA from sample C133.

with SF, the collected data do not allow to unambiguously support this assumption. In order to eventually demonstrate a collective behavior in an electron-hole system, even though unexplained, an extremely high peak power and an extremely narrow pulse width are not sufficient. One has also to provide strong evidences for a superlinear growth of peak power with injected number of carriers.

Summary of the results

In this chapter, we presented a critical review on SR and SF in semiconductors with a particular emphasis on the III-nitride case. First, we introduced the quantum theories for SR and SF originally developed by Dicke in 1954 and successively by Bonifacio and Lugiato later in the 70's for both the small and large solid-state medium cases.

Then, we developed a new set of equations based on the standard semiclassical Maxwell-Bloch equations. This formalism accounts for the evolution of the system in terms of carrier population N , electromagnetic field \mathbf{E} and internal polarization \mathbf{P} also in the specific case of a multiple-contacted cavity. In case of slow radiation dynamics (i.e., normal lasing), the new set of equations is successfully traced back to the common and standard rate equations. Indeed, with the proper driving condition, we were able to reproduce the same Q-switched emission as in the case described in Sec. 2.3.4. In addition, for a cavity with high photon losses and for a very high pumping rate, for which the polarization dephasing time T_2 was arbitrary increased to further favor the cooperative behavior to take over, we reported a strong non-linear effect that causes the carrier population n_{GS} in the GS to fall even below the transparency threshold. No such depletion was predicted using the common standard rate equations. We pointed out how it is incorrect to invoke SR or SF as no collective/self-phasing behavior has been inserted in the equations. So far, no physical model has correctly combined the microscopic quantum approach proper to a collective behavior and the macroscopic semiclassical one to successfully simulate the SF mechanism. Somehow, we should integrate in our equations the evolution of the dipole phase, that eventually locks in the case of SF. However, this would only remain a phenomenological approach.

Concerning the experimental results, neither the optically pumped structures nor the electrically pumped ones have provided unambiguous evidences supporting the collective emission interpretation. The relatively low excitation power available in the time-resolved set-up and the fast relaxation time of the polarization in solids may likely prevent the onset of collective emission. Nonetheless, optically pumped structures seem to be more promising for the investigation of superfluorescent emission. Indeed, the active region can be carefully designed in order to favor the collection of carriers in the MQWs by means of, e.g., staggered or graded index separate confinement heterostructures.

Conclusion and perspectives

Summary of the experimental results

This PhD dissertation treated various aspects related to III-nitride-based MS-LDs. It focused on the efforts and the possible ways to reach pulsed emission with several GHz of repetition rate in the short-wavelength range. The influence of the different device parameters was investigated with careful spectral and temporal characterizations. Modeling was carried out to support a better understanding of the underlying physical phenomena. Static and dynamic parameters extracted from the models then allowed for an accurate mapping of the device operating parameters.

In summary, we have demonstrated the possibility to electrically control the static and dynamic lasing action of monolithic InGaN-based MS-LDs. In particular, we pointed out the interplay between the external bias V_{AS} applied to the AS and the piezoelectric field \mathbf{F}_{int} inside the InGaN MQWs on the control of the AS absorption. In parallel to Hakki-Paoli gain spectroscopy, a simple experimental method was developed to measure the absorption of the AS MQWs. The large QCSE that takes place in InGaN MQWs grown along the polar direction generates a complex non-monotonic dependency of this absorption, which is fundamentally different from the behavior observed in conventional GaAs-based LDs. As a consequence, this allows a high degree of freedom for modulating the absorption in GaN-based MS-LDs.

The dynamics of the charge carrier and photon populations in the cavity have been discussed using standard rate equations extended from the case of standard single-section LDs. Two models have been presented to analyze the evolution of the gain as a function of the charge carrier population: the linear- and the wavelength-dependent ones. The main advantage of the wavelength-dependent model, as compared to the linear one, is that the full spectral dependency is preserved leading to a more precise description of the carrier and photon dynamics in the system. In this sense, the precise determination of the recombination coefficients turned out to be of crucial importance. The response of the active region in the different SP operating regimes has then been evaluated in terms of turn-on delay time τ_{TOD} of the lasing emission, emission intensity, pulsation frequency f_{SP} and pulse width τ_{SP} . The rate equation model adapted for the specific case of MS-LDs reveals that the carrier-free absorption α_0 has a major impact on the performance of the devices. In fact, a larger α_0 leads to a higher emitted intensity

and to a shorter pulse width τ_{SP} . In this sense, to obtain the shortest pulses with the highest peak power, the absorption in the AS must be maximized. The other controllable parameters such as the absorber carrier lifetime τ_{AS} and the absorber/total cavity length ratio L_{AS}/L_{TOT} have a stronger impact on the turn-on delay time τ_{TOD} and on the pulsation frequency f_{SP} . On the other hand, a longer AS (i.e., higher L_{AS}/L_{TOT} ratio) would reduce the risks of absorber breakdown due to avalanche carrier phenomenon.

The main achievement of this thesis is the demonstration of three ultrafast pulse regimes in III-nitride-based semiconductor lasers: SP, passive, and active (hybrid) mode-locking. Using time-resolved spectroscopy, the SP regime, with a repetition frequency of several GHz, has been found to strongly depend on the absorber bias V_{AS} and on the heterostructure design (e.g., indium composition in the wells or in the barriers). In particular, we have shown how the absorber bias V_{AS} control the carrier-free absorption α_0 and the carrier lifetime τ_{AS} in the AS. For this reason, a careful analysis of the absorber lifetime evolution as a function of the applied bias V_{AS} has been carried out. The carrier escape rate (especially the tunneling rate through the well barriers) is pointed out as the main mechanism responsible for the shortening of the carrier lifetime at large reverse biases due to the strong tilt of the MQW band structure. A proper design of the heterostructures has then allowed to reduce the absorber carrier lifetime by a factor of 3 (100 ps). We found that the best operating conditions correspond to reverse biases beyond the flat-band-conditions. Two distinct regimes in the SP dynamics are observed (self-stabilized ROs and self-Q-switching) as functions of the applied bias V_{AS} and the pump current I_{GS} . Furthermore, we have demonstrated the generation of passively and actively mode-locked pulses for the first time in a monolithic InGaN-based device. Indeed, no external cavity was required for mode-locking operation. Moreover, as for the SP regimes, stable mode-locked pulses have been obtained even at $V_{AS} = 0$. Depending on the cavity length, the pulse repetition rate of the fundamental harmonic amounted to several tens of GHz and the pulses were as short as 3 ps with peak powers up to 320 mW. Mode-locking at harmonics higher than the fundamental mode have also been observed in a central absorber MS-LD. Stable mode-locking seems to be better achieved on long cavities with a relatively short AS (i.e., $L_{AS}/L_{TOT} < 0.1$). The best results concerning the dynamic operations of our MS-LDs are listed in Table 5.1.

The last part of this thesis was dedicated to the theoretical and experimental studies of superradiant or superfluorescent emission phenomena. The various quantum and classical aspects have been emphasized for small and large sample cases. To describe the dynamics of this process, we have presented a model based on semiclassical Maxwell-Bloch equations for the specific case of a multiple-contacted cavity. The formalism that we have developed gives a simple recipe for the mutual interactions involved between the carrier populations, the medium polarization and the electric field in the cavity. In principle, using this formalism, one should be able to predict the evolution of a superradiant pulse if the correlation between dipoles is assumed *a priori*. The mathematical formalism that describes the self-phasing mechanism that should trigger the collective behavior still need to be developed. Concerning the experimental results, no unambiguous evidence for SF

	SP	Passive mode-locking	Active mode-locking	SF-like
Peak power (W)	1.1	0.32	0.07	70
Pulse width (ps)	18	3	4	1.1
Pulse energy (pJ)	23	0.8	0.3	70
Repetition rate (GHz)	1-5	28-92	28.6	-

Table 5.1: List of the best results obtained during the Femtoblue project. The repetition frequency ranges depend on I_{GS} and V_{AS} for a self-pulsating emission whereas it depends on the cavity length L_{TOT} for a mode-locked one. Note that no definitive and unambiguous evidences have been found concerning the superfluorescent-like emission.

has been observed neither under optical pumping experiments performed on special mesa etched structures nor under electrical pumping experiments performed on MS-LDs from our samples. The fast relaxation time of the polarization in solids may likely prevent the onset of superfluorescent emission.

Outlook and perspectives

This thesis provides insights into various aspects of physical processes occurring in GaN-based LDs. The devices studied in this work are a good illustration of the potential of multisection (Al,In)GaN LDs for inexpensive and robust monolithic ultrafast sources operating in the blue-violet range. At present, ultrashort optical pulses in the blue-violet spectral range can only be produced using bulky laboratory installations such as mode-locked Ti:Sapphire lasers with frequency doubling, mode-locked xenon lasers, or dye lasers. Biosensing technologies and medical applications supporting human health would also benefit from these GaN-based LDs as the most common organic materials exhibit a strong response in the short-wavelength range.

Nowadays, LDs are omnipresent in ICT or optical data storage. So far, the Blu-rayTM standard is the only major application for III-nitride-based LDs. Sony is also currently working on the development of a new kind of 3D optical data storage. The idea is to write a 3D patterning information on a medium in the form of tiny hollow bubbles. The high peak power provided, e.g., by GaN-based MS-LDs operating in the ultrafast regime may be extremely useful for 3D writing in bulk media through a non-linear process (called multi-photon absorption) while their emission in the blue-violet wavelength range would enable to keep a small pit size just as for the Blu-rayTM disk. The European Space Agency is also considering GaN-based LDs as potential photonics technology candidates for several ground-breaking experiments to be performed in space, which are related to physical constant and gravitational field measurements, mainly for all-optical clock technologies.

So far, no model has correctly predicted the dynamic evolution of a superfluorescent emission in laser-like structures although claimed in several papers. The formalism that

Conclusion and perspectives

we need to implement in the Maxwell-Bloch equations accounts for the phase-locking of the emitters remains unknown. The challenge is to combine the microscopic quantum approach and the macroscopic semiclassical one to model the superfluorescent mechanism. Phenomenologically, this could be done by introducing the polarization phase in the Maxwell-Bloch equations.

A Electro-reflectance measurements

Modulation spectroscopy techniques induce changes in the reflection or transmission coefficient of the sample by modulating specific material parameters in order to characterize the optical and/or electrical properties of semiconductors through changes in the complex dielectric function $\varepsilon(\omega)$ [148]. Modulation spectroscopy is as a powerful tool for the investigation of InGaN/GaN MQW heterostructures as it is very challenging to observe at RT low-energy and weak-oscillating transitions with standard reflectance and photoluminescence spectroscopy [233]. Photo-reflectance (PR) is an external modulation spectroscopy technique in which a periodically chopped laser beam (the so-called pump beam) is used to induce the modulation in the sample at the same spot on which a quasi-monochromatic light source is focused (the so-called probe beam). The pump laser beam generates photo-excited electron-hole pairs in the sample that in turn modulate the built-in electric field inside the sample [234]. Christian Mounir (a Master student) and Marlene Glauser (a PhD student) have developed a PR set-up at LASPE to investigate the optical properties of InGaN/GaN-based and GaN/AlGaIn-based MQW samples. Together, we have modified this set-up so that it could also be used to perform electro-reflectance (ER) measurements (Fig. A.1). ER is another external modulation technique in which a modulated electric field including a possible DC offset is applied to the sample [148]. In the ER setup that we have developed the presence of an electric field applied perpendicularly to the surface of the sample lifts degeneracies inside the energy band structure. Then, the spectra obtained by modulation spectroscopy are the superposition of the lineshapes corresponding to each critical point of the sample under investigation. To extract the position of each critical point, an advanced fitting procedure is required and details can be found in Ref. [148].

The first sample inquired (C182) is an $\text{In}_{0.13}\text{Ga}_{0.87}\text{N}/\text{GaN}$ LED structure with 3 2.3-nm wide QWs and 11-nm wide barriers that emits around 440 nm. The LEDs were processed with a special transparent top p -contact, consisting in 120 nm of indium tin oxide (ITO). Ψ_{bi} amounts to 3.1 V and the current flowing through the p - n junction is 100 mA at 6.2 V. Band structure simulations for such a structure give an estimated internal polarization field of -1.6 MV/cm. Considering an intrinsic width d_u of 20 nm, flat-band conditions are

Appendix A. Electro-reflectance measurements

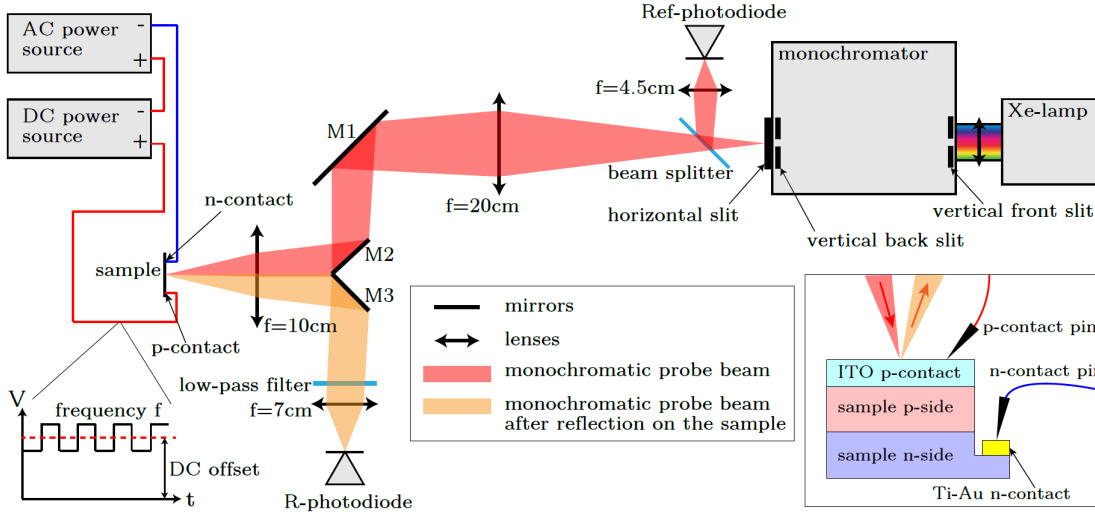


Figure A.1: Schematic view of the ER set-up developed and optimized in this thesis. The inset shows how the sample is contacted. [148]

expected at $V_{MIN} = -13$ V (see the procedure described in Sec. 3.2). As expected, already at a moderate reverse bias of -3 V the PL emission of the sample is strongly quenched due to the high escape rate that makes the carriers tunneling through the well barriers and away from the active region. ER spectroscopy has been carried out on a $500 \times 500 \mu\text{m}^2$ ITO LED to investigate how the applied reverse bias compensates for the internal polarization field F_{int} and modifies the optical transitions. An alternating current (AC) to create the electro-modulation is applied in series with a dc power supply that adds the offset for the bias voltage exactly as for V_{AS} (see Fig. A.1). By looking at the reflectance changes $\Delta R/R$ one can understand how the sample responds to a moderate excitation by means of a quasi-monochromatic source [149]. The transmission changes can then be correlated to absorption changes via the complex dielectric function $\varepsilon(\omega)$ [150]. This way, the bias voltage dependency measured in ER spectra can be linked to the absorption change spectra discussed in case of MS-LDs in Figs. 3.12 (e) and 3.12 (f), in which according to eq. 3.2 the probe beam is the absorber emission P_{AS} at $V_{AS} = 2.5$ V and the modulation is given by the applied bias V_{AS} . Further measurements implementing the ER spectroscopy technique can be found in Refs. [66, 149, 158, 159, 235, 236, 237, 238, 239] for III-nitrides (mostly on InGaN/GaN heterostructures) and in Ref. [150] for other materials.

ER spectra of sample C182 taken at RT are shown in Fig. A.2 (a) for biases ranging from 1 V down to -23 V. More details concerning the set-up parameters can be found in Ref. [148]. The strong oscillations observed around 3.1-3.2 eV are likely related to interference effects between the reflected probe beam and the different interfaces within the sample and their period can be used to determine the thickness of the layers [240]. In order to analyze the optical transition of the sample, the ER spectra are fitted as 2D confined Lorentzian-broadened band-to-band transitions for several critical points (i.e.,

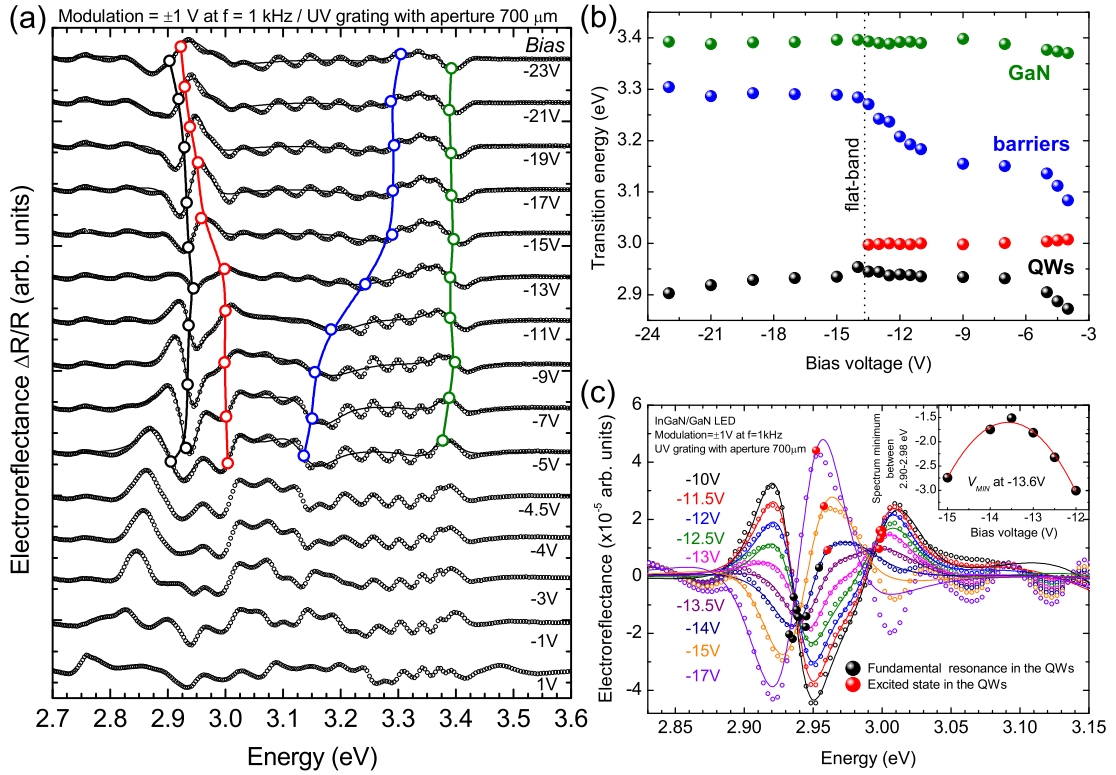


Figure A.2: (a) ER spectra of an InGaN/GaN MQW LED structure for different applied biases (sample C182). (b) Critical points extracted from (a). The critical point with the highest energy does not depend on the applied bias and is associated to transitions occurring in the GaN cap layer (green circles). The two critical points of lower energy are related to the fundamental resonance of the QWs and its first excited state (black and red circles, respectively). The critical points of intermediate energy are more likely related to well barrier emission (blue circles). Critical points of ER spectra for biases larger than -5 V have not been extrapolated as the fitting procedure is not reliable anymore around the fundamental resonance mainly because of the weaker phase oscillations. (c) Determination of the flat-band voltage of the InGaN/GaN MQWs LED structure. The phase of the fundamental resonance in the MQWs switches sign between -13 V and -15 V [see (a)], which indicates that the flat-band voltage lies within this range. The inset shows the extrapolated V_{MIN} . [148]

the main transition energies): QWs, well barriers and GaN cap layer transitions. The highest energy critical point does not depend on the applied bias as can be seen from Figs. A.2 (a) and A.2 (b) (blue circles). This transition energy at 3.4 eV corresponds to optical transitions occurring within the GaN cap layer as the applied bias is expected to have a stronger impact on the energies of the confined states [49]. The second highest energy critical point could then be ascribed to a transition somehow related to the GaN well barriers but its behavior with respect to the applied bias remains unclear [blue circles in Figs. A.2 (a) and A.2 (b)]. It may be that different critical points correspond to this transition [148]. The two remaining critical points represent the confined states in the

Appendix A. Electro-reflectance measurements

MQWs. It is very likely that the lowest one corresponds to the fundamental resonance (black circles) while the highest one corresponds to an excited state within the QWs (red circles).

To determine where flat-band conditions occur one has to look carefully for a phase change in the MQW fundamental resonance in the ER spectra when modifying the applied bias. Indeed, around the flat-band bias V_{MIN} the ER signal vanishes and flips its sign as the MQWs start to be tilted in the opposite direction. When looking at the ER spectra around the fundamental resonance it is obvious there is a phase flip for biases between -13 V and -15 V [Fig. A.2 (a)]. Figure A.2 (c) shows detailed ER spectra around 2.94 eV for a bias voltage range in which flat-band should lay. A flat-band bias V_{MIN} of -13.6 V is then extrapolated from the ER spectrum minima around the fundamental resonance [inset in Fig. A.2 (c)]. This picture is also supported by the maximal blueshift of the fundamental resonance energy when approaching -13.6 V [black circles in Fig. A.2 (b)]. Note that the high energy confined state (red circles) follows so closely the fundamental one for reverse biases larger than V_{MIN} that the fitting procedure can no more rigorously distinguish the energy difference between the two confined states. Most likely under such high external field the band structure is so tilted and asymmetrical [especially the well barriers, see Figs. 3.2 (b) and 3.2 (c)] that the MQWs cannot confine anymore the excited state and only the fundamental one can still be observed [237]. In the case of MS-LDs, this picture can imply that the strong absorption observed around V_{MAX} may not only be caused by the fundamental resonance but also by higher confined states. This means that a properly designed MQW active region can enhance or frustrate this contribution depending on the needs. Note that the ER curves for all applied biases intersect at a common photon energy corresponding to the band gap of the semiconductor material. The band gap energy of the InGaN layer can thus be experimentally and precisely determined [149, 150, 236]. For the present sample E_g^{InGaN} amounts to ~ 2.94 eV at RT [see Fig. A.2 (c)].

The second sample inquired (C161) is a structure more similar to the LDs studied during this thesis. It consists of an $In_{0.11}Ga_{0.89}N/In_{0.04}Ga_{0.96}N$ LED structure with 2 4.75-nm wide QWs and 10-nm wide barriers that emits around 430 nm. As for sample C182, the LEDs were processed with a special transparent ITO top p -contact. Ψ_{bi} amounts to 3 V and the current flowing through the p - n junction is 100 mA at 5.8 V. Band structure simulations for such a structure give an estimated internal polarization field of -1.19 MV/cm. Considering an intrinsic width d_u of 20 nm, flat-band conditions are expected at $V_{MIN} = -7.5$ V.

ER spectroscopy has been carried out on a $500 \times 500 \mu m^2$ ITO LED for different biases and at different temperatures (Fig. A.3). As the temperature is decreased the reflection oscillations become stronger and thinner indicating how the ER technique can be significantly more accurate for photogenerated carriers possessing a lower thermionic energy and that are less sensitive to phonon scattering. At the same time, the transition energies blueshift due to band gap renormalization [38]. This effect is also evident in the common intersection point for the InGaN band gap that at $T = 300$ K is about 3.04 eV while at

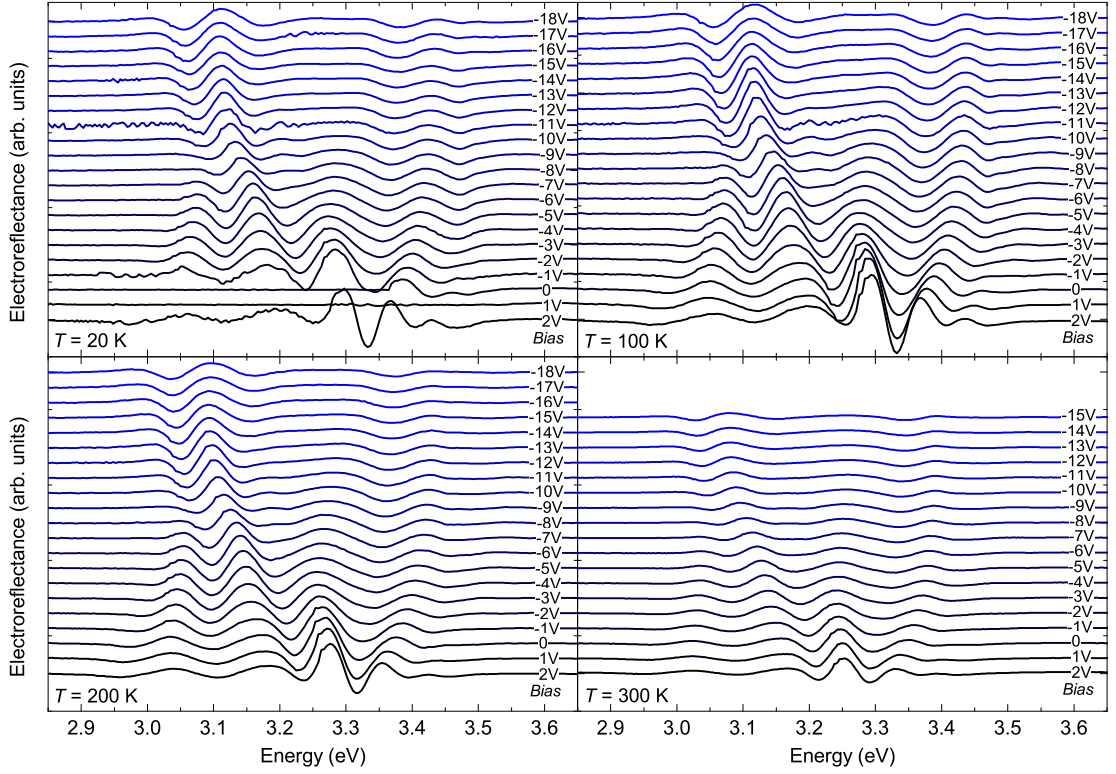


Figure A.3: (a) ER spectra of the sample C161 InGaN/InGaN MQW LED structure for different reverse biases (ranging from 2 V down to -18 V) and at different temperatures (20, 100, 200 and 300 K).

20 K is equal to 3.09 eV. Note that the lower temperature also impacts on the I - V curves of the LED. At 20 K, the measured built-in field Ψ_{bi} already amounts to 4.1 V indicating thermal parasitic capacitance effects induced by the p - n junction. As for sample C182, the critical points of the ER spectra at 3.05, 3.25 and 3.4 eV are associated to MQW, barrier and GaN cap layer transitions, respectively. The GaN cap layer transition seems to disappear for increasing reverse biases. Here, we propose that the GaN transition is no more resolved under the stress induced by a highly negative external field that destroys the excitonic resonances. On the contrary, the transitions associated to the MQWs are still well resolved even for large reverse biases thanks to the quantum confinement in the wells [45]. As for C182, we continue to associate the middle transition (around 3.25 eV) to the well barriers because its dependency on the applied voltage. The MQW transition (around 3.05 eV) exhibits a maximal blueshift for a bias ranging between -8 and -9 V. In the same voltage range the ER signal vanishes and flips its sign indicating that flat-band conditions are achieved. Therefore, we estimated a V_{MIN} of -8.5 V. The flat-band bias does not seem to change appreciably with temperature. Note that ER oscillations are thinner in the vicinity of V_{MIN} whereas for larger or shorter biases the spectra broaden. It is likely that away from flat-band conditions the carrier wavefunctions penetrate more easily into the barriers because of delocalization occurring on opposite sides of the well

Appendix A. Electro-reflectance measurements

and thus they are more sensitive to growth disorder. This broadening effect is more pronounced for shorter negative biases due to the asymmetry of the well barriers [compare Figs. 3.2 (a) and 3.2 (c)].

B Electrical beatings in reverse-biased MS-LDs

When looking for SF in electrically-pumped MS-LDs, another unexpected phenomenon has been observed in MS-LDs processed from sample C134 for $V_{AS} = -8$ V (Fig. B.1). At $I_{GS} = 150$ mA, the emission spectrum is very broad, typical of spontaneous emission. When increasing the pump current, the spectrum is still very broad but amplified spontaneous emission starts to be visible on the low energy side. For higher pump currents, the MS-LD finally starts lasing. However, unexpectedly, for even higher pump currents ranging in between 280 and 290 mA, electrical beatings appear on the oscilloscope traces. Their frequency is roughly 14 MHz and the beating amplitude slightly increases with the pump current [compare Figs. B.1 (b) and B.1 (c)]. Interestingly, the emission spectrum is much larger compared to the lasing one (~ 2 nm) and exhibits a Gaussian shape [$I_{GS} = 310$ mA in Fig. B.1 (d)]. Previously, no such electrical beating has ever been observed in any other kinds of LDs processed in our laboratory. Moreover, this feature has only been measured in MS-LDs processed from sample C134 and with a central absorber geometry. Unfortunately, we were not able to measure the dynamic response of these devices. So far, the only proposed explanation is a retro-active acoustic feedback occurring in the mode-locking regime. At such high pump current the device is likely to be mode-locked and the optical beatings in the cavity could induce acoustic beating of the cavity itself, which in turn induces a retro-active feedback on the applied bias. On the other hand, it seems fairly unrealistic that the formation of a giant macrodipole composed by all the injected carriers in the cavity could produce an electrical feedback on the pump current. In addition, this particular regime is observed well above the lasing threshold [Fig. B.1 (d)]. Anyhow, this unexpected phenomenon is extremely fascinating as it implies a feedback not on the *output* parameters of the device (as any other phenomena described in this thesis so far) but rather on the *input* parameters.

Appendix B. Electrical beatings in reverse-biased MS-LDs

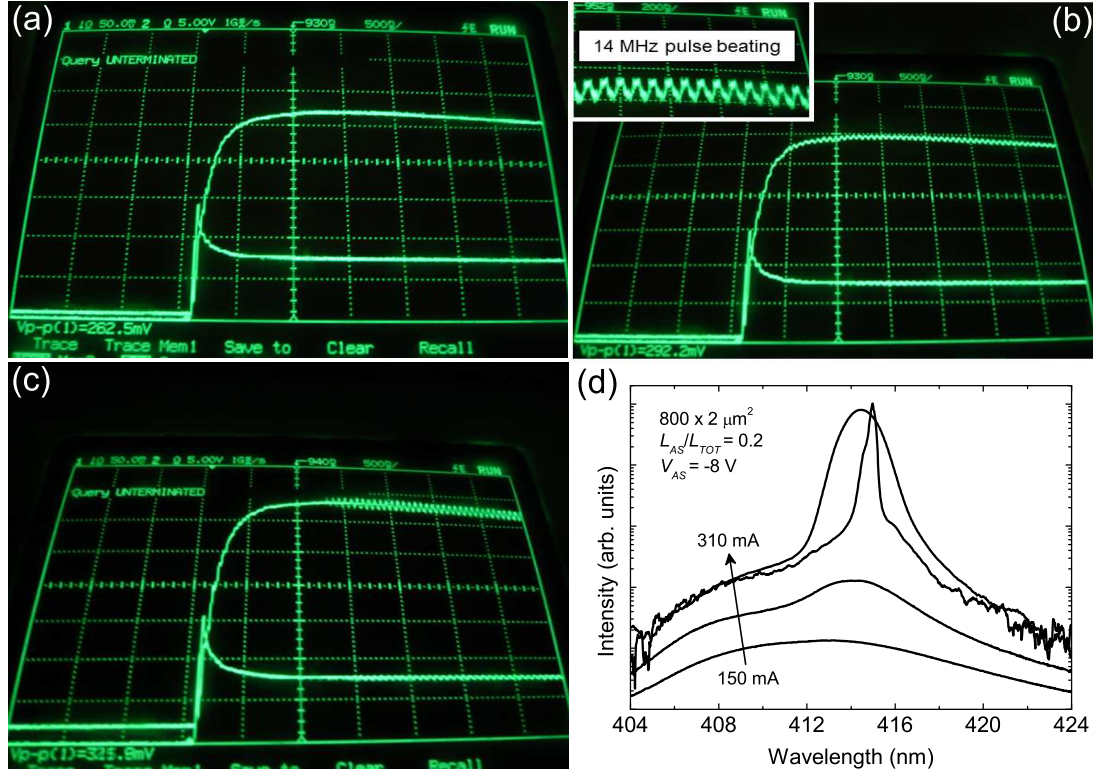


Figure B.1: Oscilloscope traces of a $800 \times 2 \mu\text{m}^2$ MS-LD with a $150 \mu\text{m}$ long central absorber biased at $V_{AS} = -8 \text{ V}$ processed from sample C134. The injected current I_{GS} is (a) 262, (b) 293 (the inset is a magnification of the electrical beatings observed at a frequency of 14 MHz and) and (c) 325 mA. (d) Emitted spectra for increasing pump currents I_{GS} . From bottom to top: 150 mA (spontaneous emission regime), 230 mA (amplified spontaneous emission regime), 240 mA (lasing regime) and 310 mA (likely passive mode-locking regime).

Bibliography

- [1] S. Nakamura and S. F. Chichibu, editors, *Introduction to Nitride Semiconductor Blue Lasers and Light Emitting Diodes* (CRC Press, New York, 2000).
- [2] J. P. Gordon, H. J. Zeiger, and C. H. Townes, *The Maser—New Type of Microwave Amplifier, Frequency Standard, and Spectrometer*, Phys. Rev. **99**, 1264 (1955).
- [3] A. L. Schawlow and C. H. Townes, *Infrared and Optical Masers*, Phys. Rev. **112**, 1940 (1958).
- [4] R. N. Hall, G. E. Fenner, J. D. Kingsley, T. J. Soltys, and R. O. Carlson, *Coherent Light Emission From GaAs Junctions*, Phys. Rev. Lett. **9**, 366 (1962).
- [5] S. Nakamura, T. Mukai, and M. Senoh, *Candela-class high-brightness InGaN/AlGaIn double-heterostructure blue-light-emitting diodes*, Appl. Phys. Lett. **64**, 1687 (1994).
- [6] H. Amano, M. Kito, K. Hiramatsu, and I. Akasaki, *P-Type Conduction in Mg-Doped GaN Treated with Low-Energy Electron Beam Irradiation (LEEBI)*, Jpn. J. Appl. Phys. **28**, L2112 (1989).
- [7] S. Nakamura, M. Senoh, S.-i. Nagahama, N. Iwasa, T. Yamada, T. Matsushita, H. Kiyoku, and Y. Sugimoto, *InGaIn-Based Multi-Quantum-Well-Structure Laser Diodes*, Jpn. J. Appl. Phys. **35**, L74 (1996).
- [8] U. Keller, *Recent developments in compact ultrafast lasers*, Nature **424**, 831 (2003).
- [9] Y. Hu, M. Dubov, and I. Khrushchev, *Spectrally-controlled, gain-switched operation of InGaIn diode laser*, Electron. Lett. **40**, 702 (2004).
- [10] C. W. Chuah, B. Xu, T. S. Tan, N. Xiang, and T. C. Chong, *Tunable GHz Repetitive ps Pulse InGaIn Laser*, IEEE Photon. Technol. Lett. **19**, 70 (2007).
- [11] T. Miyajima, H. Watanabe, M. Ikeda, and H. Yokoyama, *Picosecond optical pulse generation from self-pulsating bisectonal GaIn-based blue-violet laser diodes*, Appl. Phys. Lett. **94**, 161103 (2009).

- [12] M. Kneissl, T. L. Paoli, P. Kiesel, D. W. Treat, M. Teepe, N. Miyashita, and N. M. Johnson, *Two-section InGaN multiple-quantum-well laser diode with integrated electroabsorption modulator*, Appl. Phys. Lett. **80**, 3283 (2002).
- [13] T. Lei, M. Fanciulli, R. J. Molnar, T. D. Moustakas, R. J. Graham, and J. Scanlon, *Epitaxial growth of zinc blende and wurtzitic gallium nitride thin films on (001) silicon*, Appl. Phys. Lett. **59**, 944 (1991).
- [14] J. Levrat, *Physics of Polariton Condensates in GaN-based Planar Microcavities*, PhD thesis, EPFL, n. 5449, 2012.
- [15] M. E. Levinstein, S. L. Rumyantsev, and M. Shur, *Properties of advanced semiconductor materials: GaN, AlN, InN, BN, SiC, SiGe* (Wiley, New York, 2001).
- [16] F. Bernardini, V. Fiorentini, and D. Vanderbilt, *Polarization-Based Calculation of the Dielectric Tensor of Polar Crystals*, Phys. Rev. Lett. **79**, 3958 (1997).
- [17] I. Vurgaftman and J. R. Meyer, *Band parameters for nitrogen-containing semiconductors*, J. Appl. Phys. **94**, 3675 (2003).
- [18] A. Kasic, M. Schubert, S. Einfeldt, D. Hommel, and T. E. Tiwald, *Free-carrier and phonon properties of n- and p-type hexagonal GaN films measured by infrared ellipsometry*, Phys. Rev. B **62**, 7365 (2000).
- [19] K. Kornitzer, T. Ebner, K. Thonke, R. Sauer, C. Kirchner, V. Schwegler, M. Kamp, M. Leszczynski, I. Grzegory, and S. Porowski, *Photoluminescence and reflectance spectroscopy of excitonic transitions in high-quality homoepitaxial GaN films*, Phys. Rev. B **60**, 1471 (1999).
- [20] P. Rinke, M. Winkelkemper, A. Qteish, D. Bimberg, J. Neugebauer, and M. Scheffler, *Consistent set of band parameters for the group-III nitrides AlN, GaN, and InN*, Phys. Rev. B **77**, 075202 (2008).
- [21] F. Bernardini, V. Fiorentini, and D. Vanderbilt, *Accurate calculation of polarization-related quantities in semiconductors*, Phys. Rev. B **63**, 193201 (2001).
- [22] J. Wu, *When group-III nitrides go infrared: New properties and perspectives*, J. Appl. Phys. **106**, 011101 (2009).
- [23] O. Ambacher, J. Majewski, C. Miskys, A. Link, M. Hermann, M. Eickhoff, M. Stutzmann, F. Bernardini, V. Fiorentini, V. Tilak, B. Schaff, and L. F. Eastman, *Pyroelectric properties of Al(In)Ga_N/Ga_N hetero- and quantum well structures*, J. Phys.: Condens. Matter **14**, 3399 (2002).
- [24] S. Nakamura, *The Roles of Structural Imperfections in InGa_N-Based Blue Light-Emitting Diodes and Laser Diodes*, Science **281**, 956 (1998).

-
- [25] C. Wetzel, M. Zhu, J. Senawiratne, T. Detchprohm, P. Persans, L. Liu, E. Preble, and D. Hanser, *Light-emitting diode development on polar and non-polar GaN substrates*, J. Cryst. Growth **310**, 3987 (2008).
- [26] R. Butté and N. Grandjean, *Effects of polarization in optoelectronic quantum structures*, In *Polarization Effects in Semiconductors*, D. C. Wood and D. Jena, editors, pp. 467–511 (Springer, New York, 2007).
- [27] T. Zhu, *Non-polar GaN epilayers and heterostructures for photonic applications*, PhD thesis, EPFL, n. 4563, 2009.
- [28] J. L. Weyher, H. Ashraf, and P. R. Hageman, *Reduction of dislocation density in epitaxial GaN layers by overgrowth of defect-related etch pits*, Appl. Phys. Lett. **95**, 031913 (2009).
- [29] M. Grundmann, *The Physics of Semiconductors: An Introduction Including Devices and Nanophysics* (Springer, Berlin, 2006).
- [30] A. Dussaigne, B. Damilano, J. Brault, J. Massies, E. Feltin, and N. Grandjean, *High doping level in Mg-doped GaN layers grown at low temperature*, J. Appl. Phys. **103**, 013110 (2008).
- [31] H. Amano, T. Asahi, and I. Akasaki, *Stimulated Emission Near Ultraviolet at Room Temperature from a GaN Film Grown on Sapphire by MOVPE Using an AlN Buffer Layer*, Jpn. J. Appl. Phys. **29**, L205 (1990).
- [32] S. Nakamura, *GaN Growth Using GaN Buffer Layer*, Jpn. J. Appl. Phys. **30**, L1705 (1991).
- [33] H. Kroemer, *A proposed class of hetero-junction injection lasers*, Proc. IEEE **51**, 1782 (1963).
- [34] D. Fritsch, H. Schmidt, and M. Grundmann, *Band-structure pseudopotential calculation of zinc-blende and wurtzite AlN, GaN, and InN*, Phys. Rev. B **67**, 235205 (2003).
- [35] B. Gil and O. Briot, *Internal structure and oscillator strengths of excitons in strained GaN*, Phys. Rev. B **55**, 2530 (1997).
- [36] Y. P. Varshni, *Temperature dependence of the energy gap in semiconductors*, Physica **34**, 149 (1967).
- [37] T. Kawashima, H. Yoshikawa, S. Adachi, S. Fuke, and K. Ohtsuka, *Optical properties of hexagonal GaN*, J. Appl. Phys. **82**, 3528 (1997).
- [38] D. Brunner, H. Angerer, E. Bustarret, F. Freudenberger, R. Höpler, R. Dimitrov, O. Ambacher, and M. Stutzmann, *Optical constants of epitaxial AlGaIn films and their temperature dependence*, J. Appl. Phys. **82**, 5090 (1997).

Bibliography

- [39] M. J. Bergmann and H. C. Casey, *Optical-field calculations for lossy multiple-layer AlGa_N/InGa_N laser diodes*, J. Appl. Phys. **84**, 1196 (1998).
- [40] E. Rosencher and B. Vinter, *Optoelectronics* (Cambridge University Press, Cambridge, 2002).
- [41] B. E. A. Saleh and M. C. Teich, *Fundamentals of photonics* (Wiley-Interscience, Hoboken, N.J., 2007).
- [42] M. Leroux, N. Grandjean, M. Laügt, J. Massies, B. Gil, P. Lefebvre, and P. Bigenwald, *Quantum confined Stark effect due to built-in internal polarization fields in (Al,Ga)_N/Ga_N quantum wells*, Phys. Rev. B **58**, R13371 (1998).
- [43] S.-H. Park and S.-L. Chuang, *Crystal-orientation effects on the piezoelectric field and electronic properties of strained wurtzite semiconductors*, Phys. Rev. B **59**, 4725 (1999).
- [44] D. A. B. Miller, D. S. Chemla, T. C. Damen, A. C. Gossard, W. Wiegmann, T. H. Wood, and C. A. Burrus, *Band-Edge Electroabsorption in Quantum Well Structures: The Quantum-Confined Stark Effect*, Phys. Rev. Lett. **53**, 2173 (1984).
- [45] D. A. B. Miller, D. S. Chemla, T. C. Damen, A. C. Gossard, W. Wiegmann, T. H. Wood, and C. A. Burrus, *Electric field dependence of optical absorption near the band gap of quantum-well structures*, Phys. Rev. B **32**, 1043 (1985).
- [46] D. A. B. Miller, D. S. Chemla, and S. Schmitt-Rink, *Relation between electroabsorption in bulk semiconductors and in quantum wells: The quantum-confined Franz-Keldysh effect*, Phys. Rev. B **33**, 6976 (1986).
- [47] G. Bastard, *Wave Mechanics Applied to Semiconductor Heterostructures, Monographs of Physics* (Les Editions de Physique, Les Ulis, 1991).
- [48] N. Grandjean, B. Damilano, S. Dalmaso, M. Leroux, M. Laügt, and J. Massies, *Built-in electric-field effects in wurtzite AlGa_N/Ga_N quantum wells*, J. Appl. Phys. **86**, 3714 (1999).
- [49] S. F. Chichibu, A. C. Abare, M. S. Minsky, S. Keller, S. B. Fleischer, J. E. Bowers, E. Hu, U. K. Mishra, L. A. Coldren, S. P. DenBaars, and T. Sota, *Effective band gap inhomogeneity and piezoelectric field in InGa_N/Ga_N multiquantum well structures*, Appl. Phys. Lett. **73**, 2006 (1998).
- [50] A. E. Siegman, *Lasers* (University Science Books, Oxford, 1986).
- [51] S. M. Sze and K. K. Ng, *Physics of Semiconductor Devices* (John Wiley & Sons, Hoboken, 2006).

-
- [52] G. Y. Zhang, Y. Z. Tong, Z. J. Yang, S. X. Jin, J. Li, and Z. Z. Gan, *Relationship of background carrier concentration and defects in GaN grown by metalorganic vapor phase epitaxy*, Appl. Phys. Lett. **71**, 3376 (1997).
- [53] J. Neugebauer and C. G. Van de Walle, *Gallium vacancies and the yellow luminescence in GaN*, Appl. Phys. Lett. **69**, 503 (1996).
- [54] W. Götz, J. Walker, L. Romano, N. Johnson, and R. Molnar, *Thickness Dependence of Electronic Properties of GaN Epi-layers*, Mater. Res. Soc. Symp. Proc. **449**, 525 (1996).
- [55] S. Nakamura, T. Mukai, and M. Senoh, *Si-Doped InGaN Films Grown on GaN Films*, Jpn. J. Appl. Phys. **32**, L16 (1993).
- [56] C. Yuan, T. Salagaj, A. Gurary, A. G. Thompson, W. Kroll, R. A. Stall, C.-Y. Hwang, M. Schurman, Y. Li, W. E. Mayo, Y. Lu, S. Krishnankutty, I. K. Shmagin, R. M. Kolbas, and S. J. Pearton, *Investigation of n- and p-type doping of GaN during epitaxial growth in a mass production scale multiwafer-rotating-disk reactor*, J. Vac. Sci. Technol. B **13**, 2075 (1995).
- [57] S. Nakamura, M. Senoh, S.-i. Nagahama, N. Iwasa, T. Yamada, T. Matsushita, Y. Sugimoto, and H. Kiyoku, *Room-temperature continuous-wave operation of InGaN multi-quantum-well structure laser diodes with a lifetime of 27 hours*, Appl. Phys. Lett. **70**, 1417 (1997).
- [58] W. Götz, R. Kern, C. Chen, H. Liu, D. Steigerwald, and R. Fletcher, *Hall-effect characterization of III-V nitride semiconductors for high efficiency light emitting diodes*, Mater. Sci. Eng., B **59**, 211 (1999).
- [59] T. Schmidt, M. Siebert, J. I. Flege, S. Figge, S. Gangopadhyay, A. Pretorius, T.-L. Lee, J. Zegenhagen, L. Gregoratti, A. Barinov, A. Rosenauer, D. Hommel, and J. Falta, *Mg and Si dopant incorporation and segregation in GaN*, Phys. Status Solidi (b) **248**, 1810 (2011).
- [60] D. Huang, F. Yun, M. Reshchikov, D. Wang, H. Morkoç, D. Rode, L. Farina, C. Kurdak, K. Tsen, S. Park, and K. Lee, *Hall mobility and carrier concentration in free-standing high quality GaN templates grown by hydride vapor phase epitaxy*, Solid-State Electronics **45**, 711 (2001).
- [61] G. L. Pearson and J. Bardeen, *Electrical Properties of Pure Silicon and Silicon Alloys Containing Boron and Phosphorus*, Phys. Rev. **75**, 865 (1949).
- [62] J. Neugebauer and C. G. Van de Walle, *Role of defects and impurities in doping of GaN*, Proc. 23rd Int. Conf. on the Physics of Semiconductors (1996).
- [63] A. Castiglia, J.-F. Carlin, and N. Grandjean, *Role of stable and metastable Mg-H complexes in p-type GaN for cw blue laser diodes*, Appl. Phys. Lett. **98**, 213505 (2011).

- [64] S. Nakamura, T. Mukai, M. Senoh, and N. Iwasa, *Thermal Annealing Effects on P-Type Mg-Doped GaN Films*, Jpn. J. Appl. Phys. **31**, L139 (1992).
- [65] I. H. Brown, I. A. Pope, P. M. Smowton, P. Blood, J. D. Thomson, W. W. Chow, D. P. Bour, and M. Kneissl, *Determination of the piezoelectric field in InGaN quantum wells*, Appl. Phys. Lett. **86**, 131108 (2005).
- [66] H. Shen, M. Wraback, H. Zhong, A. Tyagi, S. P. DenBaars, S. Nakamura, and J. S. Speck, *Unambiguous evidence of the existence of polarization field crossover in a semipolar InGaN/GaN single quantum well*, Appl. Phys. Lett. **95**, 033503 (2009).
- [67] C. A. Hurni, O. Bierwagen, J. R. Lang, B. M. McSkimming, C. S. Gallinat, E. C. Young, D. A. Browne, U. K. Mishra, and J. S. Speck, *p-n junctions on Ga-face GaN grown by NH₃ molecular beam epitaxy with low ideality factors and low reverse currents*, Appl. Phys. Lett. **97**, 222113 (2010).
- [68] W. G. Scheibenzuber, U. T. Schwarz, L. Sulmoni, J. Dorsaz, J.-F. Carlin, and N. Grandjean, *Recombination coefficients of GaN-based laser diodes*, J. Appl. Phys. **109**, 093106 (2011).
- [69] W. G. Scheibenzuber, *GaN-Based Laser Diodes: Towards Longer Wavelengths and Short Pulses* (Springer, Berlin, 2012).
- [70] F. Grillot, B. Dagens, J. Provost, H. Su, and L. Lester, *Gain Compression and Above-Threshold Linewidth Enhancement Factor in 1.3-um InAs-GaAs Quantum-Dot Lasers*, IEEE J. Quantum Electron. **44**, 946 (2008).
- [71] A. Koukitu, N. Takahashi, T. Taki, and H. Seki, *Thermodynamic Analysis of InGaN Alloy Composition Grown by Metalorganic Vapor Phase Epitaxy*, Jpn. J. Appl. Phys. **35**, L673 (1996).
- [72] G. Bastard, E. E. Mendez, L. L. Chang, and L. Esaki, *Exciton binding energy in quantum wells*, Phys. Rev. B **26**, 1974 (1982).
- [73] S. Nakamura, G. Fasol, and S. J. Pearton, *The Blue Laser Diode: The Complete Story* (Springer, New York, 2nd edition, 2000).
- [74] G. Martin, A. Botchkarev, A. Rockett, and H. Morkoc, *Valence-band discontinuities of wurtzite GaN, AlN, and InN heterojunctions measured by x-ray photoemission spectroscopy*, Appl. Phys. Lett. **68**, 2541 (1996).
- [75] S. Nakamura, *III-V nitride based light-emitting devices*, Solid State Commun. **102**, 237 (1997).
- [76] E. Kioupakis, P. Rinke, and C. G. Van de Walle, *Determination of Internal Loss in Nitride Lasers from First Principles*, Appl. Phys. Express **3**, 082101 (2010).

-
- [77] G. M. Laws, E. C. Larkins, I. Harrison, C. Molloy, and D. Somerford, *Improved refractive index formulas for the AlGa_N and InGa_N alloys*, J. Appl. Phys. **89**, 1108 (2001).
 - [78] M. G. A. Bernard and G. Duraffourg, *Laser Conditions in Semiconductors*, Phys. Status Solidi (b) **1**, 699 (1961).
 - [79] B. Witzigmann, V. Laino, M. Luisier, U. T. Schwarz, G. Feicht, W. Wegscheider, K. Engl, M. Furitsch, A. Leber, A. Lell, and V. Härle, *Microscopic analysis of optical gain in InGa_N/Ga_N quantum wells*, Appl. Phys. Lett. **88**, 021104 (2006).
 - [80] W. W. Chow and S. W. Koch, *Semiconductor-laser fundamentals: physics of the gain materials* (Springer, New York, 1999).
 - [81] L. A. Coldren, S. W. Corzine, and M. L. Mašanović, *Diode Lasers and Photonic Integrated Circuits, Second Edition* (John Wiley & Sons, Inc., New York, 2012).
 - [82] U. T. Schwarz, H. Braun, K. Kojima, M. Funato, Y. Kawakami, S. Nagahama, and T. Mukai, *Investigation and comparison of optical gain spectra of (Al,In)Ga_N laser diodes emitting in the 375nm to 470 nm spectral range*, In *SPIE proceedings*, C. Mermelstein and D. P. Bour, editors, pp. 648506–648506–10, 2007.
 - [83] M. Yamanishi and Y. Lee, *Phase dampings of optical dipole moments and gain spectra in semiconductor lasers*, IEEE J. Quantum Electron. **23**, 367 (1987).
 - [84] H. Y. Ryu, K. H. Ha, J. K. Son, S. N. Lee, H. S. Paek, T. Jang, Y. J. Sung, K. S. Kim, H. K. Kim, Y. Park, and O. H. Nam, *Determination of internal parameters in blue InGa_N laser diodes by the measurement of cavity-length dependent characteristics*, Appl. Phys. Lett. **93**, 011105 (2008).
 - [85] J. Piprek and S. Nakamura, *Physics of high-power InGa_N/Ga_N lasers*, IEE Proc.-Optoelectron. **149**, 145 (2002).
 - [86] M. Fujita, R. Ushigome, and T. Baba, *Large spontaneous emission factor of 0.1 in a microdisk injection laser*, IEEE Photon. Technol. Lett. **13**, 403 (2001).
 - [87] M. Willatzen, T. Takahashi, and Y. Arakawa, *Nonlinear gain effects due to carrier heating and spectral hole burning in strained-quantum-well lasers*, IEEE Photon. Technol. Lett. **4**, 682 (1992).
 - [88] K. Petermann, *Laser Diode Modulation and Noise* (Kluwer Academic Publishers, Dordrecht, 1988).
 - [89] A. M. Weiner, *Ultrafast Optics* (John Wiley & Sons, Hoboken, 2008).
 - [90] V. Avrutin, S. d. A. Hafiz, F. Zhang, U. Ozgur, H. Morkoc, and A. Matulionis, *InGa_N light-emitting diodes: Efficiency-limiting processes at high injection*, J. Vac. Sci. Technol. A **31**, 050809 (2013).

- [91] M. Meneghini, N. Trivellin, G. Meneghesso, E. Zanoni, U. Zehnder, and B. Hahn, *A combined electro-optical method for the determination of the recombination parameters in InGaN-based light-emitting diodes*, J. Appl. Phys. **106**, 114508 (2009).
- [92] Y. C. Shen, G. O. Mueller, S. Watanabe, N. F. Gardner, A. Munkholm, and M. R. Krames, *Auger recombination in InGaN measured by photoluminescence*, Appl. Phys. Lett. **91**, 141101 (2007).
- [93] M. Zhang, P. Bhattacharya, J. Singh, and J. Hinckley, *Direct measurement of Auger recombination in InGaN/GaN quantum wells and its impact on the efficiency of InGaN/GaN multiple quantum well light emitting diodes*, Appl. Phys. Lett. **95**, 201108 (2009).
- [94] U. T. Schwarz, *Emission of biased green quantum wells in time and wavelength domain*, In *Gallium Nitride Materials and Devices IV*, volume 7216, pp. 72161U–72161U–13, San Jose, CA, 2009.
- [95] M.-H. Kim, M. F. Schubert, Q. Dai, J. K. Kim, E. F. Schubert, J. Piprek, and Y. Park, *Origin of efficiency droop in GaN-based light-emitting diodes*, Appl. Phys. Lett. **91**, 183507 (2007).
- [96] J. Hader, J. V. Moloney, and S. W. Koch, *Density-activated defect recombination as a possible explanation for the efficiency droop in GaN-based diodes*, Appl. Phys. Lett. **96**, 221106 (2010).
- [97] A. R. Vasconcellos, R. Luzzi, C. G. Rodrigues, and V. N. Freire, *Hot-phonon bottleneck in the photoinjected plasma in GaN*, Appl. Phys. Lett. **82**, 2455 (2003).
- [98] A. A. Efremov, N. I. Bochkareva, R. I. Gorbunov, D. A. Lavrinovich, Y. T. Rebane, D. V. Tarkhin, and Y. G. Shreter, *Effect of the Joule heating on the quantum efficiency and choice of thermal conditions for high-power blue InGaN/GaN LEDs*, Semiconductors **40**, 605 (2006).
- [99] G. Verzellesi, D. Saguatti, M. Meneghini, F. Bertazzi, M. Goano, G. Meneghesso, and E. Zanoni, *Efficiency droop in InGaN/GaN blue light-emitting diodes: Physical mechanisms and remedies*, J. Appl. Phys. **114**, 071101 (2013).
- [100] J. Iveland, L. Martinelli, J. Peretti, J. S. Speck, and C. Weisbuch, *Direct Measurement of Auger Electrons Emitted from a Semiconductor Light-Emitting Diode under Electrical Injection: Identification of the Dominant Mechanism for Efficiency Droop*, Phys. Rev. Lett. **110**, 177406 (2013).
- [101] J. Piprek, *Efficiency droop in nitride-based light-emitting diodes*, Phys. Status Solidi (a) **207**, 2217 (2010).

-
- [102] J. Hader, J. V. Moloney, B. Pasenow, S. W. Koch, M. Sabathil, N. Linder, and S. Lutgen, *On the importance of radiative and Auger losses in GaN-based quantum wells*, Appl. Phys. Lett. **92**, 261103 (2008).
 - [103] F. Bertazzi, M. Goano, and E. Bellotti, *A numerical study of Auger recombination in bulk InGaN*, Appl. Phys. Lett. **97**, 231118 (2010).
 - [104] P. G. Eliseev, M. Osin'ski, H. Li, and I. V. Akimova, *Recombination balance in green-light-emitting GaN/InGaN/AlGaIn quantum wells*, Appl. Phys. Lett. **75**, 3838 (1999).
 - [105] A. Laubsch, M. Sabathil, J. Baur, M. Peter, and B. Hahn, *High-Power and High-Efficiency InGaN-Based Light Emitters*, IEEE Trans. Electr. Devices **57**, 79 (2010).
 - [106] H.-Y. Ryu, W. Jun Choi, K.-S. Jeon, M.-G. Kang, Y. Choi, and J.-S. Lee, *Analysis of below-threshold efficiency characteristics of InGaN-based blue laser diodes*, J. Appl. Phys. **112**, 083109 (2012).
 - [107] X. Li, S. Okur, F. Zhang, V. Avrutin, . Özgür, H. Morkoç, S. M. Hong, S. H. Yen, T. C. Hsu, and A. Matulionis, *Impact of active layer design on InGaN radiative recombination coefficient and LED performance*, J. Appl. Phys. **111**, 063112 (2012).
 - [108] B. Galler, P. Drechsel, R. Monnard, P. Rode, P. Stauss, S. Froehlich, W. Bergbauer, M. Binder, M. Sabathil, B. Hahn, and J. Wagner, *Influence of indium content and temperature on Auger-like recombination in InGaIn quantum wells grown on (111) silicon substrates*, Appl. Phys. Lett. **101**, 131111 (2012).
 - [109] D. Schiavon, M. Binder, M. Peter, B. Galler, P. Drechsel, and F. Scholz, *Wavelength-dependent determination of the recombination rate coefficients in single-quantum-well GaInN/GaN light emitting diodes*, Phys. Status Solidi (b) **250**, 283 (2013).
 - [110] M. Brendel, A. Kruse, H. Jönen, L. Hoffmann, H. Bremers, U. Rossow, and A. Hangleiter, *Auger recombination in GaInN/GaN quantum well laser structures*, Appl. Phys. Lett. **99**, 031106 (2011).
 - [111] K. T. Delaney, P. Rinke, and C. G. Van de Walle, *Auger recombination rates in nitrides from first principles*, Appl. Phys. Lett. **94**, 191109 (2009).
 - [112] E. Goutain, J. Renaud, M. Krakowski, D. Rondi, R. Blondeau, and D. Decoster, *30 GHz bandwidth, 1.55 μ m MQW-DFB laser diode based on a new modulation scheme*, Electron. Lett. **32**, 896 (1996).
 - [113] M. C. Wu, Y. K. Chen, T. Tanbun-Ek, R. A. Logan, M. A. Chin, and G. Raybon, *Transform-limited 1.4 ps optical pulses from a monolithic colliding-pulse mode-locked quantum well laser*, Appl. Phys. Lett. **57**, 759 (1990).

Bibliography

- [114] F. Camacho, E. Avrutin, A. Bryce, and J. Marsh, *Passive modelocking in semiconductor lasers with monolithically integrated passive waveguides*, IEE Proc.-Optoelectron. **145**, 43 (1998).
- [115] E. Walker, A. Dvornikov, K. Coblentz, and P. Rentzepis, *Terabyte recorded in two-photon 3D disk*, Appl. Opt. **47**, 4133 (2008).
- [116] D. Ueda, K. Saito, T. Iwamura, Y. Takemoto, H. Yamatsu, T. Horigome, M. Oyama, K. Hayashi, N. Tanabe, H. Miyamoto, A. Nakaoki, J. Horigome, H. Uchiyama, K. Yun, and S. Kobayashi, *Dynamic Recording of 200 Gbytes in Three-Dimensional Optical Disk by a 405 nm Wavelength Picosecond Laser*, Jpn. J. Appl. Phys. **50**, 032704 (2011).
- [117] S.-H. Park, D.-Y. Yang, and K.-S. Lee, *Two-photon stereolithography for realizing ultraprecise three-dimensional nano/microdevices*, Laser & Photon. Rev. **3**, 1 (2009).
- [118] J. Schmitt, *Optical coherence tomography (OCT): a review*, IEEE J. Sel. Top. Quantum Electron. **5**, 1205 (1999).
- [119] U. Keller, K. Weingarten, F. Kartner, D. Kopf, B. Braun, I. Jung, R. Fluck, C. Honninger, N. Matuschek, and J. Aus der Au, *Semiconductor saturable absorber mirrors (SESAM's) for femtosecond to nanosecond pulse generation in solid-state lasers*, IEEE J. Sel. Top. Quantum Electron. **2**, 435 (1996).
- [120] S. Hoogland, S. Dhanjal, A. Tropper, J. Roberts, R. Haring, R. Paschotta, F. Morier-Genoud, and U. Keller, *Passively mode-locked diode-pumped surface-emitting semiconductor laser*, IEEE Photon. Technol. Lett. **12**, 1135 (2000).
- [121] S. Sanders, L. Eng, J. Paslaski, and A. Yariv, *108 GHz passive mode locking of a multiple quantum well semiconductor laser with an intracavity absorber*, Appl. Phys. Lett. **56**, 310 (1990).
- [122] J. O'Gorman, A. F. J. Levi, R. N. Nottenburg, T. Tanbun-Ek, and R. A. Logan, *Dynamic and static response of multielectrode lasers*, Appl. Phys. Lett. **57**, 968 (1990).
- [123] P. Morton, J. Bowers, L. Koszi, M. Soler, J. Lopata, and D. Wilt, *Monolithic hybrid mode locked 1.3 um semiconductor laser arrays*, In *Electron Devices Meeting, 1989. IEDM '89. Technical Digest., International*, pp. 865 –868, 1989.
- [124] A. J. DeMaria, D. A. Stetser, and H. Heynau, *Self mode-locking of lasers with saturable absorbers*, Appl. Phys. Lett. **8**, 174 (1966).
- [125] S. Sanders, A. Yariv, J. Paslaski, J. E. Ungar, and H. A. Zarem, *Passive mode locking of a two-section multiple quantum well laser at harmonics of the cavity round-trip frequency*, Appl. Phys. Lett. **58**, 681 (1991).

-
- [126] T. Oki, K. Saito, H. Watanabe, T. Miyajima, M. Kuramoto, M. Ikeda, and H. Yokoyama, *Passive and Hybrid Mode-Locking of an External-Cavity GaInN Laser Diode Incorporating a Strong Saturable Absorber*, Appl. Phys. Express **3**, 032104 (2010).
 - [127] H. Watanabe, T. Miyajima, M. Kuramoto, M. Ikeda, and H. Yokoyama, *10-W Peak-Power Picosecond Optical Pulse Generation from a Triple Section Blue-Violet Self-Pulsating Laser Diode*, Appl. Phys. Express **3**, 052701 (2010).
 - [128] R. Koda, T. Oki, T. Miyajima, H. Watanabe, M. Kuramoto, M. Ikeda, and H. Yokoyama, *100 W peak-power 1 GHz repetition picoseconds optical pulse generation using blue-violet GaInN diode laser mode-locked oscillator and optical amplifier*, Appl. Phys. Lett. **97**, 021101 (2010).
 - [129] S. Tashiro, Y. Takemoto, H. Yamatsu, T. Miura, G. Fujita, T. Iwamura, D. Ueda, H. Uchiyama, K. Yun, M. Kuramoto, T. Miyajima, M. Ikeda, and H. Yokoyama, *Volumetric Optical Recording Using a 400 nm All-Semiconductor Picosecond Laser*, Appl. Phys. Lett. **3**, 102501 (2010).
 - [130] W. G. Scheibenzuber, U. T. Schwarz, L. Sulmoni, J.-F. Carlin, A. Castiglia, and N. Grandjean, *Bias-dependent absorption coefficient of the absorber section in GaN-based multisection laser diodes*, Appl. Phys. Lett. **97**, 181103 (2010).
 - [131] L. Sulmoni, J.-M. Lamy, J. Dorsaz, A. Castiglia, J.-F. Carlin, W. G. Scheibenzuber, U. T. Schwarz, X. Zeng, D. L. Boiko, and N. Grandjean, *Static and dynamic properties of multi-section InGaN-based laser diodes*, J. Appl. Phys. **112**, 103112 (2012).
 - [132] W. G. Scheibenzuber, C. Hornuss, U. T. Schwarz, L. Sulmoni, J. Dorsaz, J.-F. Carlin, and N. Grandjean, *Self-Pulsation at Zero Absorber Bias in GaN-Based Multisection Laser Diodes*, Appl. Phys. Express **4**, 062702 (2011).
 - [133] P. P. Vasil'ev, A. B. Sergeev, I. V. Smetanin, T. Weig, U. T. Schwarz, L. Sulmoni, J. Dorsaz, J.-M. Lamy, J.-F. Carlin, N. Grandjean, X. Zeng, T. Stadelmann, S. Grossmann, A. C. Hoogerwerf, and D. L. Boiko, *Mode locking in monolithic two-section InGaN blue-violet semiconductor lasers*, Appl. Phys. Lett. **102**, 121115 (2013).
 - [134] V. Olle, A. Wonfor, L. Sulmoni, P. Vasilev, J.-M. Lamy, J.-F. Carlin, N. Grandjean, R. Penty, and I. White, *Hybrid and Passive Mode-Locking of a Monolithic Two-Section MQW InGaN/GaN Laser Diode*, IEEE Photon. Technol. Lett. **25**, 1514 (2013).
 - [135] Y. K. Chen, M. C. Wu, T. Tanbun-Ek, R. A. Logan, and M. A. Chin, *Subpicosecond monolithic colliding-pulse mode-locked multiple quantum well lasers*, Appl. Phys. Lett. **58**, 1253 (1991).

- [136] G. Arnold and K. Petermann, *Self-pulsing phenomena in (GaAl) As double-heterostructure injection lasers*, Opt. Quant. Electron. **10**, 311 (1978).
- [137] J. Dorsaz, D. L. Boiko, L. Sulmoni, J.-F. Carlin, W. G. Scheibenzuber, U. T. Schwarz, and N. Grandjean, *Optical bistability in InGaN-based multisection laser diodes*, Appl. Phys. Lett. **98**, 191115 (2011).
- [138] G. Ropars, A. Le Floch, and G. P. Agrawal, *Spectral and spatial dynamics in InGaN blue-violet lasers*, Appl. Phys. Lett. **89**, 241128 (2006).
- [139] T. Meyer, H. Braun, U. T. Schwarz, S. Tautz, M. Schillgalies, S. Lutgen, and U. Strauss, *Spectral dynamics of 405 nm (Al,In)GaN laser diodes grown on GaN and SiC substrate*, Opt. Express **16**, 6833 (2008).
- [140] W. Scheibenzuber, U. Schwarz, L. Sulmoni, J.-F. Carlin, A. Castiglia, and N. Grandjean, *Measurement of the tuneable absorption in GaN-based multi-section laser diodes*, Phys. Status Solidi (c) **8**, 2345 (2011).
- [141] T. Fleischmann, J. Ulloa, M. Moran, G. Rees, J. Woodhead, and M. Hopkinson, *Characterisation of strained (111)B InGaAs/GaAs quantum well lasers with intracavity optical modulator*, J. Microelectron. **33**, 547 (2002).
- [142] M. Ueno and R. Lang, *Conditions for self-sustained pulsation and bistability in semiconductor lasers*, J. Appl. Phys. **58**, 1689 (1985).
- [143] C. Mirasso, G. van Tartwijk, E. Hernandez-Garcia, D. Lenstra, S. Lynch, P. Landais, P. Phelan, J. O’Gorman, M. San Miguel, and W. Elsasser, *Self-pulsating semiconductor lasers: theory and experiment*, IEEE J. Quantum Electron. **35**, 764 (1999).
- [144] E. Feltin, A. Castiglia, G. Cosendey, L. Sulmoni, J.-F. Carlin, N. Grandjean, M. Rossetti, J. Dorsaz, V. Laino, M. Duelk, and C. Velez, *Broadband blue superluminescent light-emitting diodes based on GaN*, Appl. Phys. Lett. **95**, 081107 (2009).
- [145] L. Sulmoni, *Diodes superluminescentes bleues à base de GaN*, Master’s thesis, EPFL, 2009.
- [146] S. Nakamura, M. Senoh, S.-i. Nagahama, N. Iwasa, T. Yamada, T. Matsushita, H. Kiyoku, Y. Sugimoto, T. Kozaki, H. Umemoto, M. Sano, and K. Chocho, *InGaN/GaN/AlGaIn-Based Laser Diodes Grown on GaN Substrates with a Fundamental Transverse Mode*, Jpn. J. Appl. Phys. **37**, L1020 (1998).
- [147] P. J. Mares and S. L. Chuang, *Modeling of self-electro-optic-effect devices*, J. Appl. Phys. **74**, 1388 (1993).
- [148] C. Mounir, *Modulation spectroscopy on III-nitride heterostructures*, Master’s thesis, EPFL, 2012.

-
- [149] F. Renner, P. Kiesel, G. H. Döhler, M. Kneissl, C. G. Van de Walle, and N. M. Johnson, *Quantitative analysis of the polarization fields and absorption changes in InGaN/GaN quantum wells with electroabsorption spectroscopy*, Appl. Phys. Lett. **81**, 490 (2002).
 - [150] G. Schmiedel, P. Kiesel, G. H. Döhler, E. Greger, K. H. Gulden, H. P. Schweizer, and M. Moser, *Electroabsorption in ordered and disordered GaInP*, J. Appl. Phys. **81**, 1008 (1997).
 - [151] C. Lange, M. Schwalm, S. Chatterjee, W. W. Rühle, N. C. Gerhardt, S. R. Johnson, J.-B. Wang, and Y.-H. Zhang, *The variable stripe-length method revisited: Improved analysis*, Appl. Phys. Lett. **91**, 191107 (2007).
 - [152] B. W. Hakki and T. L. Paoli, *cw degradation at 300 K of GaAs double-heterostructure junction lasers. II. Electronic gain*, J. Appl. Phys. **44**, 4113 (1973).
 - [153] C. Ellmers, A. Girndt, M. Hofmann, A. Knorr, W. W. Rühle, F. Jahnke, S. W. Koch, C. Hanke, L. Korte, and C. Hoyler, *Measurement and calculation of gain spectra for (GaIn)As/(AlGa)As single quantum well lasers*, Appl. Phys. Lett. **72**, 1647 (1998).
 - [154] T. Fleischmann, M. Moran, M. Hopkinson, H. Meidia, G. J. Rees, A. G. Cullis, J. L. Sánchez-Rojas, and I. Izpura, *Strained layer (111)B GaAs/InGaAs single quantum well lasers and the dependence of their characteristics upon indium composition*, J. Appl. Phys. **89**, 4689 (2001).
 - [155] T. Miyajima, S. Kono, H. Watanabe, T. Oki, R. Koda, M. Kuramoto, M. Ikeda, and H. Yokoyama, *Saturable absorbing dynamics of GaInN multiquantum well structures*, Appl. Phys. Lett. **98**, 171904 (2011).
 - [156] K. Saito, H. Watanabe, T. Miyajima, M. Ikeda, and H. Yokoyama, *Mode locking of an external-cavity bisection GaInN blue-violet laser diode producing 3 ps duration optical pulses*, Appl. Phys. Lett. **96**, 031112 (2010).
 - [157] S. Arahira, Y. Matsui, and Y. Ogawa, *Mode-locking at very high repetition rates more than terahertz in passively mode-locked distributed-Bragg-reflector laser diodes*, IEEE J. Quantum Electron. **32**, 1211 (1996).
 - [158] I. Friel, C. Thomidis, and T. D. Moustakas, *Ultraviolet electroabsorption modulator based on AlGaIn/GaN multiple quantum wells*, J. Appl. Phys. **97**, 123515 (2005).
 - [159] E. Sari, S. Nizamoglu, T. Ozel, and H. V. Demir, *Blue quantum electroabsorption modulators based on reversed quantum confined Stark effect with blueshift*, Appl. Phys. Lett. **90**, 011101 (2007).
 - [160] M. J. Adams, A. Hurtado, D. Labukhin, and I. D. Henning, *Nonlinear semiconductor lasers and amplifiers for all-optical information processing*, Chaos **20**, 037102 (2010).

- [161] L. Barreira and Y. B. Pesin, *Lyapunov Exponents and Smooth Ergodic Theory* (American Mathematical Soc., Providence, 2002).
- [162] V. Z. Tronciu, M. Yamada, and R. A. Abram, *Analysis of the dynamics of a blue-violet InGaN laser with a saturable absorber*, Phys. Rev. E **70**, 026604 (2004).
- [163] H. Uenohara, R. Takahashi, Y. Kawamura, and H. Iwamura, *Static and dynamic response of multiple-quantum-well voltage-controlled bistable laser diodes*, IEEE J. Quantum Electron. **32**, 873 (1996).
- [164] K. Holc, T. Weig, K. Köhler, J. Wagner, and U. T. Schwarz, *Impact of Band Structure and Absorber Dynamics on Self-Q-Switching in GaN-Based Multisection Laser Diodes at High Reverse Bias*, Appl. Phys. Express **6**, 084101 (2013).
- [165] D. Derickson, R. Helkey, A. Mar, J. Karin, J. Bowers, and R. Thornton, *Suppression of multiple pulse formation in external-cavity mode-locked semiconductor lasers using intrawaveguide saturable absorbers*, IEEE Photon. Technol. Lett. **4**, 333 (1992).
- [166] W. G. Scheibenzuber, C. Hornuss, and U. T. Schwarz, *Dynamics of GaN-based laser diodes from violet to green*, Proc. of SPIE **7953**, 79530K (2011).
- [167] A. Reale, G. Massari, A. Di Carlo, P. Lugli, A. Vinattieri, D. Alderighi, M. Colocci, F. Semon, N. Grandjean, and J. Massies, *Comprehensive description of the dynamical screening of the internal electric fields of AlGaIn/GaN quantum wells in time-resolved photoluminescence experiments*, J. Appl. Phys. **93**, 400 (2003).
- [168] H. Schneider and K. v. Klitzing, *Thermionic emission and Gaussian transport of holes in a GaAs/AlGaAs multiple-quantum-well structure*, Phys. Rev. B **38**, 6160 (1988).
- [169] Y. D. Jho, J. S. Yahng, E. Oh, and D. S. Kim, *Field-dependent carrier decay dynamics in strained InGaIn/GaN quantum wells*, Phys. Rev. B **66**, 035334 (2002).
- [170] R. Shankar, *Principles of quantum mechanics* (Plenum Press, New York, 1982).
- [171] K. Köhler, H.-J. Pollard, L. Schultheis, and C. W. Tu, *Photoluminescence of two-dimensional excitons in an electric field: Lifetime enhancement and field ionization in GaAs quantum wells*, Phys. Rev. B **38**, 5496 (1988).
- [172] T. B. Norris, X. J. Song, W. J. Schaff, L. F. Eastman, G. Wicks, and G. A. Mourou, *Tunneling escape time of electrons from a quantum well under the influence of an electric field*, Appl. Phys. Lett. **54**, 60 (1989).
- [173] Y.-L. Li, T. Gessmann, E. F. Schubert, and J. K. Sheu, *Carrier dynamics in nitride-based light-emitting p-n junction diodes with two active regions emitting at different wavelengths*, J. Appl. Phys. **94**, 2167 (2003).

-
- [174] V. S. Sizov, V. V. Neploh, A. F. Tsatsulnikov, A. V. Sakharov, W. V. Lundin, E. E. Zavarin, A. E. Nikolaev, A. M. Mintairov, and J. L. Merz, *Study of tunneling transport of carriers in structures with an InGaN/GaN active region*, Semiconductors **44**, 1567 (2010).
 - [175] E. Sari, S. Nizamoglu, I.-H. Lee, J.-H. Baek, and H. V. Demir, *Electric field dependent radiative decay kinetics of polar InGaN/GaN quantum heterostructures at low fields*, Appl. Phys. Lett. **94**, 211107 (2009).
 - [176] T. Weig, U. T. Schwarz, L. Sulmoni, J.-M. Lamy, J.-F. Carlin, N. Grandjean, and D. Boiko, *Passive mode-locking in the cavity of monolithic GaN-based multi-section laser diodes*, Proc. of SPIE **8640**, 86400H (2013).
 - [177] S.-B. Choi, J.-P. Shim, D.-M. Kim, H.-I. Jeong, Y.-D. Jho, Y.-H. Song, and D.-S. Lee, *Effect of indium composition on carrier escape in InGaN/GaN multiple quantum well solar cells*, Appl. Phys. Lett. **103**, 033901 (2013).
 - [178] Y. D. Jho, J. S. Yahng, E. Oh, and D. S. Kim, *Measurement of piezoelectric field and tunneling times in strongly biased InGaN/GaN quantum wells*, Appl. Phys. Lett. **79**, 1130 (2001).
 - [179] D. B. Malins, A. Gomez-Iglesias, S. J. White, W. Sibbett, A. Miller, and E. U. Rafailov, *Ultrafast electroabsorption dynamics in an InAs quantum dot saturable absorber at 1.3 μ m*, Appl. Phys. Lett. **89**, 171111 (2006).
 - [180] A. Pinos, S. Marcinkevičius, K. Liu, M. S. Shur, J. Yang, M. Shatalov, and R. Gaska, *Carrier lifetimes in AlGaIn quantum wells: electric field and excitonic effects*, J. Phys. D: Appl. Phys. **41**, 155116 (2008).
 - [181] Y. M. Park, J. K. Son, H. J. Chung, C. Sone, and Y. Park, *InGaIn multiquantum well structure with a reduced internal electric field and carrier decay process by tunneling*, Appl. Phys. Lett. **95**, 231917 (2009).
 - [182] A. Larsson, P. Andrekson, S. Eng, and A. Yariv, *Tunable superlattice p-i-n photodetectors: characteristics, theory, and application*, IEEE J. Quantum Electron. **24**, 787 (1988).
 - [183] V. J. Goldman, D. C. Tsui, and J. E. Cunningham, *Resonant tunneling in magnetic field: Evidence for space-charge buildup*, Phys. Rev. B **35**, 9387 (1987).
 - [184] I. A. Larkin, S. Ujevic, and E. A. Avrutin, *Tunneling escape time from a semiconductor quantum well in an electric field*, J. Appl. Phys. **106**, 113701 (2009).
 - [185] J. R. Lang, N. G. Young, R. M. Farrell, Y.-R. Wu, and J. S. Speck, *Carrier escape mechanism dependence on barrier thickness and temperature in InGaIn quantum well solar cells*, Appl. Phys. Lett. **101**, 181105 (2012).

Bibliography

- [186] R. P. Leavitt and J. W. Little, *Simple method for calculating exciton binding energies in quantum-confined semiconductor structures*, Phys. Rev. B **42**, 11774 (1990).
- [187] V. Nikolaev and E. Avrutin, *Photocarrier escape time in quantum-well light-absorbing devices: effects of electric field and well parameters*, IEEE J. Quantum Electron. **39**, 1653 (2003).
- [188] A. Fox, D. Miller, G. Livescu, J. Cunningham, and W. Jan, *Quantum well carrier sweep out: relation to electroabsorption and exciton saturation*, IEEE J. Quantum Electron. **27**, 2281 (1991).
- [189] P. W. Fry, J. J. Finley, L. R. Wilson, A. Lemaître, D. J. Mowbray, M. S. Skolnick, M. Hopkinson, G. Hill, and J. C. Clark, *Electric-field-dependent carrier capture and escape in self-assembled InAs/GaAs quantum dots*, Appl. Phys. Lett. **77**, 4344 (2000).
- [190] H. Zhao, G. Liu, X. Li, R. Arif, G. Huang, J. Poplawsky, S. Tafon Penn, V. Dierolf, and N. Tansu, *Design and characteristics of staggered InGaN quantum-well light-emitting diodes in the green spectral regime*, IET Optoelectron. **3**, 283 (2009).
- [191] V. V. Nikolaev and E. A. Avrutin, *Quantum-well design for monolithic optical devices with gain and saturable absorber sections*, IEEE Photon. Technol. Lett. **16**, 24 (2004).
- [192] S. Chichibu, A. Abare, M. Mack, M. Minsky, T. Deguchi, D. Cohen, P. Kozodoy, S. Fleischer, S. Keller, J. Speck, J. Bowers, E. Hu, U. Mishra, L. Coldren, S. Den-Baars, K. Wada, T. Sota, and S. Nakamura, *Optical properties of InGaN quantum wells*, Materials Science and Engineering: B **59**, 298 (1999).
- [193] J. Palaski and K. Y. Lau, *Parameter ranges for ultrahigh frequency mode locking of semiconductor lasers*, Appl. Phys. Lett. **59**, 7 (1991).
- [194] S. Yefet, N. Amer, and A. Pe'er, *Intra-cavity gain shaping of mode-locked Ti:Sapphire laser oscillations*, Opt. Express **20**, 9991 (2012).
- [195] N. A. Naderi, F. Grillot, K. Yang, J. B. Wright, A. Gin, and L. F. Lester, *Two-color multi-section quantum dot distributed feedback laser*, Opt. Express **18**, 27028 (2010).
- [196] R. H. Dicke, *Coherence in Spontaneous Radiation Processes*, Phys. Rev. **93**, 99 (1954).
- [197] R. Bonifacio and L. A. Lugiato, *Cooperative radiation processes in two-level systems: Superfluorescence*, Phys. Rev. A **11**, 1507 (1975).
- [198] M. J. Konopnicki and A. T. Rosenberger, *Discussions at the Cooperative Effects Meeting, Redstone Arsenal, Alabama, 1-2 December 1976*, In *Cooperative Effects*

- in Matter and Radiation*, C. M. Bowden, D. W. Howgate, and H. R. Robl, editors, pp. 357–380 (Springer US, New York, 1977).
- [199] P. P. Vasil'ev, *Femtosecond superradiant emission in inorganic semiconductors*, Rep. Prog. Phys. **72**, 076501 (2009).
 - [200] A. A. Belyanin, V. V. Kocharovskiy, and V. V. Kocharovskiy, *Superradiant generation of femtosecond pulses in quantum-well heterostructures*, Quantum Semiclass. Opt. **10**, L13 (1998).
 - [201] A. M. Zheltikov, *Coherent anti-Stokes Raman scattering: from proof-of-the-principle experiments to femtosecond CARS and higher order wave-mixing generalizations*, J. Raman Spectrosc. **31**, 653 (2000).
 - [202] M. Nagel, P. H. Bolivar, M. Brucherseifer, H. Kurz, A. Bosserhoff, and R. Büttner, *Integrated planar terahertz resonators for femtomolar sensitivity label-free detection of DNA hybridization*, Appl. Opt. **41**, 2074 (2002).
 - [203] K. Suhling, P. M. W. French, and D. Phillips, *Time-resolved fluorescence microscopy*, Photochem. Photobiol. Sci. **4**, 13 (2005).
 - [204] J. L. Hall, *Nobel Lecture: Defining and measuring optical frequencies*, Rev. Mod. Phys. **78**, 1279 (2006).
 - [205] A. Kavokin and B. Gil, *GaN microcavities: Giant Rabi splitting and optical anisotropy*, Appl. Phys. Lett. **72**, 2880 (1998).
 - [206] A. A. Belyanin, V. V. Kocharovskiy, and D. S. Pestov, *Novel Schemes and Prospects of Superradiant Lasing in Heterostructures*, Laser Physics **13**, 1 (2003).
 - [207] F. T. Arecchi and E. Courtens, *Cooperative Phenomena in Resonant Electromagnetic Propagation*, Phys. Rev. A **2**, 1730 (1970).
 - [208] N. E. Rehler and J. H. Eberly, *Superradiance*, Phys. Rev. A **3**, 1735 (1971).
 - [209] N. Skribanowitz, I. P. Herman, J. C. MacGillivray, and M. S. Feld, *Observation of Dicke Superradiance in Optically Pumped HF Gas*, Phys. Rev. Lett. **30**, 309 (1973).
 - [210] R. Bonifacio and L. A. Lugiato, *Cooperative radiation processes in two-level systems: Superfluorescence. II*, Phys. Rev. A **12**, 587 (1975).
 - [211] M. Gross and S. Haroche, *Superradiance: An essay on the theory of collective spontaneous emission*, Physics Reports **93**, 301 (1982).
 - [212] R. Florian, L. Schwan, and D. Schmid, *Superradiance and high-gain mirrorless laser activity of O₂-centers in KCl*, Solid State Commun. **42**, 55 (1982).

Bibliography

- [213] P. V. Zinov'ev, S. V. Lopina, Y. V. Naboikin, M. B. Silaeva, V. V. Samartsev, and Y. E. Sheibut, *Superradiance in a diphenyl crystal containing pyrene*, Sov. Phys. JETP **58**, 1129 (1983).
- [214] J. J. Maki, M. S. Malcuit, M. G. Raymer, R. W. Boyd, and P. D. Drummond, *Influence of collisional dephasing processes on superfluorescence*, Phys. Rev. A **40**, 5135 (1989).
- [215] A. A. Belyanin, V. V. Kocharovsky, and V. V. Kocharovsky, *Collective QED processes of electron - hole recombination and electron - positron annihilation in a strong magnetic field*, Quantum Semiclass. Opt. **9**, 1 (1997).
- [216] Y. D. Jho, X. Wang, J. Kono, D. H. Reitze, X. Wei, A. A. Belyanin, V. V. Kocharovsky, V. V. Kocharovsky, and G. S. Solomon, *Cooperative Recombination of a Quantized High-Density Electron-Hole Plasma in Semiconductor Quantum Wells*, Phys. Rev. Lett. **96**, 237401 (2006).
- [217] Y. D. Jho, X. Wang, J. Kono, D. H. Reitze, A. A. Belyanin, V. V. Kocharovsky, V. V. Kocharovsky, and G. S. Solomon, Time-integrated evidence for superfluorescence from dense electron-hole magneto-plasmas in semiconductor quantum wells, arXiv e-print cond-mat/0607022, 2006.
- [218] G. Timothy Noe II, J.-H. Kim, J. Lee, Y. Wang, A. K. Wojcik, S. A. McGill, D. H. Reitze, A. A. Belyanin, and J. Kono, *Giant superfluorescent bursts from a semiconductor magneto-plasma*, Nat. Phys. **8**, 219 (2012).
- [219] D. L. Boiko and P. P. Vasil'ev, *Superradiance dynamics in semiconductor laser diode structures*, Opt. Express **20**, 9501 (2012).
- [220] J. A. Greenberg, *Collective Light-matter Interactions via Emergent Order in Cold Atoms*, PhD thesis, Duke University, 2012.
- [221] L. Kappei, *Dynamics and coherent effects of high density plasmas in semiconductor nanostructures*, PhD thesis, EPFL, n. 3187, 2005.
- [222] P. P. Vasil'ev, *Ultrafast diode lasers: fundamentals and applications* (Artech House, Boston, 1995).
- [223] J. C. MacGillivray and M. S. Feld, *Theory of superradiance in an extended, optically thick medium*, Phys. Rev. A **14**, 1169 (1976).
- [224] D. C. Burnham and R. Y. Chiao, *Coherent Resonance Fluorescence Excited by Short Light Pulses*, Phys. Rev. **188**, 667 (1969).
- [225] M. G. Benedict, *Super-radiance: multiatomic coherent emission* (Institute of Physics publishing, Bristol, 1996).

-
- [226] E. Ressayre and A. Tallet, *Conditions of availability of the Markoff approximation for the description of cooperative spontaneous emission*, Phys. Rev. A **12**, 1725 (1975).
 - [227] K. Misawa, H. Yao, T. Hayashi, and T. Kobayashi, *Quenching of the superradiative decay by confined acoustic-phonons in CdS microcrystallites*, J. Lumin. **48-49**, 269 (1991).
 - [228] P. Borri, W. Langbein, S. Schneider, U. Woggon, R. L. Sellin, D. Ouyang, and D. Bimberg, *Ultralong Dephasing Time in InGaAs Quantum Dots*, Phys. Rev. Lett. **87**, 157401 (2001).
 - [229] T. Brandes, J. Inoue, and A. Shimizu, *Dicke superradiance in a magnetoplasma*, Physica B: Condensed Matter **272**, 341 (1999).
 - [230] C. R. Ding, W. Lin, B. C. Chen, F. L. Zhao, J. W. Dong, M. Shi, H. Z. Wang, Y. F. Hsu, and A. B. Djurišić, *Super-radiance of excitons in a single ZnO nanostructure*, Appl. Phys. Lett. **93**, 151902 (2008).
 - [231] O. Hess and S. W. Koch, *Filamentation and Beam Propagation in Broad-Area Semiconductor Lasers*, IEEE J. Quantum Electron. **1**, 35 (1995).
 - [232] V. V. Zheleznyakov, V. V. Kocharovsky, and V. V. Kocharovsky, *Polarization waves and super-radiance in active media*, Sov. Phys. Usp. **32**, 835 (1989).
 - [233] T. Ochalski, B. Gil, P. Lefebvre, N. Grandjean, J. Massies, and M. Leroux, *Photoreflectance spectroscopy as a powerful tool for the investigation of GaN-AlGaIn quantum well structures*, Solid State Commun. **109**, 567 (1999).
 - [234] J. L. Shay, *Photoreflectance Line Shape at the Fundamental Edge in Ultrapure GaAs*, Phys. Rev. B **2**, 803 (1970).
 - [235] P. Kiesel, F. Renner, M. Kneissl, N. Johnson, and G. Döhler, *Electroabsorption Spectroscopy — Direct Determination of the Strong Piezoelectric Field in InGaIn/GaN Heterostructure Diodes*, Phys. Status Solidi (a) **188**, 131 (2001).
 - [236] R. Schmidt, P. Kiesel, M. Kneissl, C. Van de Walle, N. Johnson, F. Renner, and G. Döhler, *Direct determination of the built-in polarization field in InGaIn/GaN quantum wells*, In *12th International Conference on Semiconducting and Insulating Materials, 2002. SIMC-XII-2002*, pp. 48–51, 2002.
 - [237] C. Y. Lai, T. M. Hsu, W.-H. Chang, K.-U. Tseng, C.-M. Lee, C.-C. Chuo, and J.-I. Chyi, *Direct measurement of piezoelectric field in InGaIn/GaN multiple quantum wells by electrotransmission spectroscopy*, J. Appl. Phys. **91**, 531 (2002).
 - [238] L. P. Avakyants, M. L. Badgutdinov, P. Y. Bokov, A. V. Chervyakov, S. S. Shirokov, A. E. Yunovich, A. A. Bogdanov, E. D. Vasil'eva, D. A. Nikolaev, and

Bibliography

- A. V. Feopentov, *Electroreflectance spectra of InGaN/AlGaN/GaN quantum-well heterostructures*, Semiconductors **41**, 1060 (2007).
- [239] T. M. Hsu, C. Y. Lai, W.-H. Chang, C.-C. Pan, C.-C. Chuo, and J.-I. Chyi, *Electroreflectance study on the polarization field in InGaN/AlInGaN multiple quantum wells*, Appl. Phys. Lett. **84**, 1114 (2004).
- [240] L. P. Avakyants, P. Y. Bokov, A. V. Chervyakov, A. V. Chuyas, A. E. Yunovich, E. D. Vasileva, D. A. Bauman, V. V. Uelin, and B. S. Yavich, *Interference effects in the electroreflectance and electroluminescence spectra of InGaN/AlGaN/GaN light-emitting-diode heterostructures*, Semiconductors **44**, 1090 (2010).

Luca Sulmoni

#27 Rue de la Paix
CH-1020 Renens (VD)
Switzerland

swiss
30 years old
email: luca.sulmoni83@gmail.com
mobile phone: +41 76 572 13 88

Interests

GaN-based optoelectronic devices (LEDs, SLEDs, LDs, MS-LDs).

Education

- **Swiss Federal Institute of Technology (EPFL)** Lausanne
Ph.D in Photonics, Physics Sept. 2009 - Jan. 2014
- **Swiss Federal Institute of Technology (EPFL)** Lausanne
Master, Physics Sept. 2007 - Feb. 2009
- **Swiss Federal Institute of Technology (EPFL)** Lausanne
Bachelor, Physics Oct. 2005 - July 2007
 - First year performed at the Swiss Federal Institute of Technology Zurich (ETHZ).

Work Experiences

- **Doctoral assistant** EPFL, Lausanne
Laboratory of Advanced Semiconductors for Photonics and Electronics (LASPE) Sept. 2009 - Jan. 2014
 - Static and dynamic characteristics of InGaN-based laser diodes.
- **Scientific assistant** EPFL, Lausanne
Laboratory of Advanced Semiconductors for Photonics and Electronics (LASPE) Feb. 2009 - Aug. 2009
 - Material characterizations and device processing in clean room.
- **Student-Assistant** EPFL, Lausanne
General Physics III & IV for the faculty of Physics Oct. 2006 - Feb. 2009
General Physics I & II for the faculty of Life Sciences Sept. 2008 - Feb. 2009
 - Class sessions, correct and grade student's exercises.

School Projects

- **Blue Superluminescent Diode (SLED) - Prof. N. Grandjean** Master thesis, EPFL
Laboratory of Advanced Semiconductors for Photonics and Electronics (LASPE) Sept. 2008 - Feb. 2009
 - Optical and electrical characterizations of SLEDs emitting in the blue wavelength range.
- **J/ ψ production in LHCb - Prof. O. Schneider** Master internship, EPFL
Laboratory for High Energy Physics (LPHE) Mar. 2008 - June 2008
 - Analysis of the fundamental properties of the J/ ψ meson along with its production and decay processes.
- **Confinement towards the high densities - Prof. A. Pochelon** Master internship, EPFL
Plasma Physics Research Centre (CRPP) Sept. 2007 - Feb. 2008
 - Enquiry of the causes related to the saturation of the confinement's time of a hot plasma in the "Tokamak à Configuration Variable" (TCV).

Publications

- O. Vojtech, A. Wonfor, L. Sulmoni, P. Vasilev, J.-M. Lamy, J.-F. Carlin, N. Grandjean, R. Penty, I. White, *Hybrid and Passive Mode-Locking of a Monolithic Two-Section MQW InGaN/GaN Laser Diodes*, IEEE Photon. Technol. Lett. **25**, 1514 (2013).

- P. P. Vasil'ev, A. B. Sergeev, I. V. Smetanin, T. Weig, U. T. Schwarz, L. Sulmoni, J. Dorsaz, J.-M. Lamy, J.-F. Carlin, N. Grandjean, X. Zeng, T. Stadelmann, S. Grossmann, A. C. Hoogerwerf, and D. L. Boiko, *Mode locking in monolithic two-section InGaN blue-violet semiconductor lasers*, Appl. Phys. Lett. **102**, 121115 (2013).
- T. Weig, U. T. Schwarz, L. Sulmoni, J.-M. Lamy, J.-F. Carlin, N. Grandjean, and D. L. Boiko, *Passive mode-locking in the cavity of monolithic GaN-based multi-section laser diodes*, Proc. of SPIE **8640**, Novel In-Plane Semiconductor Lasers XII, 86400H (2013).
- L. Sulmoni, J.-M. Lamy, J. Dorsaz, A. Castiglia, J.-F. Carlin, W. G. Scheibenzuber, U. T. Schwarz, Z. Xi, D. L. Boiko, and N. Grandjean, *Lasing characteristics of multi-section InGaN-based laser diodes*, J. Appl. Phys. **112**, 103112 (2012).
- J. Dorsaz, D. L. Boiko, L. Sulmoni, J.-F. Carlin, W. G. Scheibenzuber, U. T. Schwarz, and N. Grandjean, *Optical bistability in InGaN-based multi-section laser diodes*, Appl. Phys. Lett. **98**, 191115 (2011).
- W. G. Scheibenzuber, C. Hornuss, U. T. Schwarz, L. Sulmoni, J. Dorsaz, J.-F. Carlin, and N. Grandjean, *Self-Pulsation at zero absorber bias in GaN-based multi-section laser diodes*, Appl. Phys. Express **4**, 062702 (2011).
- W. G. Scheibenzuber, U. T. Schwarz, L. Sulmoni, J. Dorsaz, J.-F. Carlin, and N. Grandjean, *Recombination coefficients of GaN-based laser diodes*, J. Appl. Phys. **109**, 093106 (2011).
- W. G. Scheibenzuber, U. T. Schwarz, L. Sulmoni, J.-F. Carlin, A. Castiglia, and N. Grandjean, *Measurements of the Tunable Absorption in GaN-based Multi-Section Laser Diodes*, Physica Status Solidi (c) **8**, 2345 (2011).
- W. G. Scheibenzuber, U. T. Schwarz, L. Sulmoni, J.-F. Carlin, A. Castiglia, and N. Grandjean, *Bias-dependent absorption coefficient of the absorber section in GaN-based multisection laser diodes*, Appl. Phys. Lett. **97**, 181103 (2010).
- E. Feltin, A. Castiglia, G. Cosendey, L. Sulmoni, J.-F. Carlin, N. Grandjean, *Broadband blue superluminescent light-emitting diodes based on GaN*, Appl. Phys. Lett. **95**, 081107 (2009).
- A. Pochelon, S. Brunner, Y. Camenen, S. Coda, J. Graves, A. Marinoni, A. Martynov, H. Reimerdes, O. Sauter, A. Scarabosio, S. Alberti, P. Angelino, R. Behn, A. Bortolon, A. Bottino, L. Curchod, K. Daouk, B. P. Duval, A. Fasoli, I. Furno, T. P. Goodman, M. A. Henderson, F. Hofmann, A. Karpushov, X. Lapillonne, J. B. Lister, Y. Martin, J. M. Moret, S. Medvedev, J. I. Paley, R. A. Pitts, F. Piras, L. Porte, F. Ryter, L. Sulmoni, A. Sushkov, L. Villard, M. Q. Tran, H. Weisen, *Physics Insight and Performance Benefit in MHD and Energy Transport from Plasma Shaping Experiments in the TCV Tokamak*, in *22nd IAEA Fusion Energy Conf. (FEC) - 50th Anniversary of Controlled Nuclear Fusion Research*, pages EX/P5-15, Vienna, 2008.

Presentations

Invited oral presentations

- L. Sulmoni, J. Dorsaz, A. Castiglia, J.-F. Carlin, and N. Grandjean, *Impact of the reverse bias voltage on the optical characteristics of multi-section GaN-based laser diodes*, IV Workshop on Physics and Technology of Semiconductor Lasers (Kazimierz Dolny, Poland, October 23-26, 2011)

Contributed oral presentations

- L. Sulmoni, J.-M. Lamy, J.-F. Carlin, X. Zeng, D. L. Boiko, and N. Grandjean, *Self-pulsating multi-section InGaN laser diode*, 39th International Symposium on Compound Semiconductors - ISCS 2012 (Santa Barbara, CA, USA, August 26 - 30, 2012)
- L. Sulmoni, J.-M. Lamy, J. Dorsaz, J.-F. Carlin, D. L. Boiko, X. Zeng and N. Grandjean, *Optical characteristics of multi-section GaN-based laser diodes*, 36th Workshop on Compound Semiconductor Devices and Integrated Circuits - WOCSIDICE 2012 (Island of Porquerolles, France, May 28 - June 1, 2012)
- L. Sulmoni, J. Dorsaz, J.-F. Carlin, and N. Grandjean, *Reverse bias voltage dependent optical characteristics of multi-section GaN-based laser diodes*, 9th International Conference on Nitride Semiconductors - ICNS 2011 (Glasgow, Scotland, July 10 - 15, 2011)

- L. Sulmoni, J. Dorsaz, A. Castiglia, J.F. Carlin, and N. Grandjean, *Optical characteristics of multi-section GaN-based laser diodes*, Joint Annual Meeting of the Swiss Physical Society - SPS2011 (Lausanne, Switzerland, June 15 - 17, 2011)
- L. Sulmoni, J. Dorsaz, A. Castiglia, J.-F. Carlin and N. Grandjean, *Effect of saturable absorber bias voltage on the output characteristics of multi-section GaN-based laser diodes*, International Workshop on Nitride semiconductors - IWN2010 (Tampa, FL, USA, September 19 - 24, 2010)

Seminars

- L. Sulmoni, J.-M. Lamy, J. Dorsaz, A. Castiglia, J.F. Carlin, and N. Grandjean, *Superradiance in GaN-based laser diodes: theory and experiment*, LOEQ seminar (Lausanne, Switzerland, April 24, 2012)
- L. Sulmoni, J.-M. Lamy, J. Dorsaz, A. Castiglia, J.-F. Carlin, and N. Grandjean, *Multi-section laser diodes*, LASPE internal seminar (Les Diablerets, Switzerland, March 8 - 9 2012)
- L. Sulmoni, *Émission stimulée : La diode laser*, IPEQ internal seminar (Lausanne, Switzerland, February 4 - 5, 2010)

Posters

- L. Sulmoni, J. Dorsaz, J.-F. Carlin, and N. Grandjean, *Multi-section GaN-based laser diodes*, EPFL Photonics Day 2011 (Lausanne, Switzerland, November 4, 2011)
- L. Sulmoni, J. Dorsaz, D. L. Boiko, J.-F. Carlin, and N. Grandjean, *Optical characteristics of multi-section InGaN-based laser diodes*, European Semiconductor Laser Workshop - ESLW 2011 (Lausanne, Switzerland, September 23 - 24, 2011)
- L. Sulmoni, D. L. Boiko, J. Dorsaz, J.-F. Carlin, W. G. Scheibenzuber, U. T. Schwarz and N. Grandjean, *Optical bistability in InGaN-based multi-section laser diodes: Theory and experiment*, European Semiconductor Laser Workshop - ESLW 2011 (Lausanne, Switzerland, September 23 - 24, 2011)
- L. Sulmoni, J. Dorsaz, J.-F. Carlin, and N. Grandjean, *Optical characteristics of multi-section GaN-based laser diodes*, 38th International Symposium on Compound Semiconductors - ISCS 2011 (Berlin, Germany, May 22 - 26, 2011)

Skills

Languages:	Italian (mother tongue), French (fluent), English (fluent, First Certificate), German (good, Zentrale Mittelstufenprüfung)
Operating Systems:	Windows, Unix and Linux
Programming:	C++, HTML, L ^A T _E X
Scientific Software:	Matlab, Root, Origin, Autodesk Inventor (CAD)
Experimental:	semiconductor growth (MOVPE), device processing (microfabrication techniques in cleanroom environment), characterization (XRD, AFM, SEM, <i>L-I-V</i> profiles, photo/electro-luminescence, photo/electro-reflectance, time-integrated/resolved photoluminescence)

Hobbies & Sports

Saxophone (awarded with cantonals exams FEBATI), literature, chess, billiard.
Football (trainer certificate), swimming (teacher & lifeguard), apparatus gymnastic, scuba diving, ski/snowboard.